Research Frontiers 2021

SPring-8
SACLA

ISSN 2433-5126
SPring-8 Document D2022-009

SPring-8/SACLA Research Frontiers 2021

CONTENTS

Physical Science

Chemical Science

Earth & Planetary Science

Industrial Applications

Accelerators & Beamlines Frontiers 106

SPring-8

New Apparatus, Upgrades & Methodology

SACLA

Facility Status 114

Note: The principal publication(s) concerning each article is indicated with all author's names in italics in the list of references.

PREFACE

It is my great pleasure to publish SPring-8/SACLA Research Frontiers 2021. JASRI has stewardship responsibility over SPring-8 and SACLA, whereas RIKEN has ownership. SPring-8 and SACLA are located on the same campus; thus, their synergy produces groundbreaking results.

Despite continuing COVID-19 issues, the activities of SPring-8 and SACLA in FY2021 recovered to prepandemic levels, although users from abroad are still subject to entry restrictions by the Japanese government. Moreover, many precautionary measures are still in place for users on site.
In FY2021, SPring-8 welcomed about 13,500 users who came to perform 1,996 experiments. Currently, there are more than 1,000 and about 70 research papers published by SPring-8 and SACLA users, respectively.

Two SPring-8 and SACLA users were conferred prestigious awards in 2021 for their achievements in science and technology. Professor T. Arima and Professor T. Kimura (The University of Tokyo) were awarded the Nishina Memorial Prize for the discovery and exploration of spin-induced multiferroics, developed by precise structural analysis using X-rays at SPring-8.
Director General M. Kawai (Institute for Molecular Science) was designated as a Person of Culture for the realization of the unimolecular reaction by scanning tunneling microscopy at SPring-8.
Director T. Ishikawa, Dr. H. Tanaka and Dr. M. Yabashi (RIKEN SPring-8 Center) were awarded the Yamazaki Teiichi Prize for their contribution to science through the development of a compact X-ray free-electron laser named SACLA and its application in research.

This volume includes two comprehensive review articles. In one article, Professor S. P. Cramer (University of California, Davis, USA) and Dr. H. Wang (SETI Institute, USA) describe research progress on the characterization of Fe–H bonding in hydrogenases and model compounds by nuclear resonant vibrational spectroscopy (NRVS) performed at SPring-8. In the other article, Professor K. Hirose (Tokyo Institute of Technology) and Professor S. Tagawa (The University of Tokyo) describe recent research on hydrogen and other light elements in the Earth's core on the basis of the results of X-ray diffraction (XRD) and inelastic X-ray scattering (IXS) performed at high pressures and high temperatures.

In the main part of this volume, active SPring-8 users describe the importance of their findings in various fields that include life science, physical science, chemical science, earth and planetary science, and industrial applications. In addition, report on the principal activities of SPring-8/SACLA facilities are included in the sections of Accelerators & Beamlines Frontiers and Facility Status.

I am very grateful to the many authors and experts who contributed their papers to this volume. Special thanks are due to Dr. Naoto Yagi, Ms. Marcia Obuti-Daté, and the members of the editorial board for their relentless effort.

Yoshiyuki Amemiya
President
Japan Synchrotron Radiation Research Institute (JASRI)

Editor's Note

This is the 2021 issue of SPring-8/SACLA Research Frontiers that covers outstanding scientific outcomes of SPring-8 and SACLA in 2020 and 2021, the so-called COVID-19 era. Even under this unpreceded difficult situation, users published a plenty of papers (perhaps because they could not make experiments and had time to concentrate on analysis and writing). The best scientific achievements are collected from more than 1,000 papers published using SPring-8 or SACLA each year.

The two reviews in this issue are contributed by major user groups of SPring-8. Prof. Cramer has developed the technique of NRVS and his group have been using it to investigate functions of metalloproteins. Prof. Hirose has been leading the earth core science at SPring-8 for nearly two decades. Both of these studies were carried out in long-term proposals and not only produced outcomes with high scientific significance but also gave strong impacts on other users of SPring-8.

As has been the case in recent years, there are many reports on fuel cells and Li-ion batteries reflecting the gravity of the energy crisis in the world. As for the experimental techniques, there are several reports on XPS or HAXPES at near ambient pressure or even at atmospheric pressure. There is a high demand for operand measurement of chemical reactions which is also evident in other reports. These experiments are making very good use of intense synchrotron radiation of SPring-8. Since these techniques are still being improved, we can expect more reports on them in the next few years.

In addition to the scientific results (Scientific Frontiers), there is some information on hard and soft infrastructures that support scientific research. Although some important numbers such as the operation time are given in this part, other information and more complete statistical numbers on the operation of SPring-8 and SACLA are available on the website so that more updated information can be accessed (http://www.spring8.or.jp/en/about_us/spring8data/).

The full text of SPring-8/SACLA Research Frontiers is also available on the SPring-8 website (http://www.spring8.or.jp/en). For the list of publications produced by SPring-8 users and staff, please visit the publication database at http://www.spring8.or.jp/en/science/publication_database/.

On behalf of all the editors, I would like to thank those who helped us by recommending excellent research results suitable for publication in this issue, and the users and staff of SPring-8 who contributed their reports to this issue despite this pandemic.

Naoto Yagi
Japan Synchrotron Radiation Research Institute (JASRI)

Editorial Board

Scientific Frontiers

Review Article

Iron and Hydrogen – Characterization of Fe-H Bonding in Hydrogenases and Model Compounds Using Nuclear Resonant Vibrational Spectroscopy (NRVS)

1. Introduction

Molecular hydrogen, H_2, has been offered as an ideal carbon-free energy carrier, and a sustainable 'hydrogen economy' without CO_2 emissions is one approach to mitigating climate change. Nowadays, most industrial H_2 is produced by high-temperature steam reforming of natural gas which leads to the release of at least one molecule of CO_2 for every four molecules of H_2 produced. An ideal 'hydrogen economy' would use electrochemical energy from solar or other carbon-free sources to drive the water-splitting 'hydrogen evolution reaction' (HER). The 'green hydrogen' would be consumed in fuel cells to produce electricity for a 'decarbonized' economy.

At the moment, the best human-made catalysts for producing or consuming H_2 rely on precious and rare platinum (Pt). In fact, the 2020 SPring-8 Research Frontiers contained an excellent review by Iwasawa of synchrotron-based Pt fuel cell research. Over the long term, better H_2-processing catalysts from earth-abundant materials could play an essential part of H_2 'decarbonization' plans. One source of inspiration is Nature, which employs hydrogenase (H_2ase) enzymes that are as fast as the best Pt catalysts, but use plentiful Fe or Ni at their active sites. H_2 uptake and production in these enzymes is catalyzed by two types of H_2ases, [FeFe] H_2ase [1] and [NiFe] H_2ase [2].

The active site for [FeFe] H_2ases is an 'H-cluster', which has an iron-sulfur $[4Fe–4S]_H$ subcluster linked by a cysteine thiolate to an organometallic $[2Fe]_H$ subcluster (Fig. 1(a)) [1]. The active site in [NiFe] H_2ases (Fig. 1(b)) [2] has a Ni linked to Fe by a pair of cysteine thiolate (S) ligands with two more terminal cysteine thiolate (S) ligands.

The H_2ase active sites are buried in protein matrices which have specific amino acid channels for transporting protons and additional Fe–S clusters for moving electrons (Fig. 2). This is elegant protein engineering, but it also means that the active sites in enzyme solutions are quite dilute, on the order of 1 mM or less. This constrains the types of methods that can be used to study these enzymes.

Detailed knowledge about the structures and catalytic mechanisms of H_2ases is important for using the enzymes themselves or for building synthetic catalysts that mimic their properties. Although crystal structures are available for many of these enzymes, the intermediates with bound H have not been crystallized. We thus resort to spectroscopic methods. One key goal for understanding these enzymes is to document how H is bound to Fe in various intermediate states.

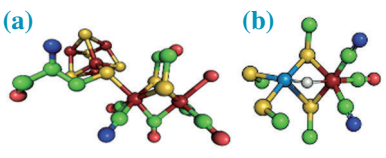

Fig. 1. **(a)** The [FeFe] H_2ase H-cluster. **(b)** The [NiFe] H_2ase active center. Color scheme: Fe, Ni, S, C, N, O, H.

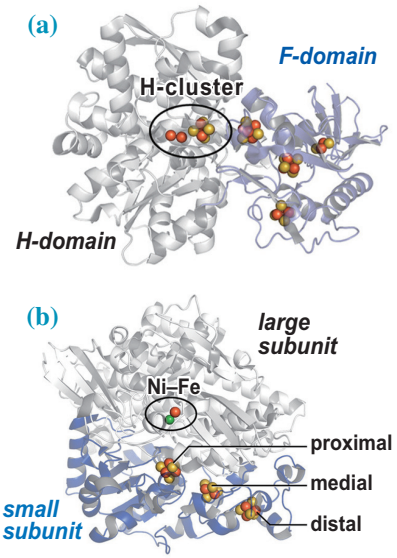

Fig. 2. **(a)** The [FeFe] H_2ase protein. **(b)** The [NiFe] H_2ase protein. Color scheme: Fe, Ni, S.

Vibrational spectroscopy is commonly used by chemists to unravel the structures of unknown species, and the two most familiar approaches are infrared (IR) and resonance Raman (RR) techniques. In fact, IR has been used to study the CO and CN stretching modes in H_2ases, and RR has been used to record Fe–S stretches. However, Fe–H vibrations are too weak to see by IR, and H-bound complexes are too photosensitive for RR. We have thus turned to a synchrotron-based method, Nuclear Resonance Vibrational Spectroscopy (NRVS).

2. Nuclear Resonance Vibrational Spectroscopy

In an NRVS experiment one observes vibrational transitions that occur as sidebands of a nuclear transition (Fig. 3). An ultra-high energy resolution monochromator is required, because vibrational linewidths are on the order of 0.5 meV (4 cm^{-1}) compared to the photon energy (for ^{57}Fe) of 14.4 keV! A very fast gated APD detector is required to see the very small fraction of nuclear events in a background of electronic events that is many orders of magnitude higher (Fig. 3). These requirements were initially met at SPring-8 BL09XU, where we began and first developed our NRVS experiments with the help of staff scientist Yoshitaka Yoda. Later, with the help of Dr. Yoda, we moved some experiments to beamline BL19LXU, to take advantage of the higher flux on a multi-undulator beamline.

For bioinorganic chemistry experiments, NRVS has several advantages over traditional vibrational spectroscopies. In the case of ^{57}Fe NRVS, one observes only vibrations which involve motion of the ^{57}Fe nucleus. Thus, although proteins have thousands of normal modes, ^{57}Fe NRVS allows us to focus on the important modes which involve ^{57}Fe motion. Furthermore, biochemists have developed techniques for labeling, for example, just the $[2Fe]_H$ subsite of [FeFe] H_2ase. This allows us to plan exquisitely selective experiments that focus on modes involving the enzyme active site. With sufficient signal averaging, we can even see vibrations with relatively little ^{57}Fe motion, such as Fe-H bending and stretching modes.

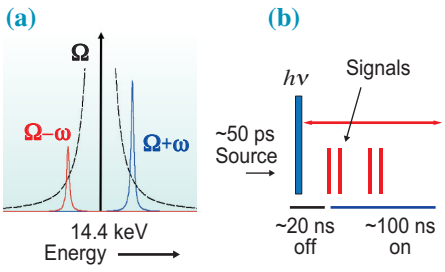

Fig. 3. **(a)** Energies involved in NRVS. The ^{57}Fe Mössbauer transition is at Ω. The vibrational energies ω are on the order of 10–100 meV. **(b)** The timing scheme that allows detection of NRVS. The ^{57}Fe excited state lifetime is ~100 ns. Detectors are turned off to reject the 'prompt' pulses and then turned back on to capture delayed nuclear events.

3. [NiFe] Hydrogenase Studies: Fe–H–Ni Wagging Modes

Our earliest hydrogenase work involved the [NiFe] H_2ase from *Desulfovibrio vulgaris* Miyazaki F (*Dv*MF). We first reported the ability to see typical Fe–CO and Fe–CN bending and stretching modes [3]. More exciting, with extensive signal averaging, we were able to discern a Fe–H–Ni wagging mode that confirmed the presence of a hydride bridge in the most reduced Ni-R form of this enzyme (Fig. 4) [2]. Key to the success of this measurement was the extra flux available on the extra-long undulator beamline BL19LXU.

The existence and location of this band provided a critical reference point for selecting the likely structure of the [NiFe] center in the 'form R' state from at least 12 models considered by density function theory (DFT) calculations [2]. Of course, all the Fe–CN and Fe–CO features were also constraints for the DFT simulations. We are now conducting similar studies on the regulatory and the membrane-bound [NiFe]-H_2ases from *Ralstonia eutropha* (*Re*RH and *Re*MBH) [4,5].

4. [FeFe] Hydrogenase Studies: Fe–H Bending Modes

With [FeFe] H_2ases, H_2 bond activation occurs at the Fe_d site in the $[2Fe]_H$ sub-cluster distal to the $[4Fe4S]_H$ cluster. At this site the aminodithiolate (ADT) group plays a fundamental role in H^+ transfer to a proton relay to the protein exterior (Fig. 5). Thanks to developments in artificial maturation, our collaborators were able to replace the NH of the ADT bridge in the *Cr*-HydA1 $[2Fe]_H$ subcluster with an O to form an oxodithiolate (ODT) variant. This replacement obstructs the H^+ transport chain, which is one approach to trapping a transient intermediate known as H_{hyd}.

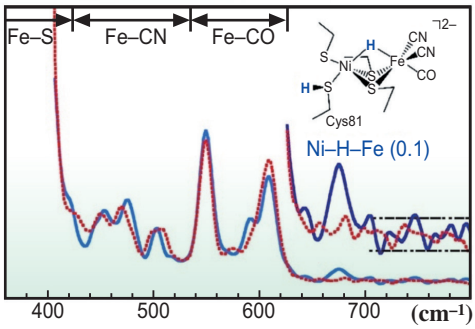

Fig. 4. NRVS PVDOS for *Dv*MF [NiFe] H_2ase in H_2O (—) *versus* D_2O (—) showing a Ni–H–Fe wagging mode at 675 cm^{-1} (signal ~0.1 cts/s). The top right insert is the best DFT model obtained *via* simulating the observed NRVS.

Another type of variant involves mutagenesis of Cys to Ser at position 169, thus changing the functional group adjacent to the H-cluster from –SH to –OH (Fig. 5). The C169S enzyme has a 100-fold reduction in catalytic activity compared to native *Cr*-HydA1, presumably due to less efficient transfer of H^+ to the H-cluster [1]. We have examined the H_{hyd} forms of the ODT variant, the C169S variant, and wild-type enzyme by NRVS, and the spectra for these three species are compared in Fig. 6.

As seen in Fig. 6, the NRVS signature for the terminal X–Fe–H bending motion in the H_{hyd} state exhibits two main bands in the 650–750 cm^{-1} range. From DFT calculations these are rationalized as arising from H^- motion perpendicular and parallel to the N-$[2Fe]_H$ plane (Fig. 7). Since the

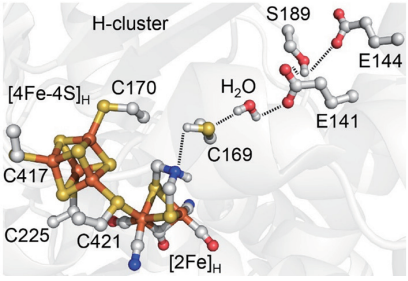

Fig. 5. The proton transfer chain in [FeFe] H_2ase from *Chlamydomonas reinhardtii* – *Cr*HydA1.

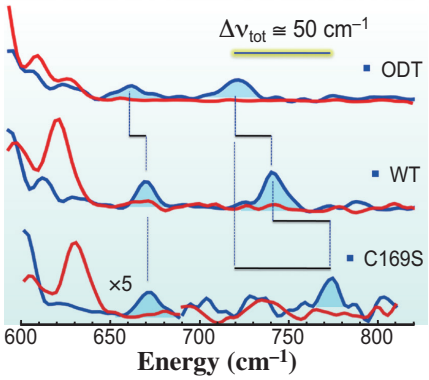

Fig. 6. NRVS PVDOS in the X–Fe–H region for H_2ase samples in the H_{hyd} form, in H_2O (—) *vs* D_2O (—): ODT variant (top), wild-type (middle), and C169S (bottom).

nitrogen of the ADT bridge is involved in transporting solvent protons H^+ to and from Fe_d through the relay of conserved amino acids that lead to the surface of the protein, understanding the motion of the Fe–H with respect to that N is directly relevant to the catalytic mechanism.

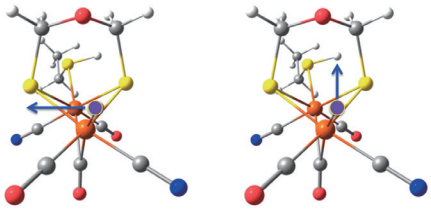

Fig. 7. Direction of hydride motion (labeled •→) associated with lower frequency (left) and higher frequency (right) bending modes seen in NRVS.

We found a significant shift to higher frequency in the X–Fe–H in-plane bending mode of C169S *Cr*-HydA1 (772 cm^{-1}) compared to the native protein (744 cm^{-1}) and ODT variant *Cr*-HydA1 (727 cm^{-1}) (Fig. 6) [1,6,7]. The large upshift of C169S band in comparison with the native enzyme is rationalized by DFT calculations to be caused by stronger interaction between the –OH of C169S with the bridgehead –NH– of the active site in comparison with the –SH/–NH– in the native enzyme. In contrast, the lower energy band, produced by the localized 'out-of-plane' normal mode, is essentially a pure Fe_d–H bending motion which is decoupled from other nuclei. Thus, the out-of-plane wagging modes have about the same frequency (670–675 cm^{-1}) for all three variants.

5. [FeFe] H_2ase with Labeled ADT: Low Frequency Modes

Site-selective labeling of the $[2Fe]_H$ subcluster alone enables other interesting features to be observed. For example, a pair of synthetic diiron precursor isotopologues were used to reconstitute the H-cluster of *Cr*-HydA1 [FeFe] H_2ase: one of them was labeled with $–^{13}CD_2–$ADT while the other had natural abundance $–CH_2–$ADT (Fig. 8) [6]. NRVS was measured on samples poised in the catalytically crucial H_{hyd} state containing a terminal hydride at the distal Fe_d site. The spectral effect of $–^{13}CD–$ *vs* $–CH_2–$ were observed in NRVS for this pair of H_{hyd} enzymes.

Among the differences in various locations, small shifts in the X–Fe–H wagging and in-plane bending modes were observed. Of special interest, changes in modes as low as 160 cm^{-1} were also observed (Fig. 9). DFT simulations of the spectra allowed identification of the ^{57}Fe motion coupled to the ADT ligand motions. A variety of normal modes involve shortening of the distance between the distal Fe–H hydride and ADT NH bridgehead hydrogen. These are presumed to be 'rate-promoting vibrations' which may be relevant to the formation of a transition state on the way to H_2 formation.

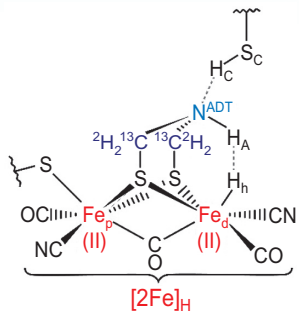

Fig. 8. Labeling of ADT ligand that allowed confirmation of assignments.

6. H–Fe–H_2 Model Complexes: Fe–H and Fe–H_2 Stretching

In addition to Fe–H bending or wagging features, Fe–D or Fe–H stretching features at higher energies can provide additional information to constrain DFT calculations of proposed structural models. As preparation for observing Fe–H/D stretching in enzyme samples, we have examined these features in various model complexes [2,8]. At the highest energy for NRVS to date, we looked for Fe–H stretching modes in *trans*-[$^{57}Fe(\eta^2$-$H_2)$(H)(dppe)$_2$][BPh_4] (Fig. 11) [8]. The vibrational modes associated with the NRVS peaks at 1774 and 1915 cm^{-1} were assigned: the former is the asymmetric Fe–H stretching mode from the Fe(H_2) component, while the latter is the Fe–H stretching from the FeH bond. These features will be useful standards for Fe(H_2) or FeH structures in planned searches for Fe(H_2) bonding in H_2ase samples. The peak at 1956 cm^{-1} is the

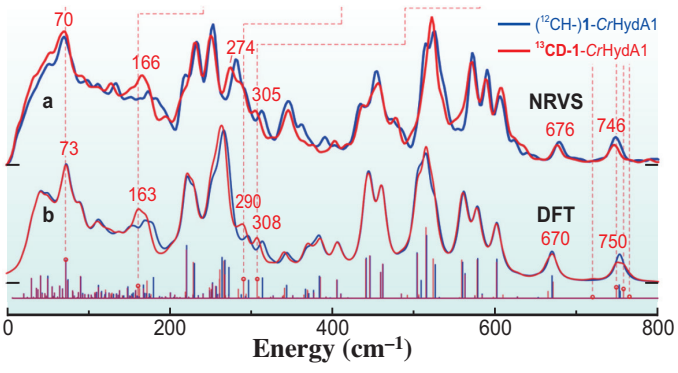

Fig. 9. Observed and calculated NRVS PVDOS.

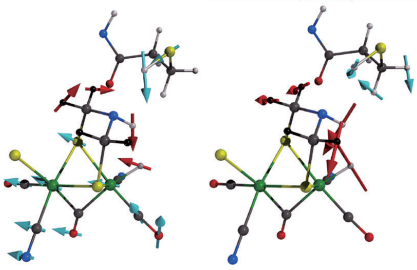

Fig. 10. Left: a low frequency mode calculated at 73 cm^{-1}. Right: a high frequency mode calculated at 758 cm^{-1}. Both modes bring Fe–H and N–H closer together (and also involve C169 S–H). Color scheme: Fe, S, C, N, O, H.

Fe–H stretching mode from a byproduct when H_2 dissociates. This is the highest energy NRVS band observed to date.

7. A summary of what have we learned so far

The NRVS results so far, combined with DFT simulations to interpret the data, have revealed important information about H_2ases that was not available from X-ray diffraction or other spectroscopies. First, we have seen that [FeFe] H_2ases bind hydrides exclusively as terminal ligands, as opposed to the bridging form used by [NiFe] H_2ases. Second, we have seen that the dynamics of the terminal hydride are exquisitely sensitive to both the nature of the dithiolate bridging ligand and to the sidechain of the amino acid in the 169 position (*Cr*HydA1 numbering, Fig. 5). Third, we have seen evidence for potential 'rate-promoting vibrations' in which flexing of the ADT bridgehead N combined with Fe–H bending brings the two H atoms closer for formation of H_2 bonding. Finally, we have seen that the –SH group of the Cys169 thiolate is actively involved in many of the normal modes which also exhibit ADT and Fe–H motions. This tells synthetic chemists seeking to mimic H_2ase properties that structures as far as 5 Å from the Fe_d active site are relevant for the initial steps in catalytic activity.

8. Where is this research going?

Where is this research going? Our current goal is to capture the earliest steps in the H_2 splitting reaction, which many believe is a fleeting Fe-H_2 complex for the [FeFe] enzyme. Since this intermediate presumably quickly splits into a hydride and a proton, our plan is to capture it at low temperature. H_2 will be generated photochemically from NH_3BH_3 and a nanoparticle catalyst, and the H_2ase will be stabilized in a cryosolvent at low temperatures. We plan to monitor the photochemistry with *in situ* IR spectroscopy.

This research has benefited from the continuing improvement in the emittance of the SPring-8 storage ring, the brightness available from improved undulators, the stability of high-resolution monochromators, and better avalanche photodiode detectors. A mobile NRVS apparatus that Dr. Yoshitaka Yoda and his colleagues made to use at other beamlines (e.g., BL19LXU) has also been critical for making this research possible.

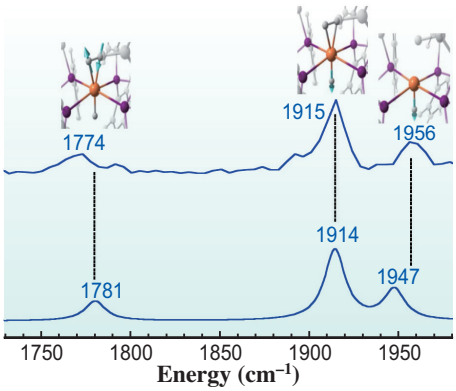

Fig. 11. NRVS PVDOS and DFT calculations for *trans*-[^{57}Fe(η^2-H_2)(H)(dppe)$_2$][BPh_4].

9. Other groups now using NRVS at SPring-8

NRVS has become popular with other groups around the world, some of whom have initially collaborated with us and now run vigorous independent programs. The group of Prof. Solomon at Stanford has at least 10 NRVS publications – we cite just one recent example [9]. The groups of Prof. Oliver Lenz at Technical University of Berlin, Dr. Serena DeBeer at the Max Planck Institute in Mulheim and Dr. Artur Braun at the Empa - Swiss Federal Laboratories are also active users of SPring-8 NRVS capabilities. The demand for NRVS capabilities, not only for ^{57}Fe but also for other isotopes, is rapidly growing and speaks to a productive future for this technique.

Hongxin Wang[a] and Stephen P. Cramer[a,b,*]

[a] SETI Institute, Mountain View, USA
[b] University of California, Davis, USA

*Email: scramer@seti.org

References

[1] C.C. Pham *et al.*: Angew. Chem. Int. Ed. **57** (2018) 10605.
[2] H. Ogata *et al.*: Nat. Comm. **6** (2015) 7890.
[3] S. Kamali *et al.*: Angew. Chem. Int. Ed. **52** (2013) 724.
[4] G. Caserta *et al.*: Chem. Sci. **12** (2021) 2189.
[5] C. Lorent *et al.*: Angew. Chem. Int. Ed. **60** (2021) 15854.
[6] V. Pelmenschikov *et al.*: J. Am. Chem. Soc. **143** (2021) 8237.
[7] V. Pelmenschikov *et al.*: J. Am. Chem. Soc. **139** (2017) 16894.
[8] M.H. Chiang *et al.*: Inorg. Chem. **60** (2021) 555.
[9] A.B. Jacobs *et al.*: J. Am. Chem. Soc. **143** (2021) 16007.

Review Article

Hydrogen and Other Light Elements in the Earth's Core

The Earth's metallic core, located at depths of 2890 to 6370 km from the surface, is not pure iron nor iron-nickel alloy but includes substantial amounts of low-atomic-number "light" elements that explain the seismologically observed ~8% density deficit and ~5% sound velocity excess with respect to pure Fe [1]. Although the presence of light elements in the core has been known since 1952, the core light element composition still remains under hot debate 70 years later. Five light elements (S, Si, O, C, and H) are considered primary candidates. Identifying the core light elements has profound implications in wide areas of earth and planetary sciences. To constrain the core composition, it is of great importance to determine the density and sound velocity of iron and iron alloys at core pressures and temperatures (>136 GPa, >~3500 K) by a combination of X-ray diffraction (XRD) and inelastic X-ray scattering (IXS) measurements at SPring-8 [2].

Recent planet formation theories [3-5] suggest that a large amount of water, ten to one hundred times as much as sea water, may have been delivered to our planet during its accretion phase. Such an extensive amount of water could have been sequestrated in the core as hydrogen with some oxygen. Indeed, *ab initio* simulations indicated that hydrogen-bearing liquid and solid alloys [6,7] can explain the observed density and velocity of the liquid outer and solid inner cores, respectively, suggesting that hydrogen is likely to be a major light element in the core.

Metal-silicate partitioning of hydrogen

The Earth was once covered with a "magma ocean", which incorporated most of the water transported to the Earth by that time. The partitioning of hydrogen between liquid metal and molten silicate (magma) is the key to understanding the fate of this water. However, its experimental determination has been challenging. Indeed, the examination of hydrogen-containing iron alloys is difficult because hydrogen is least soluble in iron under ambient conditions (it is thus difficult to determine the hydrogen content in alloys). In addition, the metal-silicate (core-mantle) partitioning occurred under high pressure and temperature (P–T) conditions, typically 50 GPa and 3500 K, in a deep magma ocean that extended to a depth of ~1200 km. There were no experimental reports on the metal-silicate partitioning of hydrogen under such high P–T conditions.

Recently, we have determined the partitioning of hydrogen between iron and silicate at 30–60 GPa and 3100–4600 K, corresponding to conditions at the bottom of a magma ocean [8]. High P–T experiments were performed in a laser-heated diamond-anvil cell (DAC) at SPring-8 BL10XU. We melted an iron foil + hydrous mid-oceanic ridge basalt (MORB) glass sample

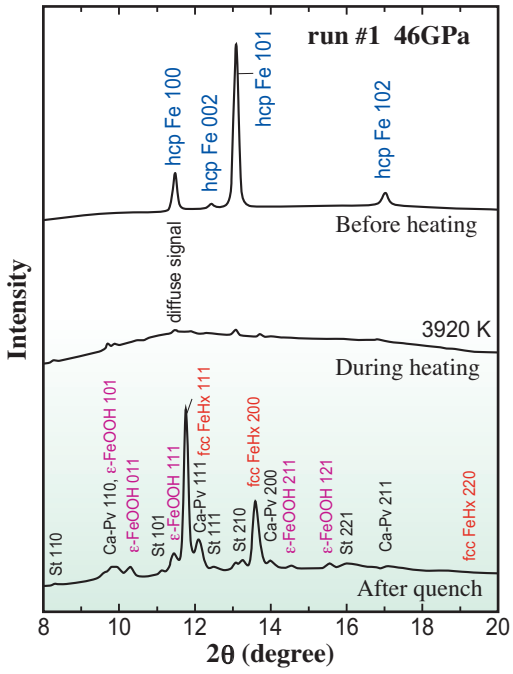

Fig. 1. XRD patterns collected at BL10XU before/during/after heating the Fe metal + hydrous MORB glass sample to 3920 K at 46 GPa [7]. Both iron and silicate were molten during heating. The hydrogen content in liquid metal was obtained from that in fcc FeH_x on the basis of its lattice volume and the proportions of FeH_x and ε-FeOOH estimated from microprobe analyses.

at high pressures and then quenched the temperature to 300 K. Since hydrogen escapes from solid iron during decompression when the iron transforms into the bcc phase, the hydrogen concentration in quenched liquid metal must be determined at high pressures. XRD measurements *in situ* under high *P–T* conditions revealed that molten iron crystallized into FeH_x and a minor amount of FeOOH upon quenching (Fig. 1). The lattice volume of FeH_x was larger than that of pure Fe under equivalent conditions because the incorporation of hydrogen in the interstitial sites of the Fe lattice causes volume expansion. We obtained hydrogen concentrations in liquid Fe based on the lattice volume of FeH_x and the proportions of FeH_x and FeOOH in quenched liquid. Earlier experiments [9] demonstrated that the thermal annealing of such FeH_x quenched crystals only slightly changed their unit-cell volume, indicating the validity of such determinations of the hydrogen content in liquid. On the other hand, hydrogen was present as water in silicate melt that coexisted with hydrogen-bearing Fe liquid in these experiments. After recovering a sample from the DAC under ambient conditions, its cross section at the center of a laser-heated portion was prepared parallel to the compression/laser-heating axis, using a focused ion beam (FIB). Subsequently, the hydrogen content in a quenched silicate melt was determined with an isotope microscope system at Hokkaido University. This system yields quantitative maps of secondary ions emitted from the sample surface (Fig. 2).

These XRD and SIMS analyses detected 5300 to 26000 ppm H (by weight) in metal at high pressures (before decompression) and 90 to 470 ppm H (present as water) in quenched silicate melts, respectively. The calculated metal-silicate partition coefficient of hydrogen, $D_H^{metal-silicate}$ (weight fraction basis), ranged from 29 to 57 (Fig. 3), indicating that

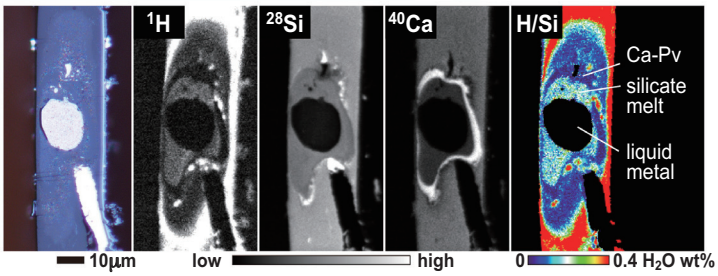

Fig. 2. Micrograph (left), secondary ion images for $^{1}H^{+}$, $^{28}Si^{+}$, and $^{40}Ca^{+}$ (middle), and a distribution map of water (right) in cross section of the sample recovered from the same metal + silicate melting experiment as in the case of Fig. 1 [7]. Hydrogen is absent in metal, because it escaped from iron upon the release of pressure. The hydrogen (water) content in the quenched silicate melt was obtained with ±2–7% uncertainty.

hydrogen is a strong siderophile (iron-loving) at high pressures. The metal-silicate partitioning of hydrogen occurs as an oxidation-reduction reaction:

$$HO_{0.5}^{silicate\ melt} + \frac{1}{2}Fe^{metal} = H^{metal} + \frac{1}{2}FeO^{silicate\ melt} \quad (1)$$

$D_H^{metal-silicate}$, therefore, changes with oxygen fugacity as well as *P* and *T*.

Hydrogen in the core

The metal-silicate partition coefficient of hydrogen is useful for estimating the concentration of hydrogen in the core based on the amount of water present in the mantle + crust + oceans, which has been estimated to be a total of 687 ppm H_2O corresponding to two times the mass of oceanic water [8]. Conceptually simple "single-stage" core formation models [10-12] reconcile the known mantle abundances of moderately siderophilic elements with core-mantle chemical equilibration at around 50 GPa and 3500 K and oxygen fugacity relevant to the FeO content in the mantle (2.3 log unit below the iron-wüstite buffer). If this is the case, $D_H^{metal-silicate}$ = 46.2 for 50 GPa and 3500 K gives 0.40 wt% H in the core (Fig. 4). When considering the minimal average mantle H_2O abundance to be as much as that found in the upper mantle (although the upper mantle is generally considered to be depleted in melt components and water), the lower bound for the core hydrogen concentration is 0.24 wt%. Furthermore, taking the estimated range of *P–T* conditions for core-mantle equilibration, the core may include 0.24–0.60 wt% H.

Previous *ab initio* calculations revealed that both the density and P-wave velocity of the liquid outer core are explained with liquid Fe containing 1.0 wt% H [6]. The 0.24–0.60 wt% H accounts for ~20–60% of the density deficit and velocity excess of the liquid core with respect to pure iron, indicating that hydrogen is an important light element in the core. It is equivalent to the amount of hydrogen included in 30–74 times the total amount of seawater on the Earth. This suggests that an extensive amount of water was transported to the growing Earth, which is consistent with recent planet formation theories [3-5].

Earth's core composition

Hydrogen accounts for ~20–60% of the density deficit and velocity excess of the outer core, indicating that the remaining 40–80% is attributed to other light elements such as sulfur, silicon, oxygen, and carbon [1]. Traditionally, sulfur has been considered to be one of the major core light elements because it is commonly included in iron

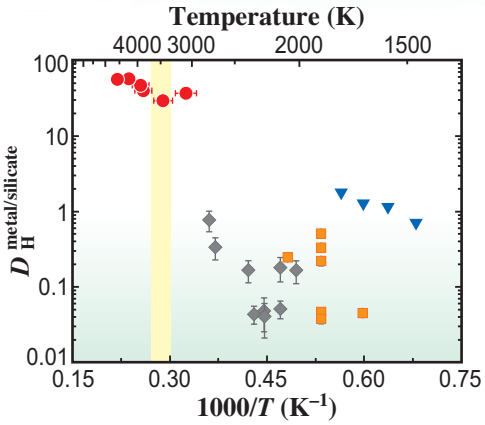

Fig. 3. Metal-silicate partition coefficient D for hydrogen as a function of reciprocal temperature. Tagawa *et al*. [7] (red circles) showed that hydrogen is highly siderophilic under the formation conditions of the Earth's core. Reported D values (gray diamonds [13], orange squares [14]) were lower by one to three orders of magnitude than the present results because hydrogen was lost from metals during decompression in those experiments. Pioneer experimental results (blue inverse triangles [15]) are also plotted.

meteorites that represent the metallic cores of small rocky bodies. The bulk Earth sulfur content can be calculated on the basis of that of chondrites (primitive meteorites); the depletion of sulfur on the Earth relative to chondrites is estimated using elements that are present only in the silicate part (mantle + crust) and exhibit volatility similar to that of sulfur. The sulfur concentration in the Earth's core is then obtained to be about 2.0 wt% by subtracting the known amount of sulfur in the silicate from the bulk Earth quantity. The 2.0 wt% S accounts for about 20% of the density deficit and velocity excess of the liquid core.

Silicon and oxygen are major elements in the silicate mantle. It is known that higher amounts of silicon and oxygen are incorporated into molten iron at high temperatures [12,13]. Recent models suggest that core-forming metals equilibrate with silicate at relatively high temperatures, typically 3500 K, and thus the core is enriched in both silicon and oxygen. However, the literature on steel making shows that simultaneous solubilities of silicon and oxygen in liquid iron are limited at 1 bar (Fig. 5(a)). Furthermore, our recent experiments also demonstrated the limited simultaneous solubilities of silicon and oxygen in molten iron at core pressures [13], indicating that the Earth's liquid core may have included large amounts of both silicon and oxygen in its early history and is now saturated with SiO_2 (Fig. 5(b)). The silicon and oxygen concentrations in the core should have decreased by the crystallization of SiO_2 upon secular cooling. With the present-day temperature at the core side of the core-mantle boundary (CMB) being 3500 K, the remaining silicon and oxygen account for ~40–80% of the outer core density deficit and velocity excess [13]. Finally, 0 to 1.3 wt% C may be present in the outer core, contributing to 0–20% of the outer core density deficit and velocity excess, in addition to hydrogen (~20–60%), sulfur (20%), and silicon + oxygen (~40–80%).

The above arguments are based on the seismologically observed density and P-wave velocity of the outer core, along with metal-silicate (core-mantle) partitioning and simultaneous solubility limits of Si+O. In addition, the outer core liquid is in chemical equilibrium with the solid inner core at the inner core boundary (ICB) located at a depth of about 5200 km. Therefore, its light element composition can be calculated from the inner core solid composition constrained by the observations of its density and P-wave and S-wave velocities using the solid-metal/liquid-metal partition coefficient of each light element [1].

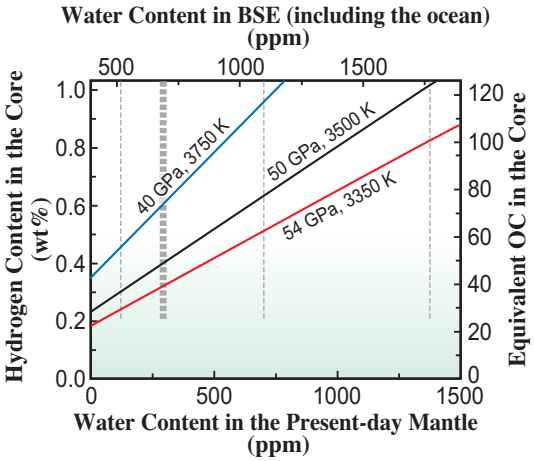

Fig. 4. Estimates of hydrogen concentration in the Earth's core. Three lines show the hydrogen content in the core relative to the water abundance in the present-day mantle + crust + ocean ("BSE", vertical lines). Hydrogen content reached chemical equilibrium with silicate under high P–T conditions (blue [9], gray [10], red [11]). Even a modest amount of water in the present-day mantle (two vertical lines showing relatively low H_2O contents in the mantle) suggests 0.24–0.60 wt% H in the core, corresponding to 30–74 times hydrogen that exists in the oceans (right vertical axis). This accounts for ~20–60% of the density deficit and velocity excess of the Earth's outer core relative to pure iron.

Furthermore, in the outer core liquid, Fe must crystallize instead of light-element-rich compounds such as FeO and FeH, otherwise the dense inner core does not form. Combining a total of eight independent constraints, the outer core composition, including five light impurity elements and ~5wt% Ni, should be tightly constrained in future studies. To do so, we plan to perform XRD measurements at SPring-8 BL10XU to obtain 1) melting phase diagrams including the solid-liquid partitioning of light elements, particularly in hydrogen-bearing Fe alloy systems and 2) the density of liquid Fe alloys, as well as IXS measurements at BL43LXU to obtain 3) sound velocities of liquid and solid Fe and Fe alloys.

Implications of core light element composition

The metallic core constitutes one-third of the Earth's mass and includes >30 atm% light elements. Since the light element composition is unknown, the chemical composition of the bulk Earth also remains unknown. It is highly possible that the core includes >90% of the Earth's carbon and hydrogen. Both are highly volatile and should have condensed outside the Earth's orbit and then somehow transported to our planet. Thus far, it is impossible to specify how, when, and how much of these elements arrived on the Earth. Recent planet formation theories such as the "Grand Tack Model" or "Pebble Accretion Model" have attracted considerable attention. They suggest that more organic matter and water were delivered to the Earth than do traditional models. An understanding of the amounts of carbon and hydrogen in the bulk Earth is indispensable to confirm of such recent theories.

In addition, because the amount of silicon present in the core is unknown, the Mg/Si ratio, the principal element ratio of the bulk Earth, remains unknown. The Mg/Si molar ratio of the accessible Earth's upper mantle composition (=1.3) is significantly different from the solar composition (=1.0), which is another important unsolved problem. The presence of silicon in the core could fill this gap. Moreover, the Earth was likely made of reducing substances that were present at the inner solar system and oxidizing substances that were from the outer solar system. Since the amount of oxygen in the core is unknown, their proportions are not yet understood.

Furthermore, the current estimates of the Earth's core temperature include large variations. For example, the previously estimated temperature at the CMB ranges from 3400 to 4600 K [1]. The liquid core composition provides the temperature at the ICB, the boundary between the solid and liquid cores, which corresponds to the liquidus (onset of crystallization) temperature of the outer core liquid at 330 GPa. The isentropic outer core temperature profile including the CMB temperature is calculated from the ICB temperature. The core temperature itself has profound implications for the present state of the core. In addition, the CMB temperature is a key to interpreting the complex seismic structures of the lowermost mantle and estimating heat flow from the core to the mantle, which is very important for the thermal histories (cooling speeds) of both the core and the mantle.

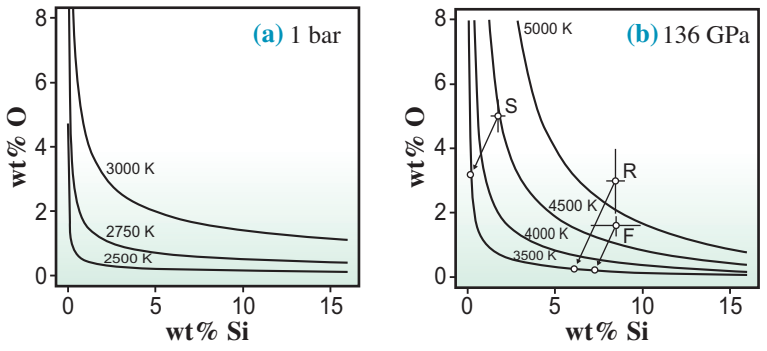

Fig. 5. Simultaneous solubility limits of Si+O in liquid Fe at (**a**) 1 bar and (**b**) 136 GPa (pressure at the CMB). The silicon and oxygen contents in the initial core indicated by 'S' [16], 'R' [17], and 'F' [11] are beyond the solubility limit in the present-day outer core, which has caused the SiO_2 crystallization and the depletion of Si and O in the liquid core over the Earth's history (see arrows).

Kei Hirose[a,b,*] and Shoh Tagawa[a]

[a] Earth-Life Science Institute (ELSI), Tokyo Institute of Technology
[b] Dept. of Earth and Planetary Science, The University of Tokyo

*Email: kei@elsi.jp

References

[1] K. Hirose *et al.*: Nat. Rev. Earth & Environ. **2** (2021) 645.
[2] S.N. Raymond *et al.*: Astrobiology **7** (2007) 66.
[3] K.J. Walsh *et al.*: Nature **475** (2011) 206.
[4] T. Sato *et al.*: Astron. Astrophys. **589** (2016) A15.
[5] K. Umemoto and K. Hirose: Earth Planet. Sci. Lett. **531** (2020) 116009.
[6] W. Wang *et al.*: Earth Planet. Sci. Lett. **568** (2021) 117014.
[7] S. Tagawa *et al.*: Nat. Commun. **12** (2021) 2588.
[8] K. Hirose *et al.*: Geophys. Res. Lett. **46** (2019) 5190.
[9] J. Wade and B.J. Wood: Earth Planet. Sci. Lett. **236** (2005) 78.
[10] J. Siebert *et al.*: Earth Planet. Sci. Lett. **321** (2012) 189.
[11] R.A. Fischer *et al.*: Geochim. Cosmochim. Acta **167** (2015) 177.
[12] K. Hirose *et al.*: Nature **543** (2017) 99.
[13] V. Clesi *et al.*: Sci. Adv. **4** (2018) e1701876.
[14] V. Malavergne *et al.*: Icarus **321** (2019) 473.
[15] T. Okuchi: Science **278** (1997) 1781.
[16] J. Siebert *et al.*: Science **339** (2013) 1194.
[17] D.C. Rubie *et al.*: Icarus **248** (2015) 89.

Structural insights into allosteric modulation of mGlu2

Metabotropic glutamate receptors (mGlus) belong to the class C G-protein-coupled receptor (GPCR) family and are involved in brain physiological functions as well as neuropathological processes. In response to glutamate, one of the major excitatory neurotransmitters, mGlu2 plays important roles in modulating cell excitability and synaptic transmission and displays potential as a drug target for the treatment of glutamate-related neuropsychiatric diseases such as depression and schizophrenia [1]. This receptor contains a large extracellular domain (ECD) composed of the Venus flytrap (VFT) domain that binds agonist and a cysteine-rich domain (CRD) connected to a seven-helical transmembrane domain (TMD) responsible for G protein coupling. Because of the highly conserved orthosteric binding pocket of mGlu receptors in ECD, the allosteric pocket in the TMD of mGlu receptors is believed to be a better site for the designation of mGlu-selective drugs (Fig. 1) [2]. However, the lack of high-resolution structural details of the mGlu2 allosteric site and the poor understanding of the allosteric modulating mechanism have hindered the development of highly selective mGlu2 negative allosteric modulators (NAMs) and positive allosteric modulators (PAMs). Here, we solved two crystal structures of the mGlu2 TMD bound to two NAMs (NAM563 and NAM597), which provided high-resolution molecular details of the NAM-binding modes of mGlu2.

To facilitate the crystallization of the mGlu2 TMD-NAM complex, the extracellular domain (residues 1 to 555) and C-terminus (residues 846 to 872) of mGlu2 were removed and a fusion protein, flavodoxin, was inserted in intracellular loop 2 to reduce the receptor flexibility. Two point mutations, $N655^{3.52}Y$ and $H815^{7.53}Y$, were further introduced to improve the receptor stability without affecting the ligand binding. The crystals of mGlu2-TMD with NAM563 and NAM597 were optimized using the lipidic cubic phase (LCP), and diffraction data were collected at SPring-8 **BL41XU**. The structures of NAM563- and NAM597-bound mGlu2 TMDs were determined by molecular replacement at final resolutions of 2.5 Å and 2.7 Å, respectively.

The overall fold of the mGlu2 TMD structure consists of a canonical seven-transmembrane (7TM) bundle of α-helices. The binding pockets of NAM563 and NAM597 are formed by helices III, V, VI, and VII of the transmembrane regions in mGlu2, which is similar to the previously reported NAM-binding pockets of mGlu1 and mGlu5 [3]. The main skeletons of these two NAMs share similar interaction patterns with mGlu2 but are different on the extracellular side (Fig. 2). Mutations of some residues within the

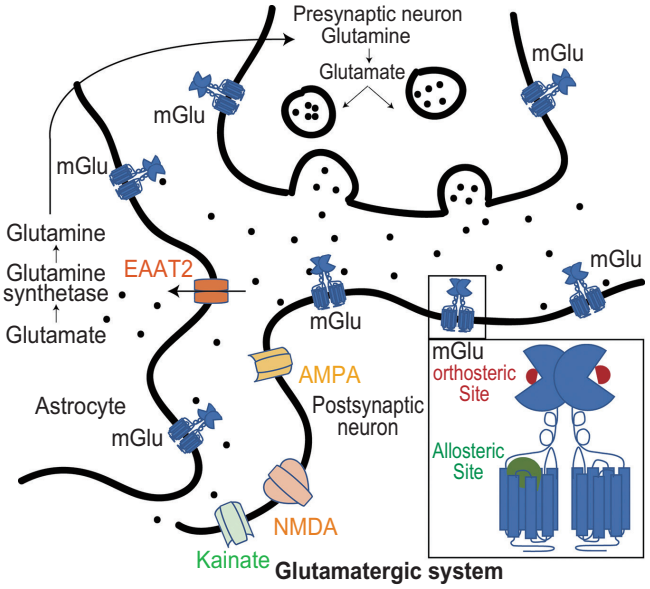

Fig. 1. Diagram of the glutamatergic system in neurons and allosteric regulation of mGlu receptors. (EAAT2: excitatory amino acid transporter-2, AMPA: α-amino-3-hydroxy-5-methyl-4-isoxazole-propionic acid receptor, NMDA: N-methyl-D-aspartic acid receptor, and Kainate: Kainate receptor)

binding pockets exhibit a 5- to 1000-fold reduction in the inhibitory activity of these two NAMs, whereas other residues display a variety of effects on NAM binding, suggesting that different NAMs may occupy similar binding cavities in mGlu2 but adopt distinct interaction patterns when binding to the receptor [3]. A detailed analysis of the NAM563-bound mGlu2 TMD and our recently solved mGlu2 in complex with PAM JNJ-40411813 structures disclosed a rotamer conformational change of the highly conserved residue W773$^{6.50}$ in class C GPCRs [4] (Fig. 3(a)). This conformational change disrupts the interaction core in the transmembrane helical bundle and releases it from the constraint of the inactive state, which potentially leads to the downward movement of helix VI. The conformational change of helix VI may further lead to the alteration of the intracellular interaction network of mGlu2 and is associated with receptor activation. Besides the typical ionic lock of class C GPCRs between the highly conserved residues K$^{3.50}$ and E$^{6.35}$, additional ionic interaction formed by R656$^{3.53}$ in helix III and E754 in the intracellular loop (ICL) 3 was observed in the mGlu2 TMD-NAM563 structure (Fig. 3(b)). However, these interactions are broken in the PAM bound structure, which is probably attributable to the downward movement of helix VI and the rearrangement of ICL3.

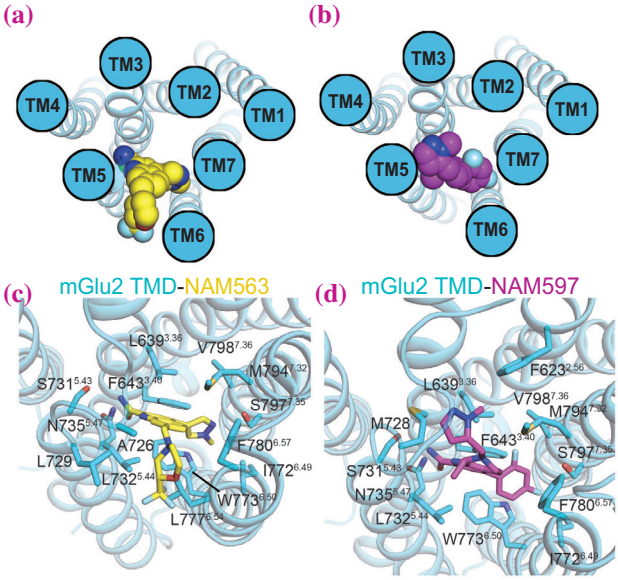

Fig. 2. Crystal structures of NAM-bound mGlu2 TMD showing the different binding patterns of NAMs. The trifluoromethyl-morpholin group of NAM563 squeezes into a gap between helices VI and VII, whereas the methyl-pyrazol group in NAM597 points to the opposite direction to interact with helix II and ECL2. **(a)** NAM563 and **(b)** NAM597 in mGlu2 TMD. **(c)** NAM563- and **(d)** NAM597-binding pocket and ligand receptor interactions.

These studies reveal the molecular details of interaction modes for two NAMs with mGlu2 TMD and explain the negative allosteric modulation mechanisms of mGlu2. Together with the recently solved PAM-bound mGlu2 structure, these structures offer direct models for the development of mGlu2 specific modulators.

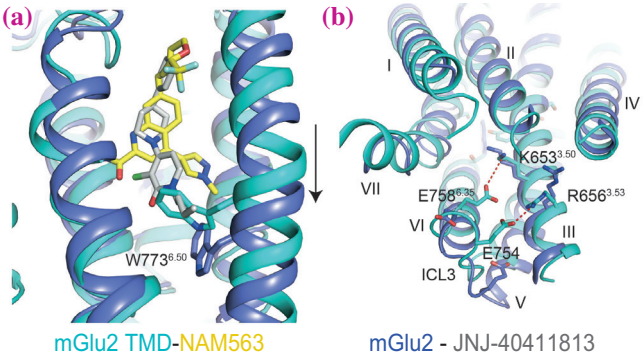

Fig. 3. Conformational change between NAM-bound mGlu2 and PAM-bound mGlu2-G_{i1} complexes. **(a)** Conformational change of W$^{6.50}$ and helix VI upon activation. In the NAM563-bound mGlu2 TMD structure, NAM563 constrains the conformation of its side chain to stabilize the receptor in the inactive state. In the JNJ-40411813-bound structure, the side chain of W773$^{6.50}$ exhibits downward rotation by approximately 90°. NAM563, PAM JNJ-40411813, and corresponding receptors are shown as yellow/gray sticks and cyan/purple cartoons. The black arrow indicates the downward shift of helix VI upon PAM binding. **(b)** Ionic locks of NAM-bound mGlu2 and PAM-bound mGlu2-G_{i1} complex. The ionic interactions are shown as red dashed lines.

S. Lin, J. Du, B. Wu* and Q. Zhao

Shanghai Institute of Materia Medica,
Chinese Academy of Sciences

*Email: beiliwu@simm.ac.cn

References

[1] S. Chaki: Adv Pharmacol. **86** (2019) 97.
[2] Z. Orgován *et al.*: Curr Top Med Chem. **19** (2019) 1768.
[3] *J. Du, D. Wang, H. Fan, C. Xu, L. Tai, S. Lin, S. Han, Q. Tan, X. Wang, T. Xu, H. Zhang, X. Chu, C. Yi, P. Liu, X. Wang, Y. Zhou, J.-P. Pin, P. Rondard, H. Liu, J. Liu, F. Sun, B. Wu and Q. Zhao: Nature* ***594*** *(2021) 589.*
[4] S. Lin *et al.*: Nature **594** (2021) 583.

A small compound 5h blocks the infectivity, replication, and cytopathicity of SARS-CoV-2 via inhibition of main protease

The novel coronavirus disease 2019 (COVID-19) caused by severe acute respiratory syndrome coronavirus 2 (SARS-CoV-2), was first reported in Wuhan, Hubei province, China and escalated into a pandemic in May 2020 [1]. As of early in 2021, except for remdesivir (RDV), which was approved as the first proven emergency therapeutic for treating COVID-19, no specific therapeutics were available. The hope that the COVID-19 pandemic subsides with "herd immunity" has been likely to be disappointing. Moreover, COVID-19-convalescent people carrying antibodies to SARS-CoV-2 are still susceptible to reinfection. It is of utmost urgency to develop effective antivirals that mitigate the lethal consequences of the disease, as well as effective vaccines. In this research, we synthesized and identified two novel antiviral small molecule compounds containing indole moiety against SARS-CoV-2 infection [2].

Based on the fact that the main protease (M^{pro}), which processes virus polypeptides of SARS-CoV-2 has an extensive homology (~96%) with the M^{pro} of SARS-CoV, we first selected a panel of previously reported (most in 2000s) compounds that had been reported to be active against SARS-CoV by targeting its M^{pro} [3]. Moreover, we have designed and synthesized novel compounds which might exert potent activity against SARS-CoV-2 [2]. We have now identified two small molecule compounds, GRL-1720 and 5h, both of which target the M^{pro} of SARS-CoV-2 and potently block the infectivity, replication, and cytopathicity of SARS-CoV-2 (Fig. 1). As assessed using the quantitative VeroE6 cell-based assay with RNA-qPCR, the 50% of effective concentration (EC_{50}) values of GRL-1720 and 5h were 15±4 and 4.2±0.7 μM, respectively, and apparent 50% of cytotoxic concentration (CC_{50}) values, which were determined with WST-8 assay, were both >100 μM (Fig. 1). Compound 5h exserted greater antiviral activity than GRL-1720, hence we used 5h for further analyses.

RDV and 5h blocked the infectivity of SARS-CoV-2 through acting as a viral RNA polymerase inhibitor [4] and as an M^{pro} inhibitor, respectively. Thus, we asked whether these two compounds worked against SARS-CoV-2 in an additive or synergistic fashion using VeroE6 cell-based assays (Fig. 2). The cells were exposed to SARS-CoV-2 and cultured in the presence or absence of various concentrations of RDV plus 5h. 4 μM of RDV and 4 μM of 5h suppressed the viral replication by 0.53-fold and 2.0-fold, respectively, while when combined, the suppression was apparently synergized by 24-fold. The apparent combination effect was maximal when RDV and 5h were combined at 20 μM, producing the suppression by as much as 1.6×10^6-fold. When examined using the Bliss additivism method, combination of 5h and RDV exerts at least additive effect. Moreover, a synergistic effect was present at 1 μM each of 5h and RDV and the synergism reached the maximum at 10 μM combination of the two compounds. As in the case of antiretroviral therapy of HIV-1 infection, in which

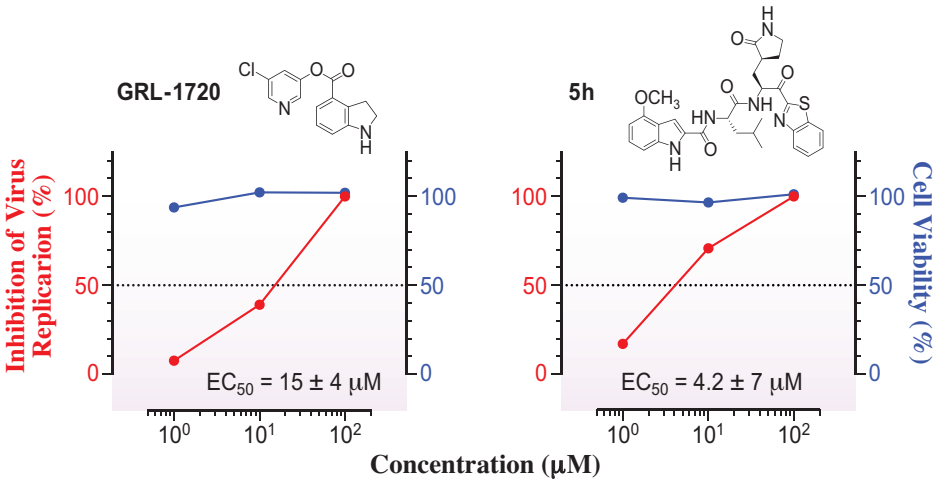

Fig. 1. The antiviral activity of GRL-1720 and 5h against SARS-CoV-2. VeroE6 cells were exposed to SARS-CoV-2 and the cells were cultured for 3 days in the presence of GRL-1720 (left) or 5h (right). The viral copy numbers in the culture supernatants were determined using RT-qPCR. Red and blue lines indicate percent reduction of viral copy numbers and cell viability, respectively. All assays were performed in duplicate.

the use of one or two reverse transcriptase inhibitors and an HIV-1 protease or integrase inhibitor results in highly favorable antiretroviral effects [5], such a combination might give much more favorable efficacy than RDV or 5h alone.

To understand the molecular basis of the inhibition of SARS-CoV-2's M^{pro} by 5h, we determined the X-ray structure of M^{pro} in complex with 5h at 1.25 Å resolution. X-ray data were collected at SPring-8 **BL41XU**. Detailed molecular interactions with M^{pro} are shown in the Figs. 3(a-d). 5h fully occupies the binding pocket (Fig. 3(a)) and is stabilized by 6 direct hydrogen bonds with the residues inside the binding groove of M^{pro}. Particularly, Glu-166 engages in two-hydrogen-bond formation, linking the main chain carbonyl and the amide group of Glu-166 (Fig. 3(b)). In the central part of 5h, additional hydrogen bonds form with the side-chain oxygen of Gln-189 and the main chain carbonyl of His-163 (Figs. 3(b-c)). Since the majority of hydrogen bonds form through the main chain carbonyl and NH groups of M^{pro}, those interactions are less likely affected by potential mutations, although whether drug-resistant mutants emerge is an open question and more studies are required. Overall, the chemical composition of 5h matches well with the surface of the binding groove in terms of the hydrophobicity scale. The observed continuous electron density of the tetrahedral ketal and the sulfur atom of Cys-145 indicates the formation of a covalently bond between 5h and M^{pro} (Fig. 3(d)). The sulfur atom of Cys-145 undergoes nucleophilic addition reaction and forms a covalent bond with the carbonyl carbon (–C=O) next to the benzothiazole of 5h, resulting in the conversion of the carbonyl to an alcohol (–C–OH) and to the formation of one direct hydrogen bond and water-mediated hydrogen bond interactions around the three oxyanion hole residues, Cys-145 and Gly-143 (Fig. 3(d)).

In conclusion, 5h, which shows potent antiviral activity and no significant detectable cytotoxicity, represents a lead compound to develop more potent anti-SARS-CoV-2 agents. Moreover, the combination therapy using different class of agents, such as an M^{pro} inhibitor and an RdRp inhibitor, might be a promising therapeutic modality for treatment of SARS-CoV-2 infection.

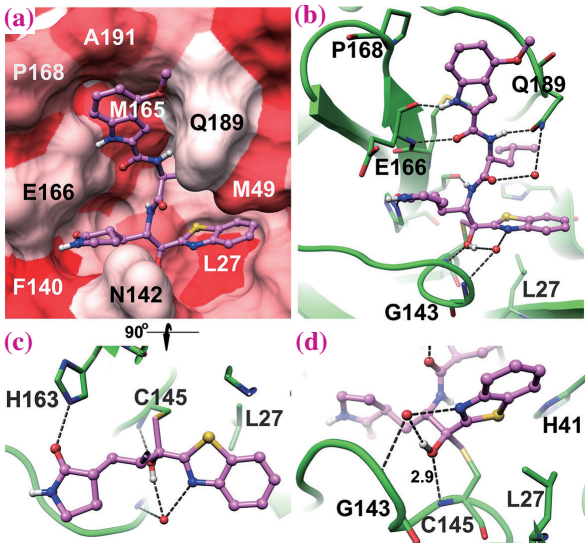

Fig. 3. The X-ray crystal structure of SARS-CoV-2 M^{pro} in complex with 5h. **(a)** Hydrophobicity of the binding pocket is represented by the intensities of red color, hydrophobic residues are shown in dark red, whereas polar or charged residues are shown in light red. **(b)** Hydrogen bond interactions between 5h (pink carbon atoms) and M^{pro} (green carbon atoms) are shown in black dash lines. **(c)** A 90°-rotated view of 5h focuses on the interactions of 2-oxopyrrolidine and benzothiazole groups. **(d)** The hydroxyl group of 5h is shown in the center. Distances between atoms are shown in Å.

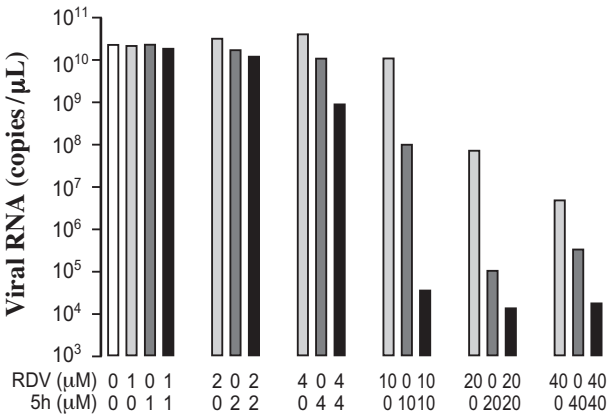

Fig.2. 5h combined with RDV does not permit viral breakthrough. Viral RNA copy numbers in the culture supernatants which VeroE6 cells were exposed to SARS-CoV-2 in the presence of compounds were determined using RNA-qPCR. Bars indicate geometric mean (n=2).

Shin-ichiro Hattori and Hiroaki Mitsuya*

Department of Refractory Viral Infections, National Center for Global Health and Medicine Research Institute

*Email: hmitsuya@hosp.ncgm.go.jp

References

[1] H. Mitsuya *et al.*: Glob. Health Med. **2** (2020) 53.
[2] *S. Hattori, N. Higashi-Kuwata, H. Hayashi, S.R. Allu, J. Raghavaiah, H. Bulut, D. Das, B.J. Anson, E.K. Lendy, Y. Takamatsu, N. Takamune, N. Kishimoto, K. Murayama, K. Hasegawa, M. Li, D.A. Davis, E.N. Kodama, R. Yarchoan, A. Wlodawer, S. Misumi, A.D. Mesecar, A.K. Ghosh, H. Mitsuya: Nat. Commun.* ***28*** *(2021) 668.*
[3] S. Hattori *et al.*: mBio **11** (2020) e01833-20.
[4] W. Yin *et al.*: Science **368** (2020) 1499.

Crystal structure of engineered ACE2 complexed with SARS-CoV-2 Spike RBD

The coronavirus disease (COVID-19) caused by severe acute respiratory syndrome coronavirus 2 (SARS-CoV-2) has become a global pandemic and has tremendously affected on our lives. Infection by SARS-CoV-2 is initiated by its binding to angiotensin-converting enzyme II (ACE2) on the surface of human cells via the viral spike protein; therefore, inhibiting the binding of spikes to ACE2 is one of the most promising therapeutic strategies against COVID-19. A number of monoclonal antibodies that bind to spikes, especially the receptor binding domain (RBD), and block ACE2 engagement are currently in preclinical and clinical development. However, because of the high mutation rate of SARS-CoV-2, there is concern that the virus may acquire resistance to drugs and vaccines. An alternative molecule to antibodies in neutralizing SARS-CoV-2 is the extracellular region of ACE2, soluble ACE2 (sACE2) (Fig. 1) [1]. The main advantage of using the sACE2-based decoy receptor is its resistance to virus escape mutations. A virus mutant escaping from the sACE2 decoy should also have limited binding affinity to native ACE2 receptors on the cell surface, resulting in diminished or eliminated infectivity. In this study, we developed a SARS-CoV-2-neutralizing drug that overcomes viral mutations through protein engineering of ACE2 [2].

Since the affinity of wild-type (WT) sACE2 to RBD is not sufficiently high to be used for therapeutic purposes [3,4], we first attempted to modify ACE2 to increase its affinity (Fig. 1). We introduced mutations into ACE2 by a directed evolution method involving several rounds of random mutagenesis and cell sorting, and we obtained an ACE2 mutant, 3N39, which was judged to have an increased RBD binding activity on the basis of the cell-based binding assay results [2]. Sequence analysis revealed that seven mutations, A25V, K26E, K31N, E35K, N64I, L79F, and N90H, were introduced into ACE2(3N39). Quantitative measurements of binding affinity to RBD by surface plasmon resonance showed that the K_D value of WT sACE2 is 17.63 nM, whereas that of the 3N39 mutant is 0.29 nM, confirming that the RBD binding activity was, in fact, greatly enhanced by mutations. We further characterized each mutation and finally found that only four of the seven mutations (i.e., A25V, K31N, E35K, and L79F) were essential for affinity enhancement.

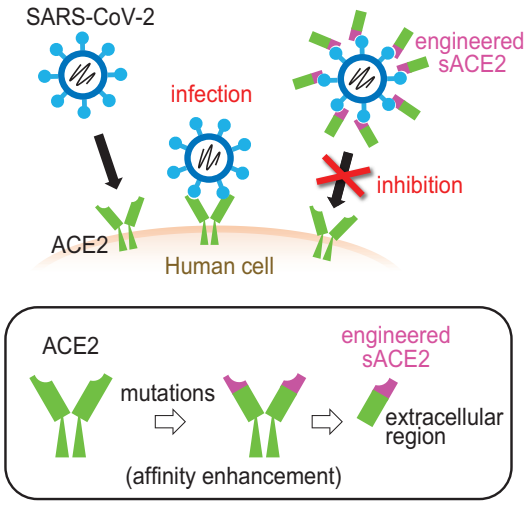

Fig. 1. Strategy for SARS-CoV-2 neutralization using engineered sACE2.

To understand the structural basis of the affinity enhancement, we next determined the crystal structure of the sACE2(3N39)-RBD complex. X-ray diffraction data were collected at SPring-8 **BL44XU**, and the structure was solved by molecular replacement at a final resolution of 3.2 Å. Structure refinement was promptly conducted, and the resulting model was deposited in PDB in December 2020 (PDB ID: 7dmu). This is the first SARS-CoV-2-related protein structure reported in Japan. From the crystal structure, it was confirmed that among the seven mutated residues in 3N39, the side chains of E26, I64, and H90, which were identified to have little or no contribution to the affinity enhancement, are exposed to solvent and not involved in either inter- or intra-molecular interactions (Fig. 2(a)). In contrast, four essential mutated residues were found to be involved in the formation of interaction sites for RBD in two regions. The first region consists of K31N and E35K mutation sites and is located at the center of the RBD binding interface. In the WT structure, E35 forms an intramolecular salt bridge with K31, making it unfavorable for direct intermolecular hydrogen bond formation with Q493 in RBD. In 3N39, simultaneous mutation of K31N and E35K resulted in the loss of this salt bridge, allowing K35 to exclusively form a direct intermolecular hydrogen bond with Q493 (Fig. 2(b)). The second region contains V25 and F79, both of which acquired larger hydrophobic side chains through mutations. These two residues, together with multiple hydrophobic residues, form a small hydrophobic pocket that accommodates F486 of RBD (Fig. 2(c)). WT ACE2 also has the corresponding pocket, but the L79F mutation in 3N39 makes the hydrophobic contacts more extensive. As for V25, it does not interact directly with F486 and may contribute to

improving the stability of the pocket by filling a space at the back of the pocket. Thus, the structure suggests that these four mutations collectively lead to the approximately 100-fold increase in the overall affinity.

Our crystal structure also provided a hint for designing an enzymatically inactive mutant of ACE2. Since the native ACE2 is an enzyme involved in blood pressure control, when sACE2 decoys are used as drugs, it may be better to eliminate their enzyme activity to prevent side effects. Interestingly, sACE2(3N39) in our crystal structure adopts a "closed" conformation where the enzymatic active site is completely inaccessible from the outside, which is quite different from the "open" conformation of the RBD-bound WT sACE2 structure reported so far (Fig. 3) [3,5]. As the residues mutated in 3N39 to improve affinity to RBD are far from the active site, we speculated that the closed conformation may be due to crystal packing. Then we introduced a double mutation, S128C/V343C, into ACE2(3N39) to fix this closed conformation with a disulfide bond.

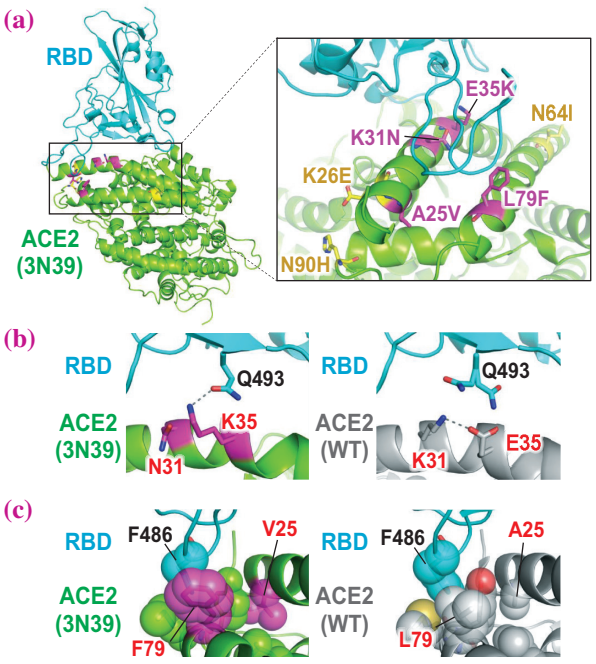

Fig. 2. Structural basis for the affinity enhancement of the ACE2(3N39) mutant. **(a)** Overall structure of the sACE2(3N39)-RBD complex. The essential and nonessential mutated residues for affinity enhancement are shown as magenta and yellow stick models, respectively. The expanded view of the RBD binding interface is provided in the inset. **(b)** Structures of the K31N/E35K mutation site in 3N39 (left panel) and its corresponding site in WT (right panel). Hydrogen-bonding interactions (within 3.0 Å) are indicated by dashed lines. **(c)** Structures of the A25V/L79F mutation site in 3N39 (left panel) and its corresponding site in WT (right panel). F486 residue of RBD and hydrophobic residues composing the F486-binding pocket of ACE2 are shown as stick models with transparent sphere models.

As expected, ACE2(3N39) with the S128C/V343C mutation completely lost its enzymatic activity without decreasing its affinity for RBD [2]. In addition, the introduction of this disulfide bond increased the T_m value of 3N39 by 7°C. The improvement in thermal stability should also be beneficial for pharmaceutical applications of the engineered ACE2.

The crystal structure confirmed that ACE2(3N39) binds to RBD through the same interface as WT ACE2, strongly suggesting a high resistance of our decoy drug to viral escape mutations. In fact, the SARS-CoV-2 escape mutation did not arise during culture in the presence of ACE2(3N39) [2]. Furthermore, we have already demonstrated the high therapeutic potency of ACE2(3N39) in a hamster model of COVID-19. These results indicate that ACE2(3N39)-based decoys can be effective therapeutic agents against various viral mutants. We are continuing our studies on engineered ACE2 with the aim of realizing its therapeutic application as soon as possible.

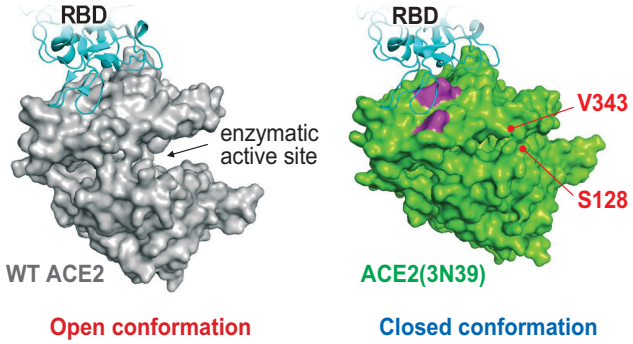

Fig. 3. Open and closed conformations of ACE2. The RBD-bound WT ACE2 (left, 6m0j) and the RBD-bound ACE2(3N39) (right) are shown as surface representations. The mutation sites in 3N39, which are essential for affinity enhancement, are shown in magenta.

Takao Arimori* and Junichi Takagi

Institute for Protein Research, Osaka University

*Email: arimori@protein.osaka-u.ac.jp

References

[1] W. Jing and E. Procko: Proteins **89** (2021) 1065.
[2] *Y. Higuchi, T. Suzuki, T. Arimori, N. Ikemura, E. Mihara, Y. Kirita, E. Ohgitani, O. Mazda, D. Motooka, S. Nakamura, Y. Sakai, Y. Itoh, F. Sugihara, Y. Matsuura, S. Matoba, T. Okamoto, J. Takagi, A. Hoshino: Nat. Commun.* ***12*** *(2021) 3802.*
[3] J. Shang *et al.*: Nature **581** (2020) 221.
[4] K.K. Chan *et al.*: Science **369** (2020) 1261.
[5] J. Lan *et al.*: Nature **581** (2020) 215.

Structural basis for FXIIa inhibition by a peptide foldamer containing cyclic β-amino acids

Foldamers are oligomers that form a specific conformation and attract attention as a novel modality for functional molecules [1]. Cyclic amino acids are known to form peptide foldamers by inducing secondary structures such as helices and sheets.

Suga and colleagues have developed a method of obtaining macrocyclic peptides with various unnatural amino acids that strongly bind to target molecules (RaPID system) by combining genetic code reprogramming and in vitro selection methods [2]. Recently, Suga and Kato modified the RaPID system to efficiently incorporate cyclic β-amino acids (cβAAs) such as (1R,2R)-2-aminocyclohexane carboxylic acid (ACHC, Fig. 1(a)) into peptides [3]. Using this modified RaPID system, they discovered macrocyclic peptides with cβAAs that strongly inhibit FXIIa (a serine protease involved in blood coagulation). Here, the crystal structure of FXIIa bound with one such peptide, F3 [3] (Fig. 1(b)). F3 consists of 18 residues and inhibits FXIIa with a Ki value of about 1.5 nM. Note that we have use the term "cyclic" in two different contexts. F3 has a macrocyclic structure due to the formation of a thioether bond while containing ACHC, an unnatural amino acid with a cyclic side-chain structure.

The FXIIa-F3 complex yielded polycrystals consisting of stacked thin plates. Diffraction experiments using ordinary synchrotron radiation beams gave smeared diffraction spots with a resolution of about 7.5 Å, but we could not process the obtained images for analysis. Using a microbeams at SPring-8 **BL32XU**, diffraction images were collected from eight crystals with the helical scheme, then processed with the program KAMO [4] to obtain a final data set at a resolution of about 3.0 Å. This is an excellent example of how advances in beamlines and fully automated measurement methods have made it possible to solve previously difficult structural problems.

In the overall structure of the FXIIa-F3 complex (Fig. 1(c)), F3 forms a β-hairpin structure. ACHC is known to induce turns, and one of the two ACHC residues of F3 (ACHC8) is located at the tip of the β-hairpin, possibly stabilizing the overall β-hairpin structure of F3 by inducing a turn. In addition, the side chain of ACHC8 forms hydrophobic interactions with Tyr515 and His507 of FXIIa. The other ACHC residue (ACHC13) also stabilizes the F3 structure by forming intramolecular hydrogen bonds via its main-chain oxygen and nitrogen and hydrophobic interactions with Ala3 and Tyr16 via its side chain. ACHC13 also induces intermolecular hydrophobic interactions with Trp586 of FXIIa.

The unique chemical structure of ACHC enables the intra- and intermolecular interactions described above. As a cβAA, ACHC has a large hydrophobic side chain capable of forming hydrophobic interactions while limiting the structural flexibility of peptide main-chain atoms. It also contains the main-chain nitrogen that can accept a hydrogen bond. The unique chemical structure of ACHC allows F3 to have a stable folded structure (peptide foldamer) and bind strongly to FXIIa.

The details of the interactions between F3 and the active center of FXIIa are shown in Fig. 2. Arg6 of F3 fits into the S1 site of the substrate recognition pocket of FXIIa and forms an intermolecular salt bridge with Asp557 of FXIIa. The peptide bond between Arg6 and Arg7 of F3 is in the vicinity of Ser563, the catalytic residue of FXIIa, and the N-terminal residue of Arg6 forms an intermolecular sheet with FXIIa. These features show that F3 acts as a "standard mechanism inhibitor" that interacts with FXIIa in a manner similar to its substrates.

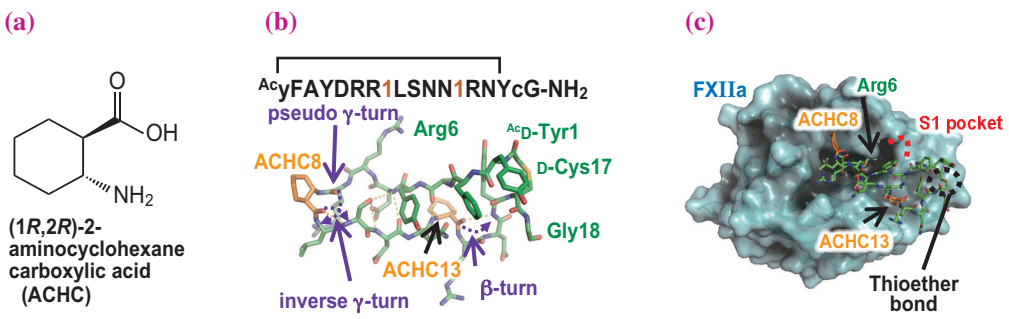

Fig. 1. Structure of F3-FXIIa complex. **(a)** Chemical structure of ACHC. **(b)** Structure of F3. 1, Acy, and c represent ACHC, acetyl-D-tyrosine, and D-cysteine, respectively. **(c)** Crystal structure of FXIIa-F3.

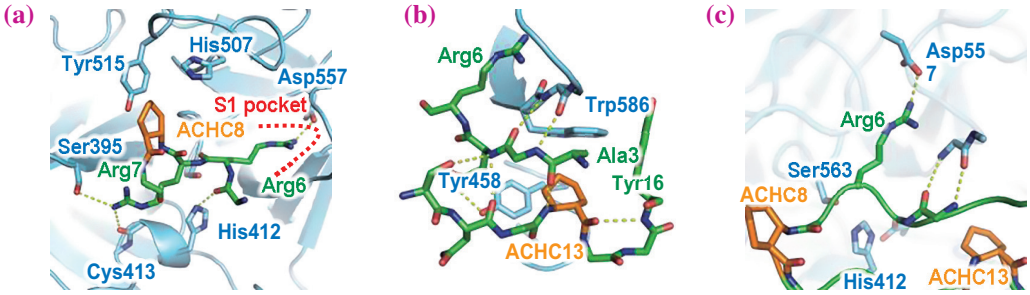

Fig. 2. Details of interaction. **(a)** Interactions near Arg6 and ACHC8. **(b)** Interactions near HCHC13. **(c)** Interactions involving Arg6 and its N-terminal region.

Protease activity in vivo must be tightly controlled, and various proteinaceous serine protease inhibitors exist naturally [5]. When we compared the inhibition mechanisms of F3 with those of the proteinaceous inhibitors, we found interesting similarities and differences (Fig. 3). They share a key basic residue that binds to the S1 site of the protease, and its N-terminal region commonly forms an intermolecular β-sheet with the protease. The interaction area of F3 with FXIIa is 703 Å^2, which is comparable to that of proteinaceous inhibitors (700–900 Å^2). ACHC8 and ACHC13 of F3 contribute to the stabilization of the compact structure, while the proteinaceous inhibitors often form disulfide bonds at the position of ACHC13 to stabilize the conformation of the basic residue. They also contain relatively large scaffold domains with various sizes and folds. The various proteinaceous inhibitors have likely developed a common inhibitory mechanism (binding of basic residues to the S1 site and intermolecular β-sheet formation) by convergent evolution to inhibit the target protease efficiently. On the other hand, F3, obtained by only a few cycles of in vitro selection, uses the same inhibitory mechanism as natural proteinaceous inhibitors, with a much smaller molecular size. The *de novo* discovery of F3 thus demonstrates the potential of the RaPID system adopted for cβAAs to obtain functional peptide foldamers.

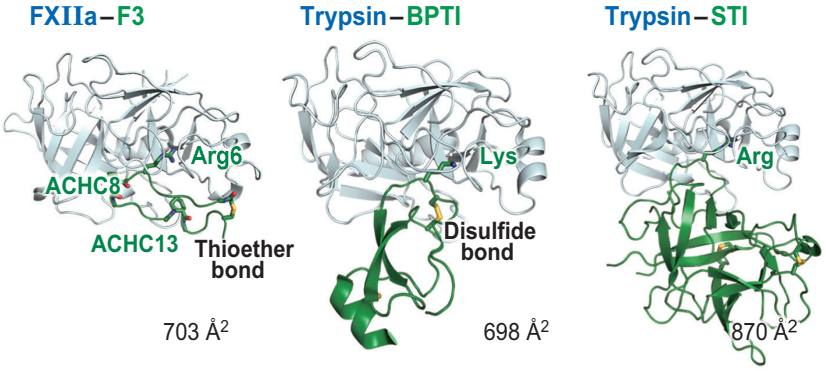

Fig. 3. Comparisons with protein-based protease inhibitors.

Toru Sengoku

Department of Biochemistry, School of Medicine, Yokohama City University

Email: tsengoku@yokohama-cu.ac.jp

References

[1] S.H. Gellman: Acc. Chem. Res. **31** (1998) 173.
[2] A.A. Vinogradov *et al.*: J. Am. Chem. Soc. **141** (2019) 4167.
[3] *T. Katoh, T. Sengoku, K. Hirata, K. Ogata and H. Suga: Nat. Chem. **12** (2020) 1081.*
[4] K. Yamashita *et al.*: Acta Crystallogr. Sect. Struct. Biol. **74** (2018) 441.
[5] C.J. Farady and C.S. Craik: ChemBioChem **11** (2010) 2341.

Structural basis of the extracellular interaction between receptor-type tyrosine-protein phosphatase δ and neuroligin 3

Billions of neurons connected in a mammalian brain form circuits to realize brain functions. The neuronal synapse is an intercellular adhesion specialized for neuronal signal transmission and is formed between the axon terminal of one neuron and the dendrites or cell bodies of another neuron (Fig. 1(a)). During neurodevelopment, synapse formation is induced by a family of cell adhesion molecules termed synaptic organizers. Synaptic organizers on the axon terminal membrane (presynaptic organizers) and those on the dendritic or cell body membrane (postsynaptic organizers) extracellularly interact with each other in the synaptic cleft and then induce the formation of subcellular structures specialized for neurotransmitter release in the presynapse and for responding to neurotransmitters in the postsynapse (Fig. 1(b)). Functional defects in synaptic organizers potentially disturb the formation of neural circuits and play a causative role in neurodevelopmental disorders such as autism spectrum disorders (ASDs).

Receptor-type tyrosine-protein phosphatase δ (PTPδ) is a member of type IIa receptor protein tyrosine phosphatases (IIa RPTPs) and serves as a presynaptic organizer along with the two other members, LAR and PTPσ. The extracellular domain of IIa RPTPs consists of three immunoglobulin-like domains (Ig1–Ig3) and four or eight fibronectin type-III domains (FN1–FN8; Fig. 2(a)). Ig1–Ig3 of IIa RPTPs are responsible for the interaction with the partner postsynaptic organizers such as IL-1 receptor accessory protein (IL-1RAcP), IL-1RAcP-like 1 protein (IL1RAPL1), Slit- and Trk-like proteins 1–6, and synaptic adhesion-like molecules 3 and 5. The interaction with these postsynaptic organizers depends on the two splice inserts derived from the two short exons termed mini-exon A (meA) and mini-exon B (meB), which are positioned within Ig2 and at the junction between Ig2 and Ig3, respectively, in IIa RPTPs. We and other groups have extensively studied such splice-insert-dependent interaction mechanisms by crystallography in combination with structure-based mutational analyses [1].

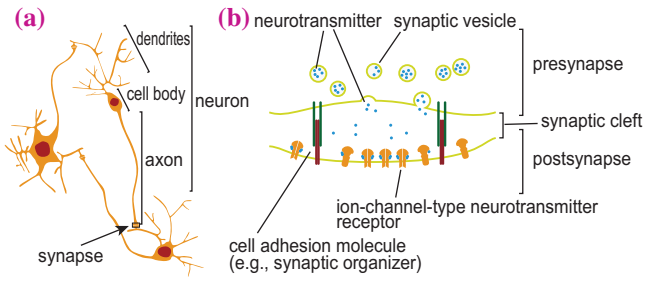

Fig. 1. Schematic of **(a)** neurons and **(b)** a synapse.

Recently, we have identified neuroligin (NLGN) 3 as a novel postsynaptic ligand for PTPδ [2]. NLGN3 is a postsynaptic adhesion molecule and interacts with presynaptic neurexins (NRXNs) to organize synaptogenesis. The NLGN3 gene is one of the best-characterized genes associated with ASDs. The esterase-like domain (ELD) in the extracellular region of NLGN3 is responsible for binding to Ig1–Ig3 of the PTPδ variant lacking the meB insert (PTPδB$^-$). To elucidate the mechanism of the extracellular interaction between PTPδ and NLGN3, we determined the crystal structure of the apo mouse NLGN3 ELD and the mouse NLGN3 ELD–mouse PTPδB$^-$ Ig1–FN1 complex at resolution of 2.76 Å and 3.85 Å, respectively [2]. X-ray diffraction data were collected at 100 K at SPring-8 **BL41XU**. The NLGN3 ELD adopts an α/β-hydrolase fold and forms a 2-fold symmetric homodimer, similarly to other NLGN family proteins [3,4]. In the complex, one PTPδ molecule binds to each protomer of the NLGN3 dimer and assembles into a W-shaped heterotetramer with a 2:2 stoichiometry (Fig. 2(b)).

Ig1, Ig2, and Ig3 of PTPδ interact with the core region of NLGN3 ELD. PTPδ Ig2 also interacts with the tail region following the core region of NLGN3 ELD. Phe170 and the aliphatic portions of Arg75, Glu77, Arg90, and Gln92 in PTPδ Ig1 form a hydrophobic pocket, which accommodates the side chain of Leu320 in NLGN3 (Fig. 3(a)). Leu141, Pro221, and Tyr225 of PTPδ Ig2 form a hydrophobic patch, which binds to Tyr302, Val305, and Ile355 of NLGN3 (Fig. 3(b)). The tail region of NLGN3 ELD lies on the 3-residue meA insertion (meA3) in PTPδ Ig2. Met614 and Phe615 of NLGN3 appear to hydrophobically interact with a hydrophobic patch formed by Leu153, Leu185, Ile190, and the aliphatic portions of Thr151 and Ser187 in PTPδ Ig2 (Fig. 3(c)). The involvement of Ile190, which is included in meA3, in this interaction is consistent with the fact that the PTPδ variant containing meA3 binds to NLGN3 with a higher affinity than the variant lacking meA3. Val257, Met261, and Ile281 of PTPδ Ig3 form a hydrophobic patch that interacts with Gly371, Leu374, and Tyr474 of NLGN3 (Fig. 3(d)). Ser236 and Arg283 of PTPδ appear to form hydrogen bonds with Asn375 and the main chain of Gly475 in NLGN3, respectively. Arg234 of PTPδ also appears to form a hydrogen bond with Glu372 of NLGN3. The spatial arrangement of Ig2 and Ig3 of PTPδ is substantially different between the ligand-free and NLGN3-bound forms (Fig. 3(e)). Upon binding to NLGN3,

PTPδ Ig3 is rearranged so that both PTPδ Ig2 and Ig3 can simultaneously interact with NLGN3. The relative positions of PTPδ Ig2 and Ig3 depend on the length of the meB-lacking linker connecting these two domains; the meB-containing linker tends to be extended and more flexible, as expected from the structure of the PTPδ variant containing meB in complex with IL1RAPL1 (Fig. 3(e)) [5].

We next designed three distinct types of NLGN3 mutant to dissect the canonical NRXN- and non-canonical PTPδB⁻-mediated NLGN3 pathways, using the structural information from the crystal structures of the NLGN–NRXN and NLGN3–PTPδB⁻ complexes. The designed mutants of NLGN3 exhibited different binding selectivities for PTPδB⁻ and NRXN1β and had potential for use as molecular tools to dissect the canonical and noncanonical transsynaptic signaling of NLGN3 (Fig. 3(f)). Then, we generated mice carrying a NLGN3 mutation that impairs either or both of the canonical and noncanonical NLGN3 pathways by CRISPR-Cas9 genome editing. The analysis of the neurons derived from the mutant mice suggested that either or both of the canonical and noncanonical NLGN3 pathways are indeed impaired in the mutant mice. The results of the analysis also suggested that the canonical and noncanonical pathways appear to counterbalance each other for inhibitory synapse formation. We further assessed the development of social behaviors in the mutant mice. The canonical pathway-impaired mice showed increased sociability, whereas the noncanonical pathway-impaired mice showed impaired social behavior and enhanced motor learning, with an imbalance in excitatory/inhibitory synaptic protein expressions. These findings from behavioral studies with the structure-based design of site-directed mutations suggest that the canonical and noncanonical NLGN3 pathways compete and regulate the development of sociality.

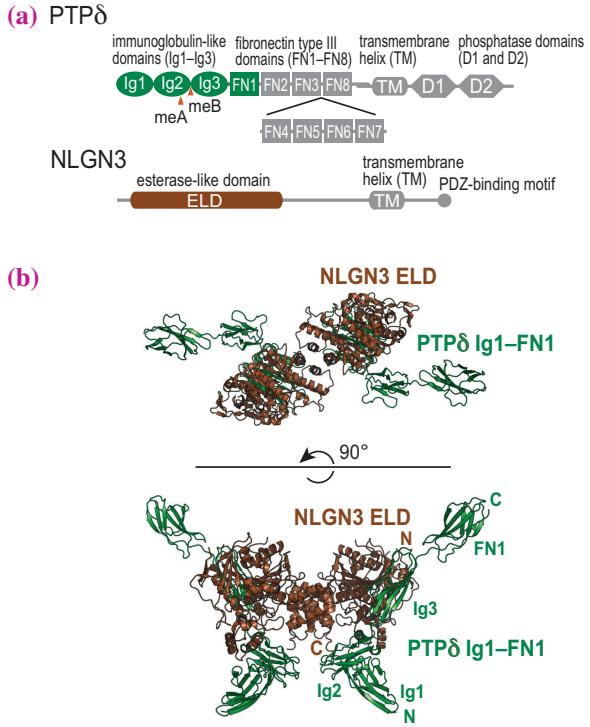

Fig. 2. **(a)** Domain organizations of PTPδ and NLGN3. The regions analyzed in this study are colored green (PTPδ Ig1–FN1) or brown (NLGN3 ELD). **(b)** Overall structure of the complex between PTPδB⁻ Ig1–FN1 and NLGN3 ELD. The coloring scheme is the same as that in (a).

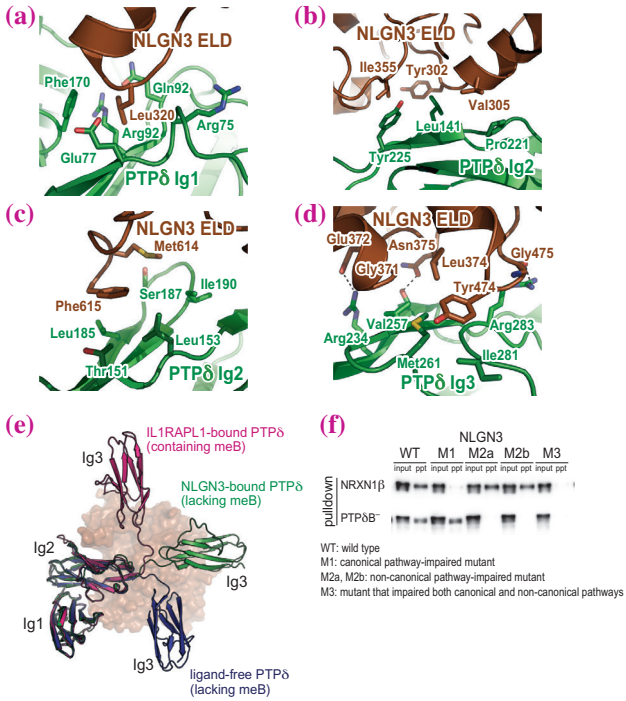

Fig. 3. **(a-d)** Close-up views of the interaction between PTPδ and NLGN3. The interacting residues are shown as sticks. Dotted lines indicate hydrogen bonding. The coloring scheme is the same as that in Fig. 2. **(e)** PTPδ structures in the apo, NLGN3-bound, and IL1RAPL1-bound states. **(f)** Pulldown analysis to test the binding selectivity of NLGN3 mutants for PTPδB⁻ and NRXN1β. Samples were analyzed by SDS-PAGE with immunostaining.

Shuya Fukai

Department of Chemistry, Kyoto University

Email: fukai@kuchem.kyoto-u.ac.jp

References

[1] S. Fukai and T. Yoshida: FEBS J. **288** (2021) 6913.
[2] *T. Yoshida, A. Yamagata, A. Imai, J. Kim, H. Izumi, S. Nakashima, T. Shiroshima, A. Maeda, S. Iwasawa-Okamoto, K. Azechi, F. Osaka, T. Saitoh, K. Maenaka, T. Shimada, Y. Fukata, M. Fukata, J. Matsumoto, H. Nishijo, K. Takao, S. Tanaka, S. Okabe, K. Tabuchi, T. Uemura, M. Mishina, H. Mori, S. Fukai: Nat. Commun.* ***12*** *(2021) 1748.*
[3] D. Alaç *et al.*: Neuron **56** (2007) 992.
[4] X. Chen *et al.*: Nat. Struct. Mol. Biol. **15** (2008) 50.
[5] A. Yamagata *et al.*: Nat. Commun. **6** (2015) 6926.

Structural basis of heme-responsive sensor protein mediating the survival of hemolytic bacteria

Iron is an essential nutrient that plays a central role in many physiological processes for the survival of all living things. For example, in humans, after breathing in air, oxygen transport via the lungs to the peripheral tissues is facilitated by oxygen binding to the heme iron (iron-protoporphyrin IX) in hemoglobin in red blood cells. In some pathogens, heme is the major source of iron. These pathogens have evolved special pathways for acquiring heme from animal host blood [1] resulting in hemolysis, which is the destruction of red blood cells and the release of hemoglobin into the blood plasma (Fig. 1). Over a billion molecules of heme are released from red blood cells in animal hosts during hemolysis. These heme molecules are directly used as prosthetic groups for hemoproteins and are also catabolized by heme-degrading enzymes for pathogenic cells to obtain iron. However, excess heme accumulated in bacterial cells is highly cytotoxic owing to the reactive oxygen species that are generated. Therefore, cellular heme homeostasis is tightly controlled and as such, bacteria have evolved sophisticated regulatory systems. The failure of these systems leads to the death of pathogens, so understanding these systems may provide new leads to developing antimicrobial agents effective against globally distributed drug-resistant pathogens.

We investigated a newly discovered heme-responsive sensor protein, PefR, involved in the underlying regulatory mechanism in the hemolytic bacterium *Streptococcus agalactiae*, which causes life-threatening neonatal infections such as septicemia, pneumonia, and meningitis [2]. PefR acts as an intracellular heme sensor and a transcriptional factor to regulate the expression of the heme exporter. When only the heme required as an iron source is present, PefR is bound upstream of the heme exporter gene and heme is not exported from *S. agalactiae* cells, but during hemolysis in host blood, heme overflows into the cell, causing PefR to bind heme and dissociate from the gene. Consequently, the heme exporter is expressed, and the excess heme is exported from the cells to prevent cytotoxicity (Fig. 2). Thus, if PefR does not function, *S. agalactiae* cells are killed owing to the toxicity of the excess heme, making PefR an important protein for this bacterium. We clarified how PefR recognizes heme and how the heme binding event is translated into the signal for DNA dissociation [3].

We prepared a highly purified PefR protein and crystallized it in the apo (heme free form)-PefR–DNA complex and heme-bound PefR and collected their X-ray diffraction data at SPring-8 **BL26B2** and **BL41XU**. The structures were determined to a resolution of 2.5 Å for the DNA-bound protein and 1.7 Å for the heme-bound protein. The crystal structures reveal that the apo-PefR has a straddling structure and sandwiches the target DNA. When heme enters the apo-PefR–DNA complex, heme binds to the protein by adopting a six-coordinate structure involving the main chain nitrogen of Met1 and the side chain of His114 of each subunit in the dimer. When heme is bound, a hydrophobic core is formed by the amino acid side chains around it. The heme binding triggers an increase in the distance between the DNA-binding domains (that sandwich the DNA of PefR) between the heme-bound and heme-free PefR, preventing PefR from interacting with the target DNA. This is the structural basis by which PefR causes DNA dissociation upon heme binding (Fig. 3). Further biochemical analysis revealed that the heme-bound PefR, once dissociated from the target DNA could stably bind carbon monoxide (CO), and this CO-bound PefR could not rebind the target DNA in the cell.

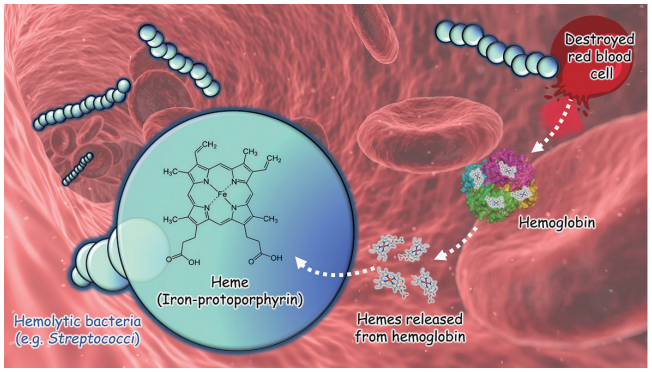

Fig. 1. Heme acquisition system in hemolytic bacteria.

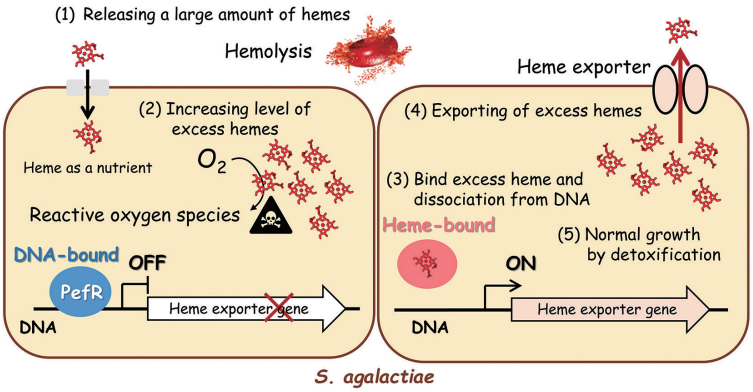

Fig. 2. Physiological function of the heme-responsive sensor protein PefR in *S. agalactiae*.

We have discovered that the heme-bound PefR have the ability to capture intracellular CO. The CO is released from host cells as a product of the heme degradation reaction, but when it flows into pathogenic cells, it shows cytotoxicity, causing cell death or dormancy [4]. The results of this study indicated that PefR is a multifunctional protein that acts as a transcriptional factor, a heme sensor, and possibly a CO scavenger involved in iron acquisition by hemolytic bacteria from animal hosts (Fig. 3) [3]. Inhibiting these detoxification mechanisms of hemolytic bacteria by using these PefR functions could be an important strategy for developing antimicrobial agents to address the global problem caused by drug-resistant pathogens.

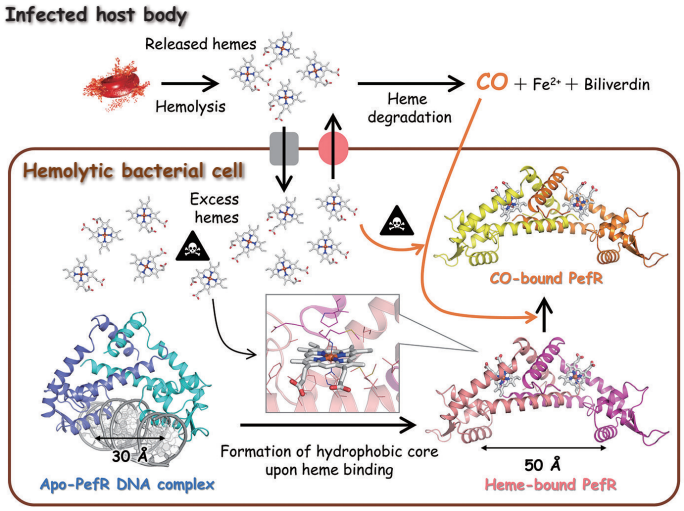

Fig. 3. Schematic diagram of the structure and function of PefR in *S. agalactiae*. A cell of the hemolytic bacterium is represented by the brown square. The area outside the square is the body of the infected host. Hemolytic bacterial cells survive by acquiring heme molecules from hemoglobin in red blood cells from their animal hosts. To avoid the cytotoxicity of excess heme during hemolysis, PefR acts as a transcriptional factor to regulate the heme efflux system in response to the cellular heme concentration. The result of crystallographic, spectroscopic, and biochemical studies indicate that the heme coordination to DNA-bound PefR controls the structural rearrangement of the DNA-binding domains to dissociate PefR from the target DNA. After dissociating from the target DNA, the heme of holo-PefR can stably bind CO, which is a by-product of heme degradation by heme oxygenase.

Hitomi Sawai*,† and Yoshitsugu Shiro

Cellular Regulation Laboratory, University of Hyogo

*Email: hitomisawai@nagasaki-u.ac.jp

† Present address: Nagasaki University

References

[1] A. Gruss *et al.*: Adv. Microb. Physiol. **61** (2012) 69.
[2] A. Fernandez *et al.*: PLoS Pathog. **6** (2010) 1.
[3] *M. Nishinaga, H. Sugimoto, Y. Nishitani, S. Nagai, S. Nagatoishi, N. Muraki, T. Tosha, K. Tsumoto, S. Aono, Y. Shiro, H. Sawai: Commun. Biol. **4** (2021) 467.*
[4] K.V. Lyles *et al.*: Front. Cell. Infect. Microbiol. **8** (2018) 198.

Molecular basis for two stereoselective Diels–Alderases that form enantiomeric decalin skeletons

The Diels–Alder (DA) reaction is one of the most important reactions for C–C bond formation in synthetic chemistry. This practical and very useful reaction, which forms two C–C bonds and up to four chiral centers to generate a cyclohexene from a conjugated diene and a substituted alkene, is also a key step in many natural product biosynthetic pathways. Recently, a number of enzymes catalyzing the DA reaction, the so-called Diels–Alderases (DAases), have been identified from bacterial, fungal, and plant origins [1]. It is noteworthy that, although DAases have no common structural features and are derived from distinct progenitor enzymes or proteins, such as *S*-adenosylmethionine (SAM)-dependent methyltransferase and FAD-dependent monooxygenase, they all exhibit high stereoselectivity and catalytic efficiency. However, the mechanisms underlying the extraordinary features of naturally occurring DAases, including the origin of stereoselectivity and catalytic efficiency, have remained elusive.

Fsa2 and Phm7 catalyze intramolecular DA reactions to form enantiomeric decalin scaffolds from similar linear polyenoyl tetramic acids during the biosynthesis of HIV-1 integrase inhibitors, equisetin and phomasetin, which have "enantiomeric" decalin skeletons (Fig. 1(a)). The replacement of *phm7* in a phomasetin-producing fungus with *fsa2* resulted in the production of an equisetin-type decalin scaffold, indicating that these enzymes control and determine the stereochemistry of the decalin scaffold during the biosynthesis [2]. To unveil the stereoselective DA reaction mechanisms of Fsa2 and Phm7, we first determined the crystal structures of these enzymes.

X-ray diffraction data of Fsa2 and Phm7 crystals were collected at SPring-8 **BL32XU** and **BL41XU** (Fig. 1(b)) [3]. The crystal structure of Fsa2 has a β-sandwich and a β-barrel domain at the N- and C-termini, respectively, and a large pocket is present between the two domains. Considering the substrate structure and volume, we speculated that the large cavity created by the two domains is a substrate binding site. Phm7 catalyzes intramolecular DA reactions to produce the decalin scaffold enantiomerically opposite to that of Fsa2. Despite their distinct stereoselectivity and low sequence similarity, the crystal structure of Phm7 is similar to that of Fsa2, and the shape and position of their large pockets are also similar. Unfortunately, however, the crystal structures of substrate-free Phm7 and Fsa2 did not reveal the mechanism of how they control the stereoselectivity.

To find productive binding conformations of the substrates in Fsa2 and Phm7, we carried out molecular dynamics (MD) simulations of substrate-bound enzymes by the gREST method [4], which can search possible binding poses more extensively than the conventional method. The MD simulations yield four major bound poses, including "folded" and "extended" conformations, for the substrates. The major "folded" poses of the Phm7 substrate were well defined (Fig. 2(a), left panel). The tetramic acid moiety and polyene tail of the folded poses were located at the upper front and back of the pocket, respectively, whereas a U-shaped folded alkyl chain was found at the lower side of the pocket. Representative conformations of the Phm7 substrate explain the expected phomasetin-type decalin configuration (Fig. 2(b)), indicating that the Phm7 pocket robustly regulates and stabilizes the substrate in a specific conformation. In contrast to Phm7, the pocket of Fsa2 allows various "folded" conformations of the substrate (Fig. 2(a), right panel). Nevertheless, similar tetramic acid-front and polyene-back poses were also found, which were consistent with the configuration of the equisetin-type decalin scaffold (Fig. 2(b)).

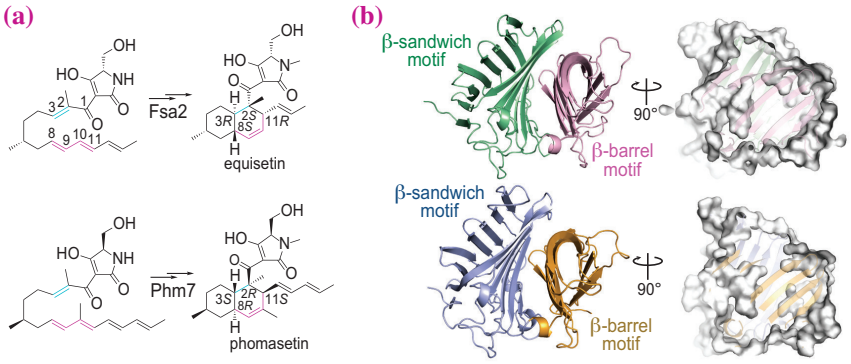

Fig. 1. **(a)** Stereoselective DA reactions catalyzed by Fsa2 and Phm7 from similar linear polyenoyl tetramic acids. **(b)** Crystal structures of Fsa2 (top) and Phm7 (bottom). Surface models show shapes of the pocket between the two domains.

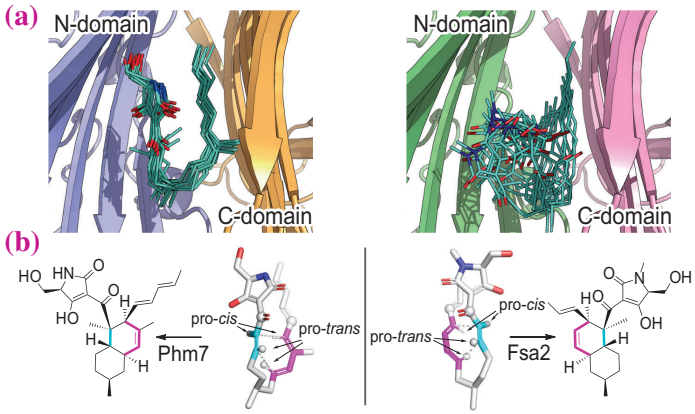

Fig. 2. Predicted binding models of Phm7 (left) and Fsa2 (right). **(a)** Collective view of 12 representative snapshots of the folded substrates in the binding pockets. **(b)** Conformations of the representative poses of the substrates and structures of the corresponding cycloadducts.

To verify the pseudo-enantiomeric substrate binding conformation and identify the amino acid residues involved in substrate binding and chemical catalysis in Phm7 and Fsa2, we carried out site-directed mutagenesis experiments of both enzymes and density functional theory calculations for Phm7. The outcomes demonstrated that the binding models predicted by the MD simulations are reliable. It was also confirmed that Phm7 tightly holds the tetramic acid moiety via multiple hydrogen bonds, and a pair of acidic and basic side chains is the chemical catalyst that activates the dienophile to promote the DA reaction. In contrast, the Fsa2 substrate undergoes a hydrogen bonding interaction with only one amino acid residue. Fsa2 likely retains the substrate affinity to the enzyme by accommodating various folded conformations and minimizing entropy loss upon binding. Moreover, there is no hydrophilic amino acid residue in proximity to the C1 carbonyl, which accelerates the reaction as a catalytic residue. Fsa2 possibly adopts a dynamic control of the reaction rate using the conformational fluctuations of the substrate.

It is likely that substrates bind to the pocket of Fsa2 and Phm7 in a similar way (tetramic acid-front and polyene-back orientation), allowing the stereoselective DA reactions to proceed. Considering that the conformation of the enzyme-bound substrate is closely correlated to the stereochemistry of the product, we propose a model of how the enzymes produce decalin scaffolds with four possible configurations via the stereoselective DA reactions (Fig. 3). The linear Fsa2 substrate is folded clockwise (Fig. 3(a)) and the Phm7 substrate counterclockwise (Fig. 3(b)) to yield (pseudo)enantiomeric conformations in the enzyme pocket. When the folded Phm7 substrate is flipped horizontally, it binds to the Phm7 pocket in the tetramic acid-front and polyene-back orientation. A key difference between the transition state structures for *trans*- and *cis*-decalin scaffolds is created by the rotation of the polyene tail at the C7–C8 bond. Thus, the *cis*-decalin forming conformation of the substrate in the enzyme pocket is predictable. More than 100 homologs of Fsa2 and Phm7 are available in the public database. A highly accurate protein structure prediction from amino acid sequences using deep learning algorithms, such as AlphaFold2, is now feasible. A combination of computational calculations, including protein structure prediction, MD-based docking simulation, and quantum chemical calculation, with biochemical experiments will provide further insight into the structure-function relationship of this stereoselective DAase family catalyzing bioactive decalin scaffolds, as well as a guiding principle to create artificial DAases.

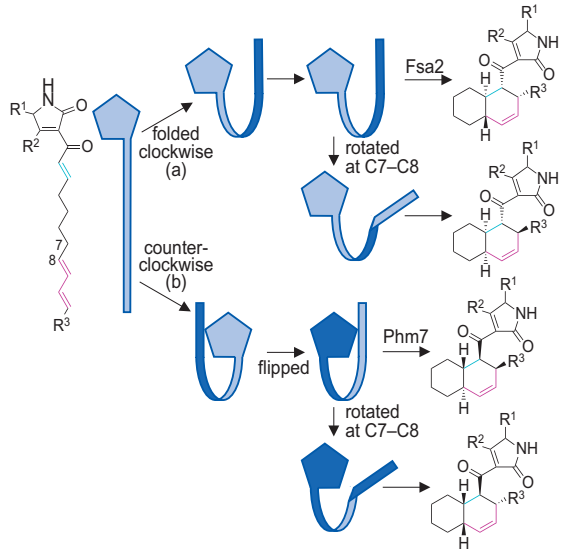

Fig. 3. Model of the enzyme-mediated formation of four diastereomeric decalin scaffolds. Linear polyenoyl tetramic acid substrates are shown schematically as a pentagon and a ribbon. Folded substrates bind to the enzymes in the tetramic acid-front and polyene-back manner.

Naoki Kato[a], Keisuke Fujiyama[b] and Shingo Nagano[c,*]

[a] Faculty of Agriculture, Setsunan University
[b] RIKEN Center for Sustainable Resource Science
[c] Department of Chemistry and Biotechnology, Tottori University

*Email: snagano@tottori-u.ac.jp

References

[1] B.R. Lichman *et al.*: Chem. Eur. J. **25** (2019) 6864.
[2] N. Kato *et al.*: Angew. Chem. Int. Ed. **57** (2018) 9754.
[3] *K. Fujiyama, N. Kato, S. Re, K. Kinugasa, K. Watanabe, R. Takita, T. Nogawa, T. Hino, H. Osada, Y. Sugita, S. Takahashi, S. Nagano: Angew. Chem. Int. Ed.* ***60*** *(2021) 22401.*
[4] M. Kamiya and Y. Sugita: J. Chem. Phys. **149** (2018) 072304.

Characterization of short-lived reaction intermediate in enzymatic nitrous oxide generation by XFEL crystallography and time-resolved spectroscopy

Nitrous oxide (N_2O) is a powerful greenhouse gas that is 310-times more potent than carbon dioxide, as well as a major ozone-depleting substance. The concentration of atmospheric N_2O has been increasing for more than 100 years, contributing to global warming [1]. The major anthropogenic cause of global N_2O emission is the microbial breakdown of nitrogen-based compounds contained in fertilizers for agriculture. A key biochemical process related to N_2O formation from fertilizers is microbial denitrification, a form of anaerobic respiration, in which nitrate (NO_3^-) is sequentially reduced to dinitrogen gas ($NO_3^- \rightarrow NO_2^- \rightarrow NO \rightarrow N_2O \rightarrow N_2$). In this process, nitric oxide reductase (NOR) catalyzes the formation of N_2O from nitric oxide (NO). Therefore, the elucidation of the catalytic mechanism of N_2O formation by NOR will help us resolve this aspect of global warming.

NOR isolated from the fungus *Fusarium oxysporum* (P450nor) is an enzyme involved in fungal denitrification. P450nor has a heme coordinated by a cysteine thiolate as an active site and catalyzes the reduction of NO to N_2O using a proton and electrons from NADH ($2NO + NADH + H^+ \rightarrow N_2O + NAD^+ + H_2O$) (Fig. 1). In addition to the global impact described above, the catalytic mechanism of P450nor has intrigued chemists since its first isolation in 1993 [2], because the P450nor-catalyzed reaction involves N–N bond formation and N–O bond cleavage. In the late 1990s, spectroscopic studies provided clues to the catalytic mechanism [3]. The binding of the first NO molecule to the resting ferric state produces the Fe^{3+}–NO form. Then, the Fe^{3+}–NO species is reduced with hydride (H^-) from NADH to form a short-lived reaction intermediate called intermediate I (*I*). Finally, the second NO molecule reacts with *I* to yield N_2O. Thus, knowing the chemical structure of *I* is crucial for understanding the mechanism of N_2O formation, i.e., N–N bond formation, by P450nor. However, despite extensive efforts over the decades by several approaches, including synthetic model and theoretical studies, the chemical structure of *I* remains to be solved, although four possible models, Fe^{2+}–NHO, Fe^{3+}–$NHO^{\bullet -}$, Fe^{3+}–$NHOH^{\bullet}$ and Fe^{4+}–$NHOH^-$, have been proposed. To establish the catalytic mechanism in P450nor, we need to obtain conclusive experimental information on the structure of *I*.

Most recently, we have developed time-resolved (TR) techniques using caged NO, which quantitatively releases NO, on the microsecond time scale upon UV irradiation to directly observe the catalytic reaction of P450nor and successfully characterized the Fe^{3+}-NO species by TR serial femtosecond crystallography (TR-SFX) at SACLA [4]. In this study, we utilized this technique of using caged NO to determine the coordination and electronic structures of the key reaction intermediate *I* in P450nor. Our work in this study is briefly summarized in Fig. 2. Our previous TR visible absorption measurement for the microcrystals of P450nor soaked in a solution containing NADH and caged NO showed that the formation of *I* in the microcrystal took ~5 s after UV light illumination, though it took only 1 ms in the solution state [4]. From this information, the microcrystals soaked with NADH and caged NO were scooped using a mesh

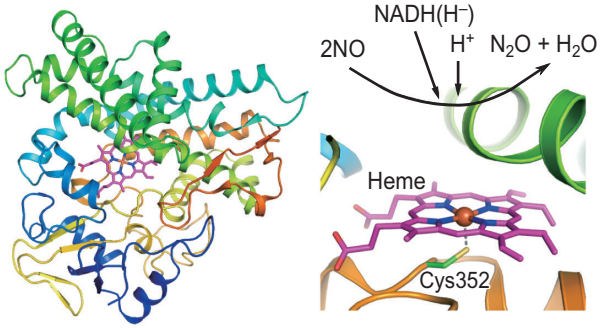

Fig. 1. Structure of P450nor. P450nor catalyzes the reduction of NO using NADH and proton.

loop, and *I* was captured by rapid freezing 5 s after UV illumination. To avoid the radiation-induced redox change at the active site and precisely determine the structure of *I*, the X-ray diffraction data for the state of *I* free of radiation-induced damage were collected by fixed-target SFX at SACLA **BL3**. Compared with the Fe^{3+}–NO state in which the NO ligand adopts a slightly bent configuration (Fe–NO = 1.6 Å, N–O = 1.15 Å, Fe–N–O = 158°) [4], the FeNO unit is more bent in *I* (Fe–NO = 1.91 Å, N–O = 1.27 Å, Fe–N–O = 138°), as shown in Fig. 3. In addition to the crystal structure, the TR-infrared (TR-IR) measurement of the microcrystal sample showed that a NO stretching frequency (νNO) sensitive to the electronic structure was observed at 1298 cm^{-1} in *I* [5], which is distinct from νNO of 1853 cm^{-1} in the Fe^{3+}–NO state. Using such structural and spectroscopic information on *I* in the theoretical calculation, we can conclude that *I* is a singly protonated radical species, Fe^{3+}–$NHO^{\bullet-}$ [5]. Our finding of the radical character of *I* demonstrates that the radical coupling of *I* and the second NO molecule forms the N–N bond, as shown in Fig. 3. Thus, the recent progress of the time-resolved technique and XFEL crystallography has enabled us to answer a long-standing question regarding the mechanism of enzymatic N_2O formation.

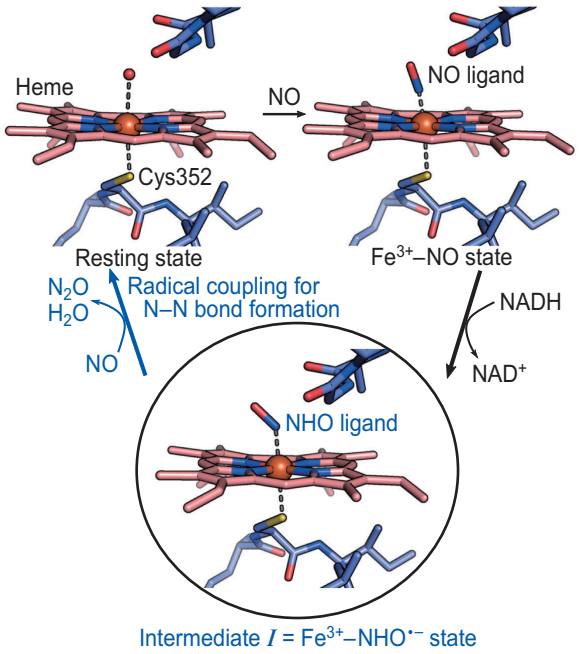

Fig. 3. Reaction mechanism of N_2O formation by P450nor. Current results reveal that *I* is Fe^{3+}–$NHO^{\bullet-}$. The radical character of *I* facilitates the formation of N–N bond via the radical coupling mechanism.

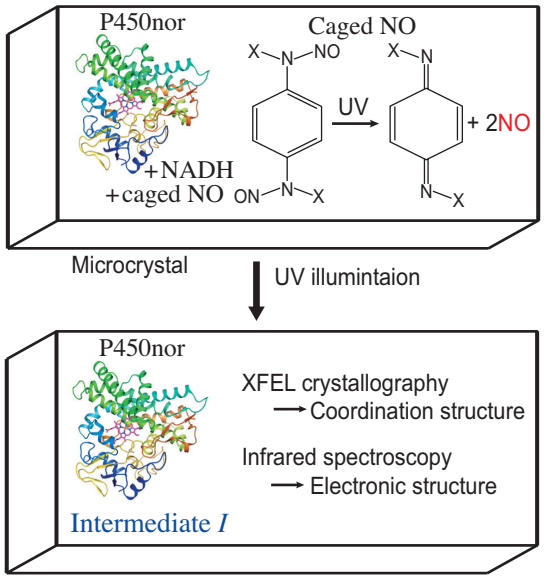

Fig. 2. Schematic representation of the method used in this work.

Takehiko Tosha[a,*], Minoru Kubo[b] and Yoshitsugu Shiro[b]

[a] RIKEN SPring-8 Center
[b] Graduate School of Life Science, University of Hyogo

*Email: ttosha@spring8.or.jp

References

[1] H. Tian *et al.*: Nature **586** (2020) 248.
[2] K. Nakahara *et al.*: J . Biol. Chem **268** (1993) 8350.
[3] Y. Shiro *et al.*: J. Biol. Chem. **270** (1995) 1617.
[4] T. Tosha *et al.*: Nat. Commun. **8** (2017) 1585.
[5] *T. Nomura, T. Kimura, Y. Kanematsu, Y. Daichi, K. Yamashita, K. Hirata, G. Ueno, H. Murakami, T. Hisano, R. Yamagiwa, H. Takeda, C. Gopalasingam, R. Kousaka, S. Yanagisawa, O. Shoji, T. Kumasaka, M. Yamamoto, Y. Takano, H. Sugimoto, T. Tosha, M. Kubo, Y. Shiro: Proc. Natl. Acad. Sci. USA* ***118*** *(2021) e2101481118.*

Direct observation of capsaicin-induced intramolecular dynamics of TRPV1 channel

The transient receptor potential vanilloid type 1 (TRPV1) is a multimodal receptor that responds to various stimuli such as the chemical ligand capsaicin (a component of chili peppers), protons (H^+), and a physical stimulus of heat (high temperature). Professor David Julius was awarded the 2021 Nobel Prize in Physiology or Medicine for his discovery of the TRPV1 channel. Recent advances in cryoelectron microscopy (cryo-EM) have revealed the detailed structures of TRPV1. In addition to its apo structure (ligand-unbound), capsaicin-bound structures and a complex with a spider toxin DkTx and with a highly potent capsaicin analogue RTX have been reported. However, because of the large size of TRPV1 (400 kDa) and the complexity of its structure, the real-time motion of channel gating has not been well documented. Information about the intramolecular dynamics, as well as structural information, is necessary to understand the molecular mechanisms of protein functions. In this study, we applied diffracted X-ray tracking (DXT) to purified TRPV1 protein and successfully visualized its capsaicin-induced intramolecular torsional motion [1].

DXT uses fine gold nanocrystals with a diameter of 20–60 nm as quantum probes. Domains of the target proteins were chemically labeled by the gold nanocrystals, and their motion (orientation) was tracked as X-ray Laue spots with microsecond time resolution (Fig. 1(a)). Professor Yuji C. Sasaki designed this technique in 1997 and demonstrated it in 2000 at SPring-8 [2]. DXT can be measured under various solution conditions of pH and temperature, and this is one of the single-molecule motion measurement techniques with ultrahigh spatiotemporal resolution [3,4]. DXT can be used with various X-ray sources from large synchrotron radiation facilities to ordinary laboratory X-ray generators [5]. To measure the movement of diffracted spots from nanocrystals, we used the high-flux beamline SPring-8 **BL40XU** with a wide energy bandwidth ($\Delta E/E = 0.08$) for DXT. To prevent damage to the sample, the exposure time was strictly controlled by synchronizing a galvanometer-type X-ray high-speed shutter and a low-noise X-ray image intensifier (Hamamatsu Photonics V5445P). A high-speed CMOS camera (Photron FASTCAM SA1.1) was used at a frame rate of 100 μs. One hundred frames were captured for each spot (Fig. 1(b)).

For the specific binding of gold nanocrystals, a Met-tag sequence (MGGMGGM) was introduced to a S1-S2 loop (for the "voltage-sensor-like-domain" label) or a S5-Pore loop (for the "pore-domain" label) of the TRPV1 proteins. The rotation angles of all the bright spots were analyzed separately at positive angles (counterclockwise axis direction; CCW) and negative angles (clockwise direction; CW) viewed from the top (extracellular) side. First, we observed the ligand effect on rotation bias. It was found that the rotation signals were evenly distributed on both sides, and no information about rotation bias was obtained. After some consideration about it, we concluded that rotational biases must be canceling out owing to the repetitive "twisting" and "untwisting" motion of each channel protein.

To segregate the opening and closing movement of TRPV1, a lifetime filtering technique was applied. Diffraction spots from gold nanocrystals can be recorded within the energy range of synchrotron radiation. The spots of fast-moving proteins have a short duration between appearance and disappearance, while those of slow-moving proteins exist for a long time. Hence, the duration of the bright spots represents the overall movement of the target protein (lifetime). Therefore, the data were divided into a short-lifetime group [lifetime (LT) < 2.5 ms], a medium-LT group [2.5 ≤ LT < 4 ms], and a long-LT group [8 ≤ LT < 10 ms], and statistical analysis was applied to each group independently (Fig. 2). This allowed us to detect the ligand-induced internal motions of TRPV1. The short-LT data were mostly nondirectional or slightly CW biased for both S5-P and S1-S2 loops. In the medium-LT group, both apo and capsaicin-bound TRPV1 showed CW bias, while AMG9810 was nondirectional (S5-P loop)

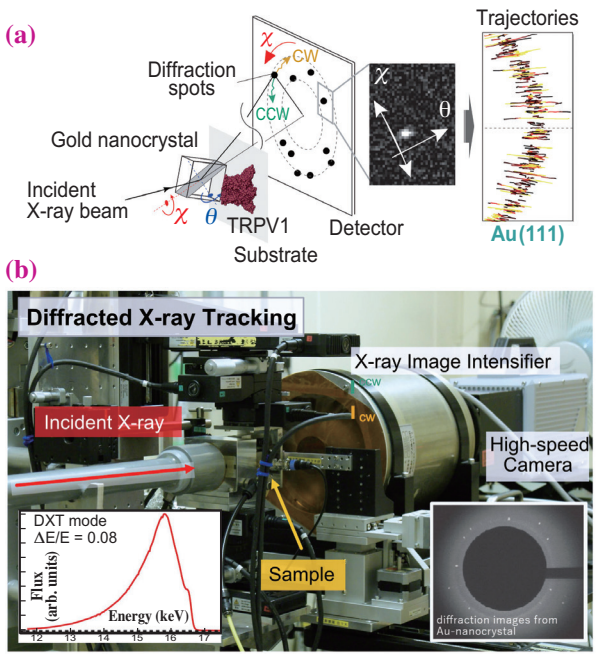

Fig. 1. DXT measurement system. **(a)** Schematic of the DXT data collection. Pink-beam X-rays from SPring-8 yielded trackable diffraction spots from the gold nanocrystals. The trajectories were separately projected and analyzed on $\chi-\theta$ coordinates. **(b)** DXT measurement system at BL40XU, and the X-ray spectrum of the incident beam measured by a PIN diode detector.

or CCW-biased (S1-S2 loop). The long-LT group exhibited CW bias for capsaicin, but CCW bias for apo-TRPV1. The CW torsional motion (observed for both apo and capsaicin-bound TRPV1) was considered to be channel opening motion from the cryo-EM observations. Although the obtained motions were extremely small, detailed information on the motions was obtained by the lifetime filtering method and theoretical calculations using the cryo-EM structure (Fig. 3). The diffusion constant of glycine 602 at the OP-labeled position was calculated to be 12.8 pm^2/ms. Interestingly, the channel antagonist AMG9810 generated the opposite torsional bias to that of capsaicin.

We also examined the motion of the capsaicin-insensitive Y511A mutant to confirm whether the CW bias is indeed related to gating. It is noteworthy that the torsional motion of the Y511A mutant was strongly biased in the CCW direction, which resembles well the AMG9810-induced CCW bias observed for the wild type. The TRPV1 channel has two gates in the ion pass; the upper gate is located on the extracellular side of the membrane and the lower gate on the cytoplasmic side. The capsaicin-bound structure presented by cryo-EM was a closed form, because the lower gate was opened and the upper gate was closed. Our DXT results showed that both apo and capsaicin-bound TRPV1 had a CW rotational bias, and this bias was observed even in the long-LT group bound by capsaicin. These results suggest that the main action of capsaicin is not only to open the lower gate, but also to increase the oscillation frequency at the upper gate by pulling a small trigger, thereby promoting calcium influx.

TRPV1 channels are abundantly expressed in primary sensory nerves such as unmyelinated C-fibers and myelinated small Aδ fibers, which act as nociceptors to induce pain and burning sensations. Therefore, search for new inhibitors from the viewpoint of analgesic drug development is anticipated. New insights gained from structural dynamism must be useful for understanding pain recognition mechanisms and developing new analgesics. Several TRP species have been reported to be closely related to the pathogenesis of diseases, and the DXT measurement technique can contribute widely to the discovery and understanding of therapeutic agents for these diseases.

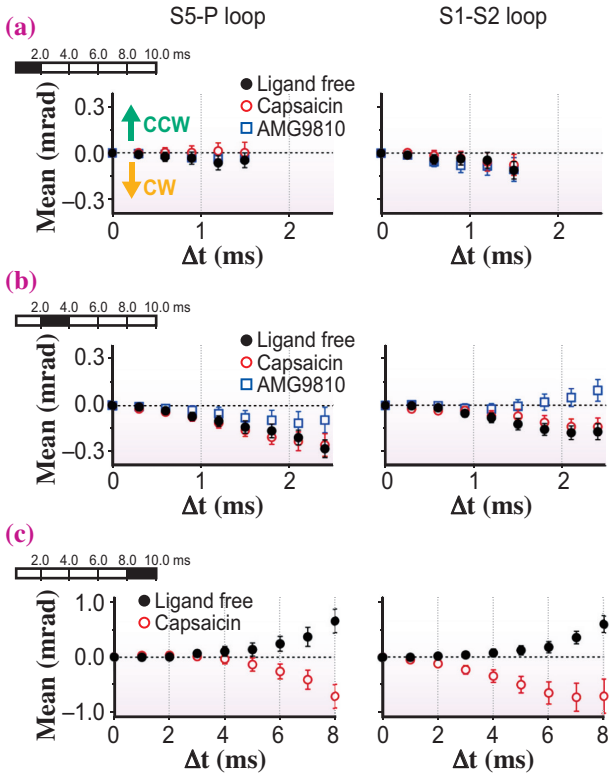

Fig. 2. Lifetime filtering analysis. Mean plot for angle χ for **(a)** data for short-LT group (< 2.0 ms), **(b)** medium-LT group (2.0 ≤ LT < 4.0 ms), and **(c)** long-LT group (8.0 ≤ LT < 10.0 ms). In the long-LT group, capsaicin-bound TRPV1 sustained CW bias, while apo-TRPV1 showed CCW bias.

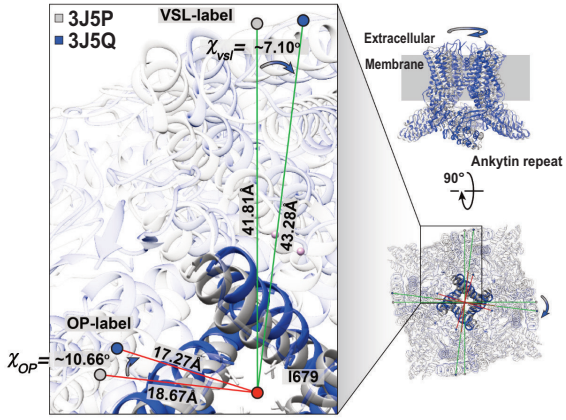

Fig. 3. Superimposed views of closed and open forms of TRPV1. Superimposition of apo-TRPV1 (PDB: 3J5P, gray) and DkTx/RTX-TRPV1 (3J5Q, blue). Rotational angles after DkTx/RTX binding were calculated at glycine 602 (OP-label) and tyrosine 463 (VSL-label). Both the OP and VSL positions rotated in the clockwise direction, resulting in 10.6 and 7.1 degrees, respectively.

Kazuhiro Mio[a,*], Shoko Fujimura[a] and Yuji C. Sasaki[a,b]

[a] OPERANDO-OIL, National Institute of Advanced Industrial Science and Technology (AIST)
[b] Graduate School of Frontier Sciences, The University of Tokyo

*Email: kazu.mio@aist.go.jp

References

[1] *S. Fujimura, K. Mio, M. Kuramochi, H. Sekiguchi, K. Ikezaki, M. Mio, K. Hengphasatporn, Y. Shigeta, T. Kubo, Y. C. Sasaki: J. Phys. Chem. B.* ***124*** *(2020) 11617.*
[2] Y.C. Sasaki *et al.*: Phys. Rev. E **62** (2000) 3843.
[3] H. Sekiguchi *et al.*: Sci. Rep. **4** (2014) 6384.
[4] K. Mio *et al.*: Biochem. Biophys. Res. Commun. **529** (2020) 306.
[5] H. Sekiguchi *et al.*: Sci. Rep. **8** (2018) 17090.

3D imaging of auditory osteoblasts using a Talbot phase-sensitive X-ray tomographic microscope

In many mammals, hearing-related bones of the middle and inner ear are among the densest bones. Three auditory ossicles in the middle ear—namely the malleus, incus, and stapes—for a chain that transmits vibration from the tympanic membrane to the inner ear. The cochlea and semicircular canals, the delicate organs of the inner ear, are surrounded by a highly calcified bony labyrinth. Density of the ossicles and the bony labyrinth is functionally important, as insufficient mineralization seen in conditions such as osteogenesis imperfecta, cleidocranial dysplasia, or X-linked hypophosphatemia can lead to hearing loss.

During development, bone formation by osteoblasts occurs via either endochondral or intramembranous ossification. In intramembranous ossification, bone develops directly from sheets of osteoblasts, while endochondral ossification requires a cartilaginous template (anlage). Hearing-related bones mainly undergo endochondral ossification, like long bones. Osteoblasts produce matrix vesicles containing calcium and phosphate ions, which are crystallized into biological apatite, the major inorganic component of bone material. Bone mineralization is initiated by nucleation and growth of apatite crystals in fibrillar collagen secreted by osteoblasts. Orientation and arrangement of collagen fibrils and biological apatite have been analyzed using various imaging techniques, all of which confirm that collagen fibrils are the major determinant of bone matrix mineralization. We previously identified “osteogenic capillaries” composed of endothelial cells and pericytic osteoblasts during endochondral ossification of mouse ear bones [2]. However, cellular mechanisms underlying formation of dense ear bones by osteoblasts during development remain largely unknown.

In this study [1], we found that in young mice, hearing-related bones are highly mineralized immediately after they are produced (Figs. 1(a) and 1(b)) and that pericytic osteoblasts, a structural element of osteogenic capillary, in hearing-related bones produce both type I and type II collagens as bone matrix, while conventional osteoblasts and chondrocytes primarily produce type I and type II collagens, respectively (Fig. 1(c)). Type II collagen-producing pericytic osteoblasts were genuine osteoblasts as they express osteocalcin, localize along alizarin-labeled osteoid, and form osteocyte lacunae and canaliculi, as do conventional osteoblasts. Analysis using quantitative backscattered electron imaging (qBEI) revealed that calcium concentration (weight%) in newly formed bone was much higher in ear bones (malleus) than in femur in the same mouse at the same time after new bone formation (Fig. 1(d)). Furthermore, ear bones exhibit not only greater mineral content, but better arranged collagen fibrils than that found in conventional osteoblasts (Fig. 1(e)). Based on these results, we conclude that organic and inorganic components of hypermineralized ear bones exhibit properties distinct from conventional bones and that these type II collagen-producing hypermineralizing osteoblasts (termed auditory osteoblasts) represent a new osteoblast subtype [1].

Vascular networks also develop during endochondral ossification of conventional bone, whereas osteogenic capillaries associated with hypermineralizing osteoblasts are unique to ear bones. To define cellular structure

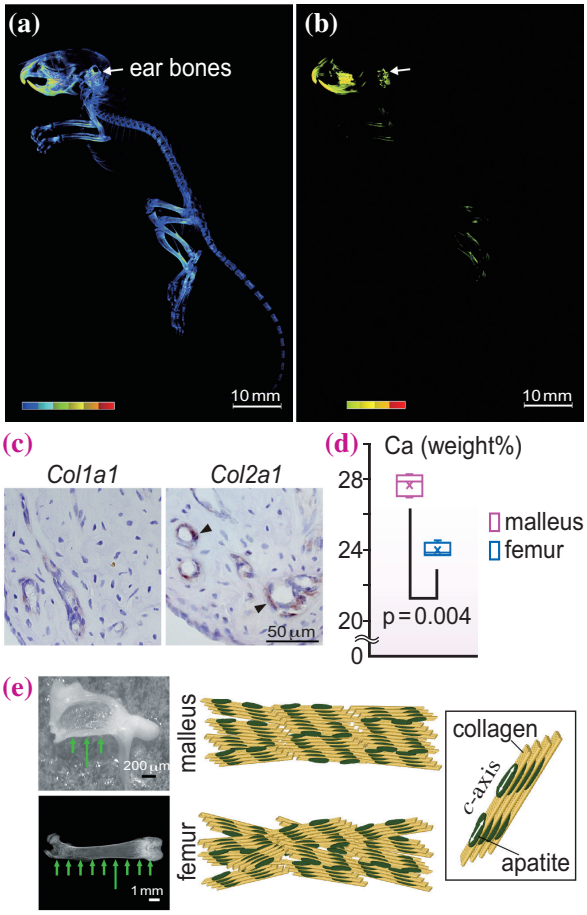

Fig. 1. Identified features of ear bones. **(a)** Heat map of tissue mineral density (TMD) (100–1500 mg/cm^3) in a microCT image of a P21 mouse. **(b)** High TMD regions (500–1500 mg/cm^3) of (a). **(c)** *In situ* hybridization of *Col1a1* and *Col2a1* in the malleus of P21 mouse. Arrowheads: *Col2a1*-positive cells. **(d)** Calcium concentration (Ca weight%) in malleus and femur of P21 mice. **(e)** Left: Representative images of malleus and femur showing points (green arrows) assessed using a microbeam X-ray diffraction system. Right: Schematic diagram constructed based on that analysis showing alignment of the apatite *c*-axis on collagen fibrils in malleus and femur. [1]

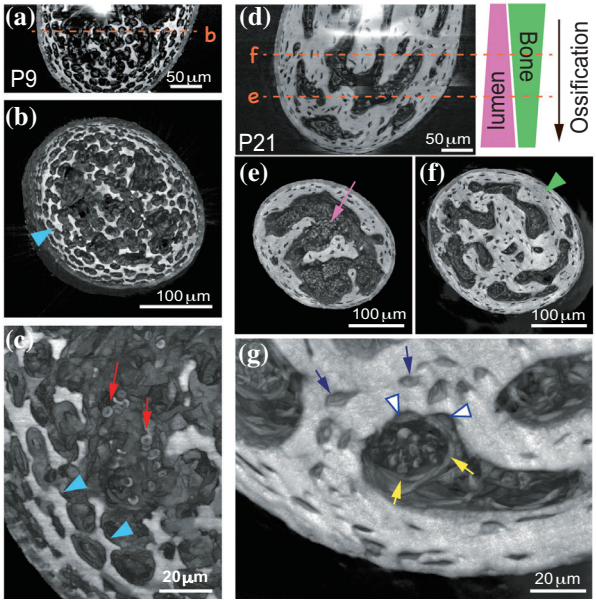

Fig. 2. Synchrotron X-ray phase images of osteogenic capillaries during endochondral ossification. **(a)** Mineralized lattice-like cartilaginous matrix in the malleus of P9 mice. Vertical section. Dotted line **b** indicates the horizontal cutting plane shown in (b). **(b)** Horizontal section showing partially resorbed cartilaginous matrix (arrowhead) at P9. **(c)** Magnified view of (a) showing capillary invasion. Arrows: red blood cells; arrowheads: cartilaginous matrix. **(d)** Mineralized bone matrix in the malleus of P21 mice. Vertical section. Dotted lines **e** and **f** indicate horizontal cutting planes shown in (e) and (f), respectively. **(e)** Horizontal section near the tip of the malleus, showing enlarged osteogenic capillary lumen (arrow) at P21. **(f)** Horizontal section of the malleus, showing osteogenic capillaries with narrower lumens surrounded by increased regions of bone matrix (arrowhead) as compared to those seen in (e). **(g)** Magnified view of osteogenic capillaries in (f). Yellow arrows: endothelial cells; open arrowheads: auditory osteoblasts; blue arrows: osteocytes. Cell types were identified by morphology and proximity to red blood cells. [1]

of osteogenic capillaries accompanied by auditory osteoblasts within hard tissues, we performed Talbot phase-sensitive X-ray tomographic microscope imaging [3] at SPring-8 **BL37XU** using a monochromatic X-ray beam (9.0 keV). At the initial stage of endochondral ossification of the malleus (postnatal day 9, P9), mineralized lattice-like cartilaginous matrix was partially resorbed (Figs. 2(a) and 2(b)). Higher magnification revealed that capillary vessels, which contained red blood cells, had invaded cartilaginous matrix (Fig. 2(c)). Based on analysis of the ossification progress, the entire malleus had been replaced by bone matrix by P21 (Fig. 2(d)) and osteogenic capillaries narrowed as bone rapidly formed (Figs. 2(e) and 2(f)). We also observed that auditory osteoblasts adjacent to endothelial cells were in contact with bone matrix and that osteocytes were embedded in bone matrix around osteogenic capillaries (Fig. 2(g)). Such close association of auditory osteoblasts with endothelial cells in osteogenic capillaries likely supports efficient bone matrix production and mineralization during and after endochondral ossification of hearing-related bones.

In summary, we found that ear bones exhibit a higher tissue mineral density (TMD) as well as higher degree of apatite orientation (reflecting collagen fibril orientation) than do long bones (Fig. 3). The higher the TMD and anisotropic arrangement of apatite crystallites, the more rapid the speed of sound in a bone [4]. These data collectively suggest that hypermineralization of hearing-related bones likely optimizes the material properties required for conductive and sensorineural hearing function. Overall, our study reveals that auditory osteoblasts, a new osteoblast subtype, form the densest hearing-related bones using collagen types distinct from those found in conventional bone.

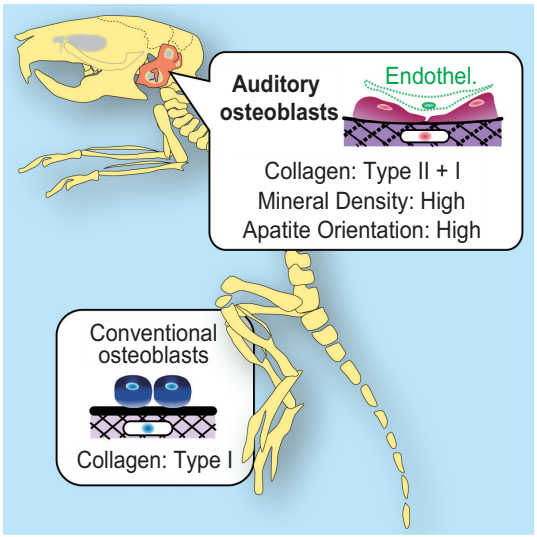

Fig. 3. Summary of properties of auditory osteoblasts. Endothel, endothelial cell. [1]

Yukiko Kuroda

Laboratory of Cell and Tissue Biology,
Keio University School of Medicine

Email: kuro.z6@keio.jp

References

[1] *Y. Kuroda, K. Kawaai, N. Hatano, Y. Wu, H. Takano, A. Momose, T. Ishimoto, T. Nakano, P. Roschger, S. Blouin, K. Matsuo: JBMR.* ***36*** *(2021) 1535.*
[2] K. Matsuo *et al.*: Development **142** (2015) 3912.
[3] A. Momose *et al.*: Proc SPIE **10391** (2017) 103910Y.
[4] T. Ishimoto *et al.*: Bone **127** (2019) 82.

In search of real images of insect cuticular lipids: Synchrotron radiation FTIR ATR microspectroscopy study on insect body surfaces

The exoskeleton of insects is covered with lipid compounds called “cuticular lipids.” Until the early 1960s, these lipids had been studied from the viewpoint of protective coats. However, the development of microchemical analyses revolutionized cuticular-lipid research [1]. We now understand that cuticular lipids are involved in various activities of insects; for instance, some components contribute to chemical communication.

Although microchemical analyses have revealed the physiological roles of cuticular lipids, the state of the lipids on the body surface is not well understood. This situation is due to the difficulty in accessing the cuticular lipid layer, which is assumed to have thickness of 0.01 to 1 μm order on average. Therefore, cuticular lipids are still vaguely regarded as a thin film that cover the body surface uniformly.

To fill this void, we take note of the characteristics of Fourier-transform infrared (FTIR) spectroscopy, which can provide a wide range of structural information of lipid compounds, although it has rarely been employed in cuticular lipid research except by Gibbs [2]. We previously combined FTIR spectroscopy and attenuated total reflection (ATR) sampling for *in situ* structure analyses and demonstrated the potential of this technique [3]. What stands out is that the ATR method provides the IR spectrum of the cuticular lipid layer while avoiding the strong absorption of the underlying thick chitin layer. As the next step, we aim to clarify how lipids are distributed over the insect body surface, which is essential for considering their diverse functionalities.

FTIR ATR microspectroscopy is suitable for our purpose as it enables a two-dimensional (2D) IR absorption intensity map to be drawn focusing on a specific IR band. However, the ATR measurement requires a considerably larger number of spectral scans than the standard transmission measurement because the efficiency of infrared light utilization is much lower and the change in absorbance is much smaller. In addition, we must measure and integrate spectra at many measurement points to construct 2D images. To obtain reliable information, we must confirm the reproducibility and investigate the effects of differences in species and sex; it is essential to measure high-quality spectra as efficiently as possible. We have performed FTIR ATR microspectroscopy measurements using the high-luminance infrared synchrotron radiation at SPring-8 **BL43IR** as a light source to meet this requirement [4].

Figure 1 shows an example of 2D measurements on a forewing of a male two-spotted cricket (Fig. 1(a)), where the IR bands of cuticular lipids show significant position-dependent intensity changes; two pronounced IR absorptions, a CH_2 symmetric stretch $\nu_s(CH_2)$ at about 2850 cm^{-1} and a CH_2 antisymmetric stretch $\nu_a(CH_2)$ at about 2920 cm^{-1}, show an intensity variation of one order of magnitude among 15 sampling points (Fig. 1(b)). As if to keep up with this, the amide group bands of the underlying cuticular layer, such as the N–H stretch band at around 3280 cm^{-1}, the amide I band (mainly due to C=O stretch) at around

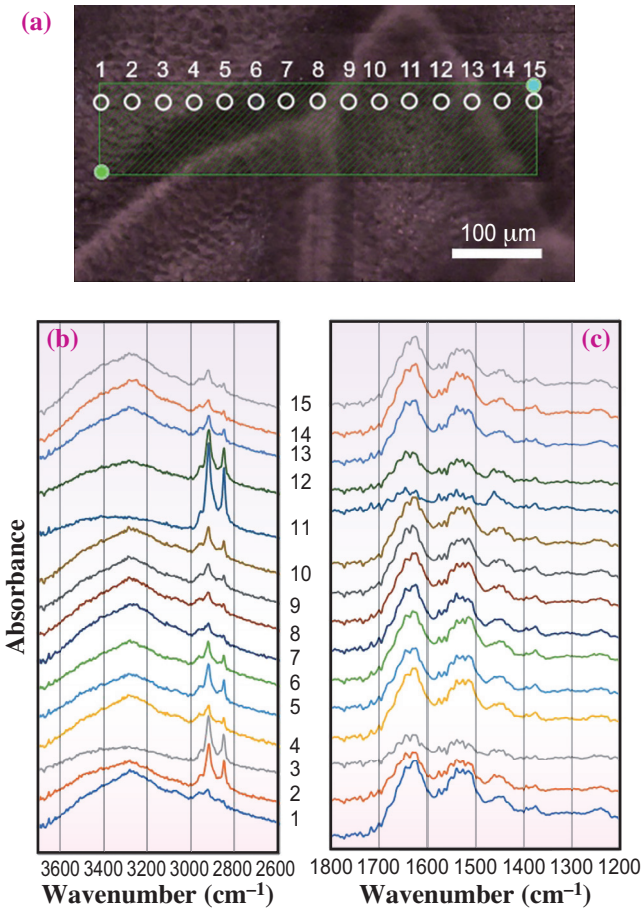

Fig. 1. Visible image and microscope FTIR-ATR spectra of a forewing. **(a)** Image of the measured sample. The rectangle delineated by the green dotted line represents the mapping measurement area with 90 sampling points (6 rows × 15 columns). Shown are 15 sampling points in the second row from the top. **(b)** Spectra in the 3700 to 2600 cm^{-1} region at the sampling points in the second row. **(c)** Spectra in the 1800 to 1200 cm^{-1} region measured at the same sampling points.

1630 cm^{-1}, and the amide II band (N–H bend) at around 1530 cm^{-1}, also change markedly in intensity. However, the changes are in the opposite direction; as the intensities of lipid bands increase, that of the amide band decreases, and vice versa (Fig. 1(c)). The tendency of the hydrocarbon and amide bands to show mutually opposite intensity changes is evident in the two 2D images obtained from $\nu_s(CH_2)$ and amide I bands (Fig. 2). The ATR spectral analysis using the two-layer model (Fig. 3), which includes the characteristics of the evanescent wave, reveals that the relative intensity varies several tens of times in the range of 0.01 to 1 μm thickness of the lipid layer. These spectral features are observed in the two-spotted cricket, regardless of sex or body site, and in the American cockroach, which strongly suggests that this uneven distribution of cuticular lipids occurs in a wide range of insect species.

The $\nu_s(CH_2)$ and $\nu_a(CH_2)$ bands tend to shift to lower frequencies as their intensities increase, which implies that the marked uneven distribution of cuticular lipids has been induced by solid-liquid phase separation and the coarsening of solid-phase domains [5]. Each cuticular lipid component is considered to play a different physiological role. Therefore, the separation of lipid components during lipid-layer thickening should significantly affect the body surface function. The results of the present experiments using infrared synchrotron radiation at SPring-8 strongly suggest that the topological features of cuticular lipids should be taken into account in the study of physiological functions.

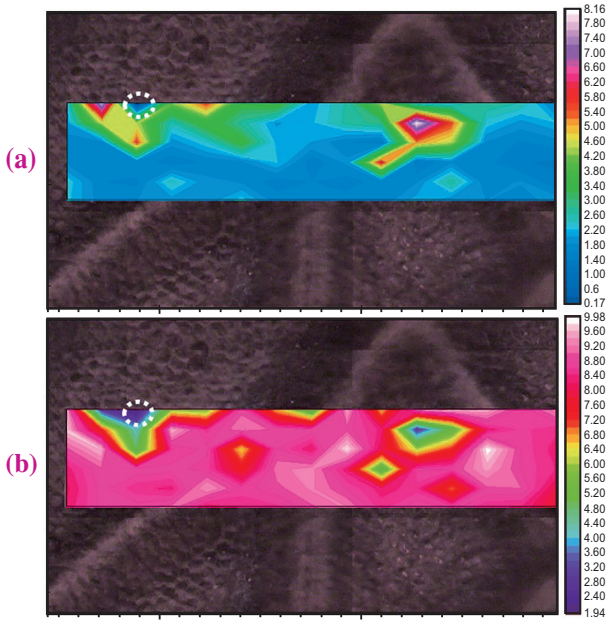

Fig. 2. FTIR images synthesized from the spectra at 90 sampling points (Fig. 1(a)). **(a)** FTIR images obtained by integrating the area under the 3020–2880 cm^{-1} region, where the $\nu_a(CH_2)$ band predominantly contributes. **(b)** FTIR images obtained by integrating the area under the 1727–1588 cm^{-1} region, where the amide I band predominantly contributes. The region inside the white dotted circle shows weak absorption in both spectra, which is due to poor contact between the internal reflection element (IRE) and the sample surface.

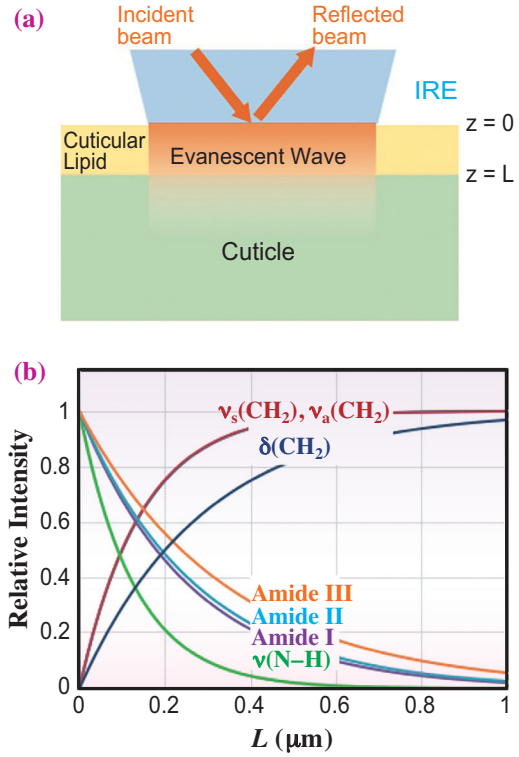

Fig. 3. Effect of the lipid-layer thickness on the IR band intensity. **(a)** The two-layer model used for evaluation consists of an upper lipid layer with thickness *L* and a lower cuticle. The ATR method employs the electric field called evanescent waves, generated by IR total reflection at the interface between the prism (IRE) and the sample surface. **(b)** Estimated relative intensity changes of each band against its maximum intensity.

Fumitoshi Kaneko[a,*] and Chihiro Katagiri[b]

[a] Graduate School of Science, Osaka University
[b] Mathematical Assist Design Laboratory

*Email: toshi@chem.sci.osaka-u.ac.jp

References

[1] Insect hydrocarbons: biology, biochemistry, and chemical ecology. Cambridge University Press: 2010.
[2] A.G. Gibbs: J. Insect Physiol. **48** (2002) 391.
[3] F. Kaneko *et al.*: J. Phys. Chem. B **122** (2018) 12322.
[4] *F. Kaneko, C. Katagiri, K. Nagashima, G. Sazaki and Y. Ikemoto: J. Phys. Chem. B* ***125*** *(2021) 9757.*
[5] R. Mendelsohn, R.G. Snyder: Biological Membranes, Springer: 1996; p.145.

Observation and modeling of multicomponent ceramics synthesis: A case study of $YBa_2Cu_3O_{6+x}$

Solid-state synthesis from powder precursors is the primary processing route to advanced multicomponent ceramic materials. While precursors and products of the synthesis have been characterized intensively, the reaction in the furnace is still a "black box" [1]. In order to peel off this black box, *in situ* characterization studies are essential. These analyses have revealed that solid-state reactions often evolve through a variety of nonequilibrium intermediates, some of which are recognized as new phases, prior to the formation of the equilibrium phase [2].

From the end of the 18th century to the beginning of the 19th century, Gibbs and Ostwald built the fundamental of thermodynamics and kinetics, and solid-phase reactions were also understood using these theories. The Gibbs free energy can distinguish whether reactions can proceed in infinite time, and kinetic requirements for diffusion, nucleation, and crystal growth are utilized for the explanation of how fast thermodynamically favorable reaction can proceed. Reactions in organic chemistry, which normally involve small molecules, are generally predicted well by computational approaches and depicted as "an energy landscape" with thermodynamic states joined with kinetic barriers. On the other hand, a similar computational analysis of solid-phase reactions, which handle particles of submicron to tens of microns, are not as straightforward. As a result, understanding the solid-phase reaction mechanism continues to be a challenging issue.

Recent advances in density functional theory provide the structure-property relationships of countless experimental and hypothetical compounds. Theory and computation can also help guide synthesis planning by evaluating thermodynamic stability or overall reaction energies [3]. Nonetheless, they do not provide mechanistic insights into which nonequilibrium intermediates will appear during phase evolution. Indeed, solid-state reactions have too many parameters: composition, starting materials, heating temperature, heating rate, atmosphere, etc. For example, Martin Jansen shows the thought experiment that investigates how many samples need to be synthesized and tested to definitely include YBCO in the output of a high-throughput method [4]. Using a throughput rate of 105 samples per day, a systematic and unbiased, one might even say "mechanical", search through the parameter space would take about 27000 years. Thus, one needs to find reasonable criteria to restrict the parameter space under investigation.

The complexity of phase evolution in solid-state synthesis arises from the various pathways by which an initially heterogeneous mixture of precursor particles can transform to a homogeneous target phase. At the microscopic level, solid-state reactions initiate in the interfacial regions between precursors as the system is heated. Because interfacial reactions can only occur between two solid phases at a time, we hypothesize that by determining which pair of precursors exhibits the most reactive interface, we can anticipate which interfacial reaction initiates the overall solid-state reaction, as illustrated schematically in Fig. 1. Once two precursors react to form a new phase, this nonequilibrium intermediate will then react through its interface with other precursors and intermediate phases. By decomposing the overall phase evolution into a sequence of pairwise reactions, we can calculate the thermodynamics and analyze the kinetics of each reaction step separately, providing a simplified theoretical picture to conceptualize and navigate ceramic synthesis [5].

We demonstrate how this concept of sequential pairwise reactions enables us to model phase evolution in the ceramic synthesis of the classic high-temperature superconductor, $YBa_2Cu_3O_{6+x}$ (YBCO).

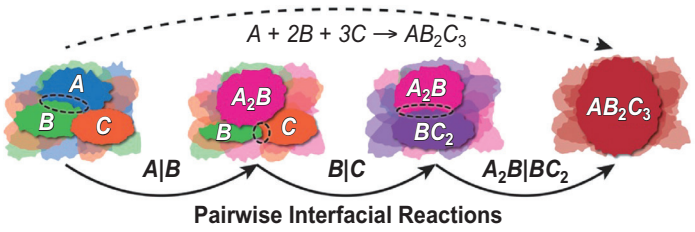

Fig. 1. Schematic of sequential pairwise interfacial reactions. [5]

Figure 2 shows *in situ* synchrotron X-ray diffraction patterns measured at SPring-8 **BL02B2** for phase evolution in YBCO synthesis in air from the mixture of Y_2O_3, BaO_2 and CuO in 30 minutes. The fast formation of YBCO when starting from BaO_2 originates from the large thermodynamic driving force at the BaO_2|CuO interface, which is larger than other Y_2O_3|CuO and Y_2O_3| BaO_2 interfaces. SEM/DF-STEM provides direct observation of the microstructural evolution during the solid-state reaction. In a later stage, liquidus Ba-Cu-O react with Y_2O_3 solid to form YBCO, suggesting the fast diffusion is the key for this quick formation of YBCO.

In situ X-ray diffraction and microscopy observation were essential to prove the framework of subsequent interfacial reactions and inform our understanding of the interplay between thermodynamic and kinetics during the synthesis of multi-component ceramics. DFT calculations can be used in concert to predict which intermediate phases form by comparison of thermodynamic driving forces. This work enables solid-state and materials chemists to design crystallization pathways that target (or avoid) specific intermediates, which will accelerate the design of time- and energy-efficient ceramic synthesis recipes for new materials.

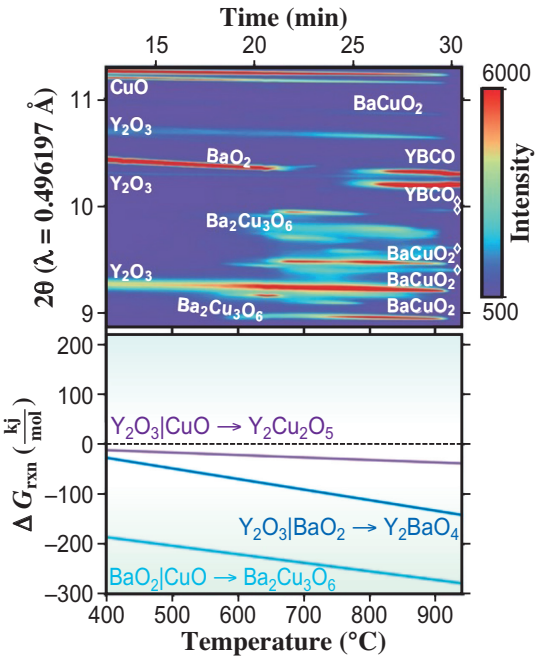

Fig. 2. *In situ* synchrotron XRD pattern for heating of the Y_2O_3 + BaO_2 + CuO precursor mixture and Gibbs reaction energies for the lowest energy reactions at each interface in the Y_2O_3 + BaO_2 + CuO precursor mixture. [5]

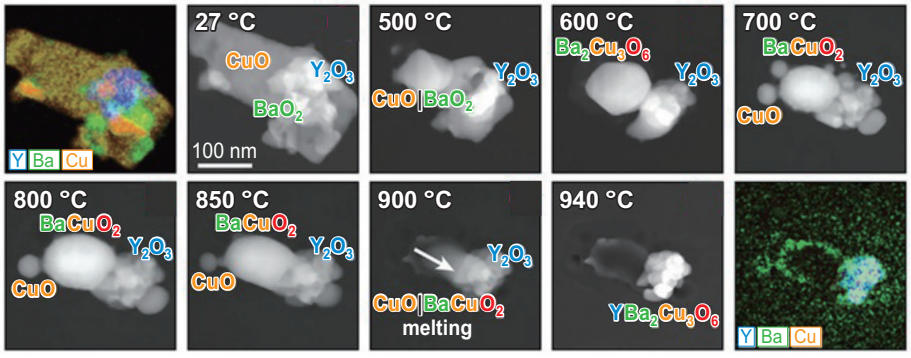

Fig. 3. *In situ* microscopy of YBCO formation from Y_2O_3, BaO_2, and CuO particles. A video of the reaction is provided as video S1 (https://onlinelibrary.wiley.com/doi/full/10.1002/adma.202100312#support-information-section) in Supporting Information. [5]

Akira Miura[a,*], Christopher J. Bartel[b] and Wenhao Sun[c]

[a] Department of Engineering, Hokakido University
[b] Department of Materials Science and Engineering, UC Berkeley, USA
[c] Department of Materials Science and Engineering, University of Michigan, USA

*Email: amiura@eng.hokudai.ac.jp

References

[1] F.J. DiSalvo: Science **247** (1990) 649.
[2] D.P. Shoemaker *et al.*: Proc. Natl. Acad. Sci. USA **111** (2014) 10922.
[3] W. Sun *et al.*: Nat. Mater. **18** (2019) 732.
[4] M. Jansen: Angew. Chem. Inter. Ed. **41** (2002) 3746.
[5] A. *Miura, C.J. Bartel, Y. Goto, Y. Mizuguchi, C. Moriyoshi, Y. Kuroiwa, Y. Wang, T. Yaguchi, M. Shirai, M. Nagao, N.C. Rosero-Navarro, K.and W. Sun: Adv. Mater.* ***33*** *(2021) e2100312.*

In situ time-resolved synchrotron radiation nanobeam X-ray diffraction analysis of inverse-piezoelectric-effect-induced lattice deformation in AlGaN/GaN high-electron-mobility transistors

Gallium nitride (GaN) is expected to be used as an alternative material for power electronic devices owing to its superior physical properties of higher breakdown voltages and greater thermal stability than Si. In particular, AlGaN/GaN high-electron-mobility transistors (HEMTs) have attracted considerable attention for use in high-frequency and high-power operations. As a characteristic of group III nitride semiconductors, a polarization-induced two-dimensional electron gas (2DEG) is introduced at the AlGaN/GaN interface, where both the effects of the spontaneous polarization difference and the piezoelectric polarization produced by the lattice mismatch strain between AlGaN and GaN contribute to the high-concentration 2DEG. Although such piezoelectricity occurring in an AlGaN/GaN HEMT gives rise to a high current density, it has been reported that the inverse piezoelectric effect (IPE) can also cause deterioration in the device performance through the inhomogeneous distribution of strain and the formation of defects in the localized area of the device. Knowledge of the local IPE, especially during device operation, is indispensable for precisely controlling the piezoelectric properties; however, an appropriate measurement technique for the piezoelectric properties has not yet been fully established.

Diffraction is an effective tool for directly observing lattice structures and clarifying the process of defect formation that adversely affects the properties of crystalline materials and the performance of devices. The observation of lattice distortion in piezoelectric materials such as lead zirconate titanate under an applied voltage using time-resolved stroboscope X-ray diffraction techniques in previous studies has been reported [1]. Compared with the piezoelectric constants of these piezo compounds, those of AlGaN or GaN are two orders of magnitude smaller. Thus, the observation of IPE-induced lattice deformation in AlGaN and GaN using diffraction techniques is challenging.

In this work, we developed an *in situ* measurement system based on a synchrotron radiation nanobeam X-ray diffraction (nanoXRD) technique combined with a pump-probe method to investigate local lattice deformation in operating nitride devices [2]. By utilizing synchrotron radiation X-ray pulses with very small widths, we observed the dynamic behavior in the process of lattice deformation with a high time resolution on the order of nanoseconds. We quantitatively investigated the local lattice deformation of an AlGaN barrier layer caused by the IPE in an AlGaN/GaN HEMT device under an applied gate voltage.

A schematic of the sample device structure used is shown in Fig. 1(a). The sample was an AlGaN/GaN MOS-HEMT device [3]. The thickness and Al content of the AlGaN barrier layer were 20 nm and 20%, respectively. The diffraction geometry is shown in Fig. 1(b). The synchrotron X-ray beam (200 nm×500 nm) focused by a zone plate at SPring-8 **BL13XU** was used for the experiments. The X-ray nanobeam was incident on the gate electrode from the *m* direction to obtain the AlGaN 0004 diffraction as a gate voltage was applied to the device. Three-dimensional (3D) ω–2θ–φ mapping was performed for the diffraction [4]; to quantify the 2θ value corresponding to the lattice spacing, the measured 3D diffraction profiles were integrated over the ω (lattice tilting) and φ (lattice twisting) directions to obtain one-dimensional 2θ profiles. In the pump–probe experiments, we applied a gate voltage as a pump pulse that was synchronized with the X-ray irradiation as a probe pulse and changed the phase of the voltage pulse with respect to the X-ray pulse.

Figures 2(a) and 2(b) show AlGaN(0004 2θ profiles recorded under static negative gate voltages from 0 to –7 V and positive voltages from 0 to +7 V, respectively. The 2θ profiles and peaks clearly shifted to lower angles with negatively increasing voltage, whereas no marked shifts were observed when a positive voltage was applied. Figure 2(c) shows the gate-voltage dependence of the AlGaN *c*-plane lattice spacing calculated from the 2θ profile using a Bragg equation. We observed that the lattice spacing increases linearly with the applied negative gate voltage. This behavior is quantitatively consistent with the piezoelectric response estimated from the exerted electric field on the AlGaN layer and piezoelectric coefficients as well as the clamping effect from the substrate.

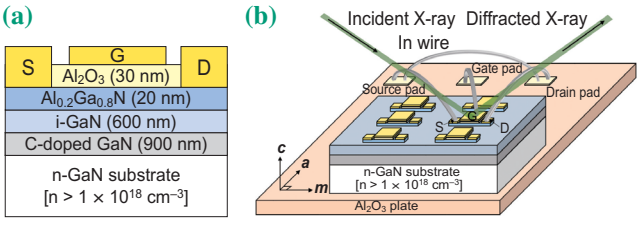

Fig. 1. **(a)** Schematic of the AlGaN/GaN MOS-HEMT device structure characterized in the present study and **(b)** schematic of the diffraction geometry in which the source and drain electrodes of the device are equipotential with In wire (S, source; G, gate; D, drain).

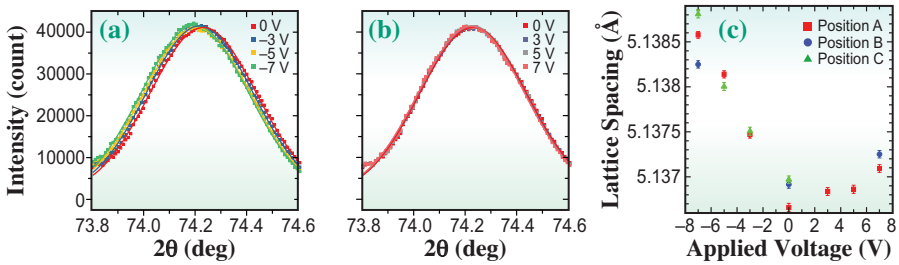

Fig. 2. Observed AlGaN 0004 diffraction 2θ profiles for **(a)** negative and **(b)** positive applied gate voltages. **(c)** Gate-voltage dependence of the AlGaN (0001) lattice spacing derived from the 2θ profile peaks.

Further dynamic measurements of AlGaN strain responses were performed using the application sequence for X-rays and gate-voltage pulses shown in Fig. 3(a). For the dynamic analysis, the single-bunch (SB) section of the hybrid-bunch mode was selectively used by employing an X-ray chopper device [5] and 60-ps-wide X-ray pulses were emitted at an arbitrary delay time during the application of the gate voltage pulse. Figures 3(b) and 3(c) show the variations in AlGaN *c*-plane lattice spacing as a function of the delay time during the application of the gate voltage for pulse-width and edge-time dependences, respectively. In all cases, we observed that the lattice spacing started to increase at the onset of voltage application to a certain value less than ~5.1385 Å and then decreased to the initial value of ~5.137 Å at the end of the voltage application. The present results successfully revealed the dynamic behavior of the *c*-plane lattice spacing change due to the IPE caused by the applied gate voltage on the nanosecond time scale. Interestingly, these lattice-spacing variations show a time lag following the application of voltage; this time lag is on the order of tens to hundreds of nanoseconds, depending on the pulse width and edge time, and was attributed to the voltage drop due to transient current. This nanoscale time-resolved analysis revealed the effect of transient current flowing in the device on the lattice deformation response during the application of a gate voltage.

In summary, we developed a measurement system that can perform detailed analyses of IPE-induced lattice deformation in an AlGaN/GaN HEMT device via synchrotron radiation X-ray diffraction combined with the pump-probe method. The present results are enlightening in that high-time-resolution strain analysis revealed that seemingly stationary nitride semiconductor devices actually experience significant dynamic deformations under their operating conditions. An extended nanoXRD-based analysis with high spatial and temporal resolutions will provide further details of local dynamic strain behaviors related to device structures or lattice defects in nitride semiconductors.

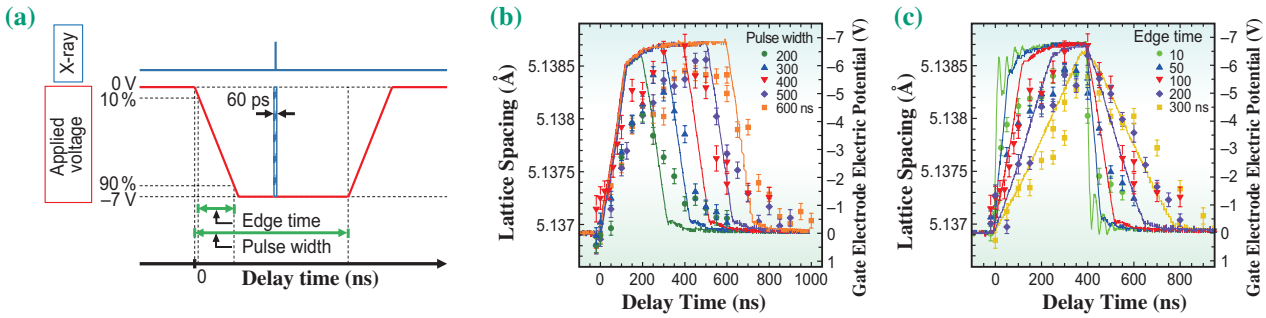

Fig. 3. **(a)** Application sequence of X-ray and gate-voltage pulses in the measurements. Time dependence of the AlGaN (0001) lattice spacing (left axis, color plot) and the measured electric potentials of the gate electrode (right axis, color line) for **(b)** pulse-width and **(c)** edge-time dependences of the gate-voltage application.

Tetsuya Tohei[a,*], Yasuhiko Imai[b] and Akira Sakai[a]

[a] Graduate School of Engineering Science, Osaka University
[b] Japan Synchrotron Radiation Research Institute (JASRI)

*Email: tohei@ee.es.osaka-u.ac.jp

References

[1] T. Sato *et al.*: Jpn. J. Appl. Phys. **57** (2018) 0902B8.
[2] *H. Shiomi, A. Ueda, T. Tohei, Y. Imai, T. Hamachi, K. Sumitani, S. Kimura, Y. Ando, T. Hashizume and A. Sakai: Appl. Phys. Express* ***14*** *(2021) 095502.*
[3] Y. Ando *et al.*: Appl. Phys. Express **12** (2019) 024002.
[4] S. Kamada *et al.*: Appl. Phys. Express **9** (2016) 111001.
[5] H. Osawa *et al.*: Jpn. J. Appl. Phys. **56** (2017) 048001.

Liquid-like and gas-like dynamics in supercritical fluids

It is common knowledge that, in most systems, the liquid-gas transition terminates at a critical point with a specific temperature, T_c, and pressure, P_c. In the region beyond this point ($T > T_c$, $P > P_c$), a first-order phase transition no longer exists. This region is usually referred to as the supercritical fluid state and thought of as a single featureless continuum. However, it is known that the properties of the fluid can undergo dramatic changes within the supercritical region, especially near the critical point, and many applications take advantage of precisely this aspect [1]. A detailed description of the supercritical fluid state is thus important from both a fundamental physics point of view and a practical perspective.

Thanks to years of research and a vast amount of available data, the thermodynamics of supercritical fluids has become well understood. It is found that the line of maxima of a given response function (e.g., the isobaric heat capacity, C_P) indicates the location of a rapid crossover between liquid-like and gas-like properties, especially in the near-critical region. This line is referred to as the "Widom line" [2] and it serves as a natural extension of the liquid-gas binodal beyond the critical point.

However, it remains unclear what happens on the microscopic level. Particularly, a systematic study of the molecular-scale dynamics in supercritical fluids is lacking. To investigate this, we used a combination of inelastic X-ray scattering (IXS) measurements and molecular dynamics (MD) simulations. The sample of choice was water, with a critical point at P_c = 221 bar and T_c = 647 K. The IXS measurements were carried out at SPring-8 **BL43LXU**, using the Si(999) reflection with 17.8 keV incident X-rays. The resolution function was measured with plexiglass and had a full width at half maximum around 3 meV for all 20 analyzers used in the experiment. A pressure cell with diamond windows was used to reach supercritical conditions. The MD simulations were performed using LAMMPS. We chose the TIP4P/2005 potential [3], which has been shown to well reproduce various properties of water particularly in the sub- to supercritical region, with simply a 75 bar shift in pressure (i.e., 300 bar in experiment corresponds to 225 bar with TIP4P/2005) [4].

We focus on the P = 300 bar isobar and examine the longitudinal current correlation function, $J_l(Q,\omega)$, where Q is the momentum transfer and $\hbar\omega$ the energy loss of the X-ray photon. It bears a simple relation with the dynamic structure factor, $S(Q,\omega)$: $J_l(Q,\omega) = (\omega^2/Q^2)\, S(Q,\omega)$, and the latter can be measured with IXS. In MD, $J_l(Q,\omega)$ can be calculated directly. Details of data treatment can be found in [4]. Note that J_l can be conveniently normalized by a factor M/k_BT, where M is the molecular mass, after which the spectra under different temperatures can be compared.

Figure 1 presents the normalized $J_l(Q,\omega)$ spectra along P = 300 bar with temperatures from 400 K to 800 K. Results from MD and IXS agree well. It is known that various physical properties undergo a liquid-like to gas-like transition in this temperature range, and here the microscopic picture becomes clear. Notably, J_l appears to contain two components, one peaked at lower ω and one higher. With increasing temperature, the former (referred to as the G component) grows and the latter (L component) diminishes, as indicated by the arrows, leading to a liquid-like to gas-like dynamical transition.

To quantify this transition, we decompose the spectra and extract the L and G components using non-negative matrix factorization (NMF) [4]. The results are shown in Fig. 2(a,b). We can then define a parameter f representing the spectral weight of the L component and study its temperature evolution. As shown in Fig. 2(c), f decreases with temperature as expected, and with a rapid crossover near the Widom line indicated by the maximum in C_P or κ_T.

It is natural to ask whether these phenomena are specific to water, whose liquid-like dynamics are closely related to hydrogen bonding [4]. Thus, we performed MD simulations of three other systems

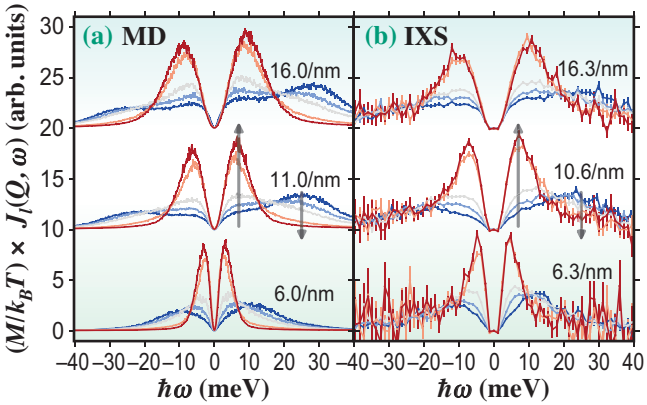

Fig. 1. Normalized $J_l(Q,\omega)$ along P = 300 bar obtained from **(a)** MD and **(b)** IXS at three different Q values, as annotated in the plots. The spectra from blue to red are from 400 K to 800 K at 100 K steps. MD spectra are multiplied by the detailed balance factor. An offset is applied between different Q values. Arrows indicate the trend with increasing temperature.

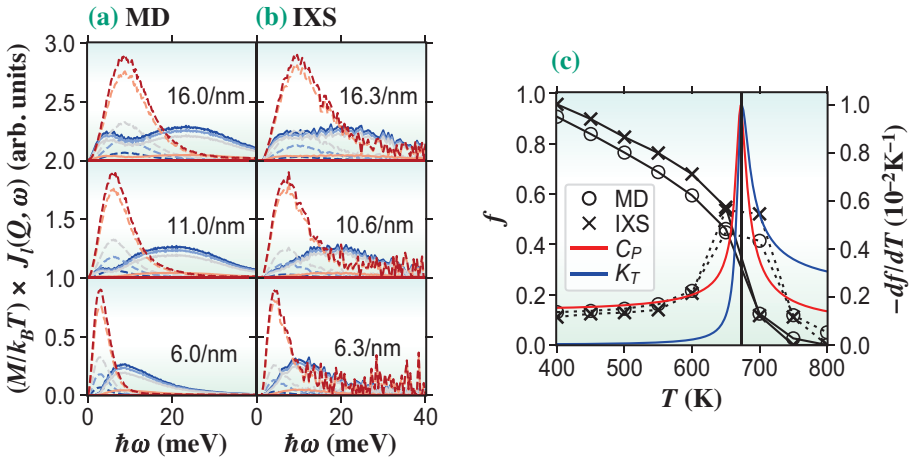

Fig. 2. **(a)** L (dashed) and G (solid) components of the MD spectra; **(b)** the same for IXS spectra; colors and Q values correspond to Fig. 1. **(c)** Circles: MD; crosses: IXS. Black solid lines: fraction of the L component, f; dotted lines: its temperature derivative; these lines are a guide to the eye. Also shown are C_P (red) and κ_T (blue) scaled to match the derivative of f. Solid vertical line indicates the approximate position of the Widom line.

represented by diverse potentials—Si, Te, and Lennard-Jones (LJ) fluid (see [5] for details). Figure 3 shows, for each system, three representative J_l spectra taken at low, intermediate, and high temperatures along an isobar $P \approx 1.6P_c$. It can be seen that, as in the case of water, these spectra consist of two components. In particular, the intermediate spectrum clearly contains the characteristics of both the low-T and the high-T spectra. Using the NMF method, the components can be extracted as shown in Fig. 3, allowing further quantitative analysis.

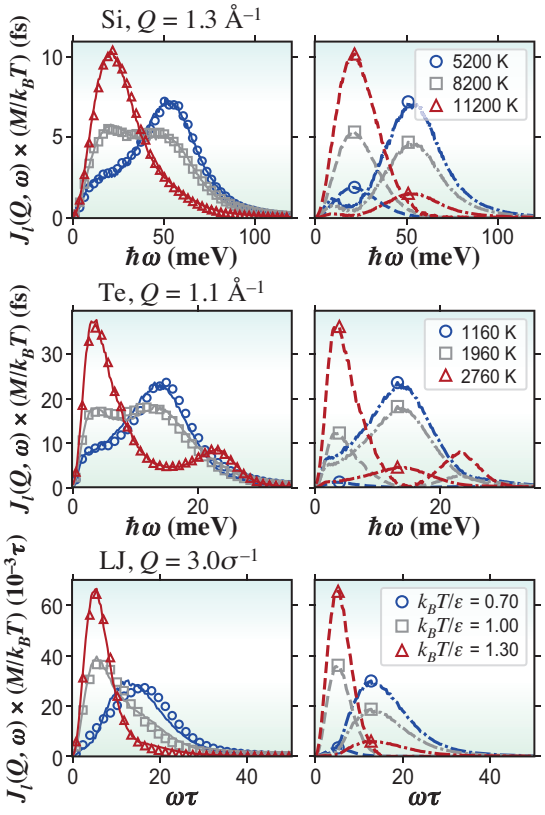

Fig. 3. Two-component behavior in other fluids. Each row shows a system in low- (blue), intermediate- (gray), and high- (red) temperature states. Left column: MD data (symbols) and NMF fit (solid lines). Right column: extracted L (dash-dotted) and G (dashed) components; the peak positions are marked by symbols. σ and ε are LJ units.

In conclusion, with a combination of IXS measurements and MD simulations, we find a two-component behavior in the molecular-scale dynamics of water near its critical point. The change in the ratio between the components leads to a liquid-like to gas-like transition, which happens most rapidly near the thermodynamic Widom line. Further MD simulations indicate that the two-component behavior is common among diverse supercritical fluid systems and may be a universal phenomenon.

Peihao Sun[a,b], Jerry B. Hastings[a,*] and Giulio Monaco[b]

[a] SLAC National Accelerator Laboratory, USA
[b] Università degli Studi di Padova, Italy

*Email: jbh@slac.stanford.edu

References

[1] C. Eckert *et al.*: Nature **383** (1996) 313.
[2] L. Xu *et al.*: Proc. Natl. Acad. Sci. **102** (2005) 16558.
[3] J.L.F. Abascal and C. Vega: J. Chem. Phys. **123** (2005) 234505.
[4] *P. Sun, J.B. Hastings, D. Ishikawa, A.Q.R. Baron, and G. Monaco: Phys. Rev. Lett.* ***125*** *(2020) 256001.*
[5] P. Sun *et al.*: J. Phys. Chem. B 125 (2021) 13494.

Molecular origins of two-dimensional membrane viscosity measured by X-ray and neutron spectroscopies

Our body is composed of more than one trillion cells, and each cell is defined by a border that distinguishes its inner and outer regions. The boundary is a molecular membrane that is only two molecules thick and is known as the cell membrane. The variety of lipids, sugars and proteins that form cell membranes serves as a fluid matrix that facilitates interactions between individual lipids and proteins, formation of domains, and reorganization of membrane components to form multimeric signaling complexes. Understanding the transport properties in two-dimensional lipid membranes is, thus, both fundamentally interesting and biologically relevant.

Although viscosity is an intrinsic material property that characterizes the transport of momentum in a material, there have been both experimental and computational challenges in measuring two-dimensional membrane viscosity. Most of the experimental techniques use optical methods to access the membrane viscosity as a macroscopic membrane property on length scales much larger than the individual lipids, and estimates for the membrane viscosity vary by orders of magnitude depending on the experimental method used [1]. As such, there is a growing need for a more detailed understanding of the molecular origins of membrane viscosity. This is where the power of quasielastic X-ray and neutron scattering techniques was used to open new avenues to understanding the molecular origins of membrane viscosity by an extension of the length and time resolutions to cover structural dynamics at the molecular level [2].

It is not straightforward to realize a molecular understanding of the membrane viscosity without good theoretical models. In three-dimensional liquid systems, the relaxation time of the structural relaxations at a structural correlation peak follows the same temperature dependence as the liquid viscosity [3]. This relation suggests a universal feature in that the friction within liquids likely originates from the structural rearrangements of the constituent molecules. Accordingly, here we extended these studies to two dimensional systems and the measured relaxation times of the structural relaxations of the lipid acyl tails were used to calculate the membrane viscosity of a lipid bilayer [2].

We employed both Mössbauer time-domain interferometry (MTDI) [4] and neutron spin echo (NSE) spectroscopies. As a model cell membrane, we used dimyristoyl phosphatidylcholine (DMPC) bilayers at a concentration of 400 mg/mL in water. Protiated DMPC was dissolved in H_2O for the MTDI experiments while tail-deuterated DMPC dissolved D_2O was used for the NSE experiments. The experiments were performed above and below the lipid molecular melting transition temperature T_m (T_m = 24°C and 20.5°C for protiated and tail-deuterated DMPC, respectively) in order to see dynamics of lipid acyl tails both in the fluid ($T > T_m$) and gel ($T < T_m$) phases.

A priori neutron scattering experiment on TAIKAN at J-PARC showed a structural correlation peak from the lipid acyl tails at the scattering vector transfer of $q \approx 1.5$ Å^{-1}, where $q = 4\pi\sin(\theta/2)/\lambda$ with θ and λ being the scattering angle and the incident wavelength of the neutrons, respectively. The orientational order in the gel phase is higher than that in the fluid phase, and a sharper peak was observed in the gel phase [2]. Further dynamics measurements were performed at this q to measure the dynamics of the acyl tail correlations at a distance of about 5 Å. Synchrotron radiation from SPring-8 **BL09XU** was used to record MTDI signals from the samples at temperatures mainly in the gel phase. This is because the time coverage of the MTDI was from ≈10 ns up to ≈300 ns which allowed us to measure the slowest dynamics in the membrane gel phase that were otherwise inaccessible with other experimental techniques. On the other hand, NSE was used to measure relaxations both in the fluid and gel phases as the time coverage of the NSE was from

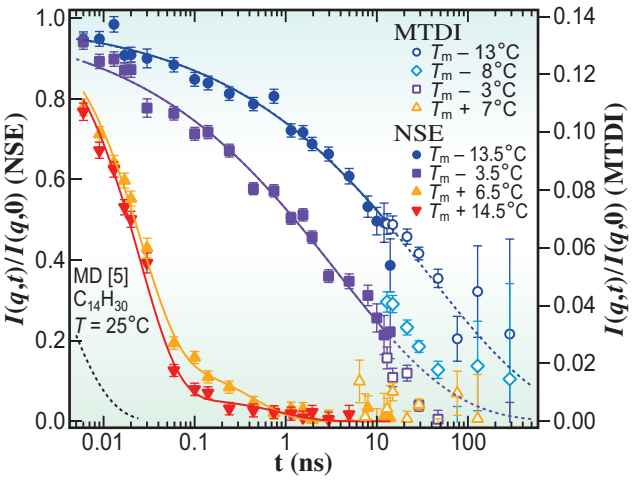

Fig. 1. Normalized intermediate scattering functions measured by the MTDI and NSE. The MTDI data are shown by open symbols on the right axis, while the NSE data are shown by full symbols on the left axis. The scale of the MTDI data is shifted to match the NSE data. The black dashed line shows molecular dynamics simulation results for tetradecane [5]. Error bars represent ±1 standard deviation in this article.

5 ps up to 16 ns on the NGA-NSE at NIST. Both these techniques measure normalized intermediate scattering function, $I(q,t)/I(q,0)$, of the lipid acyl tail correlations.

We observed fast relaxation dynamics in the fluid phase ($T > T_m$) compared to those in the gel phase ($T < T_m$) as shown in Fig. 1. In the fluid phase, two relaxation processes were identified, where the majority component had a faster relaxation time of ≈0.03 ns, and the second minor component had a slower relaxation time of ≈0.5 ns. The faster relaxation time that relates to the structural rearrangements of the individual DMPC lipid acyl tails was about an order of magnitude slower than the structural relaxation dynamics of the analogous three-dimensional linear alkane (tetradecane, $C_{14}H_{30}$), where a computer simulation result showed a relaxation time of about 0.003 ns [5]. The two-dimensional confinement and orientational ordering of the $C_{14}H_{30}$ lipid tails as well as the restricted motions due to the binding of one end of the tail to the headgroup significantly slows the chain relaxations. The slower relaxation time originates from the entire lipid escaping from the cage and rearranging with the neighboring lipid molecules, and its origins were confirmed by comparing the molecular diffusion time measured by nuclear magnetic resonance spectroscopy with the present results. This result indicates that the lipid molecules are moving out of their molecular cages on time scales of 0.5 ns.

Meanwhile, when the temperature is decreased below T_m, the relaxation dynamics are significantly slowed down to ~10 ns to ~100 ns depending on temperature. Interestingly, the data clearly show that the molecular motions persist even as the temperature is lowered into the gel phase, and the membranes are increasingly solidified at the molecular level as the temperature decreases further. However, we were not able to resolve the two relaxation modes seen in the fluid phase in the MTDI and NSE data for the lipid gel phase, indicating that the relaxation dynamics became much more heterogeneous.

Our estimates for the membrane viscosity, η_m, calculated from the structural relaxation times are summarized in Fig. 2. In the fluid phase, the slower relaxation gives a membrane viscosity on the order of 1 nPa·s·m, which falls in the middle of broadly distributed η_m values for DMPC in literature [1]. This result indicates that the membrane viscosity has a clear relationship with the lipid molecular structural relaxations. In the present study, we estimated membrane viscosity in the gel phase for the first time. The estimated membrane viscosity in the vicinity of T_m is about 10 times larger than that in the fluid phase, and significantly increases with decreasing temperature.

In summary, the combination of MTDI and NSE accessed the structural relaxation dynamics of lipid acyl tails over more than 4 orders of magnitude in time. This is a unique opportunity offered by the combination of the X-ray and neutron spectroscopic techniques and provided new insights into the collective acyl tail dynamics. The slower relaxation of the two modes in the fluid phase relates to the structural relaxation of the lipid molecules, and the time required for a lipid molecule to escape from its molecular cage is relevant to determining the macroscopic membrane viscosity. The present results provide new insights into how the individual lipid molecule motions can influence the membrane viscosity and may one day lead to future applications in drug discovery and membrane function control.

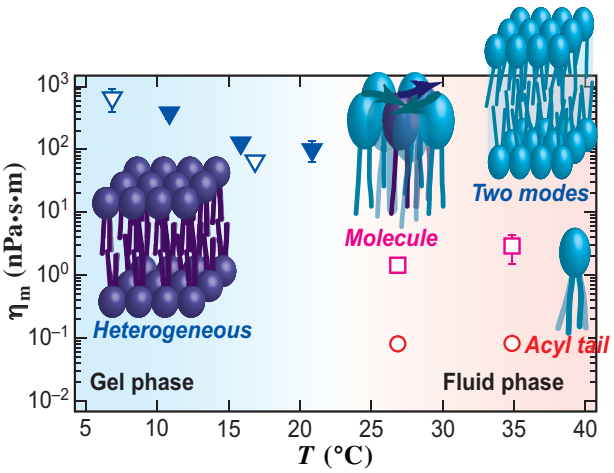

Fig. 2. Estimated membrane viscosity, η_m, from the structural relaxation time measured by the MTDI (full symbols) and NSE (open symbols) experiments. Schematic illustrations show molecular origins of the estimated η_m. Viscosity estimated from the slower relaxation in the fluid phase should correspond to apparent membrane viscosity, which appears around the middle of a large distribution of estimated η_m in literature. [1]

Michihiro Nagao[a,b,c]

[a] NIST Center for Neutron Research, National Institute of Standards and Technology, USA
[b] Department of Materials Science and Engineering, University of Maryland, USA
[c] Department of Physics and Astronomy, University of Delaware, USA

Email: michihiro.nagao@nist.gov

References

[1] H.A. Faizi *et al.*: Biophysical J. **121** (2022) 910.
[2] *M. Nagao, E.G. Kelley, A. Faraone, M. Saito, Y. Yoda, M. Kurokuzu, S. Takata, M. Seto and P.D. Butler: Phys. Rev. Lett.* ***127*** *(2021) 078102.*
[3] F. Mezei *et al.*: Phys. Rev. Lett. **58** (1987) 571.
[4] M. Saito *et al.*: Sci. Rep. **7** (2017) 12558.
[5] T. Yamaguchi: J. Chem. Phys. **146** (2017) 094511.

Structural characterization of nano-confined liquids by synchrotron X-ray diffraction measurement

The properties of liquids confined between solid surfaces with a nanometer-scale gap (nano-confined liquids) are known to be different from those of bulk liquids owing to the restriction of their motions and interactions with solid surfaces [1-5]. The measurements of both the surface and shear forces using a surface force apparatus (SFA) have been performed to study various liquids confined between solid surfaces taking advantages of the ability to freely changing the surface separation distance (D) [1-4,6]. Generally, nano-confined liquids exhibit solid-like properties, i.e., the effective viscosity increases more than several orders of magnitude. This significant change has been ascribed to the decrease in the freedom of movement as a result of the confinement of liquid molecules in a nanospace, similar to the effect of the decrease in temperature. However, the molecular-level understanding of nano-confined liquids is still limited because of the lack of techniques appropriate for characterizing the structure of the nano-confined liquids.

For example, the surface force measurement revealed the formation of layered structures of simple liquids, e.g., a quasi-spherical molecule (octamethylcyclotetrasiloxane (OMCTS)) and *n*-alkane, when they are confined between atomically smooth mica surfaces at D's less than about 10 molecular diameters [4]. These reports prompted a discussion about the solidification mechanism of confined liquids; however, information on the in a plane structure parallel to the surfaces is imperative for understanding. Also, the structural variation of the liquid molecule and the properties of confining surfaces make the behavior of the confined liquids complicated [5].

One of the most effective techniques for understanding the specific properties of nano-confined liquids is a structural analysis with X-ray diffraction (XRD) measurements used in combination with an SFA, which enables the investigation of the structures in a plane parallel to the confining surfaces. However, this technique was only applied to liquids in a submicron-scale thickness range until recently [7]. We have established the X-ray diffraction measurement of nano-confined liquids by using the high-brilliance synchrotron X-ray beam of SPring-8 **BL40B2** [8]. This technique has enabled us to obtain new insights into nano-confined liquids, e.g., (i) changes in diffraction peak intensity revealed that a nano-confined liquid crystal (4-cyano-4' octyl biphenyl (8CB)) exhibited a 10^{10}-fold slower diffusion than did the bulk 8CB [8]; (ii) the specific organization of cations and anions of confined ionic liquids could help to determine the mechanism behind the specific lubricity of nano-confined ionic liquids [9].

Recently, we developed a device for the XRD measurement of nano-confined liquids under shear and investigated the effects of shear on the orientational behavior of a room-temperature smectic-A liquid crystal 8CB confined between mica and silica surfaces (Fig. 1) [10]. As shown in Fig. 2(a), the X-ray diffraction intensity profiles of 8CB confined between mica surfaces measured at the hard wall thickness (D = 1.7 nm) showed the two centrosymmetric diffraction spots corresponding to spacing (d) = 3.13 nm. This result demonstrated the uniaxial orientation of the lamellar axis of 8CB most probably due to the preferential alignment of its long axis along the crystallographic axis (*a*-axis) of the mica. On the other hand, the ring diffraction pattern observed for 8CB confined between silica surfaces (D = *ca.* 2 nm) demonstrated the omnidirectional orientation of the lamellar axis of 8CB in-plane (Fig. 2(b)). These results clearly demonstrated the significant effects of surface properties on the structure of nano-confined liquids and should be important for liquid crystal applications such as optical devices and lubricants in which the effects of surface properties are becoming more significant for finer and smaller devices.

As shown in Fig. 3(a), the two centrosymmetric diffraction spots for the nano-confined 8CB between mica surfaces were rotated only *ca.* 3 degrees within the plane parallel to the surface by applying shear. The ring diffraction pattern of 8CB confined between silica surfaces showed almost no change on applying shear. These results demonstrated, for the first time, that the effect of shear on the orientation of 8CB was significantly suppressed when the surface

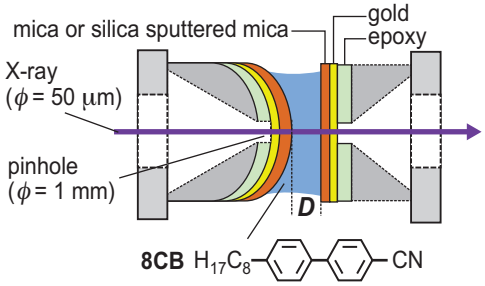

Fig. 1. Schematic diagram of XRD measurement of nano-confined 8CB.

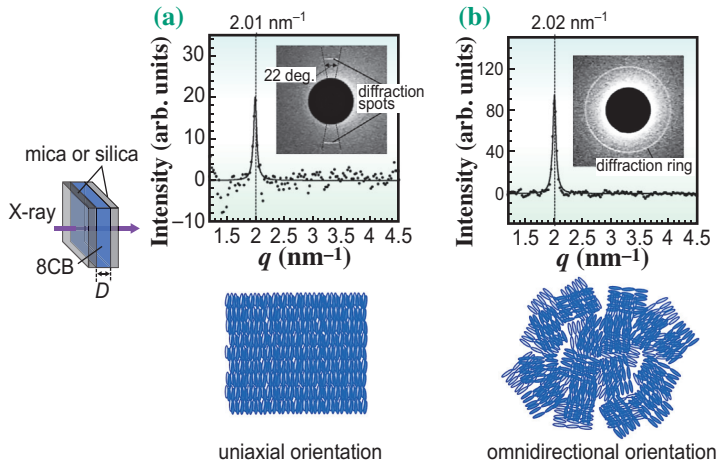

Fig. 2. **(a)** X-ray diffraction intensity profiles of 8CB confined between mica surfaces whose crystal axes were adjusted to be parallel to each other at D = 1.7 nm. **(b)** X-ray diffraction intensity profiles of 8CB confined between silica surfaces at D = *ca.* 2 nm. Filled black symbols are the obtained diffraction data, and solid lines are the fitting curves of the Lorentz function. The insets show the diffraction images at q < *ca.* 2.5 nm^{-1}.

separation distance (D) was at the nanometer scale regardless of the types of surface examined. On the other hand, when shear was applied to 8CB at a large D (= 3.3 μm) that was then returned to D = *ca.* 2 nm, the orientation of 8CB confined between mica surfaces was rotated, and the diffraction ring pattern of 8CB confined between silica surfaces disappeared. These results indicated that 8CB was significantly rotated or disordered by the shear applied at a large D where the mobility of 8CB was not suppressed.

The X-ray diffraction measurement of confined liquids has great potential to advance the molecular-level understanding of confined liquids, which exhibit complex behavior, and can also provide useful information for the innovative design of materials such as lubricants, micro/nanofluids, and nanomolds.

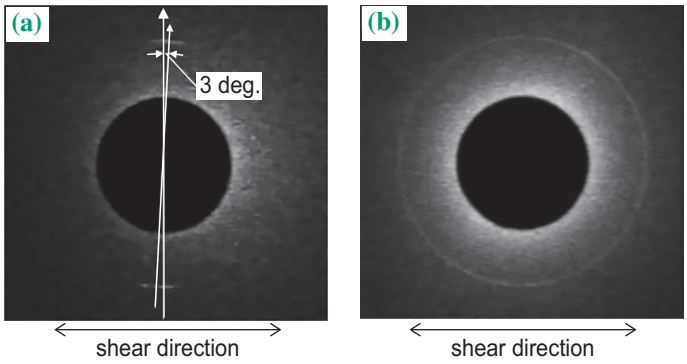

Fig. 3. X-ray diffraction images of 8CB under shear confined between **(a)** mica surfaces at D = 1.7 nm and **(b)** silica surfaces at D = *ca.* 2 nm.

Masashi Mizukami

New Industry Creation Hatchery Center, Tohoku University

Email: masashi.mizukami.e7@tohoku.ac.jp

References

[1] R.G. Horn *et al.*: J. Chem. Phys. **75** (1981) 1400.
[2] S. Granick: Science **253** (1991) 1374.
[3] J. Klein *et al.*: Science **269** (1995) 816.
[4] M. Ruths *et al.*: Nanotribology and Nanomechanics, B. Bhushan, Ed. (Springer, 2005), Chapter 13, pp. 107.
[5] K. Kurihara: Pure Appl. Chem. **91** (2019) 707.
[6] C. Dushkin *et al.*: Colloids Surf. A: Physicochem. Eng. Asp. **129-130** (1997) 131.
[7] S.H.J. Idziak *et al.*: Science **264** (1994) 1915.
[8] S. Nakano *et al.*: Jpn. J. Appl. Phys. **52** (2013) 035002.
[9] K. Tomita *et al.*: Phys. Chem. Chem. Phys. **20** (2018) 13714.
[10] *M. Mizukami, N. Ohta, K. Tomita, T. Yanagimachi, Y. Shibuya, N. Yagi, K. Kurihara: Phys. Chem. Chem. Phys.* ***23*** *(2021) 131.*

Elongation of Fe–Fe atomic pairs in $Fe_{65}Ni_{35}$ Invar alloy determined by RMC method

Face-centered cubic (fcc) Fe–Ni alloys containing 35–36 at.% Ni are characterized by the Invar effect, which shows a nearly zero thermal expansion coefficient ($\alpha = 1.19 \times 10^{-6}$/K) within a wide temperature range up to the Curie temperature ($T_C \sim 505$ K). After the discovery of the Invar effect by Guillaume in 1897 [1], the macroscopic origin of this anomalous thermoelastic property has been interpreted as a cancellation of the thermal expansion by the shrinkage due to the magnetovolume effect. On the other hand, the atomic-scale origin of the large magnetovolume effect has not been understood thus far.

Since the zero thermal expansion of the lattice is related to the shallow curvature of the interatomic potential, the Invar alloy exhibits anomalously soft elastic properties under high pressures. The shallow interatomic potential has been interpreted theoretically as a 2γ-state model, in which two distinct spin states are hypothesized below T_C: a high-spin (HS) configuration associated with a large volume and a low-spin (LS) configuration with a small volume. More recent *ab initio* calculation results [2] indicated that the noncollinear spin alignment of Fe moments develops with increasing pressure, whereas Ni spin moments maintain linear spin alignments even under pressure, which also explains the elastic softening behavior in the Invar alloy. The element-dependent response of the magnetic structure under pressure motivated us to experimentally determine the local structures around Fe and Ni atoms separately.

This study focuses on the atomic-scale origin of the magnetovolume effects in Invar alloy [3]. The atomic arrangement in a model structure composed of 4000 Fe/Ni atoms was investigated using the reverse Monte Carlo (RMC) algorithm combined with complementary datasets of extended X-ray absorption fine structure (EXAFS) and X-ray diffraction (XRD) under high pressures. The pressure dependences of XRD and EXAFS were measured at SPring-8 **BL39XU** independently. Typically, it is difficult to distinguish the Fe and Ni atoms neighboring the X-ray absorbing atoms by conventional EXAFS analysis because of the small difference between the backscattering amplitudes of Fe and Ni. In contrast, the RMC method constructs an atomic cluster and finds the best atomic cluster model that matches the experimental EXAFS profiles at the Fe and Ni edges as well as the XRD patterns by trial-and-error iterations. Consequently, the length of each atomic pair can be evaluated from the determined cluster.

The RMC fits provided good agreement between the experimental and calculated profiles of the absolute values of Fourier transformed profiles ($|\mathrm{FT}[k^2\chi(k)]|$) at both the Fe and Ni edges of the Invar alloy (Fig. 1). The determined atomic cluster conserves the sequential stacks of (111) atomic planes, although much of the atoms are displaced from the ideal positions of the fcc lattice. Therefore, the RMC fits successfully visualize the structure of the alloy, where the local structure was largely distorted, although the disordered atomic cluster maintained the long-range periodicity to satisfy the Bragg law owing to the pseudo-fcc symmetry.

The partial pair distribution functions $g_{ij}(R)$ are determined from the atomic cluster and demonstrate the elongation of the first-nearest neighboring (1NN) Fe–Fe pairs in comparison with 1NN Fe–Ni and Ni–Ni pairs at 0.6 GPa (Fig. 2). As the pressure increases, the difference in $g_{ij}(R)$ profiles gradually decreases;

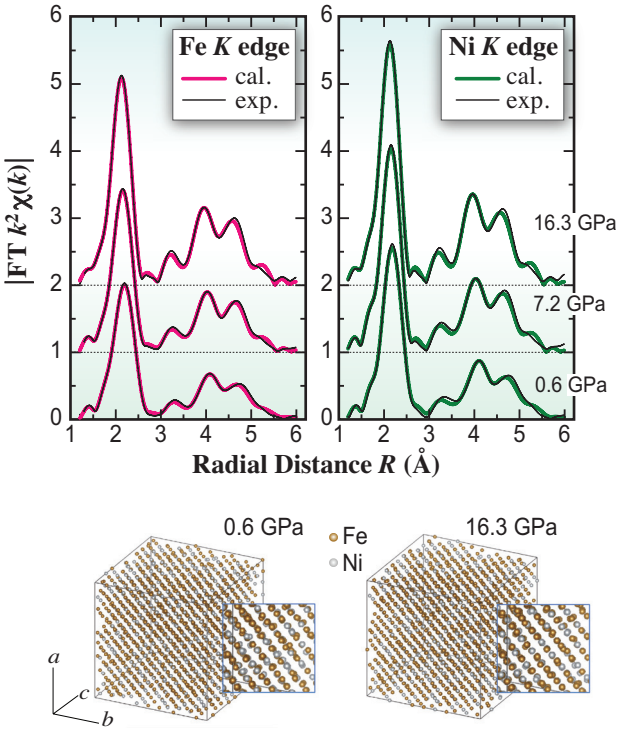

Fig. 1. Top: absolute values of Fourier transformed EXAFS profiles ($|\mathrm{FT}[k^2\chi(k)]|$) of $Fe_{65}Ni_{35}$ Invar at Fe and Ni *K*-edges. Bottom: atomic clusters of the Invar alloy obtained by the RMC method. The clusters viewed from the [11$\bar{2}$] direction are shown. The illustrations represent enlargements of the atomic cluster.

the profiles of these three pairs exhibit peaks at approximately the same position of $R \sim 2.455$ Å at 16.3 GPa. To highlight the elongation of Fe–Fe atomic pairs, the average lengths of the 1NN atomic pairs, R_{Fe-Fe}, R_{Fe-Ni}, and R_{Ni-Ni}, were quantitatively determined and are plotted in Fig. 3. Compared with R_{Fe-Ni} and R_{Ni-Ni}, the expansion of R_{Fe-Fe} is of the size of 0.02 Å at the lowest pressure of the Invar alloy (0.6 GPa). Because the Fe–Fe pairs are more compressive than others, the elongation of R_{Fe-Fe} decreases rapidly with increasing pressure; the evaluated R_{Fe-Fe} reaches the values of R_{Fe-Ni} and R_{Ni-Ni} at pressures above 10 GPa.

The Invar alloy undergoes a pressure-induced magnetic transition from the ferromagnetic phase to the paramagnetic phase at $P_c \sim 7$ GPa. The elongation and subsequent shrinkage of Fe–Fe pairs accompanied by the magnetic transition reveals that the volume changes owing to the magnetovolume effect originating mainly from the Fe–Fe pairs, while the lengths of Fe–Ni and Ni–Ni pairs seem to contribute less. Interestingly, the elongation of Fe–Fe pairs occurred also in the $Fe_{55}Ni_{45}$ non-Invar alloy [4], indicating that the existence of longer Fe–Fe pairs because of the magnetovolume effect is a common phenomenon in the Fe–Ni alloy with fcc symmetry. Because the $Fe_{55}Ni_{45}$ non-Invar alloy undergoes a pressure-induced Invar effect at ~7.5 GPa [4], we conclude that the delicate balance between the number of Fe–Fe pairs and their elongation depending on the magnetization play a crucial role in initiating the Invar effect. In this study, using the RMC method, we successfully demonstrated the feasibility of atomic-arrangement visualization for disordered alloys.

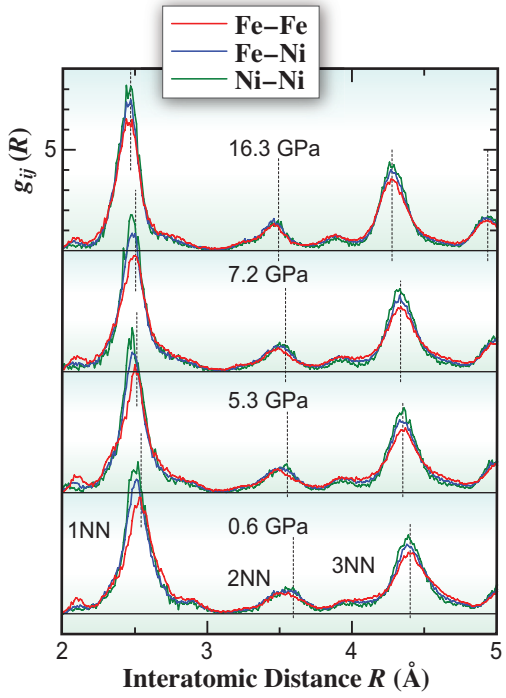

Fig. 2. Partial pair distribution functions $g_{ij}(R)$ of i and j atomic pairs up to third-nearest-neighboring (3NN) pairs, where i, j = Fe or Ni.

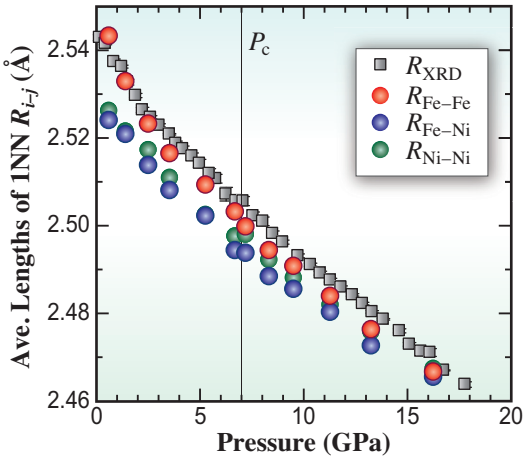

Fig. 3. Pressure dependences of the average length within a range of 0.6 Å centered on the 1NN peaks of Fe–Fe, Fe–Ni, and Ni–Ni pairs. Squares show average bond lengths determined from XRD.

Naoki Ishimatsu* and Naoto Kitamura

Division of Advanced Science and Engineering, Hiroshima University

*Email: ishimatsunaoki@hiroshima-u.ac.jp

References

[1] C. Guillaume and C.H. Seances: Acad. Sci. **125** (1897) 235 .
[2] M. van Schilfgaarde *et al.*: Nature **400** (1999) 46.
[3] *N. Ishimatsu, S. Iwasaki, M. Kousa, S. Kato, N. Nakajima, N. Kitamura, N. Kawamura, M. Mizumaki, S. Kakizawa, R. Nomura, T. Irifune, and H. Sumiya: Phys. Rev. B* ***103*** *(2021) L220102.*
[4] L. Dubrovinsky *et al.*: Phys. Rev. Lett. **86** (2001) 4851.

Tomographic reconstruction of "orphaned" oxygen orbitals in Li-rich battery material $Li_xTi_{0.4}Mn_{0.4}O_2$

Toward the achievement of a sustainable society, the electrification of mobility by means of lithium-ion technology is now gaining wider acceptance. However, the electrification of heavy-duty vehicles and aviation will require batteries with a much higher specific energy than that of existing lithium-ion batteries (LIBs). Each LIB is composed of an anode and a cathode immersed in an electrolyte and produces energy as lithium ions are shuttled between the two electrodes through a separator. The energy density of LIBs is determined by the combination of anode and cathode materials. Lithium metal and silicon are candidate materials for high-capacity anodes because they have theoretical capacities of 3860 $mAhg^{-1}$ and 4200 $mAhg^{-1}$, respectively. These values are about 10 times higher than that of a conventional graphite anode. On the other hand, for the cathode, there is an urgent need to find materials beyond those of the existing layered cathodes. Lithium-rich oxides present a promising class of cathode materials in this regard, with their high capacity of about 300 $mAhg^{-1}$ [1]. This capacity is significantly greater than that of conventional cathode materials; for example, $LiCoO_2$ has a capacity of 140 $mAhg^{-1}$, $LiMn_2O_4$ has a capacity of 120 $mAhg^{-1}$, and $LiFePO_4$ has a capacity of 170 $mAhg^{-1}$. Such capacities of lithium-rich oxides have been suggested to result from a combination of cationic and anionic redox processes. The conventional cathode materials such as $LiCoO_2$ and $LiFePO_4$ involve only the cationic redox reaction; therefore, it has been difficult to increase the capacity. The anionic redox mechanism underlying the electrochemical process of lithium-rich oxides, however, has been difficult to understand fully using only the known probes and techniques. In this research, using high-energy X-ray Compton measurements together with first-principles modeling, we show how the electronic orbital that lies at the heart of the reversible and stable anionic redox activity can be imaged and visualized, and its character and symmetry are determined. Our results not only provide a picture of the workings of a lithium-rich battery at the atomic scale but also suggest pathways to improving existing battery materials and designing new ones [2].

High-energy X-ray Compton scattering experiments were performed at SPring-8 **BL08W**. The sample is the cation-disordered rock salt $Li_xTi_{0.4}Mn_{0.4}O_2$ (lithium concentration x = 0, 0.4, 0.8, and 1.2). This material is attracting attention as a lithium-rich oxide that has a high capacity of more than 300 $mAhg^{-1}$ even though it does not include rare metals. The lithium concentration of $Li_xTi_{0.4}Mn_{0.4}O_2$ was changed chemically. In this material, it has been reported that the cationic redox reaction is dominant over the lithium concentration range of $0 < x < 0.4$, whereas the anionic redox reaction is dominant over the lithium concentration range of $0.4 < x < 1.2$ [3]. The change from the cationic to the anionic redox reaction at around x = 0.4 has also been confirmed by the spin magnetic moment obtained from magnetic Compton scattering studies [4].

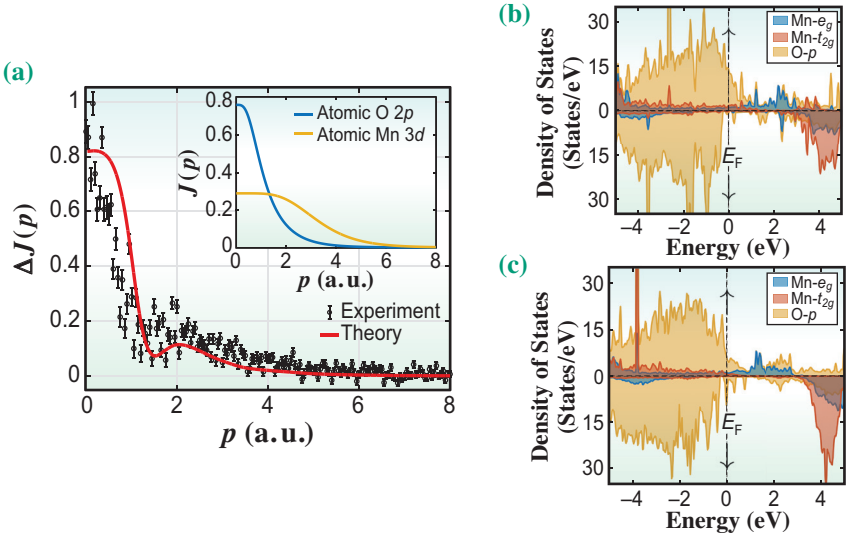

Fig. 1. **(a)** Difference Compton profiles between materials with lithium concentrations of x = 0.4 and 0.8. The solid line is a theoretical difference Compton profile obtained by the first-principles calculation. The inset shows theoretical Compton profiles of O 2*p* and Mn 3*d* orbitals obtained by atomic model calculation. **(b)** and **(c)** show spin-dependent partial densities of states for x = 0.4 and 0.8, respectively. The dashed line shows Fermi energy.

Figure 1(a) shows the difference Compton profile corresponding to the difference in the profiles of $Li_xTi_{0.4}Mn_{0.4}O_2$ with x = 0.8 and 0.4. The solid line in Fig. 1 is the theoretical difference Compton profile obtained by the first-principles density functional theory (DFT)-based modeling of lithium-rich battery materials. The comparison of the experimental and theoretical difference Compton profiles reveals the presence of O 2*p* anionic states in the range of electron momentum $p_z < 2$ atomic units. The long tail in the difference Compton profiles can be explained by the transfer of about 0.19 of Mn 3*d* electrons from the delocalized to localized 3*d* states. This localization is caused by the Coulomb repulsion between an occupied state at the O site and the 3*d* states in the neighboring Mn ions, without the formation of a substantial covalent bond. Therefore, the O 2*p* orbital appears to be orphaned [5]. Figures 1(b) and 1(c) show the spin-dependent partial densities of states (PDOSs) associated with Mn e_g, Mn t_{2g}, and O *p* orbitals for x = 0.4 and 0.8, respectively. The PDOS for x = 0.4 shows the presence of a peak of a localized hole state right above the Fermi level, as shown in Fig. 1(b).

Figure 2(a) shows two-dimensional electron momentum densities (2D-EMDs) for the redox orbitals, which are one-dimensional integrals along a crystallographic axis of the three-dimensional EMD. The features in Fig. 2(a) reveal the presence of repulsive Coulomb (nonbonding) interactions between the O 2*p* and Mn t_{2g} orbitals. A weak π-type antibonding interaction exists between the O 2*p* and Mn t_{2g} orbitals, as shown in the left-side diagram in Fig. 2. Sharp box-like features (colored light blue) in the high-momentum region are associated with Fermi surface breaks related to the t_{2g} band. In contrast, the repulsive Coulomb interaction produces a substantial delocalization of O 2*p* orbitals in momentum space (or localization in real space) in comparison with the redox orbital in the spinel material $Li_xMn_2O_4$ (Fig. 2(b)). In the spinel case, the O 2*p* orbitals are modified by the covalent bond involving the e_g states on the Mn atoms, which induces them to localize in momentum space (or to delocalize in real space). The visualization of the interaction between the O 2*p* and transition metal t_{2g} electrons to estimate the number of electrons displaced by the Coulomb interaction provides useful descriptors for designing stable, high-capacity oxygen-redox electrode materials. Our study enables the direct visualization of the orbitals involved in the anionic redox processes and offers quantitative analyses based on new descriptors derived from the electron momentum density.

In this study, we revealed the anionic redox mechanism and visualized the nonbonding O 2*p* redox orbital in a lithium-rich battery material, $Li_xTi_{0.4}Mn_{0.4}O_2$, by combining high-energy X-ray Compton measurements and first-principles calculations. The obtained results are based on the bulk sensitivity of Compton scattering technique using high-energy synchrotron X-rays. A detailed understanding of the redox mechanism on an atomic scale will pave the way to improving existing battery materials and designing new ones.

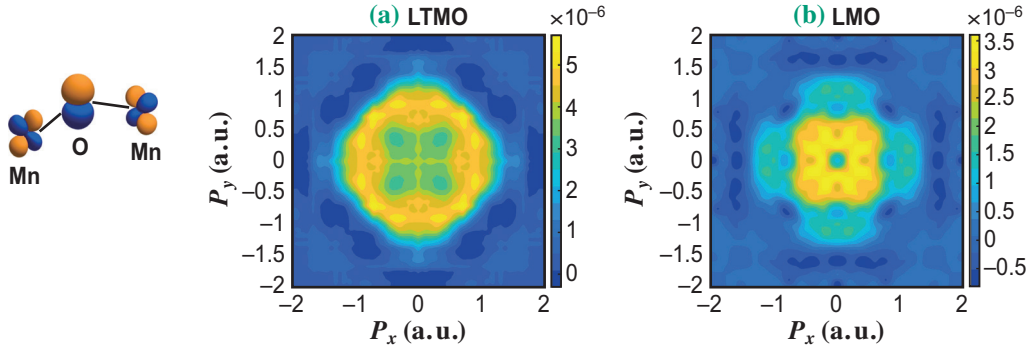

Fig. 2. **(a)** Reconstructed electron momentum density map of the O 2*p* orbital in $Li_xTi_{0.4}Mn_{0.4}O_2$ with x = 0.8 and 0.4. **(b)** Reconstructed electron momentum density map of the O 2*p* orbital in $Li_xMn_2O_4$ with x = 1.079 and 0.496. The left-side diagram shows O 2*p* and Mn t_{2g} orbitals. A weak π-type antibonding interaction exists between the O 2*p* and Mn t_{2g} orbitals, and this interaction causes the nonbonding O 2*p* state in (a).

Kosuke Suzuki[a,*] and Hasnain Hafiz[b]

[a] Graduate School of Science and Technology, Gunma University
[b] Department of Mechanical Engineering, Carnegie Mellon University, USA

*Email: kosuzuki@gunma-u.ac.jp

References

[1] G. Assat *et al.*: Nat. Energy **3** (2018) 373.
[2] *H. Hafiz, K. Suzuki, B. Barbiellini, N. Tsuji, N. Yabuuchi, K. Yamamoto, Y. Orikasa, Y. Uchimoto, Y. Sakurai, H. Sakurai, A. Bansil, V. Viswanathan.: Nature **594** (2021) 213.*
[3] N. Yabuuchi *et al.*: Nat. Commun. **7** (2016) 13814.
[4] K. Suzuki *et al.*: Condens. Matter **7** (2022) 4.
[5] M. Okubo *et al.*: ACS Appl. Mater. Interfaces **9** (2017) 36463.

Probing spin-polarized electronic structures of half-metallic Heusler alloys using resonant inelastic soft X-ray scattering in a magnetic field

Toward the next-generation spintronics application using the spin degrees of freedom, it is essential to optimize the spin-polarized electronic structures of magnetic materials under *operando* conditions in magnetic fields. In particular, the spin polarization in the vicinity of the Fermi level (E_F) for the conducting electrons and the size of the spin-dependent band gap are key parameters to designing functional devices. However, it was not straightforward to probe the spin-polarized electronic structures of the buried magnetic systems using the *standard* spin-polarized photoemission technique, which is rather surface-sensitive, since the magnetic layers are usually covered by capping layers in the device.

Resonant inelastic X-ray scattering (RIXS) is a photon-in/photon-out spectroscopy technique using a high-brilliance synchrotron light source to probe the electronic structures of any kind of specimens such as metal, insulator, liquid, and gas phases in an element-specific manner by tuning the incoming photon energy to the core-level absorption edges. Moreover, it is possible to apply any external perturbation, such as a magnetic field, during the measurements. This gives the great advantage of enabling the probing of the buried electronic states under the *operando* conditions for the active magnetic layers in the device structures.

Recently, we established a versatile experimental technique to study the spin-polarized electronic structures of the magnetic materials by RIXS at the transition metal (TM) $2p_{3/2}$ absorption edges in an external magnetic field [1-3]. The effective magnetic field of the TM 3*d* states yields the spin-polarized 2*p* core states due to the effective Zeeman splitting, as shown in Fig. 1, and thus the magnetic circular dichroism (MCD) in the RIXS spectra can probe the spin-polarized electronic structures owing to the strong selection rule of the dipole-allowed transition between the core-level 2*p* states and the 3*d* states for the circularly polarized light.

We utilized this technique to probe the spin-polarized electronic structures of half-metallic Heusler alloys [2,3] in which one of the spin subbands is metallic and the other is semiconducting with a band gap, as illustrated in Fig. 1 [4]. To investigate the intrinsic electronic structures, we measured high-quality single-crystalline samples of ferromagnetic Co_2MnSi and ferrimagnetic Mn_2VAl. The experiments were performed at SPring-8 **BL07LSU** HORNET end-station, where linear and circular polarizations are available. Moreover, the beam position and energy resolution do not change upon polarization switching in BL07LSU, and thus the switching technique is suitable for MCD experiments. In addition, a compact magnetic circuit with an external magnetic field of 0.25 T is installed for RIXS-MCD measurements, as shown in Fig. 2 [1].

Figures 3(a) and 3(b) respectively show the photon energy dependence of the RIXS spectra at the Co and Mn $2p_{3/2}$ edges for Co_2MnSi. The fluorescence components, which shift linearly with increasing incoming photon energy, are dominant for both edges. The fluorescence signals in the RIXS spectra on Co_2MnSi occur at around 1.0 eV for Co and 1.5 eV for Mn away from the elastic line, as shown in Figs. 3(a) and 3(b), respectively. This suggests that the partial density of states (PDOS) differs between the Co and Mn 3*d* states in Co_2MnSi. On the other hand, the fluorescence signals in the RIXS on Mn_2VAl branch off from the elastic line, as shown in Fig. 3(c), indicating the difference in Mn 3*d* PDOS between the two materials [2-4].

Figure 3(d) shows the Co $2p_{3/2}$ RIXS-MCD spectra for Co_2MnSi with a clear MCD contrast, which are attributed to the spin-polarized electronic structures of the Co 3*d* states. The *dd* excitation around 1.5 eV is observed at around 778 eV, indicating that the Co 3*d* states on the unoccupied side are rather localized.

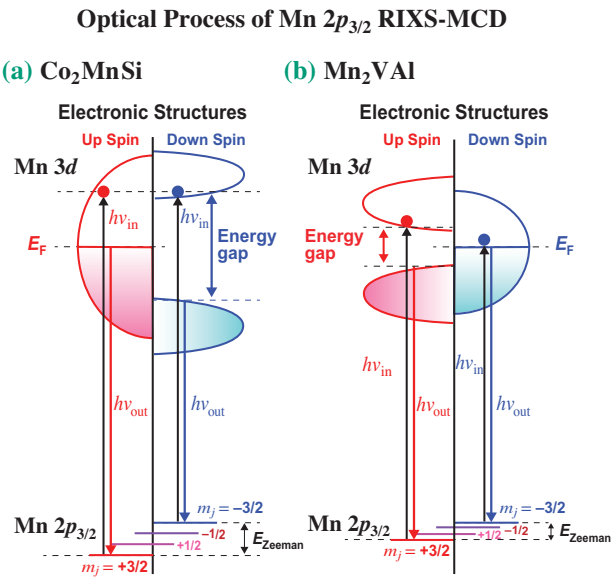

Fig. 1. Optical process of Mn $2p_{3/2}$ RIXS-MCD and the electronic structures of **(a)** Co_2MnSi and **(b)** Mn_2VAl.

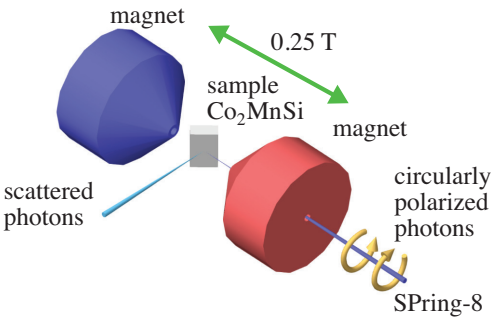

Fig. 2. Geometry of the RIXS-MCD measurements in an external magnetic field.

Moreover, the negative MCD signals (blue), which are mainly due to the Co $2p_{m_j=-3/2}$ states, reflect the down-spin components of the Co 3*d* states. Therefore, the gap structures between the elastic line and the *dd* excitation consist of the band gap of the Co 3*d* down-spin states. On the other hand, the positive MCD signals (red), originating mainly from the Co $2p_{m_j=+3/2}$ states, show the up-spin components. Interestingly, the positive MCD components are observed in the down-spin gap (green downward arrow), indicating the half-metallic electronic structures of the Co 3*d* states.

Figures 3(e) and 3(f) display the Mn $2p_{3/2}$ RIXS-MCD spectra for Co_2MnSi and Mn_2VAl. The distinct MCD contrasts indicate the high spin polarization of the Mn 3*d* states in both cases. The RIXS-MCD spectra for Co_2MnSi show the negative fluorescence MCD with the energy gap from the elastic line, reflecting the down-spin gap of the half-metallic electronic structures of the Mn 3*d* states shown in Fig. 1(a). On the other hand, the negative RIXS-MCD signals in Mn_2VAl are observed in the vicinity of the elastic line, suggesting that the down-spin states contribute to E_F. This is consistent with the predicted electronic structures of Mn_2VAl, in which the half-metallic gap opens the up-spin side, as shown in Fig. 1(b) [2,4,5]. Therefore, RIXS-MCD allows us to reveal which spin subband opens the half-metallic gap, providing important information for designing functional spintronic devices.

By utilizing RIXS-MCD, it will be possible to analyze the density of spin-polarized carriers induced at the buried interface of heterojunctions or magnetic layers under *operando* conditions. RIXS-MCD is a promising tool for probing useful information for designing spintronics devices.

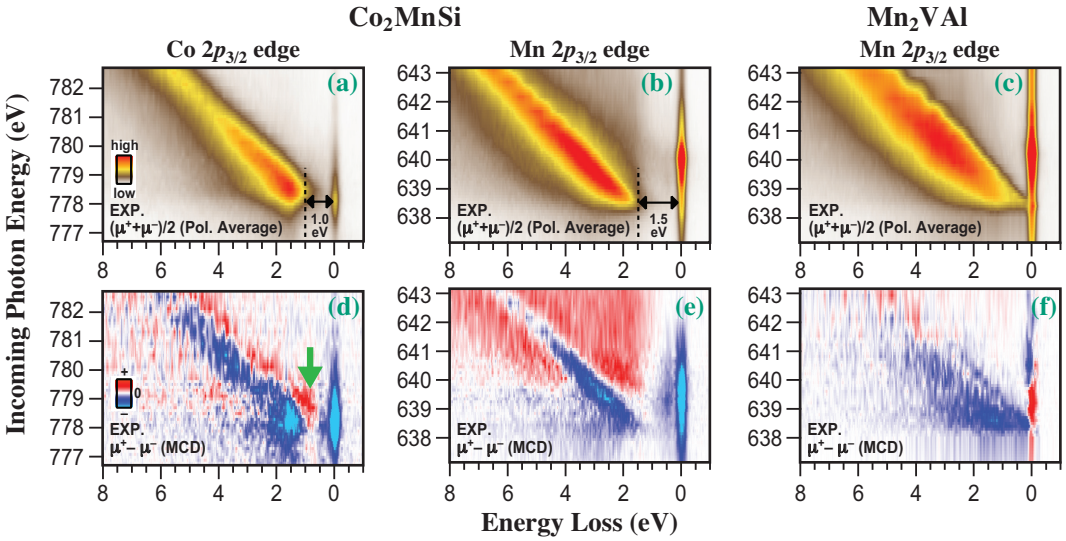

Fig. 3. Photon energy dependence of RIXSMCD spectra at the **(a)** Co and **(b)** Mn $2p_{3/2}$ edges for Co_2MnSi and the **(c)** Mn $2p_{3/2}$ edge for Mn_2VAl. Those RIXS-MCD spectra are plotted in **(d)**–**(f)**, respectively.

Hidenori Fujiwara[a,*] and Rie Y. Umetsu[b]

[a] Division of Materials Physics, Osaka University
[b] Institute for Materials Research, Tohoku University

*Email: fujiwara@mp.es.osaka-u.ac.jp

References

[1] J. Miyawaki *et al.*: J. Synchrotron Rad. **24** (2017) 449.
[2] R.Y. Umetsu *et al.*: Phys. Rev. B **99** (2019) 134414.
[3] *H. Fujiwara, R.Y. Umetsu, F. Kuroda, J. Miyawaki, T. Kashiuchi, K. Nishimoto, K. Nagai, A. Sekiyama, A. Irizawa, Y. Takeda, Y. Saitoh, T. Oguchi, Y. Harada, S. Suga: Sci. Rep.* ***11*** *(2021) 18654.*
[4] S. Ishida *et al.*: J. Phys. Soc. Jpn., **53** (1984) 2718.
[5] K. Nagai *et al.*: Phys. Rev. B **97** (2018) 035143.

Probing spin-resolved valence band electronic structures of buried Fe film with hard X-ray photoemission

Photoemission spectroscopy (PES), which is a powerful tool for investigating the electronic structures of solids, has been performed using various excitation light sources in a wide photon energy range from several eV to ~15 keV. In particular, hard X-ray PES (HAXPES: photon energy > ~3 keV) is recognized as one of the most powerful methods for detecting the bulk and buried interface electronic states of materials owing to the large inelastic mean free path (IMFP) of electrons with a kinetic energy of several keV [1]. The IMFP in HAXPES experiments is several nm, which is larger than that in soft X-ray PES (~1 nm). In contrast, the photoionization cross section for the hard X-ray region is ~2–4 orders of magnitude lower than that for the soft X-ray region. Therefore, high-brilliance hard X-rays from undulators at third-generation synchrotron facilities such as SPring-8 and the optimization of the experimental geometry are required to conduct the HAXPES experiments with a total energy resolution better than 0.3 eV [1,2]. To date, X-ray polarization-dependent HAXPES for linear or circular dichroism, angle-resolved HAXPES for band dispersions, and X-ray standing-wave HAXPES for depth profiling have been realized through the development of X-ray optics and electron analyzers as well as synchrotron light sources [1]. Although spin-resolved HAXPES is expected to be suitable for studying the bulk-sensitive spin-dependent electronic structures of magnetic materials, it is still difficult to access the spin resolution in the valence band region by HAXPES owing to two unfavorable aspects: (i) small photoionization cross section in valence electrons and (ii) low efficiency of a typical spin detector such as a Mott detector [3]. To realize spin-resolved HAXPES in the valence band region, we have developed an ultracompact Mott-type Au spin filter to conduct spin-resolved HAXPES measurements without modifying the HAXPES apparatus [4]. This ultracompact spin filter can be mounted on a sample holder, as shown in Fig. 1(a). The compact sample holder with the spin filter can be easily adapted to the existing HAXPES apparatus without modifying the apparatus. Figure 1(b) shows a schematic illustration of the experimental setup of our proposed spin-resolved HAXPES [4]. The scattering induced by the Au spin filter involves Mott scattering [3], and the Au spin filter partially selects electrons with one spin direction in the geometry shown in Fig. 1(b). To detect electrons with the opposite spin direction, magnetization reversal is necessary [4]. Although magnetization reversal of the sample is essentially required in this method, we can utilize the advantage of two-dimensional (2D) multichannel detection, which enhances the electron detection efficiency, used in a recent high-resolution electron analyzer.

The spin-resolved HAXPES measurements were performed at SPring-8 **BL15XU**. The sample used for spin-resolved HAXPES was a MgO(2 nm)-capped epitaxial Fe(30 nm) film on a MgO(001) substrate. The photon energy and total energy resolution were set to 5.95 keV and 0.68 eV, respectively. Note that the single-channel figure of merit (FOM) in this spin-resolved HAXPES with the geometry shown in Fig. 1(b) was evaluated to be $\sim 2 \times 10^{-4}$ when the effective Sherman function (S_{eff}) of –0.07 was

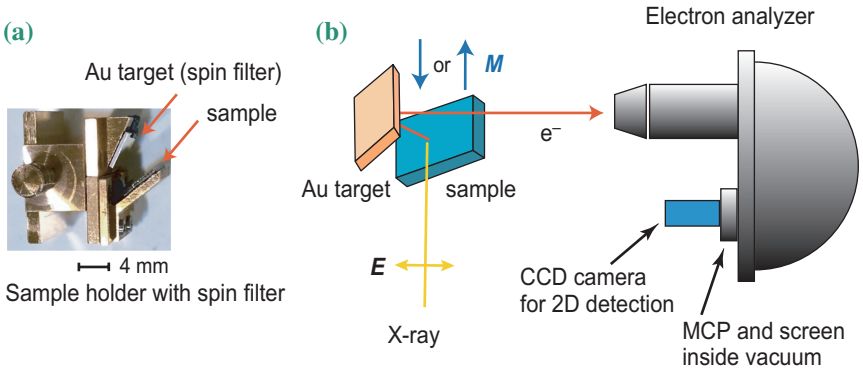

Fig. 1. **(a)** Photo of the sample holder, which can mount both thin films of the sample and Au target simultaneously. **(b)** Schematic illustration of the experimental geometry of spin-resolved HAXPES in this work. The photoelectrons emitted from the sample scattered by the Au target are introduced into the electron analyzer. The scattering angle of photoelectrons by the Au target is 127±7°. The magnetization direction (***M***) is indicated by arrows. The incident angle of X-rays is set to about 5° with respect to the sample surface and ***M***.

adopted [4]. This value is comparable to that of the typical Mott detector [3]. Since we can utilize the 2D multichannel detector in spin-resolved HAXPES, the effective FOM is enhanced by a factor of ~4×10^4, which is the number of active channels in the 2D detector, in comparison with the case when only one channel of the 2D detector is used. Note that the spin polarization (P), majority (I_{maj}), and minority (I_{min}) spin spectra are obtained by using the measured spectra (I^+ and I^-) with two magnetization directions shown in Fig. 1(b) as follows: $P = (I^+ - I^-)/(I^+ + I^-)/S_{eff}$, $I_{maj} = (I^+ + I^-)(1+P)/2$, and $I_{maj} = (I^+ + I^-)(1-P)/2$.

Figure 2(a) shows the experimental spin-resolved valence band HAXPES spectra of the buried Fe film. Although the energy resolution in spin-resolved HAXPES (0.68 eV) is lower than that in standard (spin-integrated) HAXPES (<0.3 eV), the spin-resolved HAXPES spectra show a clear difference between the majority and minority spin spectral shapes. The sharp peak and broad structure were found in the majority spin states at the binding energy (E_B) of ~1 and ~4 eV, respectively. In contrast, fine structures were not found in the minority spin states. The background intensity on the high E_B side differed between the majority and minority spin states owing to the spin-polarized secondary electrons. By comparing the experimental spectra with the spin-resolved partial densities of states (DOSs) obtained by density functional theory (DFT) calculation [5], we see that the sharp peak and broad structure arise from the Fe 3*d* and 4*s* majority spin states, respectively. In contrast, the Fe 3*d* minority spin states are located near the 4*s* minority spin states, so that the minority spin spectrum shows the broad structure due to the low energy resolution. Note that the Fe 4*s* states are emphasized in the observed HAXPES spectra owing to the characteristic large photoionization cross-sectional ratio of Fe 4*s* to 3*d* in HAXPES [5]. Figure 2(b) shows the spin polarization curve of the buried Fe film. The large spin polarizations at E_B of ~0 and ~5 eV are mainly due to the Fe 3*d* and 4*s* states, respectively. The spin polarization curve is reproduced by the calculated spin polarization obtained from the spin-resolved cross section weighted DOSs, except for the energy scale of E_B. Even though the energy resolution is low in the present spin-resolved HAXPES, the spin resolution allows us to detect the deviation between experiments and calculations, which is caused by bandwidth narrowing due to the strong electron correlation effects in Fe [4,5].

Owing to the high-brilliance hard X-rays at SPring-8 and the 2D multichannel detection of the electron analyzer, we have successfully observed the bulk-sensitive valence band spin-resolved HAXPES spectra for the buried Fe film. At the present stage, the energy resolution is low and the statistical error is large in spin-resolved HAXPES. Further development of spin-resolved HAXPES (effective FOM, energy resolution, and statistical error) is required to study genuine spin-resolved electronic states of advanced magnetic materials such as a half-metal, which shows unique spin-dependent electronic states (e.g., perfect spin polarization at the Fermi level).

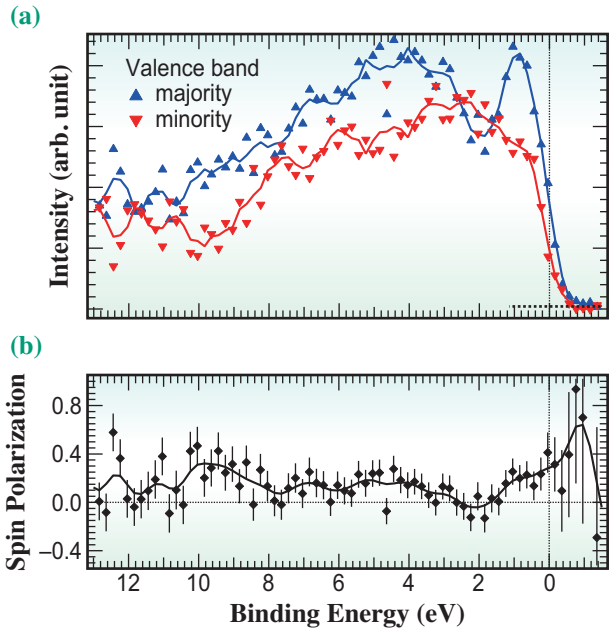

Fig. 2. **(a)** Spin-resolved valence band HAXPES spectra of the buried Fe film. **(b)** Spin polarization curve of the buried Fe film. Vertical bars represent statistical errors. The total data acquisition time is ~13 hours.

Shigenori Ueda

Research Center for Functional Materials,
National Institute for Materials Science

Email: UEDA.Shigenori@nims.go.jp

References

[1] C. Kalha *et al.*: J. Phys.: Condens. Matter **33** (2021) 233001.
[2] Y. Takata *et al.*: Nucl. Instrum. Methods Phys. Res., Sect. A **547** (2005) 50.
[3] K. Iori *et al.*: Rev. Sci. Instrum. **77** (2006) 013101.
[4] *S. Ueda and Y. Sakuraba: Sci. Technol. Adv. Mater.* ***22*** *(2021) 317.*
[5] S. Ueda and I. Hamada: J. Phys. Soc. Jpn. **86** (2017) 124706.

Dynamic nanoimaging of extended objects via hard X-ray multiple-shot coherent diffraction with projection illumination optics

The functional properties of materials and devices often depend on their spatially hierarchical structures ranging in size from micrometer to nanometer scale. Thus, there is increasing importance in the *in situ*/*operando* observation of their heterogeneous structures and structural changes during their operation. Coherent diffraction imaging (CDI) and its variants [1] in the hard X-ray regime are promising techniques for the nondestructive visualization of the internal structures of micrometer-thick objects at a nanometer-scale resolution owing to the short wavelength and high penetration depth. In CDI, a sample object is illuminated with spatially coherent X-rays, yielding Fraunhofer diffraction patterns, and then the spatial distribution of the complex refractive index of the object projected along the direction of the incident beam is reconstructed from the diffraction patterns via iterative phase retrieval (PR) calculation.

The measurement schemes of CDI are designed so that PR solution is efficiently constrained in real space. The local imaging of an extended object is achieved by a scanning variant of CDI, known as ptychography, where a set of diffraction patterns is collected such that illumination areas are sufficiently overlapped (Fig. 1(a)). In accordance with the constraints on the consistency of the object structures in the illumination-overlapped area (in real space) and the data fidelity to the Fourier magnitude of the exit wave (in reciprocal space), ptychographic PR reconstructs both the phase and absorption contrast image of the object together with the illumination wave field on the object. The "overlap constraint" yields the robust convergence of ptychographic PR, which greatly expands the application of ptychography [1]. However, the overlap constraint restricts the application to static objects. The overhead time included in the scanning measurement, which is typically 0.1–0.2 s per point, limits the temporal resolution of ptychography to several tens of seconds.

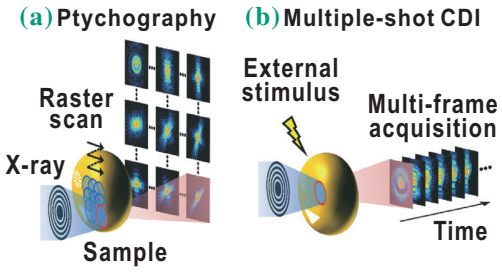

Fig. 1. Schematic illustration of ptychography **(a)** and multiple-shot CDI **(b)** experiments.

Therefore, nanometer-scale dynamics on the seconds to milliseconds time scale are still difficult to access in real space and are investigated by measurement in the reciprocal space such as by time-resolved small-angle X-ray scattering and X-ray photon correlation spectroscopy.

In this work, we develop multiple-shot CDI, an extension of CDI to dynamic nanoimaging, and demonstrate, with numerical simulations and a proof-of-concept experiment at SPring-8 **BL24XU**, that the proposed method is capable of achieving temporal resolutions of 10–100 ms, which is ~100 times faster than that of ptychography [2]. Figure 1(b) shows the experimental setup of multiple-shot CDI, where a movie of local structural changes in an object is reconstructed from a set of time-evolving diffraction patterns. The multiple-shot CDI system also allows the complementary use of ptychography, where the two methods can be switched by changing the measurement scheme (Fig. 1). The development includes a multiframe PR algorithm dedicated to a video reconstruction of a dynamic object

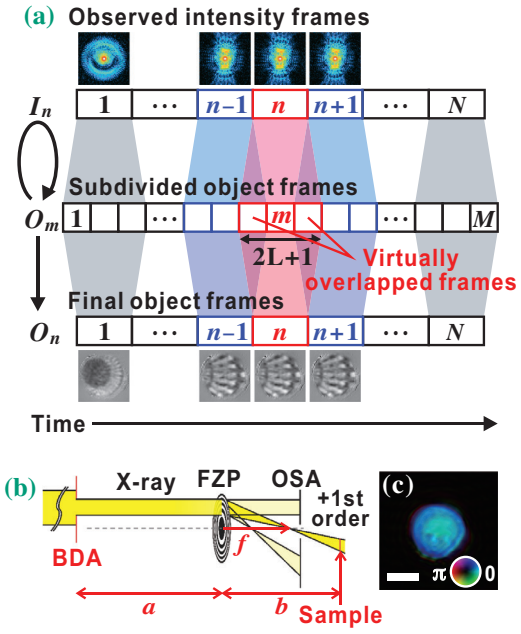

Fig. 2. Key developments in multiple-shot CDI. **(a)** Schematic illustration representing multiframe PR. Correspondences among the observed intensity frames I_n, numerically subdivided object frames O_m, and actual object frames O_n are shown. **(b)** Projection illumination optics. BDA beam-defining aperture, FZP Fresnel zone plate, OSA order-sorting aperture. BDA, FZP, and Sample are arranged in accordance with the thin lens formula $\frac{1}{a}+\frac{1}{b}=\frac{1}{f}$. **(c)** Illumination beam generated with projection illumination optics. Experimentally measured by ptychography. The scale bar indicates 1 μm.

and projection illumination optics for the generation of a top-hat-intensity beam to enhance the convergence of the proposed algorithm.

The key concepts of the proposed algorithm are illustrated in Fig. 2(a). (1) For a dynamic object, the diffraction pattern will change continuously even during a single-frame exposure, but previously, this was not taken into account. In the proposed algorithm, each frame of the object movie is divided into subframes, and each frame of measured diffraction patterns is represented as a sum of patterns calculated from the object subframes. (2) In real space, it is expected that the structural changes of the object will be smooth in both spatial and temporal dimensions. Thus, we introduced two types of spatiotemporal smoothness constraint. First, each object subframe between two adjacent measured frames is constrained by both frames to ensure temporal smoothness. Second, we applied the total variation regularization [3] along both the spatial and temporal directions. The total variation regularization restricts the spatiotemporal gradient of the object to be small, and thus, it facilitates the convergence of the object to the spatiotemporally smooth solution.

Illumination uniformity is also critical for multiframe PR. The main lobe of the conventional focused beam shows a Gaussian-like intensity profile, which causes the slow recovery of the object periphery because of the dim illumination and prevents the convergence to the optimum solution. We generated the top-hat-intensity beam by developing the projection illumination optics employing a zone plate as an imaging lens (Fig. 2(b)). Here, a beam-defining aperture is illuminated with a spatially coherent X-ray, and a real image of the aperture is formed on the sample with size reduction. Figure 2(c) shows an illumination beam generated by the proposed optics with 12.5-fold reduction, which was experimentally measured by ptychography. The generation of a nearly uniform illumination beam with a well-defined boundary is demonstrated.

We constructed a multiple-shot CDI system at BL24XU. First, the performance of multiple-shot CDI was investigated with numerical simulations based on the experiment at the photon energy of 8 keV. Brownian motions of colloidal gold particles were calculated with a time step of 1 ms and various diffusion coefficient values, yielding Brownian motions with root mean square displacements (RMSDs) ranging from 0.16 to 3.22 pixels/10 ms. The largest RMSD was ~30% of the particle size. Time-evolving diffraction patterns were simulated at a frame time of 10 ms, and real-space movies were reconstructed from the datasets. Compared with the conventional PR algorithm, the proposed algorithm markedly improves the reproducibility of the object. The fastest Brownian motion was also reconstructed with the twofold deterioration of spatial resolution, even though their diffraction patterns are blurred owing to accumulation over the frame time. This result indicates the robustness of the proposed method. Figure 3 shows the results of the proof-of-concept experiment, where a resolution test chart made of 500-nm-thick tantalum was continuously moved at a speed of 125 nm/s and imaged at a frame time of 100 ms via multiple-shot CDI. On average, ~79 nm lines and spaces are resolved in each frame. These results demonstrate the feasibility of visualizing dynamic phenomena, including those difficult to understand in reciprocal space, at temporal resolutions of 10–100 ms. It is also expected that the use of a partially coherent beam and/or an upcoming next-generation synchrotron radiation source will increase the spatiotemporal resolution. We expect that the proposed method will contribute to the understanding of the dynamical properties of heterogeneous systems in the materials and biological sciences and industry.

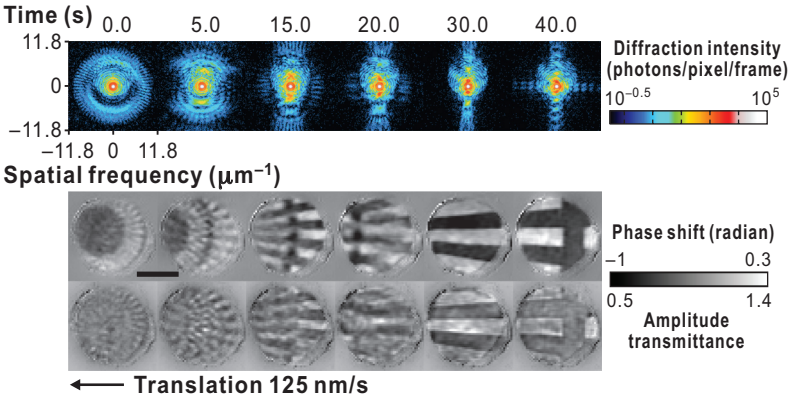

Fig. 3. Proof-of-concept experiment of multiple-shot CDI. The selected frames of the observed diffraction patterns (upper) and corresponding reconstructed frames of the phase (middle) and absorption (lower) images of the object are shown. . The scale bar indicates 1 μm.

Yuki Takayama[a,b,c,*] and Yasushi Kagoshima[a,b]

[a] Graduate School of Science, University of Hyogo
[b] Synchrotron Radiation Research Center, Hyogo Science and Technology Association
[c] RIKEN SPring-8 Center

*Email: takayama@sci.u-hyogo.ac.jp

References

[1] F. Pfeiffer: Nat. Photon. **12** (2018) 9.
[2] *Y. Takayama, K. Fukuda, M. Kawashima, Y. Aoi, D. Shigematsu, T. Akada, T. Ikeda, and Y. Kagoshima: Commun. Phys. **4** (2021) 48.*
[3] A. Chambolle: J. Math. Imag. Vis. **20** (2004) 89.

Observation of magnetic octupole order producing anomalous Hall effect by X-ray magnetic circular dichroism

The anomalous Hall and thermoelectric (Nernst) effects in magnetic materials have recently been attracting considerable attention because of their potential applications to spintronics, energy harvesting, and magnetic sensing, for example. Thus far, these functionalities have mostly been studied in ferromagnets since it might be considered that large uniform magnetization is necessary to produce strong effects. On the other hand, large anomalous Hall and Nernst effects have recently been found in an antiferromagnetic metal, Mn_3Sn [1]. Mn_3Sn has a two-dimensional kagome lattice, and the total magnetization is vanishingly small (~0.002 μ_B/Mn) owing to the triangular antiferromagnetic spin structure, as shown in Fig. 1(a). Therefore, the mechanism of these large responses is expected to be completely different from that of conventional ferromagnets, where the magnitude of anomalous Hall effect is roughly proportional to the magnetization. The origin of anomalous Hall effect is currently understood to be a novel type of order parameter called the cluster magnetic octupole, that, in principle, breaks time reversal symmetry (TRS) without net magnetization [2]. However, the presence of magnetic octupole order has not been well established because of the lack of a suitable experimental approach. To solve this problem, we have applied X-ray magnetic circular dichroism (XMCD) to Mn_3Sn, since the circularly polarized X-ray can generally couple with the TRS-broken order [3]. Indeed, recent theoretical studies [4,5] indicate the detection of the XMCD signal in a triangular antiferromagnet such as Mn_3Sn through the magnetic dipole term called the T_z term.

Figure 1(a) shows a schematic of the experimental setup for XMCD measurement. The experiment was performed at SPring-8 **BL25SU**. The right and left circularly polarized X-ray beams are irradiated to the (0001) plane of the crystal. The angle between the magnetic field and the (0001) plane is defined as θ. The direction of the X-ray beam is tilted 10 more degrees from the field direction. Figure 1(b) shows the typical XMCD and XAS spectra of Mn_3Sn for $B = 1$ T and $T = 300$ K. As can be seen in the figure, clear positive and negative XMCD signals were observed at L_3 and L_2 edges, and this feature is indeed opposite to those of conventional ferromagnetic Mn compounds, where the XMCD signal is negative and positive for L_3 and L_2 edges, respectively. The observed XAS shows broad absorption peaks similarly to the other Mn metallic compounds, indicating the formation of a dispersive itinerant band of Mn *d* orbitals.

The main panel of Fig. 2 shows the field orientation dependence of XMCD for B = 1 T. As can be seen in the figure, the signal intensity is anisotropic. Since the anisotropy of magnetization with B = 1 T is small (see the right inset), the intensity variation of XMCD cannot be explained by the magnetization anisotropy. The left inset of Fig. 2 shows the XMCD spectrum for B = 0 T, i.e., the residual spontaneous component. The intensity and shape of this XMCD spectrum are mostly identical to those for B = 1 T, and this feature also cannot be explained by the magnetization process, where the magnetization increases about 4-fold between 0 and 1 T with a linear slope, as shown in the right inset. These features clearly show that the present XMCD is decoupled from the magnetization behavior, indicating that the origin of the present XMCD is completely different from that of the conventional XMCD, in which the XMCD response is proportional to the static magnetization.

To reveal the origin of the present XMCD signal, we performed a theoretical calculation of the XMCD spectrum (Figs. 3(a)-(d)). Thick blue lines show the total XMCD signal, and thin magenta, light green, and orange lines correspond to individual XMCD contributions from spin sublattices A, B, and C, respectively. In Fig. 3(a), a clear XMCD signal appears even though the total

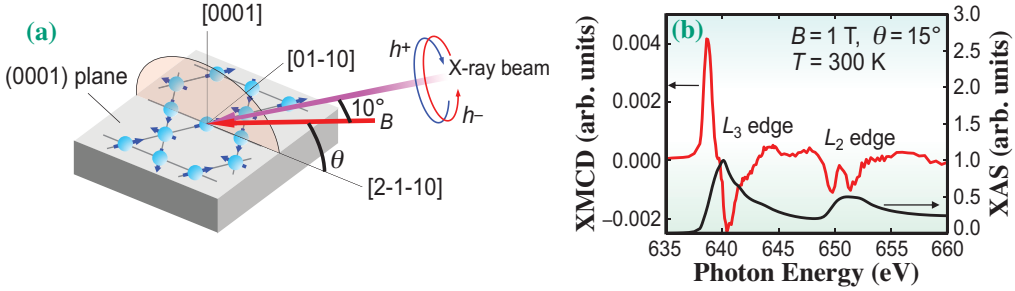

Fig. 1. **(a)** Schematic of experimental setup of XMCD measurement. **(b)** Typical XMCD (left axis) and XAS (right axis) spectra of Mn_3Sn for B = 1 T (θ = 15°) and T = 300 K. [3]

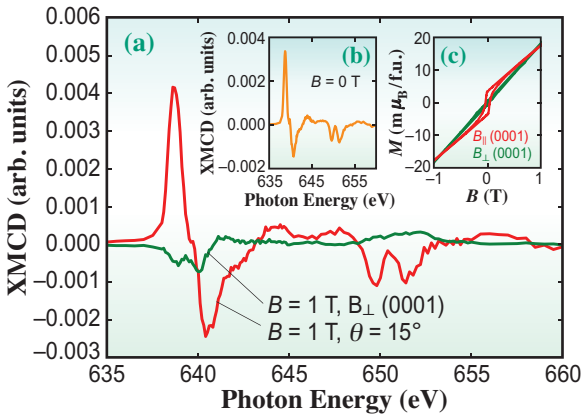

Fig. 2. **(a)** Magnetic field orientation dependence of XMCD signal. Both spectra are measured at 1 T. **(b)** XMCD spectrum for B = 0 T. **(c)** Field orientation dependence of magnetization curve. [3]

spin moment is zero. On the other hand, in Fig. 3(b), individual XMCD contributions compensate each other and the total XMCD is zero. Although the two magnetic structures in Figs. 3(a) and 3(b) have a triangular antiferromagnetic structure, the difference is the sign of spin chirality, i.e., the rotation direction of spin moment. For the inset of Fig. 3(a), the spin moment rotates counterclockwise (–120°) when the position of spin is changed on the triangular Mn sites clockwise as A to C. In this case, the spin chirality is negative. On the other hand, in Fig. 3(b), the spin direction is clockwise (+120°) for the same operation, i.e., the spin chirality is positive. Importantly, from the group theory consideration, the TRS-broken cluster magnetic octupole only appears when the spin chirality is negative [2]. Thus, our model calculation shows the complete correspondence between the appearance of XMCD and the cluster octupole order. Note that the magnetic structure shown in Fig. 3(a) is realized in Mn_3Sn, while that in Fig. 3(b) is a fictitious magnetic structure for comparison.

The additional model calculations (Figs. 3(c) and 3(d)) also show that the unconventional XMCD behavior observed in the experiment (field-strength-independent in-plane XMCD signal, and different spectral signs and shapes between parallel and perpendicular field directions) can be reproduced by our model. Figure 3(c) shows the calculated XMCD for the in-plane field configuration with a slight in-plane magnetic moment of ~18 $m\mu_B$ corresponding to $B_{\parallel} \approx 1$ T. The spectral shape and intensity are mostly identical for B = 0 T. This means that the origin of the present XMCD is not the field-induced moment, but the inverse triangular magnetic structure itself, which is mostly preserved in such a weak field region as shown in the inset. When the magnetic field is perpendicular to the kagome plane (Fig. 3(d)), a weak XMCD signal from a paramagnetic contribution due to spin canting was expected, and this is also consistent with the experimental observation.

In summary, we have demonstrated that the unconventional XMCD in Mn_3Sn arises from the inverse triangular antiferromagnetic structure characterized by the TRS-broken cluster magnetic octupole order. Although the XMCD detection of the magnetic octupole moment was predicted theoretically, our experimental observation shows the efficiency of XMCD in detecting ferroic higher-rank multipole order. This result may increase the variety of applicable targets of X-ray magnetic spectroscopy.

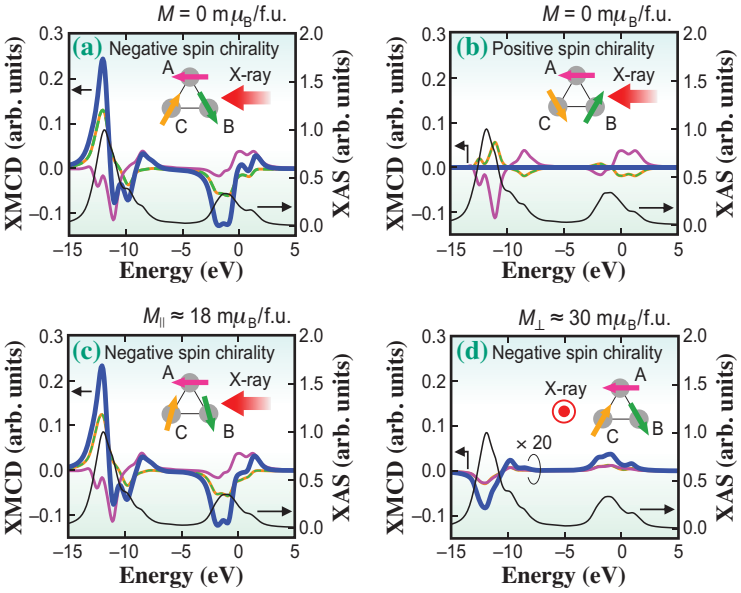

Fig. 3. Calculated XMCDs for different field and X-ray configurations. **(a,b)** Spin chirality dependence of XMCD signal. **(c,d)** Calculated XMCDs for parallel and perpendicular field (and X-ray) configurations, respectively. [3]

Motoi Kimata[a,*], Norimasa Sasabe[b] and Tetsuya Nakamura[a,b]

[a] Institute for Materials Research, Tohoku University
[b] Japan Synchrotron Radiation Research Institute (JASRI)

*Email: motoi.kimata.b4@tohoku.ac.jp

References

[1] S. Nakatsuji *et al.*: Nature **527** (2015) 212.
[2] M.-T. Suzuki *et al.*: Phys. Rev. B **95** (2017) 094406.
[3] *M. Kimata, N. Sasabe, K. Kurita, Y. Yamasaki, C. Tabata, Y. Yokoyama, Y. Kotani, M. Ikhlas, T. Tomita, K. Amemiya, H. Nojiri, S. Nakatsuji, T. Koretsune, H. Nakao, T.-H. Arima, and T. Nakamura: Nat. Commun.* ***12*** *(2021) 5582.*
[4] Y. Yamasaki *et al.*: J. Phys. Soc. Jpn. **89** (2020) 083703.
[5] *N. Sasabe, M. Kimata and T. Nakamura: Phys. Rev. Lett. 126 (2021) 157402.*

Magnetic Friedel oscillation at Fe(001) surfaces: Direct observation by atomic-layer-resolved synchrotron radiation ^{57}Fe Mössbauer spectroscopy

A study of the surface and interface magnetism of 3*d* transition metals is of interest because of the essential role that magnetism plays in determining magnetic interactions and spin-transport properties of nanomagnets and magnetic heterojunctions. Over the past few decades, various techniques have advanced the studies on surface and interface magnetism. However, few experimental studies on the depth-dependent local magnetic structures of surfaces and interfaces at the atomic layer level have been carried out. This situation is a result of the difficulties encountered when performing depth-resolved studies at the uppermost surface of a metal, e.g., by scanning tunneling microscopy, or the signal arising from a relatively broad range of depth, e.g., in X-ray magnetic circular dichroism spectroscopy.

The surface magnetism of Fe(001) is a fascinating research subject for atomic-layer-resolution magnetic analysis. Theoretical studies predict 30% enhancement of the magnetic moment M_{Fe} at the surface and an oscillatory behavior with increasing depth in the individual layers, i.e., a magnetic Friedel oscillation [1]. As a relevant phenomenon, Ohnishi *et al.* theoretically predicted that hyperfine magnetic field H_{int} is reduced by 30% relative to the bulk value despite a significant increase in the surface M_{Fe} [2].

Recently, we have determined the layer-by-layer H_{int} of the Fe(001) surface by the *in situ* ^{57}Fe probe layer method with a high-brilliance synchrotron Mössbauer source [3]. In this method, a resonant isotope probe layer is embedded in a thin film prepared with a nonresonant isotope. The observed H_{int} at the nucleus provides details on the local surface magnetism.

An *in situ* measurement system was developed to observe the magnetic Friedel oscillations on the surface of Fe. It consists of a molecular beam epitaxy (MBE) chamber and an ultrahigh-vacuum measurement chamber (Fig. 1(a)). The latter chamber is equipped with a liquid helium flow cryostat and electromagnetic coils, which enables low-temperature measurements and polarized Mössbauer study using a magnetized thin film.

Fe(001) films were fabricated by alternately evaporating ^{56}Fe and ^{57}Fe from 99.94% iron-56 and 95.93% ^{57}Fe isotopic sources onto precleaned 10×10×0.5 mm^3 MgO(001) substrates under a vacuum pressure of approximately 10^{-8} Pa. A 0.8-ML-thick ^{57}Fe probe layer, t = 0.1 nm, was embedded to the depth of the N^{th} atomic layer, N = 1 to 4 and 7, below the surface. These samples are hereafter referred to as "N^{th} probe layer samples".

The experiments were performed at SPring-8 **BL11XU** using linearly π-polarized 14.4 keV Mössbauer γ-rays with a 15.4 neV bandwidth produced by a synchrotron Mössbauer source. The γ-ray beam was vertically focused by an elliptical mirror. The beam size was 15 μm(V)×1.6 mm(H) and the beam flux was about 2.9×10^4 photons/s. This beam was introduced into the measurement chamber to perform grazing incidence measurements (Fig. 1(b)).

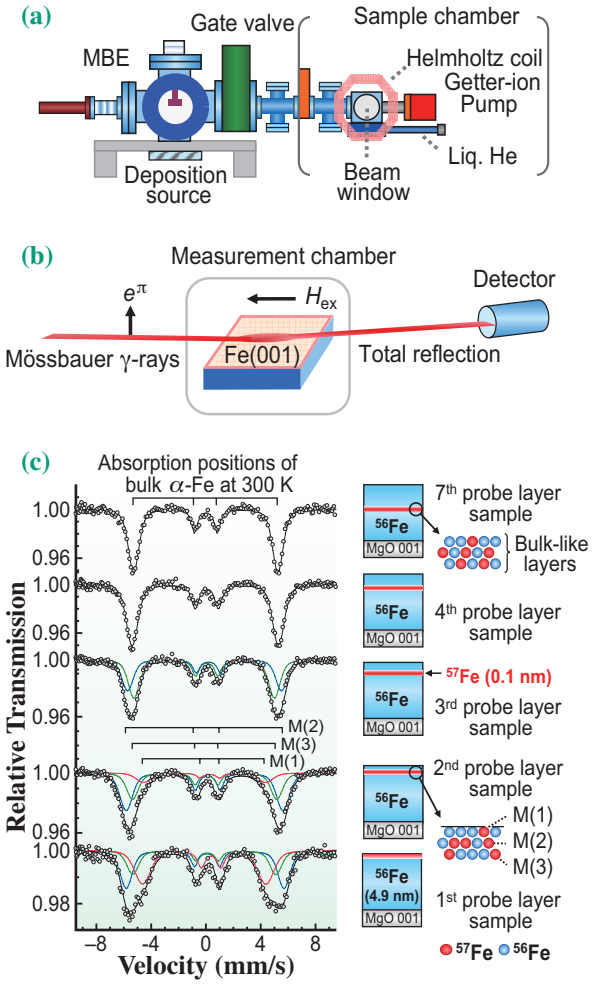

Fig. 1. **(a)** Experimental setup. H_{ex}: Magnetic field (300Oe). **(b)** Mössbauer spectra of the N^{th} probe layer samples measured at 300K. Black solid lines represent fitted curves. Red, blue, and green lines represent three different magnetic components. M(*i*) represents the magnetic component assigned to the ^{57}Fe atoms located in the *i*th layer below the surface.

An external field of 300 Oe was applied antiparallel to the beam direction to magnetize the Fe(001) film. In this arrangement, the π-polarized incident beam interacted with the four nuclear transitions of $\Delta m = \pm 1$. The Mössbauer absorption spectra were measured by collecting the totally reflected γ-rays from the sample surface at an incident angle of 0.1° with a reflectivity of about 80%. Each spectrum was obtained within a few hours of sample preparation. Such short-time measurements significantly reduced the residual gas absorption and oxidation on the Fe(001) surfaces.

Figure 1(c) shows the Mössbauer spectra of the N^{th} probe layer samples, N = 1 to 4 and 7, recorded at 300 K. All samples showed magnetically split Mössbauer patterns. The spectra of the first, second, and third probe layer samples exhibited complex profiles composed of different magnetic components [i.e., small H_{int} (red lines, around 28 T), large H_{int} (blue lines, around 36 T), and bulk-like H_{int} (green lines, around 32 T)].

The ideal probe layer in the sample was surrounded by finely distributed ^{57}Fe atoms, which stemmed from the random deposition and surface diffusion of iron atoms during the growth process. Figure 1(c) (right) shows a conceptual diagram. In this case, if the first, second, and third layers of the iron surface have different H_{int} values, the spectra should exhibit a complex profile with multiple components. On the basis of the systematic behavior of the three components, the small H_{int}, large H_{int}, and bulk-like H_{int} represented the intrinsic hyperfine fields for the first, second, and third layers from the surface, respectively. In contrast, the spectra of the fourth and seventh probe layer samples exhibited a single magnetic component with four absorption lines, even in the presence of finely distributed ^{57}Fe atoms. This is because the hyperfine fields of the neighboring layers in these depth regions are bulk-like, and the overlapping subspectra result in a simple absorption profile. The prominent subspectrum with the largest percent area in the N^{th} probe layer sample was assigned to the spectrum characterizing the ^{57}Fe atoms located in the N^{th} atomic layer from the surface.

The experimentally determined layer-by-layer H_{int} exhibited a marked decrease at the surface and an oscillatory decay toward the bulk value. This behavior was successfully reproduced by theoretical calculations (Fig. 2). The result provides the first experimental evidence for magnetic Friedel oscillations, which penetrate several layers from the Fe(001) surface. Theoretically, the oscillatory decay of H_{int} should be strongly coupled with the Friedel oscillation of M_{Fe}, which is caused by the surface electronic structure with a large spin imbalance and *d*-band narrowing [1-3]. A schematic diagram of the magnetic Friedel oscillations in M_{Fe} and H_{int} is shown in Fig. 3.

This study yielded a clear answer to the mystery of the surface magnetism of iron, which has been discussed since the 1980s. In the future, the *in situ* ^{57}Fe probe layer method with a synchrotron Mössbauer source should facilitate additional studies on the surface and interface magnetism in advanced magnetic and spintronic materials and devices.

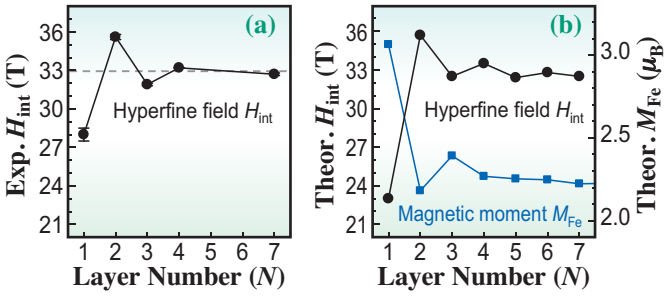

Fig. 2. Plots of the experimental and theoretical layer-by-layer H_{int} and M_{Fe}.

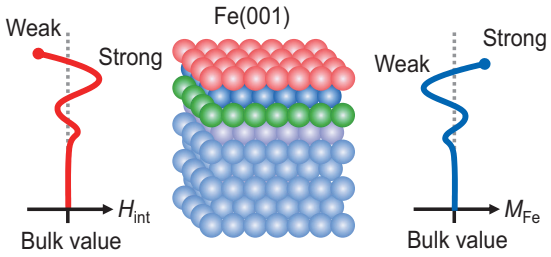

Fig. 3. Schematic diagram of the observed magnetic Friedel oscillation of Fe(001) surface.

Takaya Mitsui

Synchrotron Radiation Research Center, QST

Email: taka@spring8.or.jp

References

[1] C.S. Wang and A.J. Freeman: Phys. Rev. B **24** (1981) 4364.
[2] S. Ohnishi *et al.*: Phys. Rev. B **28** (1983) 6741.
[3] *T. Mitsui, S. Sakai, S. Li, T. Ueno, T. Watanuki, Y. Kobayashi, R. Masuda, M. Seto and H. Akai: Phys. Rev. B* ***125*** *(2020) 236806.*

Local lattice-plane orientation mapping of 6-inch GaN wafer using X-ray diffraction topography

X-ray diffraction topography (XRDT) has a long history. Many methods of XRDT were derived and modified in laboratories and in synchrotron X-ray facilities. Various books for understanding the methods and reviews of their historical developments, for example [1], can be found so we do not explain the details of XRDT here. Such XRDT techniques have been helpful for visualizing crystal imperfections such as extended defects, dislocations, and stacking faults. Accordingly, from an industrial viewpoint, the methods have provided feedback for improving the crystallinity, or crystal perfection, to develop silicon (Si), III-V, oxide, wide-bandgap crystals, and so on.

The authors proposed a modified XRDT method [2] to map local lattice-plane orientation, that is, to visualize the local lattice-plane shape of a whole wafer. The method records rocking curves around a Bragg condition from a whole wafer using a monochromatic and sufficiently large X-ray beam and an X-ray two-dimensional (2D) detector for two reflections without sample translation, enabling us to perform a simple measurement compared with one using a small beam and requiring sample translation. Many reports regarding synchrotron X-ray diffraction imaging have discussed sample crystallinity in terms of diffracted intensities, rocking-curve widths, and peak positions. A few research groups, however, have discussed the lattice-plane shape using rocking curves from selected sparse positions along several directions [3].

Applying the method to the visualization of a local lattice shape, our group has intensively studied c-plane 2-inch and 4-inch GaN wafers and an m-plane substrate as well as their homoepitaxial thin films. Several of our articles have been cited not only to introduce the results, but also to explain the concept behind our proposed method and the application limitations related to a local d spacing and a local lattice-plane curvature [4].

Next, we present the key point of the concept. We use center angular positions of rocking curves from many positions on a sample surface with a 2D detector and evaluate local deviation angles on two respective diffraction planes. Local reciprocal-lattice (q) vectors for respective sample surface positions are evaluated using the deviation angles via the rotation matrix.

Let us also introduce an example of information obtained from the 4-inch wafer. The q vector components evaluated from the two rocking-curve images at different azimuthal angles combined with the rotation matrix revealed that overall lattice planes bowed towards the diagonal direction.

We here introduce the synchrotron X-ray diffraction characterization results of a 6-inch free-standing GaN (0001) wafer grown using a Na-flux-based LPE method and the crystallinity and local lattice plane shape of the whole wafer [5]. The crystallinity and local lattice plane shape of the whole wafer were discussed using the maps of $11\bar{2}4$ peak intensities and the rocking curve FWHM widths for the two azimuthal angles ϕ = 0 and 120°. In addition, the local q vector maps were visualized. The following findings were obtained. 1) Huge boundaries were observed between the high- and low-crystallinity areas. 2) The lattice plane was observed to be anisotropically bowed along

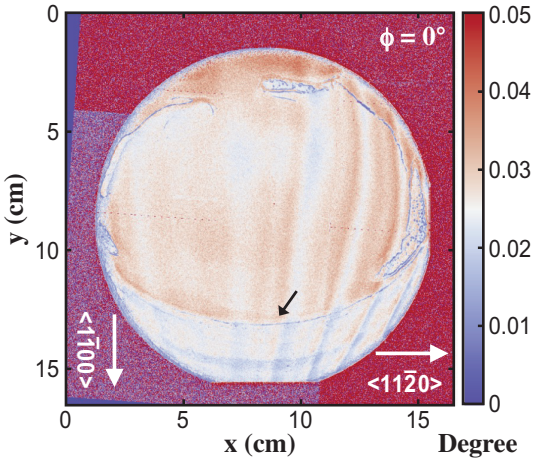

Fig. 1. X-ray diffraction topography images reconstructed from the rocking curve width. The higher crystalline area (blue) and lower crystalline area (red) are separated by the border in the substrate bottom. The undulation of the FWHM along the X-ray direction on the substrate is seen at $\phi = 0°$. [5]

the [10$\bar{1}$0] direction. 3) The mean width of the rocking curves over the wafer was 0.024°.

An X-ray diffraction topography measurement was performed at SPring-8 **BL20B2**. X-rays of 1.3 Å were chosen and the X-ray beam size was adjusted to be larger than 100 mm (h) × 3 mm (v). Because of the limitation of the detection area of a flat panel detector (Hamamatsu, C7942CA-22), the 6-inch substrate was required to be translated to almost perpendicular and parallel directions with respect to the X-ray incident beam to achieve full-area illumination. The detector was placed almost parallel to the sample surface with a sample-to-detector distance of 30 cm. The detector pixel size was 50 × 50 μm^2, and the pixel numbers were 2368 × 2240. The 6-inch substrate was placed at the rotation center by minimizing tension. The interplanar angle between GaN (0001) and (11$\bar{2}$4) is 39.16°, and the 11$\bar{2}$4 Bragg angle was 40.25°, resulting in an incident angle of about 1°, which was small enough to cover the whole substrate. Under this asymmetric X-ray illumination, the X-ray incident angle was scanned using 5 arcsec steps. The X-ray exposure time was 5 s, and more than 2000 diffracted images were recorded at the fixed azimuthal angle ϕ.

The FWHM map of the 6-inch free-standing GaN substrate at ϕ = 0° is illustrated in Fig. 1. Striped lines are seen along the [10$\bar{1}$0] direction. The value at the substrate edge area at the top is higher than those in other places. Around the substrate bottom below the border, the FWHM is even smaller than that at the substrate center, which indicates a localized higher crystallinity area. We attribute this to strain relaxation followed by dislocation formation. It is known that the strain of a free-standing GaN crystal is dependent on the GaN thickness on foreign substrates. Therefore, during the crystal growth or laser lift-off process, some parts in the substrate may be strained so that the substrate undergoes local deformation. Although the mechanism of this phenomenon remains unclear, substrate bending and dislocation may provide a plausible explanation that may be related to the striped FWHM patterns. The same analysis was conducted at ϕ = 120° (not shown here). The overall features appear similar, and the stripe patterns are inclined compared with those at ϕ = 0°. The FWHM map does not change continuously on the borderline around the substrate bottom, indicating that the substrate has already deformed along the boundary.

To evaluate the 2D lattice-plane tilting, we analyzed the local *q*-vectors of GaN 11$\bar{2}$4. The *q*-vector analysis method is described elsewhere [2]. Two rotation matrices for the calculation of the angular change of the *q* vector were introduced. The projection of the *q* vector to the (x, y)-plane is depicted in Fig. 2(a). In the vector plot, the direction of the arrow indicates 2D inclination with respect to the mean lattice-plane bending angle. In particular, for the left and the right sides, the lattice plane moved significantly toward the substrate center. Interestingly, substrate bending from top to bottom is much less than that in other directions. Figure 2(b) shows the amplitude of the projected vector in Fig. 2(a) and indicates cylindrical bowing.

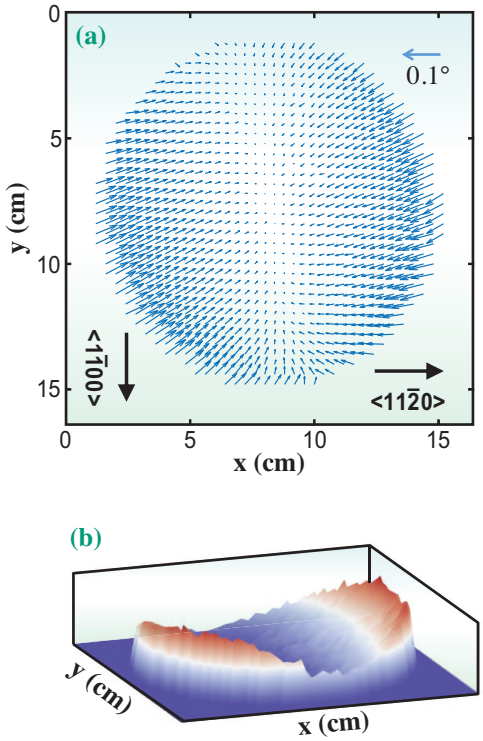

Fig. 2. **(a)** Lattice plane bending direction projected to the (x, y)-plane. Symmetrical substrate bending with respect to the y-direction is observed. **(b)** Degree of substrate bending visualized from the magnitude of projected vectors. [5]

Osami Sakata[a,*] and Jaemyung Kim[b]

[a] Japan Synchrotron Radiation Research Institute (JASRI)
[b] RIKEN SPring-8 Center

*Email: sakata.osami@spring8.or.jp

References

[1] B.K. Tanner: X-ray Diffraction Topography (Pergamon Press Ltd., Oxford, UK, 1976).
[2] J. Kim *et al.*: Appl. Phys. Express **11** (2018) 081002.
[3] Y. Cui *et al.*: CrystEngComm **19** (2017) 3844.
[4] O. Sakata and J. Kim: "Local Lattice Plane Orientation Mapping of Entire GaN Wafer", Chapter 6 in Characterization of Defects and Deep Levels for GaN Power Devices, AIP Books. pp. 6-1.
[5] *J. Kim, O. Seo, L.S.R. Kumara, T. Nabatame, Y. Koide, and O. Sakata: CrystEngComm **23** (2021) 1628.*

Diagnosing plasma turbulence down to the micrometer scale

Turbulence appears in the late evolution of many fluid systems. This remains true even when considering plasma flows, where nonlocal phenomena affect the fluid dynamics. Its most iconic example might be turbulence in astrophysics, which organizes density and velocity perturbations inside the filaments and ultimately affects star formation rates. As classically depicted by Kolmogorov theory, turbulence is a phenomenon that locally transports energy from its injection scale (large spatial scale) to its dissipation scale (small spatial scale), thus forming an energy cascade. However, this theoretical approach may be inadequate in the more complex framework of high energy density (HED) and plasma physics, as nonlocal transport and collective phenomena also play a role. The numerical approach is also limited since turbulent scales extend spatially over several orders of magnitude, and both the injection and the dissipation are needed to correctly described the turbulence cascade. The only remaining approach is the experimental measure of a portion of the turbulent spectrum to constrain theories. The main difficulty, in the laboratory, is to measure the smallest spatial scale. Indeed, the best measure has been limited to scales larger than 100 μm in HED [1]. With the achievement of high-resolution X-ray radiography (HRXR), we managed to measure the turbulent spectrum of HED plasma down to the micrometer, thus revealing unforeseen features.

The first step is to produce a turbulent plasma and diagnose its spatial fluctuations with micrometer-scale spatial resolution. To that end, we work on the hutch EH5 of the X-ray free electron laser (XFEL), SACLA **BL3**. At this station, a high-power laser was employed with a hybrid phase plate to deliver ~20 J in ~4.3 ns onto a focal spot of ~240 μm on a solid multilayer target (~10^{13} W·cm^{-2}) (Fig. 1). Its first layer, a plastic ablator, is ablated, launching a shock wave, which sets into motion the second target layer, a brominated plastic pusher where a sinusoidal modulation is preimposed. The pusher then expands into a plastic foam and decelerates. This leads to the development of Rayleigh–Taylor instability (RTI) [2], which ultimately results in the formation of turbulence. To diagnose the evolving system, HRXR was performed. The quasi-monochromatic, collimated XFEL beam (Gaussian envelope centered on 7 keV, with a 30 eV full width at half-maximum) of SACLA was employed as a probe beam. An effective snapshot (~8 fs) of the system can be obtained with no geometrical constraints on the resolution. In this configuration, the spatial resolution of X-ray radiographs is only limited by the intrinsic resolution of the detector and its distance to the observed system (phase contrast imaging (PCI)). By employing a lithium fluorine crystal (LiF) as a detector (~0.5 μm resolution) placed 10 cm away from the target, ~1.5-μm-resolution (PCI) radiographs were obtained [3]. The radiograph contrast is ensured by the bromine in the pusher, which absorbs more X-rays than a simple plastic of the foam.

Our experimental configuration allows us to diagnose the dynamics of the system from the early stage of its evolution up to its late stage (80 ns after laser shot). From the sequence of snapshots obtained, the global dynamic can be reconstructed (see Fig. 2). At the interface between the expanding pusher and the foam, RTI grows from its linear phase to its nonlinear phase before its transition to turbulence after 50 to 60 ns. The growth of RTI already provides a wealth of information that can be used to constrain numerical simulations. For instance, the resolved images of the RTI spike extremity, a novelty in HED physics, differ from simulations and yield information on the plasma viscosity.

What interests us here is the late time phase (after 50 ns), where only isotropic fluctuations of the pusher concentration occur (no RTI). We analyzed this phase like a turbulent field of concentration. In other words, we performed the 2D spatial Fourier transform of the region of interest in the radiographs. Since the resulting power spectra were isotropic, we took the average over the angle to obtain 1D radial spectra. Figure 3 shows the spectra we obtained at different times. In this figure, the reference corresponds to

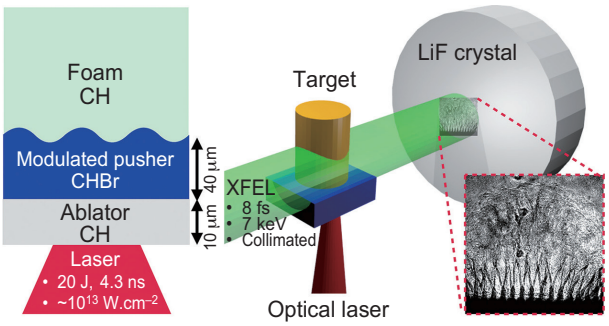

Fig. 1. Target design and experimental setup. A collimated XFEL beam is used in conjunction with a LiF crystal to perform high-resolution radiography.

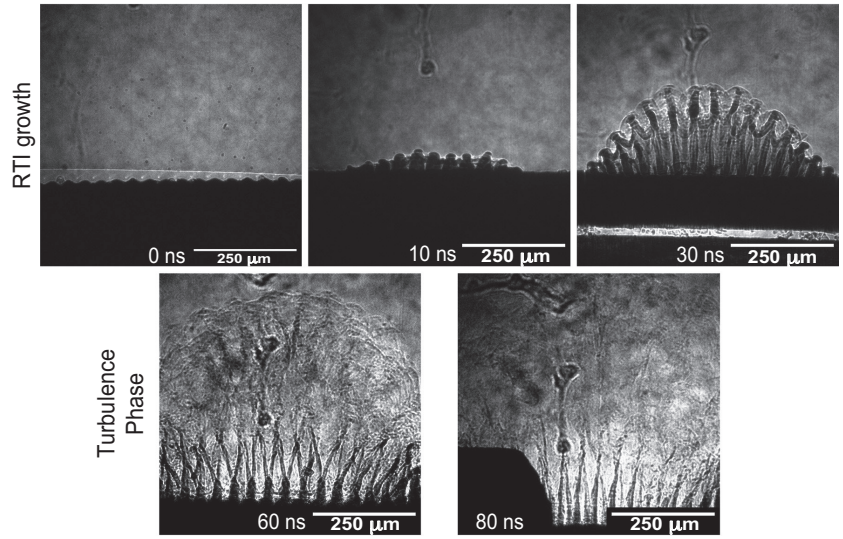

Fig. 2. X-ray radiographs recreating the evolution of the system.

a foam without an expanding pusher, and the early spectra (before 50 ns) are shown as reference as the situation was not yet isotropic. The power-law fitting of the "lower" part (spatial frequency <10 μm^{-1}) of the late time spectra shows a slope (–1.75 ± 0.25) compatible with Kolmogorov turbulence theory (–5/3), depicted by the black dashed line. The observed situation is thus turbulent.

However, two aspects of the spectra are not in accord with the turbulence theory. First, the bump, which appears with a spatial scale of 3.9±0.1 μm, is a feature that we cannot explain yet. It may correspond to an energy injection scale due to magnetic coupling for instance, or to the development of small-scale instability that we could not identify. Then, there is an inflection point in the power spectra at around 7 μm. This inflection of the turbulent spectra is unexpected as it appears at a spatial scale much larger than the dissipation scale (~0.5 nm). This may correspond to a transition between the inertial range of the turbulence and a sub-ionic range, as this scale corresponds to the ion inertial length. This would indicate the importance of ionic phenomena in the plasma turbulence.

New experiments are now under way to ascertain the nature of these unexpected features.

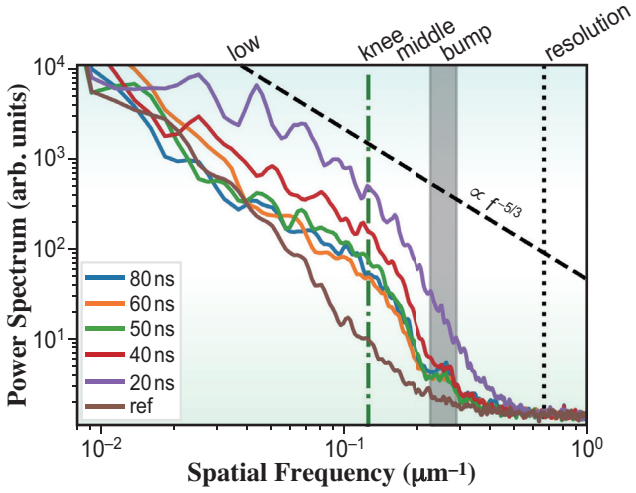

Fig. 3. Evolution of the spectra as a function of time. The late-time spectra are consistent with turbulence, but some features remain unexplained.

Gabriel Rigon[a,b,*] and Bruno Albertazzi[b]

[a] Graduate School of Science, Nagoya University
[b] LULI, IPP Paris, France

*Email: gabriel.rigon@ens-lyon.org

References

[1] T.G. White *et al.*: Nat. Commun. **10** (2019) 1758.
[2] G. Rigon *et al.*: Phys. Rev. E **100** (2019) 021201.
[3] P. Mabey *et al.*: Rev. Sci. Instrum. **90** (2019) 063701.
[4] *G. Rigon, B. Albertazzi, T. Pikuz, P. Mabey, V. Bouffetier, N. Ozaki, T. Vinci, F. Barbato, E. Falize, Y. Inubushi, N. Kamimura, K. Katagiri, S. Makarov, M.J.-E. Manuel, K. Miyanishi, S. Pikuz, O. Poujade, K. Sueda, T. Togashi, Y. Umeda, M. Yabashi, T. Yabuuchi, G. Gregori, R. Kodama, A. Casner, M. Koenig: Nat. Commun.* ***12*** *(2021) 2679.*

X-ray laser illuminates the local motion of water molecules

Liquids are essential to our daily life and energy-related applications, but many fundamental questions remain unanswered. A major challenge is understanding the molecular-level correlated dynamics in liquids, which helps bridge the knowledge gap between microscopic motions in liquids and macroscopic transport properties such as viscosity and electronic conductivity. Now, split-pulse X-ray photon correlation spectroscopy (XPCS) enables the measurement of molecular-level correlated motion in the pico- to nanosecond range, taking advantage of unprecedented brilliance and short pulse duration of an X-ray free electron laser (XFEL) [1]. The nearly fully coherent X-ray beam at SACLA allows the determination of the correlation in speckled scattering.

Analyses of molecular-level correlated dynamics in liquids using XPCS have been explored globally since the project of XFEL was initiated. In conventional XPCS, the temporal correlation of speckled scattering images provides the intermediate scattering function—the temporal correlation function of electron density in reciprocal space. Its temporal resolution is set by the frame rate of the detector (in synchrotron facilities) or the repetition rate of X-ray pulses (in XFEL), making it difficult to measure the dynamics in picoseconds and nanoseconds. The limitation is mitigated by using two X-ray pulses generated from a single XFEL pulse. The X-ray pulses are separated in time, and the sum of speckle scattering patterns from a sequence of two separate X-ray pulses is recorded in a single scattering image. The scattering images are then analyzed using the concept of speckle visibility spectroscopy (SVS) [2], which was originally developed using visible light. The contrast of speckled scattering images is related to the intermediate scattering function, so the dependence of contrast on the time separation between the two pulses provides information about the molecular-level dynamics. The accessible timescale in this approach is determined by the time separation between the two pulses, making it possible to study the dynamics at the femtosecond, picosecond, and sub-nanosecond scales.

The key components to realizing this approach are the split-delay optics (SDO) installed in SACLA **BL3** and the self-seeding of X-rays (Fig. 1) [1]. Reflection self-seeding produced bright X-ray pulses at a photon energy of 10 keV [3]. Each X-ray pulse was split into two sub-pulses using wavefront-division SDO [4]. The time difference Δt between the sub-pulses was controlled by the path length difference between the variable-delay branch and the fixed-delay branch. The exiting beams were overlapped and focused at the sample position with X-ray mirrors. The focused X-ray beam irradiated a continuous stream of water with a flow rate of 0.7 mL/min, and three multiport charge-coupled devices recorded the scattering from the sample. The water stream diameter was 50 μm, which is larger than the variation in beam position at the sample during the experiment (Fig. 2). The relative position between two sub-pulses, ΔX and ΔY, remained stable enough to assume that the two sub-pulses overlapped on the sample. The high stability of the SDO system is a crucial factor for successful measurement.

A major concern about this approach was a possible heating effect by the first sub-pulse. Because of the high pulse energy, the sample temperature may have risen before the second sub-pulse hit the sample. Figure 3(a) shows the scattering intensity around Q = 2 Å^{-1}, which was binned on the basis of the pulse energy of the first pulse (I_{fixed}), where Q is the magnitude of momentum transfer. The peak position shifted to a high Q with a larger Δt and a higher I_{fixed}. Using the temperature dependence of the peak position, we estimated the temperature rise ΔT (Fig. 3(b)). The result shows a heating effect for the water samples only after Δt = 0.5 ps when the X-ray pulses with $I_{\mathrm{fixed}} < 3$ μJ were selected.

The speckle visibility $\beta(Q = 2.0$ Å^{-1}, $\Delta t)$ was determined by maximum likelihood estimation on the assumption that the probability of observing photons at a single pixel is determined by a negative binomial distribution (Fig. 3(c)). With $I_{\mathrm{fixed}} < 3$ μJ, the

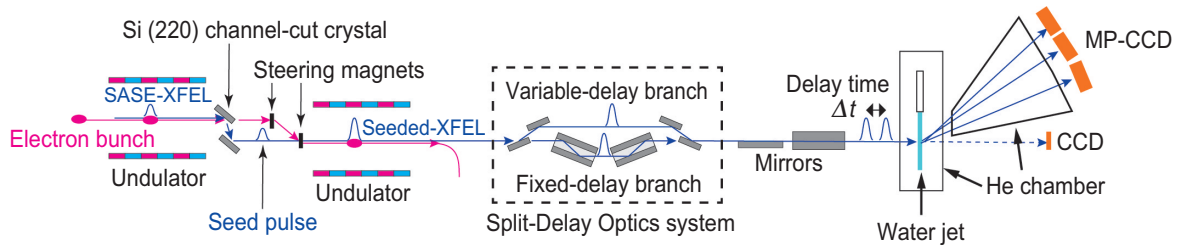

Fig. 1. Experimental setup using the SDO and reflection self-seeding at SACLA BL3. [1]

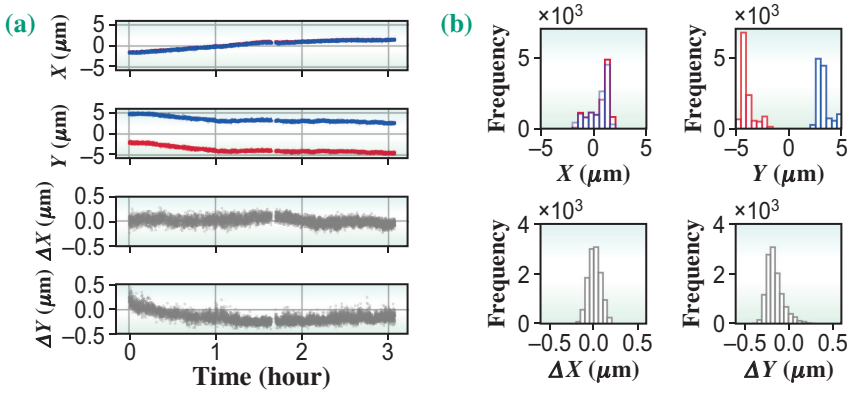

Fig. 2. **(a)** Time course of X-ray beam position of two sub-pulses at the sample position, X and Y, and their relative position, ΔX and ΔY. **(b)** Histograms of X, Y, ΔX, and ΔY. The position of two X-ray pulses was shifted in the Y direction for ease of viewing. [1]

visibility decreased as Δt increased, reflecting the dynamics of water molecules. The baseline values at a larger Δt agree with the values determined using the uncorrelated beams without spatial overlap. The decaying behavior of the visibility is comparable to those calculated from the result of inelastic X-ray scattering [5], indicating that the decrease in the visibility at short timescales with $I_{\mathrm{fixed}} < 3$ μJ is reliable. With $I_{\mathrm{fixed}} < 1$ μJ, meaningful estimations of β were not possible owing to the low count rate. The number of shots with 1 μJ < I_{fixed} < 3 μJ was ~65 % of the total number of shots with the seeded X-rays. Without the seeded X-rays, the average pulse energy of all X-rays (both branches) was 0.38 μJ. This result demonstrates the capability of the X-ray SVS with the control of the picosecond-scale time delay using the SDO and the necessity of self-seeded X-rays when studying the molecular-level correlated dynamics. This success at SACLA results from the use of the highly brilliant XFEL and the high stability of X-ray optics available at SACLA. Further studies at a higher Q and a larger Δt would determine the detailed molecular-level correlated dynamics at a timescale that is difficult to measure using other techniques.

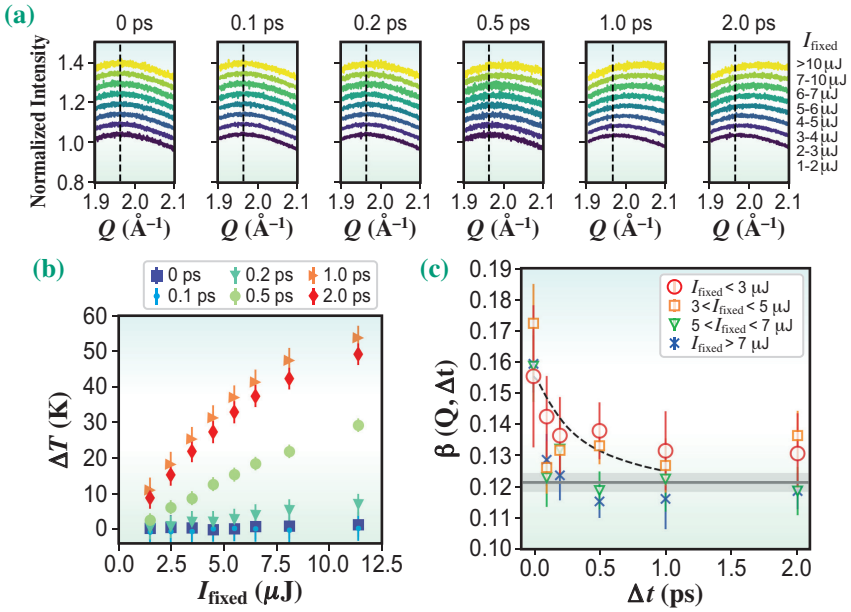

Fig. 3. **(a)** Normalized scattering intensity around Q = 2 Å^{-1}. Δt is shown at the top of the panels and the profiles are vertically shifted for clarity. **(b)** Estimated values of the temperature rise due to the energy of the sub-pulse from the fixed delay branch. The error bars represent the standard deviation of the fitting of the peak position in (a). **(c)** X-ray speckle contrast obtained by maximum likelihood estimation. The solid line represents the contrast measured when there was no overlap between the two sub-pulses, and the uncertainty was calculated using the second derivative of the log-likelihood. The dashed line represents the decaying behavior, which was estimated using the result of inelastic X-ray scattering [5]. [1]

Yuya Shinohara[a,*], Taito Osaka[b] and Ichiro Inoue[b]

[a] Oak Ridge National Laboratory
[b] RIKEN SPring-8 Center

*Email: shinoharay@ornl.gov

References

[1] *Y. Shinohara, T. Osaka, I. Inoue, T, Iwashita, W. Dmowski, C.W. Ryu, Y. Sarathchandran and T. Egami: Nat. Commun.* ***11*** *(2020) 6213.*
[2] P.K. Dixon, D.J. Durian: Phy. Rev. Lett. **90** (2003) 184302.
[3] I. Inoue *et al.*: Nat. Photonics **13** (2019) 319.
[4] T. Hirano *et al.*: J. Synchrotron Rad. **25** (2018) 20.
[5] Y. Shinohara *et al.*: Phys. Rev. E **98** (2018) 022604.

Simultaneous analytical system of electrochemical reaction rate and *operando* hard X-ray photoemission spectroscopy

Electrochemical technologies, such as for fuel cells, secondary batteries, photocatalysts, semiconductor systems, plating, corrosion protection, biochemistry, electrochemical sensors, metal refining, and electrolytic synthesis/polymerization, are the backbone of modern science and industry. To quantitatively understand the electrochemical reaction, the reaction rate must be accurately measured. For example, in the development of fuel cell catalysts, power generation can be estimated by quantitatively measuring the electrochemical reaction rate per unit area by supplying a reactant to a catalyst at a constant rate. The degradation of the catalyst can also be elucidated. In the development of anticorrosion materials, the effect of anticorrosion can be quantitatively understood by measuring the rate of corrosion.

For the analysis of the electrochemical reaction rate, a solution must be constantly supplied to the electrode surface, and material diffusion must be controlled to reproducibly and quantitatively measure the activity of electrode reactions or charge transfer processes. For this purpose, hydrodynamic voltammetry is used. An example of hydrodynamic voltammetry is the rotating disk electrode (RDE) method, where a disk electrode is placed in solution, and the current associated with the electrochemical reaction is measured while the electrode is rotated at a constant speed. The reactant is supplied to the surface of the electrode and carried outward along the surface by the rotation of the electrode, realizing a steady mass transport over the surface of the electrode. The setup of the RDE measurement is relatively simple, but maintaining the temperature and pressure is not always easy because the solution is usually placed in a container such as a flask. Furthermore, long-time measurement could be relatively difficult because of the decrease in the concentration of reactants and the increase in the concentration of products in the container. As another method of hydrodynamic voltammetry, the channel flow electrode (CFE) method has attracted attention in fields such as fuel cells, secondary batteries, metal corrosion, and surface treatment [1]. Figure 1 schematically shows a diagram of electrochemical measurement by the CFE method. A rectangular parallelepiped channel with a thickness of 1 mm or less is constructed in a cell made of an insulation resin. A conductive electrode, often used as a substrate of specimens, is embedded in the cell to make the walls of the electrode and the cell the same level. In the CFE method, instead of rotating the sample, the electrolyte solution is supplied in a laminar flow as Hagen-Poiseuille flow from the solution reservoir into the cell to the sample. In this way, the electrochemical reaction rate is measured with the diffusion of the reactant being accurately controlled. Since the temperature and the concentration of reactants in solution are controlled in the solution reservoir, a steady-state reaction is easily reached, and the reproducibility is high. Usually, the CFE method can be suitably applicable to long-time measurements.

The electronic states of the electrode surface are closely related to the bonding of atoms and molecules, as well as to the reaction mechanisms, at the electrode surface. Therefore, data on the electronic state offer important information for the control of electrochemical reactions. The structures and electronic states of electrode surfaces during electrochemical reactions have been analyzed by infrared and Raman spectroscopies, probe spectroscopies, and X-ray photoelectron spectroscopy (XPS), for example. In recent years, synchrotron X-ray has been used, and the structures and electronic states have been actively studied by, for examples, X-ray diffraction, X-ray scattering, X-ray absorption spectroscopy, and photoemission spectroscopy (PES). The targets are also expanding to practical systems, such as nanoparticles used in fuel cell catalysts.

In the 1970s, hard X-ray photoemission spectroscopy (HAXPES) was reported, but at that time, the intensity of hard X-rays was still low. Around 2000, SPring-8 started to supply high-brilliance synchrotron hard X-rays concurrently with the improvement of photoelectron detectors. Since then, many studies of HAXPES using synchrotron X-rays have been reported [2]. In industry, HAXPES was first applied to semiconductors, but now, it is used in a wide range of fields including battery materials and catalysts. In addition, *in situ* and *operando* ambient-pressure XPS measurements on solid samples reacting with gases using soft, tender, and hard X-rays are reported. In some cases, even the liquid itself was measured. For *in situ* measurements on an electrode surface, a small container or a microcell enclosing an electrolyte solution was placed in ultrahigh vacuum (UHV), and the electronic states

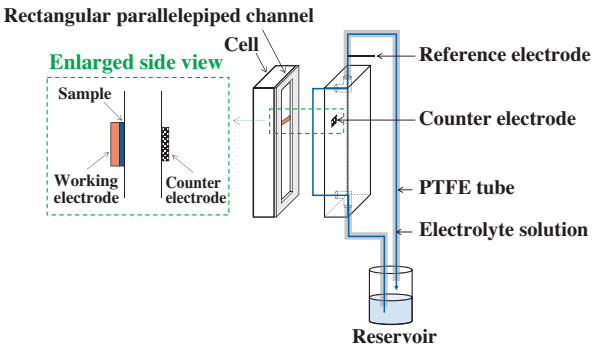

Fig. 1. Schematic illustration of the channel flow electrode method.

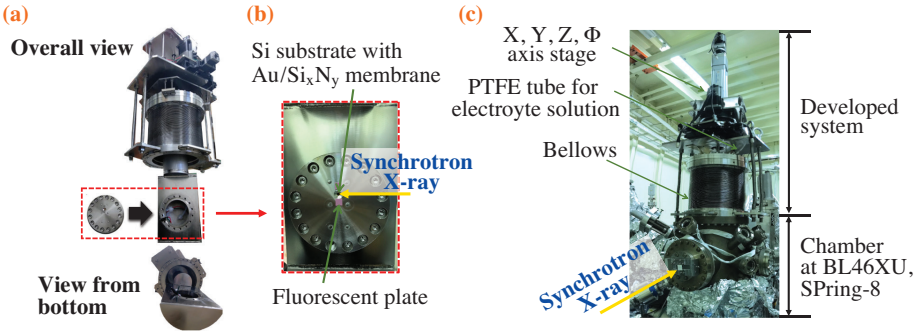

Fig. 2. Photographs of the constructed analytical system **(a)**, the stainless flange (ICF152) with a Si substrate with a Au/Si_xN_y membrane **(b)**, and the system installed in the UHV chamber at BL46XU **(c)**. A fluorescent plate was attached to the stainless-steel flange to confirm the irradiation position of the synchrotron X-ray.

of electrodes during electrochemical reactions were measured by HAXPES [3]. For PES measurement during the electrochemical reactions, the solution, in most cases, was not continuously supplied from the outside to the electrochemical system.

We have developed an *operando* technique designed to measure the electronic state of an electrode immersed in electrolyte solution by HAXPES while measuring or even controlling the electrochemical reaction rate. Our system is expected to make a large contribution to the development of materials and to industrial processes [4].

Figure 2 shows photographs of the analytical system installed in the HAXPES chamber at SPring-8 **BL46XU**. For sample positioning by moving the lower part of the system for HAXPES measurements, the X, Y, Z, and Φ stages were used with a positioning rod connecting the lower part of the chamber to the 4-axis stage. A flexible stainless-steel bellows between the positioning stages and the lower part of the chamber enabled sample movement. To simultaneously perform HAXPES measurements in ultrahigh vacuum while measuring the electrochemical reaction rate in solution under atmospheric pressure, a Si substrate was used with an ultrathin window of a 20-nm-thick Au/Si_xN_y membrane (15-nm-thick Si_xN_y coated with 5-nm-thick Au).

Figure 3(a) shows the chronoamperometry results obtained at 0.4 V. A cathodic current of approximately 8 μA was observed, which is considered to be a reduction current due to a trace amount of oxygen contained in the solution as an impurity. The reaction rate was calculated to be 0.04 nmol·s^{-1}. Figure 3(b) shows a Au3$d_{5/2}$ spectrum of HAXPES measured while measuring the current in Fig. 3(a). The blue circles and solid line were the experimental data and curve-fitting result, respectively, for the Au thin film electrode on the Si_xN_y membrane surface at 0.4 V in solution, while the green triangles and solid line were those of the metal Au in vacuum measured as a reference spectrum. The Au thin film electrode was observed to be in a metal state during this electrochemical measurement. In this way, we succeeded in developing an *operando* system designed for measuring the electronic state of a sample by HAXPES while measuring (or controlling) the electrochemical reaction rate under Hagen-Poiseuille flow by the CFE method. This concept of simultaneous measurements can be expanded to different analytical methods. We are now working on *operando* small-angle X-ray scattering using a CFE cell [5].

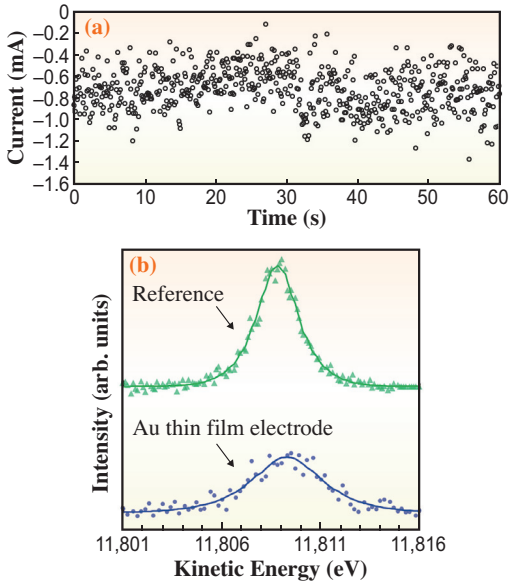

Fig. 3. **(a)** Chronoamperometry (flow rate = 25 cm·s^{-1}) measured at 0.4 V *vs* Ag/AgCl sat. KCl in 0.1 M $HClO_4$ at room temperature. **(b)** Au3$d_{5/2}$ HAXPES spectrum of Au thin film electrode measured during electrochemical reaction (blue circles for data and solid line for fitting). The horizontal axis indicates the kinetic energy of photoelectrons. The green triangles and solid line are of the spectrum of the reference metal Au. From all data, Shirley backgrounds were subtracted.

Junji Inukai[a,b]

[a] Clean Energy Research Center, University of Yamanashi
[b] Fuel Cell Institute, Universiti Kebangsaan Malaysia, Malaysia

Email: jinukai@yamanashi.ac.jp

References

[1] H. Nishikawa *et al.*: Langmuir **34** (2018) 13558.
[2] K. Kobayashi *et al.*: Appl. Phys. Lett. **83** (2003) 1005.
[3] T. Masuda *et al.*: Appl. Phys. Lett. **103** (2013) 111605.
[4] *K. Suda, T. Kawamoto, S. Yasuno, T. Watanabe, T. Koganezawa, M. Matsumoto, H. Imai, I. Hirosawa and J. Inukai: J. Electrochem. Soc.* ***168*** *(2021) 054506.*
[5] T. Watanabe *et al.*: ECS Trans. **98** (2020) 477.

Sulfur poisoning of Pt and PtCo anode catalysts in polymer electrolyte fuel cells studied by *operando* near ambient pressure hard X-ray photoelectron spectroscopy

Ambient pressure X-ray photoelectron spectroscopy has become a powerful tool for the investigation of surface chemical reactions of functional catalytic systems. The SPring-8 **BL36XU** beamline was dedicated to the investigation of the degradation and poisoning mechanisms in polymer electrolyte fuel cells (PEFCs), and was maintained by University of Electro-Communications and financially supported by New Energy and Industrial Technology Development Organization (NEDO). We installed an ambient pressure hard X-ray photoelectron spectroscopy (AP-HAXPES) apparatus at BL36XU. In the present work, we investigated the sulfur poisoning phenomenon in Pt and PtCo anodes of polymer electrolyte fuel cells (PEFCs) before and after acceleration degradation tests (ADTs) and found significant dissimilarities in the sulfur poisoning feature between the Pt and PtCo electrodes. The PtCo anodes catalyst is revealed to be much more tolerant to S poisoning even after ADTs [1].

We investigated the S adsorption behaviors on Pt (average particle diameter of ~2.6 nm) and Pt_3Co (~3.0 nm) anode and cathode catalysts in PEFCs under working conditions for fresh specimens immediately after aging as well as degraded specimens after ADTs by recording the HAXPES data. Figure 1 shows the results of S 1*s* HAXPES at the anodes. The principal peaks appearing at ~2478 eV are ascribed to the S species from the sulfonic acid group (–SO_3H) in the Nafion electrolyte. Peaks of other characteristic S species such as anionic S (S^{2-}) and zero-valent S (S^0), which are regarded as poisonous S species, are also found in Fig. 1. By plotting the electric potentials evaluated from the binding energies (see Figs. 2(b) and 2(d) below), both the S^{2-} and S^0 species are found to have the same potential as the Pt and C electrodes. This implies that S^{2-} is the S species absorbed on the Pt electrode, while S^0 is the species adsorbed on the C support. In all the samples shown in Fig. 1, the amount of S^{2-} increases significantly with an increase in cathode-anode bias voltage, indicating that reductive conditions at the anode induce poisonous S^{2-} adsorption. This observation can be understood easily because S^{2-} adsorption occurs through the reductive reaction between the Pt electrode and the SO_3^{2-} or SO_4^{2-} species dissolved in the electrolyte.

The most striking result found in Fig. 1 is an appreciable difference in the amount of S^{2-} between the Pt and Pt_3Co anodes after ADTs. The amount of S^{2-} are depicted in Figs. 2(a) and 2(b). Although the aged (fresh) Pt and Pt_3Co electrodes give similar amounts of S^{2-}, the degraded Pt anode after ADTs

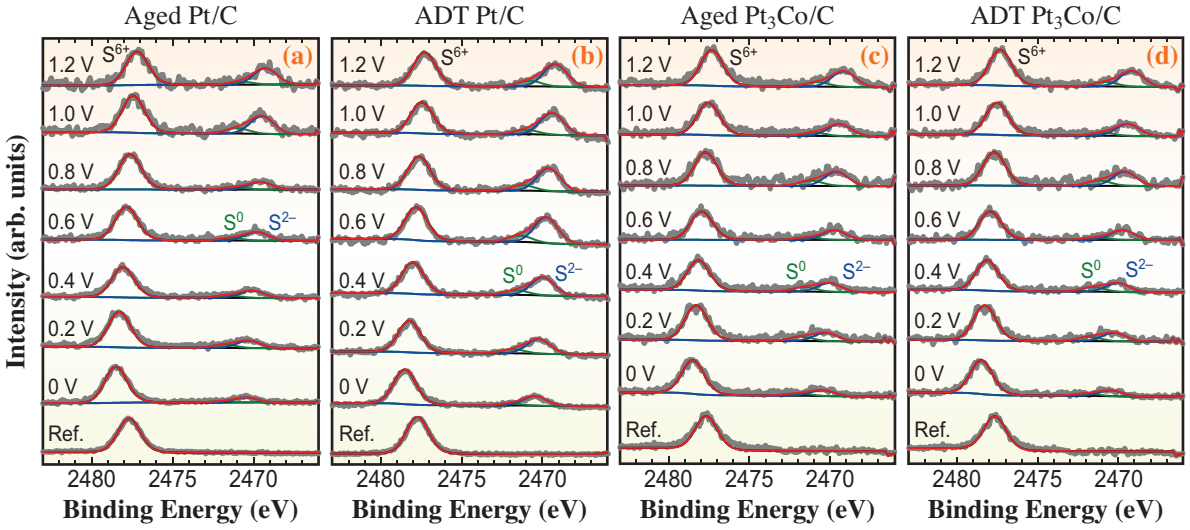

Fig. 1. S 1*s* HAXPES of **(a)** the fresh Pt/C anode immediately after the aging treatment before ADTs, **(b)** the degraded Pt/C anode after ADTs, **(c)** the fresh Pt_3Co/C anode (aged), and **(d)** the degraded Pt_3Co/C anode after ADTs. The main peaks at ~2778 eV are the S^{6+} species originating from the sulphonic acid group in the Nafion electrolyte, and other species (S^0 and S^{2-}) are the poisonous S impurities. The amount of S^{2-} is found to be much more significant at the Pt/C anode than at the Pt_3Co/C anode.

exhibits much more S^{2-} adsorption than the Pt_3Co anode. This finding implies that the Pt_3Co anode is more tolerant to the adsorption of poisonous S^{2-} than the Pt anode.

It is well known that the Pt_3Co cathode exhibits a higher activity in the oxygen reduction reaction (ORR). The reason for this higher ORR activity could be applied to gain an understanding of the present finding. It is reported that the surface Pt atoms are significantly negatively charged in the Pt(skin)/Pt_3Co(111) system compared with the pure Pt case [2] because of the difference in electronegativity between Pt and Co. It is believed that, as a result, the negatively charged surface Pt destabilizes O^{2-} adsorption on the Pt cathode, leading to a higher ORR activity. In the present electrode, a similar structure of the Pt skin and Pt_3Co core is elucidated by scanning transmission electron microscopy (STEM) energy dispersive X-ray spectroscopy (EDS) measurement [3]. The surface Pt atoms are thus negatively charged in the Pt_3Co electrode, which exhibits a weaker (repulsive) interaction with anionic sulfur species such as SO_3^{2-}, SO_4^{2-}, or S^{2-}. The adsorption of poisonous S^{2-} may eventually be suppressed.

S^{2-} adsorption is much more serious in the anode because, at the cathode, adsorbed S^{2-} on the Pt catalyst is desorbed at a high bias voltage owing to the oxidative environment, while the anode is in a more reductive environment at a higher bias voltage. The adsorbed S^{2-} cannot be removed easily. The Pt_3Co electrode has a higher tolerance to poisonous S^{2-} adsorption at the anode and a higher ORR activity at the cathode. The Pt_3Co electrode is found to be suitable not only at the cathode but also at the anode.

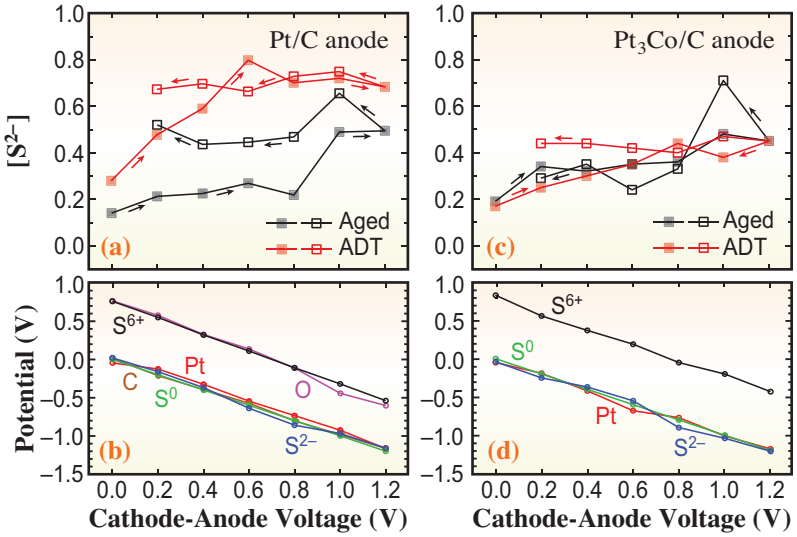

Fig. 2. **(a, c)** Amounts of S^{2-} species on the fresh (black) and degraded (red) Pt/C (a) and Pt_3Co/C (c) anode, and **(b, d)** electric potentials of S^{6+} (electrolyte), S^{2-}, S^0, O (liquid H_2O), C, and Pt (electrode). Because of the potential difference between the electrode and the electrolyte, the S^{2-} and S^0 species are found to adsorb on the electrode.

Toshihiko Yokoyama

Institute for Molecular Science,
National Institutes of Natural Sciences

Email: yokoyama@ims.ac.jp

References

[1] *S. Chaveanghong, T. Nakamura, Y. Takagi, B. Cagnon, T. Uruga, M. Tada, Y. Iwasawa and T. Yokoyama: Phys. Chem. Chem. Phys.* ***23*** *(2021) 3866.*
[2] S. Takao *et al.*: ACS Appl. Mater. Interfaces **12** (2020) 2299.
[3]S. Kobayashi *et al.*: ACS Omega **3** (2018) 154.

Quick *operando* ambient-pressure hard X-ray photoelectron spectroscopy for reaction kinetic measurements of polymer electrolyte fuel cells

Operando ambient-pressure hard X-ray photoelectron spectroscopy (AP-HAXPES) has become a powerful tool for the investigation of surface catalytic reactions. It is, however, very important to perform time-resolved measurements to gain an understanding of the reaction mechanisms. In the present work, we have exploited a subsecond *operando* AP-HAXPES system for the investigation of reaction kinetics in electrochemical cells under working conditions and have conducted demonstrative experiments concerning the redox cycles of the Pt cathode in the polymer electrolyte fuel cell (PEFC) upon applying stepwise bias voltage and the poisonous S^{2-} adsorption/desorption kinetics at the Pt cathode of PEFC.

The present HAXPES apparatus, Scienta-Omicron R4000 Hipp-2, installed at SPring-8 **BL36XU** allows us to measure a photoelectron spectrum with one shot. The available energy range is ~19 eV at the electron pass energy of 200 eV, which is sufficiently wide to detect many species with different oxidation numbers. The one-shot exposure time of the present CCD camera is 14 ms (70 fps), which corresponds to the maximum ideal time resolution. Figure 1(a) shows the one-shot XPS signals from a Au(111)/mica single crystal obtained using the laboratory X-ray source of monochromatized Al Kα. Although there can be seen only some pulse signals within one shot, the repeated accumulation with the time resolution of 14 ms for 0.42, 4.2, and 42 s successfully yields the Au 4*f* XPS with a good signal-to-noise ratio, as is seen in Fig. 1(b).

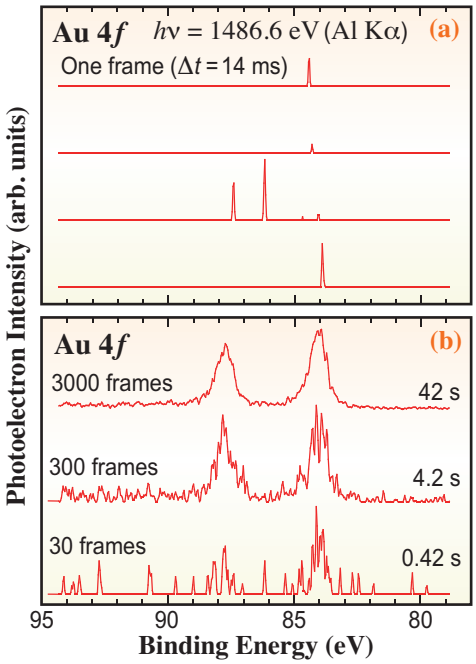

Fig. 1. Time-resolved XPS from the Au(111)/mica single crystal measured using the laboratory Al Kα monochromatized X-ray source. **(a)** One-shot spectra with the time resolution of 14 ms. **(b)** Accumulated one-shot XPS signals for 0.42, 4.2, and 42 s, with constant time resolution.

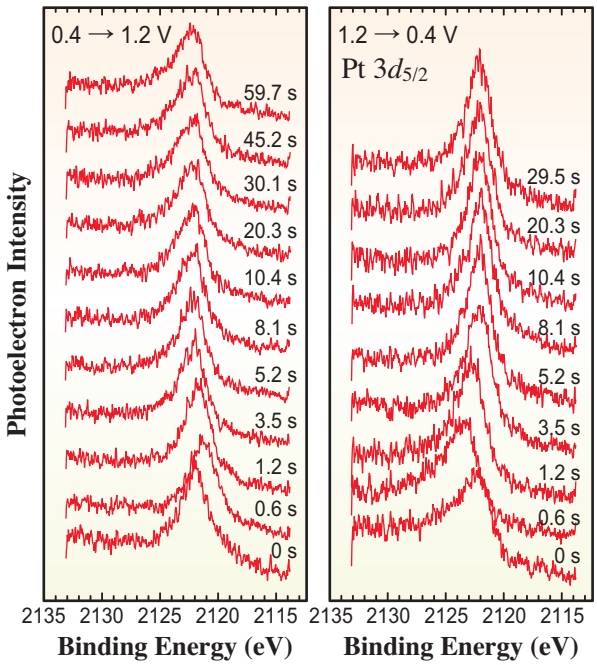

Fig. 2. Time dependence of Pt $3d_{5/2}$ HAXPES from the Pt cathode of working PEFC upon applying abrupt cathode-anode bias voltage steps of 0.4 → 1.2 V (left panel, oxidation process) and 1.2 → 0.4 V (right panel, reduction process). The time resolution was set at 500 ms and the measurements were repeated for 300 cycles (60 s for the oxidation process and 30 s for the reduction process) in both experiments.

The redox cycles of the Pt cathode electrode in a working PEFC have been investigated at BL36XU by measuring the Pt $3d_{5/2}$ HAXPES upon applying abrupt cathode-anode bias voltage steps (0.4 ↔ 1.2 V). It takes around 90 s to complete one cycle at room temperature and we set the time resolution at 500 ms. 300 cycles (30 s at 0.4 V and 60 s at 1.2 V) were repeated, and the total measurement period amounted to ~27,000 s. The time evolution of the resultant Pt $3d_{5/2}$ spectra is shown in Fig. 2. Through the curve-fitting analysis for the spectra in Fig. 2, the time dependence of the Pt amounts of Pt^0, Pt^{1+} (oxygen-

adsorbed Pt), and Pt^{2+} (oxidized Pt) are obtained as shown in Fig. 3. In the oxidation of the bias voltage step from 0.4 to 1.2 V, the Pt^0 species (metallic Pt) gradually decreases with an increase in the amount of oxidative Pt^{1+} and Pt^{2+} species. On the other hand, in the reduction of the bias voltage step from 1.2 to 0.4 V, the metallic Pt species is reproduced very quickly. By assuming the two-step reaction mechanism shown in Fig. 4, we can evaluate the reaction rate constants; the obtained results are k_1=0.11 s^{-1}, k_2=0.017 s^{-1}, k_{-1} = 0.37 s^{-1}, and k_{-2} = 1.09 s^{-1}. These results are consistent with those obtained by time-resolved XAFS measurements, although the measurement temperatures are different (HAXPES at 30°C and XAFS at 80°C). The reduction process is found to be much faster than the oxidation process, because the oxidation process consists of several steps to overcome the rather high activation energies, such as dissociative oxygen adsorption, Pt–Pt metallic bond cleavage, and oxygen embedding into the subsurface area.

The adsorption/desorption kinetics of poisonous S^{2-} have also been investigated at the Pt cathode upon applying abrupt bias voltage steps of 1.0↔0.0 V. At the 1.0→0.0 V step, the S^{2-} species is adsorbed rather slowly, while it is desorbed rather quickly at the 0.0→1.0 V step. The reason for a much slower adsorption step is that the adsorption step requires dissociation of SO_3^{2-} or SO_4^{2-} to yield S^{2-}, the activation energy barrier of which may be larger than any reaction step in the desorption process. For details, see the original literature [1].

The present quick *operando* HAXPES measurement technique has never been reported, to the best of our knowledge, and is widely applicable for the investigation of surface chemical kinetics not only for fuel cells but also for various catalytic reactions.

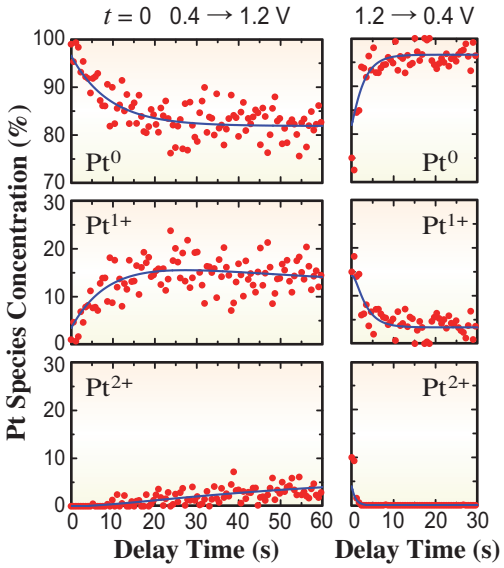

Fig. 3. Time dependence of the amounts of Pt species, Pt^0 (metallic), Pt^{1+} (O adsorbed), and P^{2+} (oxidized). The blue lines are the data fitted assuming the reaction mechanism shown in Fig. 4.

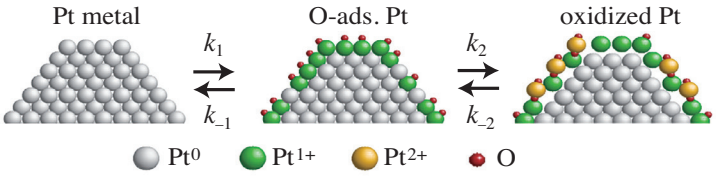

Fig. 4. Assumed reaction mechanism of the redox cycle in the Pt cathode upon changing bias voltage. At the first step, oxygen is dissociatively adsorbed on the Pt surface to yield Pt^{1+}, and at the second step, oxygen is embedded into the subsurface to provide oxidized Pt^{2+} at the surface. The rate constants are evaluated using the experimental data shown in Fig. 3.

Toshihiko Yokoyama

Institute for Molecular Science,
National Institutes of Natural Sciences

Email: yokoyama@ims.ac.jp

References

[1] *T. Nakamura, Y. Takagi, S. Chaveanghong, T. Uruga, M. Tada, Y. Iwasawa and T. Yokoyama: J. Phys. Chem. C* ***124*** *(2020) 17520.*

Spin reorientation of Fe^{3+} induced by peculiar Pb charge ordering in $PbFeO_3$

The cross interplays and correlations among lattices, charges, spins, and orbital degrees of freedom in transition metal perovskite oxides give rise to various fascinating electronic and magnetic properties, such as high-temperature superconductivity, colossal magnetoresistance, metal-insulator transition, multiferroicity, electrocatalysis, and negative thermal expansion. Such functions generally originate from transition metal ions, but Pb also has a charge degree of freedom stemming from the possibility of having either the $6s^2$ (Pb^{2+}) or $6s^0$ (Pb^{4+}) electronic configuration. Perovskite oxide $PbMO_3$ (M: 3d transition metal) shows systematic charge distribution changes depending on the depth of the 3d level of M [1]. $PbVO_3$ is $Pb^{2+}V^{4+}O_3$, similar to $Pb^{2+}Ti^{4+}O_3$ [2], but $PbCrO_3$ has been found to be $Pb^{2+}{}_{0.5}Pb^{4+}{}_{0.5}Cr^{3+}O_3$ with charge disproportionated Pb^{2+} and Pb^{4+} [3]. $PbCoO_3$ has been found to be $Pb^{2+}Pb^{4+}{}_3Co^{2+}{}_2Co^{3+}{}_2O_{12}$ [4]. $PbNiO_3$ has a valence distribution of $Pb^{4+}Ni^{2+}O_3$ [5]. That is, $PbMO_3$ changes from $Pb^{2+}M^{4+}O_3$ to $Pb^{2+}{}_{0.5}Pb^{4+}{}_{0.5}Cr^{3+}O_3$ (average valence state of $Pb^{3+}M^{3+}O_3$) to $Pb^{2+}{}_{0.25}Pb^{4+}{}_{0.75}Co^{2+}{}_{0.5}Co^{3+}{}_{0.5}O_3$ ($Pb^{3.5+}Co^{2.5+}O_3$) and finally to $Pb^{4+}M^{2+}O_3$ following the order of M in the periodic table corresponding to the depth of the M d level. However, the charge distribution of $PbFeO_3$ remains a mystery.

Our hard X-ray photoemission spectroscopy (HAXPES) measurement performed at SPring-8 **BL09XU** revealed the $Pb^{2+}{}_{0.5}Pb^{4+}{}_{0.5}Fe^{3+}O_3$ charge distribution [6]. Figure 1 shows the HAXPES results for $PbFeO_3$ and other $PbMO_3$ compounds with M = Ti, Cr, Co, and Ni used as standard references. Two components appeared in both the Pb 4$f_{7/2}$ and Pb 4$f_{5/2}$ peaks for $PbCrO_3$ ($Pb^{2+}{}_{0.5}Pb^{4+}{}_{0.5}CrO_3$), $PbCoO_3$ ($Pb^{2+}{}_{0.25}Pb^{4+}{}_{0.75}CoO_3$), and $PbFeO_3$. Each peak can be deconvoluted into two Gaussians, as reported previously. The $6s^0$ electronic configuration in Pb resulted in a binding energy lower than that of $6s^2$ because of a strong screening effect; hence, the components at lower binding energies are attributable to Pb^{4+} ions. The peak energies of $PbFeO_3$ were close to those of $Pb^{2+}{}_{0.5}Pb^{4+}{}_{0.5}Cr^{3+}O_3$, indicating the coexistence of Pb^{2+} and Pb^{4+} ions. We estimated the fractions of Pb^{2+} and Pb^{4+} from their area ratios using $PbCrO_3$ data as the standard for $Pb^{2+}{}_{0.5}Pb^{4+}{}_{0.5}$ and concluded that $PbFeO_3$ also had the $Pb^{2+}{}_{0.5}Pb^{4+}{}_{0.5}Fe^{3+}O_3$ charge distribution.

On the bases of the above-estimated valence distribution, the crystal structure was determined by comprehensive scanning transmission electron microscopy, synchrotron X-ray powder diffraction (SPring-8 **BL02B2**) and neutron powder diffraction analyses. $PbFeO_3$ crystallized into a unique charge-ordered state in which a layer of Pb^{2+} ions was interleaved by two layers each made up of a mixture of Pb^{2+} and Pb^{4+} ions in a 1:3 ratio, along

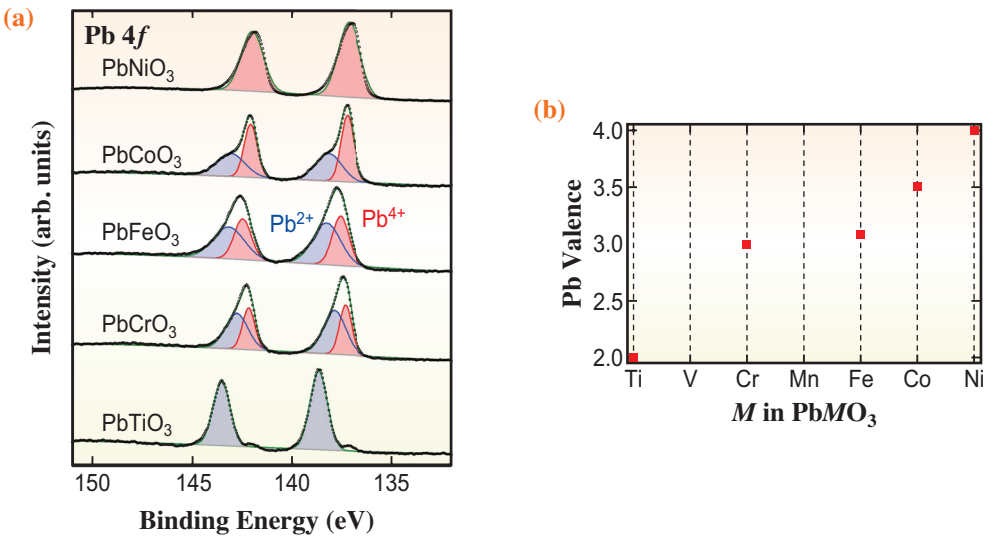

Fig. 1. Determination of the charge distribution of $PbFeO_3$ by HAXPES. **(a)** Pb-4f HAXPES results for $PbTiO_3$, $PbCrO_3$, $PbFeO_3$, $PbCoO_3$, and $PbNiO_3$ at RT. Predominant Pb^{4+} and Pb^{2+} are evident in the spectrum for $PbFeO_3$. **(b)** Average Pb valence state calculated from area ratios of Pb^{2+} and Pb^{4+} components. $PbTiO_3$, $PbCrO_3$, and $PbNiO_3$ are standards for Pb^{2+}, Pb^{3+} ($Pb^{2+}{}_{0.5}Pb^{4+}{}_{0.5}$) and Pb^{4+}, respectively.

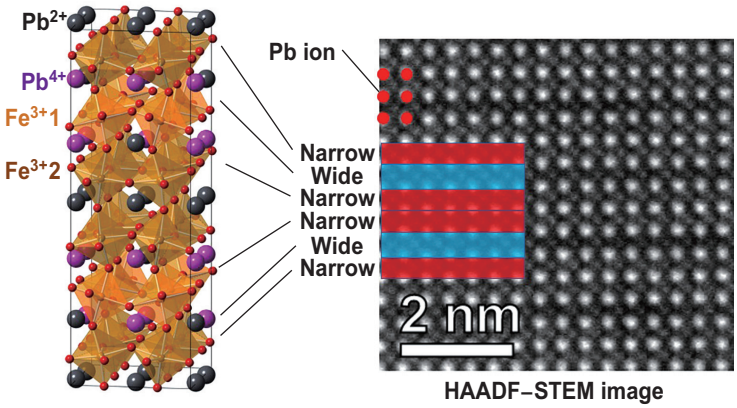

Fig. 2. Crystal structure of $PbFeO_3$. Left part: illustration of structure revealing the Pb^{2+}/Pb^{4+} ordering and presence of two Fe^{3+} sites. Right part: HAADF image of $PbFeO_3$. Distances for the bright spots, which are the locations of Pb, indicate a modulation with a narrow–wide–narrow pattern.

the direction of layer stacking (Fig. 2). Two distinct Fe sites with different types of Pb coordination are therefore generated. Upon cooling the sample from high temperature, two distinct magnetic phase transitions were observed, as shown in Fig. 3: a weak ferromagnetic transition occurring at 600 K owing to canted antiferromagnetic spin ordering and a continuous spin reorientation (SR) transition at 418 K despite the absence of magnetic rare-earth ions that are believed to be necessary for the appearance of spin reorientation in $RFeO_3$ (R: rare-earth element). Our DFT calculations revealed that the unique charge ordering in $PbFeO_3$ led to the formation of two Fe^{3+} sublattices with competing energies that, in turn, caused the peculiar SR transition [6]. This finding provides a new avenue for studying the charge ordering phase and distinctive SR transition with potential applications in spintronic devices because of the high transition temperature and possibility of tuning.

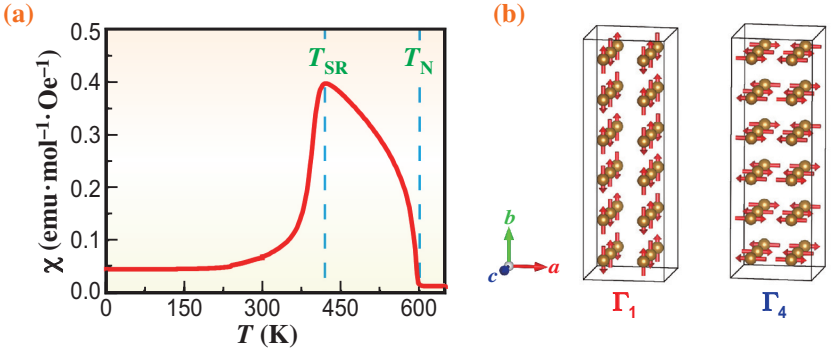

Fig. 3. Spin reorientation observed in $PbFeO_3$. **(a)** Temperature dependence of magnetic susceptibility of $PbFeO_3$ measured at 0.01 T. **(b)** Magnetic structures of $PbFeO_3$ between T_{SR} and T_N (Γ_4) as well as below 300 K (Γ_1) determined by neutron diffraction studies.

Masaki Azuma[a,b,*], Youwen Long[c] and Takumi Nishikubo[b,a]

[a] Laboratory for Materials and Structures, Tokyo Institute of Technology
[b] Kanagawa Institute of Industrial Science and Technology
[c] Beijing National Laboratory for Condensed Matter Physics, Institute of Physics, CAS, China

*Email: mazuma@msl.titech.ac.jp

References

[1] M. Azuma *et al.*: Annu. Rev. Mater. Res. **51** (2021) 329.
[2] A. Belik *et al.*: Chem. Mater. **17** (2005) 269.
[3] R.Z. Yu *et al.*: J. Am. Chem. Soc. **137** (2015) 12719.
[4] Y. Sakai *et al.*: J. Am. Chem. Soc. **139** (2017) 4574.
[5] Y. Inaguma *et al.*: J. Am. Chem. Soc. **133** (2011) 16920.
[6] *X. Ye, J. Zhao, H. Das, D. Sheptyakov, J. Yang, Y. Sakai, H. Hojo, Z. Liu, L. Zhou, L. Cao, T. Nishikubo, S. Wakazaki, C. Dong, X. Wang, Z. Hu, H.-J. Lin, C.-T. Chen, C. Sahle, A. Efiminko, H. Cao, S. Calder, K. Mibu , M. Kenzelmann, L.H. Tjeng, R. Yu, M. Azuma, C. Jin and Y. Long: Nat. Commun.* ***12*** *(2021) 1917.*

Structural characterization of the delithiated noncrystalline phase in a Li-rich Li_2VO_2F cathode material

Lithium-ion batteries (LIBs) have been widely used in various portable products as energy storage devices. The properties of LIBs, including energy density, power density, and rate performance, are mostly determined by the cathode material and its crystal structure. Currently, the most widespread cathode materials are those in which Li ions are extracted and inserted by topochemical reactions, such as spinel-structure layered rock salt. The energy density of these cathode materials is limited by the presence of their well-ordered framework, although they have superior rate performance. Further improvements of LIBs for practical applications will require the development of alternatives to layered rock salt and spinel structures as cathode materials.

A disordered rock-salt (DRS, space group $Fm\bar{3}m$) cathode material, Li_2VO_2F (LVOF), was reported by Chen *et al.* [1]. The estimated theoretical capacity of 462 mA h/g is higher than that of current commercial cathodes. Moreover, there is little volume expansion of the LVOF lattice upon cycling, which reduces stress on the device. Unfortunately, the LVOF materials suffer from rapid capacity decay and increased polarization in applications. Very recently, Baur *et al.* have carried out *operando* X-ray powder diffraction measurements for LVOF and reported the amorphization of the DRS crystal upon delithiation [2]. Hence, the DRS structure of LVOF collapses owing to a decrease in Li ion concentration because the framework is not strongly fixed in the system. Because the local structure around V ions changes upon charging, it is likely that the amorphous structure is related to cycling performance. The structural analysis of both the crystalline and noncrystalline phases is important for understanding the origin of the properties of cathode materials.

The structural analysis of disordered materials, such as amorphous materials lacking a long-period structure, is challenging because no Bragg peaks are observed in X-ray powder diffraction measurements. Atomic pair distribution function (PDF) analysis is a powerful method that provides insights into the structure of disordered materials. The PDF corresponds to the correlation strength between atomic pairs, which provides structural information in a short-range region. However, PDF analysis for a mixture of crystalline and noncrystalline phases such as an LVOF sample in the charged state cannot be quantitatively evaluated by a conventional technique. If the PDF of mixed material could be evaluated quantitatively, we would be able to characterize the noncrystalline phase.

For the structural characterization of the noncrystalline phase in delithiated LVOF, the PDF analysis method proposed by Hiroi *et al.* was applied [3]. This method precisely evaluates the scattering intensity from the crystal structure and refines the structural parameters based on the experimental PDF. It is suitable to analyze the PDF measured under the nonideal optical condition because structural parameters that depend on the momentum transfer, such as the instrumental resolution function, can also be treated correctly. When structural parameters of the crystalline phase in a mixture are precisely optimized by the method, the partial PDF of the noncrystalline phase can be extracted from the experimental PDF by subtraction [4]. To obtain the quantitative PDF under several cycling conditions, X-ray total scattering measurements for LVOF materials were performed at a high-energy X-ray diffraction beamline, SPring-8 **BL04B2**. Figure 1(a,b) shows the experimental scattering intensity and the partial component including the crystalline and noncrystalline phases. The partial scattering intensity from the noncrystalline phase shown in the grey area was markedly enhanced by the lithiation of the LVOF sample. This supports the idea that the noncrystalline phase forms from the broken DRS crystal via delithiation. Figure 1(c,d) shows experimental and

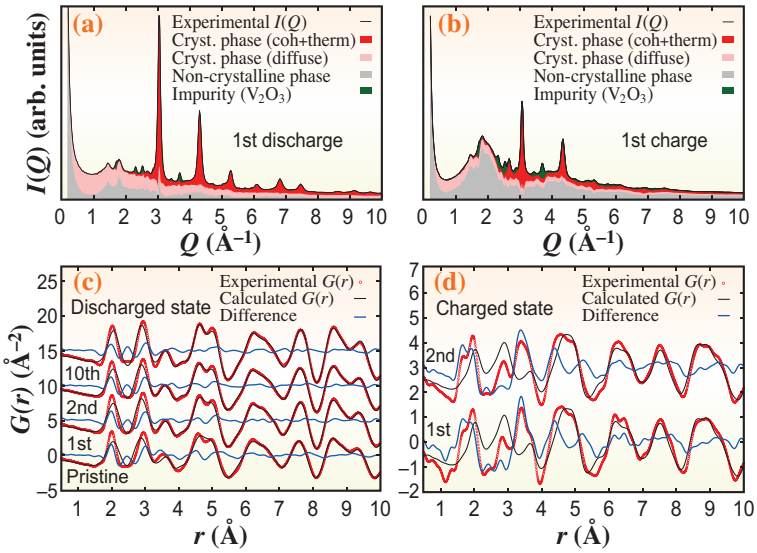

Fig. 1. Partial scattering components of crystalline, noncrystalline, and impurity phases in the **(a)** discharged and **(b)** charged states. Experimental and calculated atomic PDFs in the **(c)** discharged and **(d)** charged states.

calculated PDFs under several conditions in the range of $r < 10$ Å. A noteworthy change in PDF by delithiation in this range was observed. A shoulder of the first peak at the short-range side and a correlation at 3.4 Å were derived from the noncrystalline phase. These peaks are ascribed to a V–O bond (1.7 Å) and a V–V pair (3.4 Å), respectively. It is suggested that delithiation of the crystalline phase leads to the formation of an amorphous structure through local structural changes that increase the V–V distance. Inversely, the noncrystalline phase returned to the DRS crystal in the discharged state. However, the difference between the experimental and calculated PDFs, shown as blue curves in Fig. 1(c), decreased with an increase in the number of cycles. This reveals that the crystallinity of the DRS crystal in the discharged state was irreversibly improved by cycling.

To analyze the structure of the noncrystalline phase in the charged state, the partial PDF was extracted by the subtraction of the contribution from the crystalline phase. The extracted partial PDF is drawn as red points in Fig. 2(a). Notably, although the PDF of the crystalline phase had a strong atomic correlation at around 2.8 Å, weak contributions were found here in the extracted PDF. This indicates that the noncrystalline phase consists of not the $V(O,F)_6$ octahedral structure but the other polyhedrons. We performed reverse Monte Carlo [5] (RMC) and density functional theory (DFT) atomic configurational modelling using the extracted PDF to elucidate the local structure in the noncrystalline phase. Figure 2(b) shows the three-dimensional structural model obtained from RMC and DFT. The local atomic configuration in the noncrystalline phase is characterized by a network of tetrahedral and pyramidal units consisting of V ions and anions. During the charging process, delithiation creates many defects at cation sites in the DRS crystal. A rotation of octahedra in the DRS crystal would be allowed because these defects generate the free volume. The octahedral structure will change to the tetrahedral structure involving the oxidation of V ions at the same time as the delithiation. Figure 3 shows a schematic diagram of the structural transformation of the LVOF crystalline phase upon cycling. With every repetition of V-ion recovery on the cation site upon lithiation, the local disorder may be relaxed owing to the acceleration of the uniform random distribution of V ions. Simultaneously, the short-range order on the anion site near V ion is also likely to change upon cycling.

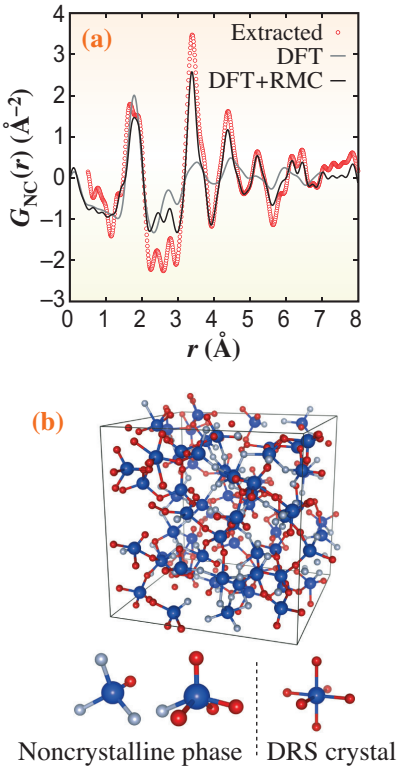

Fig. 2. **(a)** Extracted atomic PDFs of the noncrystalline phase in the charged state and calculated by RMC and DFT modelling. **(b)** Atomic structural model obtained by the DFT and RMC model (blue: V, red: O, gray: F). Extracted tetrahedral and pyramidal units from the model and an octahedral structure in the DRS crystal are also shown here.

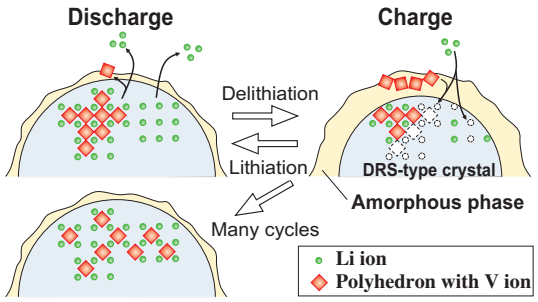

Fig. 3. Schematic diagram of the structural transformation of the LVOF crystalline phase upon cycling.

Satoshi Hiroi*, Koji Ohara and Osami Sakata

Japan Synchrotron Radiation Research Institute (JASRI)

*Email: s_hiroi@spring8.or.jp

References

[1] R. Chen *et al.*: Adv. Energy Mater. **5** (2015) 1401814.
[2] C. Baur *et al.*: J. Mater. Chem. A **7** (2019) 21244.
[3] S. Hiroi *et al.*: J. Appl. Crystallogr. **53** (2020) 671.
[4] *S. Hiroi, K. Ohara and O. Sakata: Chem. Mater. **33** (2021) 5943.*
[5] R.L. McGreevy *et al.*: J. Phys.: Condens. Matter **13** (2001) R877.

Control of spin transition by interface strain in heterostructured metal-organic framework thin film

Metal-organic frameworks (MOFs) are formed by the self-assembly of metal ions and ligands, and thus have a tailor-made framework structure. MOFs show various physical properties (gas separation, switching, catalysis, and so on). For future practical applications of MOFs such as high performance catalysts or chemical sensors, crystalline oriented MOF thin films have been intensively pursued in recent years. Among the proposed thin film fabrication techniques, layer-by-layer method is one of the most well-established bottom-up approaches. In this method, substrates with self-assembled monolayers (SAMs) are fabricated by alternately immersing them in a solution of building blocks. However, during the fabrication process, step-by-step growth at the surface sometimes result in unconventional structures that are not seen in the bulk. For example, heterostructured MOF thin films, in which one MOF is epitaxially grown on top of another MOF, are known to exhibit unique gas separation ability. It should be noted that the heterostructured MOF thin films have tunable interfaces between different MOFs. Thus, the heterostructured MOF thin films have the ability to realize the rational design of MOF interfaces and provide a new research platform.

As a research platform for the heterostructured MOF thin films, Hoffmann-type MOF {Fe(pz)[M(CN)$_4$]} [pz = pyrazine; M = Ni (Nipz), M = Pt (Ptpz)] is a very attractive candidate because it is an iron(II) coordination compound with a 3d^6 electron configuration and exhibits spin transitions induced by temperature, light, and so on [1]. These electronic configurations can move between paramagnetic high-spin (HS) and diamagnetic low-spin (LS) states, with accompanying structural changes.

In this study, we show the first example of strain-controlled spin transition in a heterostructured MOF thin film [2]. As shown in Fig. 1, we fabricated a heterostructured MOF thin film **Nipz5L-Ptpz30L**, composed of 5 layers of **Nipz** (bottom buffer layer) and 30 layers of **Ptpz** (upper layer), using the layer-by-layer method to control the spin transition behavior. **Nipz5L-Ptpz30L** showed a remarkable increase in the spin transition temperature.

In order to confirm the structure and orientation of **Nipz5L-Ptpz30L**, synchrotron XRD measurements were carried out using SPring-8 **BL13XU** (λ = 1.550 Å, room temperature). Figure 2 shows the synchrotron XRD profiles of different scattering geometries of **Nipz5L-Ptpz30L** in horizontal (in-plane) and vertical (out-of-plane) directions with respect to the substrate. The in-plane XRD pattern shows peaks indexed as *hk*0, showing periodic ordering of cyano-bridged 2D layers. However, the out-of-plane pattern shows two peaks, 001 and 002, showing interlayer ordering through pyrazine. *hk*0 and 00*l* diffraction peaks are observed separately in the in-plane and out-of-plane patterns. The data clearly show that **Nipz5L-Ptpz30L** has high crystallinity and well-controlled orientations of crystal growth in both in-plane and out-of-plane directions. Furthermore, the lattice constants of **Nipz5L-Ptpz30L** (tetragonal, P4/mmm, a = 7.28 Å, c = 7.08 Å) were determined from the XRD results. These lattice constants are significantly smaller than the bulk **Ptpz** in the HS state (a = 7.53 Å, c = 7.32 Å, 293 K), but similar to the bulk **Ptpz** in the LS state (a = 7.33 Å, c = 6.94 Å, 293 K) [1], which indicates that **Nipz5L-Ptpz 30L** is in LS state at room temperature.

The Raman spectrum of MOF shows a strong pyrazine internal vibration mode between 600 and 1600 cm^{-1}. As a probe of the change in spin state, it is well known that the strong intensity enhancement of the pyrazine stretching mode ν(ring) at 1030 cm^{-1} is a useful marker for the transition from the LS state to the HS state. When ν(ring) is normalized to the intensity of the CH bending mode δ(CH) at 1230 cm^{-1}, the ν(ring) mode becomes a quantitative measure of the spin state. Therefore, VT Raman spectra were measured in order to investigate the spin transition behavior. As shown in Fig. 3(a), the intensity ratio between the ν(ring) and δ(CH) modes clearly explains the spin transition behavior. During the heating process, **Nipz5L-Ptpz30L** shows a spin transition from 370 K to 400 K, and during the cooling process, it shows

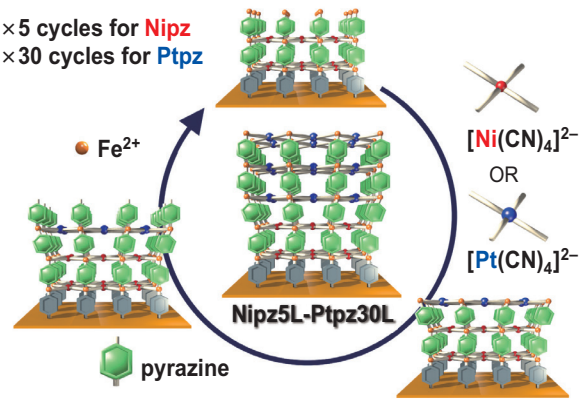

Fig. 1. Fabrication process of heterostructured thin film (**Nipz5L-Ptpz30L**).

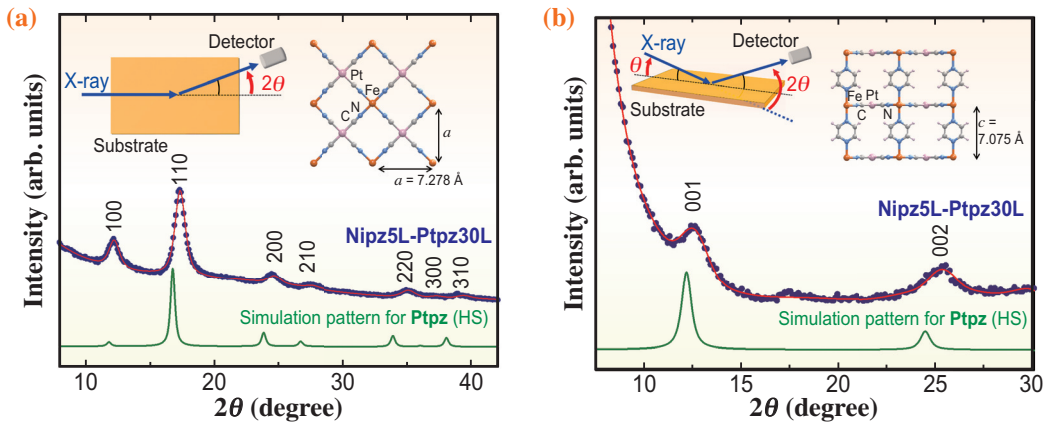

Fig. 2. Synchrotron XRD profiles of **Nipz5L-Ptpz30L**. **(a)** In-plane XRD patterns. **(b)** Out-of-plane XRD patterns.

hysteresis at ~380K, indicating that a first-order spin transition occurs. The spin transition temperatures (T_c) of **Nipz5L-Ptpz30L** during the cooling process ($T_c^{\downarrow}$) and heating ($T_c^{\uparrow}$) were 362K and 388K, respectively, where T_c is defined as the intermediate temperature at which the normalized intensity ratio reaches 0.65. **Ptpz30L** showed little change compared to bulk **Ptpz**. On the other hand, **Nipz5L-Ptpz30L** showed an increase in T_c of ~80K.

In the case of spin-transition compounds such as Hoffmann-type MOFs, a strong ligand field stabilizes the LS state: compressive strain on the **Ptpz** layer brings the CN ligand closer to Fe^{2+} (Fig. 3(b)), the level of $d_{x^2-y^2}$ orbitals increases due to σ-donation from CN ligand to Fe^{2+}, and the level of t_{2g} orbitals decreases due to π-back donation from Fe^{2+} to CN ligand. As a result, the ligand field around Fe^{2+} becomes stronger and the LS state becomes more stable.

Therefore, we have demonstrated for the first time that the spin transition behavior of MOFs can be controlled by fabricating nanometer-sized heterostructured thin films. These results provide useful insights into basic science for the future practical application of MOFs with various physical properties by rationally verifying the interfacial strain of heterostructured thin films.

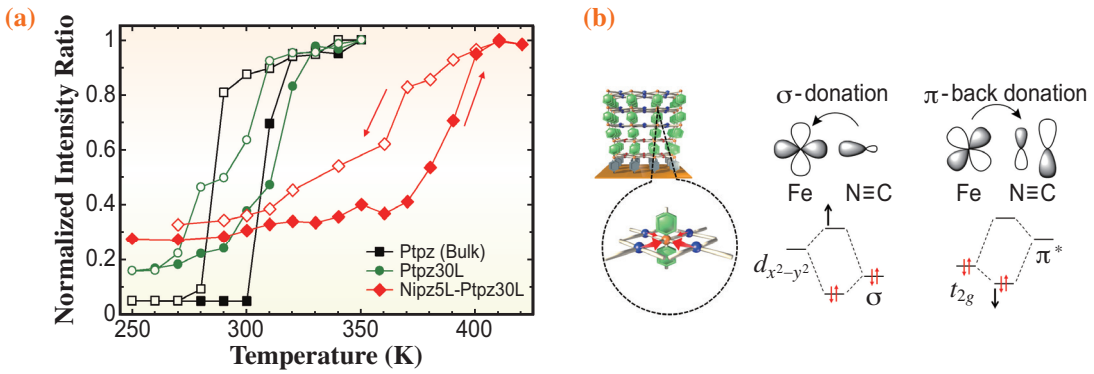

Fig. 3. **(a)** Temperature dependence of the normalized Raman intensity ratio. **(b)** Schematic representations of increase in spin transition temperature induced by compressive strain.

Tomoyuki Haraguchi

Department of Chemistry, Tokyo University of Science

Email: haraguchi@rs.tus.ac.jp

References

[1] M. Ohba *et al.*: Angew. Chem. Int. Ed. **48** (2009) 4767.
[2] *T. Haraguchi, K. Otsubo, O. Sakata, A. Fujiwara, H. Kitagawa: J. Am. Chem. Soc.* ***143*** *(2021) 16128.*

Molecular crystalline capsules that release their contents upon irradiation

Photosalient phenomena are well-known marked responses of organic crystals, such as jumping of crystals, or breaking or scattering of crystals into small pieces upon photoirradiation [1]. When the crystalline lattice breaks upon light irradiation, the strained energy is released and transformed into kinetic energy. Therefore, the crystals jump or scatter with high speed. Photosalient phenomena have also been observed in crystals of photochromic diarylethenes [2].

We previously created a photosalient crystal with a cavity formed during sublimation and demonstrated the scattering of 1-μm diameter beads from inside the cavity upon UV-irradiation [3]. This was a biomimetic system mimicking the seeds of *Impatiens*, except that the closed edge of the crystal was cut and the 'seeds' were artificially implanted by capillary action by dipping the edge of the hollow crystal into a reservoir of beads dispersed in water. In addition, there was no lid for the cavity, and thus it was always open. Here, we discovered a photosalient crystalline capsule that naturally traps organic solutions during recrystallization. The capsule is sealed and can contain any solute in solvent, in principle.

Photochromic crystals showing photosalient effect

We prepared a new diarylethene with *m*-trimethylsilylphenyl groups at both ends of the molecule (**1o**) (Fig. 1(a)). Diarylethenes are extensively studied compounds with photochromism and show a reversible transformation between open and closed forms upon photoirradiation. Diarylethene **1o** showed photochromism between **1o** and **1c** in solid and in solution. When the crystals were continuously irradiated with UV light (λ = 313 nm), they turned blue and then showed slight bending followed by fragmentation (a photosalient effect). Then, we attempted to obtain single crystals of **1o** by a common evaporation method. From a hexane solution, 7.7% of the crystals (668 out of 7967) had capsule structures. We analyzed the capsule structured crystals at SPring-8 **BL02B1** and **BL40XU** beamlines, and found them to have the same molecular packing as the noncapsule crystals.

We observed the formation of the capsule structure by optical microscopy and captured the moment of formation of primary liquid inclusions. The mechanism of formation of the capsule is attributed to the

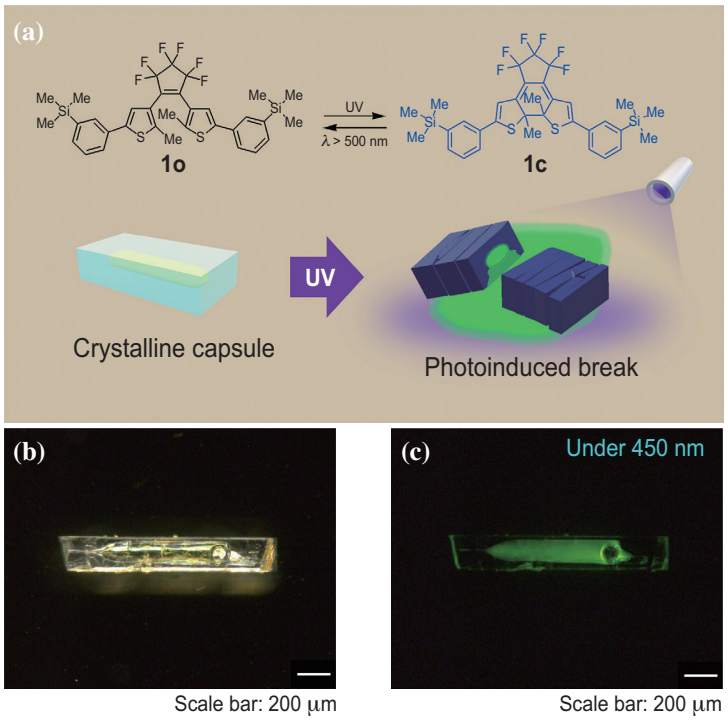

Fig. 1. Molecular crystalline capsule that releases the content, 5(6)-carboxyfluorescein (**5(6)-FAM**). **(a)** Molecular structures of open (**1o**) and closed-ring isomer (**1c**) and photorelease from a crystalline capsule. **(b)** Crystalline capsule containing **5(6)-FAM** inside under daylight. **(c)** Capsule under 450 nm light irradiation. **5(6)-FAM** inside emits green fluorescence.

inhomogeneous growth of crystals. The appearance of cavities due to this inhomogeneous growth of the crystals and the trapping of the solution in the cavities were observed.

To visually demonstrate the photoinduced property of a crystalline capsule of **1o**, we made crystalline capsules containing 5(6)-carboxyfluorescein (5(6)-FAM), a fluorescent dye used as a fluorescent tracer. The crystalline capsules were prepared from an acetone–methanol (3:1) solution of **1o** and 5(6)-FAM in 21% yield. The included 5(6)-FAM was ascertained by green fluorescence from the dye under 450 nm light irradiation. If a chemical can be dissolved in a solvent and can coexist with **1o** under recrystallization conditions, it is assumed that the capsule can include any such chemicals in solution.

Photorelease of the included florescence dye from the crystalline capsule upon 365 nm light irradiation

A crystal was floated on an aqueous buffer droplet (pH = 9.18 at 25°C) under a microscope (Fig. 1(b)), and the green fluorescence of 5(6)-FAM was visualized by 450 nm LED light irradiation, which does not induce the photoreaction of **1o** (Fig. 1(c)). Upon UV irradiation, the green fluorescence emission from 5(6)-FAM diffused in the aqueous buffer that appeared after the capsule was broken. The area of fluorescence of 5(6)-FAM expanded over the water surface around the crystal, indicating successful photoinduced release from the crystalline capsule (Fig. 2).

To control the crystal size, we changed the recrystallization period to obtain crystalline capsules. When the crystalline capsules containing 5(6)-FAM were prepared by recrystallization from the mixture of acetone and methanol with dissolved dye, the sizes of the obtained capsules were 2 mm in length and 300–400 μm in width for a 48 h recrystallization period. The size was reduced to less than 400 μm in length and less than 50 μm in width by shortening the recrystallization period to 12 h. The smaller capsules also released the 5(6)-FAM.

Such photorelease was also induced by multiphoton excitation with a femtosecond laser pulse at 802 nm without raising the temperature of the crystals. Additionally, the photorelease of the crystal of **1o** depends on the polarization direction of light, since all of the molecules are regularly aligned in the single crystals. A crystal whose long axis was perpendicular to the polarization direction showed coloration followed by jumping out from the field of view, whereas another crystal whose long axis was parallel to the polarization direction showed almost no change.

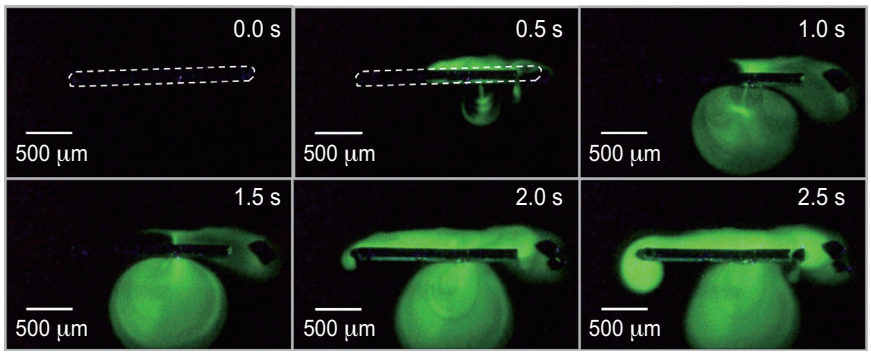

Fig. 2. Photoinduced scattering of diarylethene capsule under 365 nm light irradiation.

Kingo Uchida[a,*], Akira Nagai[a] and Ryo Nishimura[b]

[a] Department of Materials Chemistry, Ryukoku University
[b] Department of Chemistry and Research Center for Smart Molecules, Rikkyo University

*Email: uchida@rins.ryukoku.ac.jp

References

[1] P. Naumov *et al.*: Chem. Rev. **115** (2015) 12440.
[2] I. Colombier *et al.*: J. Chem. Phys. **126** (2007) 011101.
[3] K. Uchida *et al.*: Angew. Chem. Int. Ed. **56** (2017) 12576.
[4] *A. Nagai, R. Nishimura, Y. Hattori, E. Hatano, A. Fujimoto, M. Morimoto, N. Yasuda, K. Kamada, H. Sotome, H. Miyasaka, S. Yokojima, S. Nakamura, and K. Uchida: Chem. Sci.* ***12*** *(2021) 11585.*

Impact of *operando* X-ray spectromicroscopy for constructing Beyond 5G toward the realization of Society 5.0

5G is the current wireless communication technology that connects things and humans via cyberspace, and is being rapidly introduced into our lives owing to the COVID-19 pandemic. The next-generation wireless communication, Beyond 5G, seamlessly connects things, humans, and matter. Beyond 5G serves as the fundamental infrastructure of the forthcoming Society 5.0, which will incorporate the effective solutions for attaining sustainable development goals (SDGs) that were adopted at the United Nations sustainable development summit. Domestically, wireless communication is one of the last scientific and technology fields in which Japan maintains global competitiveness, and it accounts for 10% of its GDP. For instance, Sumitomo Electric Industries succeeded in commercializing GaN-based high-electron-mobility transistors (GaN-HEMTs) using two-dimensional electron gas (2DEG) formed at the AlGaN/GaN interface for the first time and boasts the world's top share. For Beyond 5G, more than a trillion devices are anticipated to be always-on in Japan. Possible candidates of Beyond 5G devices will utilize high-environmental-load elements, such as As, In, and Cu. Therefore, we should expend much effort to reduce the environmental load of Beyond 5G. For this purpose, low-environmental-load materials consisting of, for example, C, B, N, and Ga, which have excellent electronic properties, such as graphene, the AlGaN/GaN interface, and the two-dimensional boron-based layer (borophene) should be used for Beyond 5G devices. The frontier in material sciences is hence the realization of the full potential of low-environmental-load materials.

Among low environmental-load devices, GaN-HEMTs are promising for Beyond 5G base-station communication. This is because GaN-HEMTs operate at high frequencies up to around 200 GHz with a high output owing to a high electron mobility and a large bandgap. However, one critical issue, that is, current collapse phenomenon, must be resolved to enable stable long-period device operations (Fig. 1) [1]. The current collapse phenomenon is a significant reduction in output drain current upon applying high voltage stresses during the operation of GaN-HEMTs. The current collapse phenomenon has been suggested to originate from surface electron trapping near the gate electrode on the drain side. The surface electron trapping is induced by a large local electric field due to the high voltage stresses, i.e., the large bias applied to the gate and drain electrodes. The mechanism of surface electron trapping has not been clarified in detail because conventional macroscopic electric measurements and scanning probe microscopies cannot reveal the surface and interface properties site-specifically or element-selectively.

To elucidate device operation mechanisms in detail, we developed *operando* X-ray spectromicroscopy under bias application [2,3]. In fact, we demonstrated that *operando* X-ray spectromicroscopy is a powerful tool for elucidating operation mechanisms of cutting-edge devices owing to the site specificity and element selectivity that enable the information of target materials, i.e., Ga atoms, to be distinguished from that of carbon contaminants.

First, we applied *operando* X-ray photoelectron spectromicroscopy on GaN-HEMTs to precisely elucidate the mechanism of surface electron trapping under DC bias at SPring-8 **BL07LSU** [4]. Contrary to the previous suggestion base on macroscopic electrical measurements that surface electron trapping occurs near the gate electrode on the drain side [1], it was found that surface electron trapping occurs both near the gate electrode on the drain side and near the drain electrode. This result indicates that the mechanism of surface electron trapping under DC bias is different from that under non-DC bias in the actual operation of GaN-HEMTs. We then speculated that surface electron trapping changes spatiotemporally.

To verify this speculation, we carried out an experiment of spatiotemporally resolved *operando* X-ray absorption near edge structure (ST-XANES) of the Ga L_3 edge using the photoemission electron microscope (PEEM) at SPring-8 **BL25SU**, as shown in Fig. 2(a). The experiment involves tuning the pulsed X-ray radiation, illuminating an entire sample, and imaging the spatial variation of the yield of subsequently emitted Auger electrons. The incident X-ray is absorbed owing to the excitation of an electron in a core level to unoccupied states. The hole in the core level resulting from this absorption process can then be filled by an

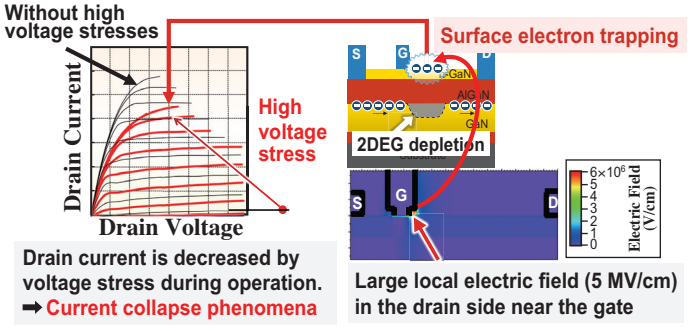

Fig. 1. Schematic of current collapse phenomenon in GaN-HEMT, originating from surface electron trapping.

outer electron falling into the core level. The resultant excess energy is channeled into the ejection of Auger electrons. By collecting the Auger electrons, with the help of PEEM, as a function of the incident X-ray energy and the delay time relative to the bias voltage pulses, we obtained ST-XANES spectra. To simultaneously achieve a high temporal resolution, soft X-ray pulse trains (train width: 1.813 μs) were extracted using an X-ray chopper with 220 μs intervals. The bias voltage pulses (gate: –5 V, drain: 30 V, pulse width: 4 μs) were synchronized with the X-ray pulse trains. The ST-XANES measurement using the pulsations of X-ray and bias voltages was repeated 25000 times to obtain ST-XANES spectra and ensure statistical accuracy.

It was found that peak A of the ST-XANES spectrum near the gate electrode on the drain side immediately (1 μs) after switching off the bias application changed, as shown in Fig. 2(a). According to the previous theoretical work [6], the weakening of peak A indicates an increase in the covalency of the Ga–N bond. The explanation for this is that donorlike surface states, i.e., positively charged Ga atoms, accept electrons, leading to the neutralization of the surface states. Hence, the neutralized surface states exist only near the gate electrode on the drain side. As shown in Fig. 2(b), it can be concluded that surface electron trapping occurs only near the gate on the drain side because of the large local electric field with a short-period bias application (ps–ns), as observed in this work [5]. This is followed by the hopping of the surface-trapped electrons to the drain electrode, as observed in our previous work [4]. By comparing the result of this work with those of high-frequency electrical characterization, the surface electron trapping was demonstrated to markedly affect the paramount figure of merit, that is, the cutoff frequency, which is the upper limit frequency of current amplification.

In summary, to contribute to the realization of low-environmental-load Beyond 5G, we have succeeded in directly observing the spatiotemporal dynamics of surface trapping in GaN-HEMTs by using spatiotemporal *operando* X-ray spectroscopy and newly proposing a new mechanism of surface electron trapping. Note that our findings cannot be obtained by conventional electrical characterization and non-element-specific scanning probe microscopies. Considering the timescale of the bunch mode and X-FEL, we believe that SPring-8 is the core facility for exploring new physics appearing in millimeter-wave and THz-frequency regions, where carriers in materials move at the critical speed, and Beyond 5G developments for realizing Society 5.0 and attaining SDGs.

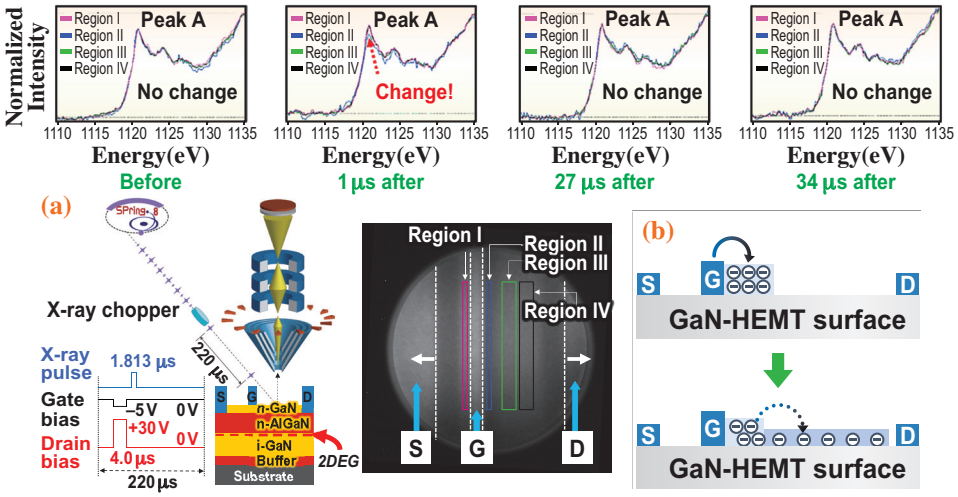

Fig. 2. **(a)** Spatiotemporal observation of surface electron trapping in GaN-HEMT using spatiotemporal *operando* X-ray absorption spectroscopy and schematics of the experimental system. **(b)** Proposed mechanism of surface electron trapping based on results of DC *operando* X-ray photoelectron microscopy and spatiotemporal *operando* X-ray absorption spectroscopy. S, G, and D indicate the source, gate, and drain electrodes, respectively.

Hirokazu Fukidome

Research Institute of Electrical Communication,
Tohoku University

Email: hirokazu.fukidome.e7@tohoku.ac.jp

References

[1] D. Soldani *et al.*: IEEE Veh. Technol. Mag. **10** (2015) 32.
[2] H. Fukidome *et al.*: Sci. Rep. **4** (2014) 3713.
[3] H. Fukidome *et al.*: APEX. **7** (2014) 065101.
[4] K. Omika *et al.*: Sci. Rep. **8** (2014) 13268.
[5] *K. Omika, K. Takahashi, A. Yasui, T. Ohkochi, H. Osawa, T. Kouchi, Y. Tateno, M. Suemitsu and H. Fukidome: Appl. Phys. Lett.* ***117*** *(2020) 171605.*
[6] T. Mizoguchi *et al.*: Mater. Trans. **45** (2004) 2023.

Effect of submicron structures on the mechanical behavior of polyethylene

Polyethylene (PE) is one of the most widely used polymers in daily life owing to its excellent mechanical properties and processability, and is used for products such as plastic bags, plastic wrap, stretch wrap, pipes, and covering of cables. High-density polyethylene (HDPE) is a PE produced by the polymerization of ethylene. Linear low-density polyethylene (LLDPE) is a PE commonly made by the copolymerization of ethylene with α-olefins such as butene, hexene, or octene to reduce crystallinity. The type and quantity of the α-olefins have significant effects on the physical properties of LLDPE. In this study, we first observed changes in the structures of LLDPE that are on the order of 100 nm to 1 μm (submicron scale) by time-resolved ultra small-angle X-ray scattering (USAXS), then showed that the changes on the submicron scale dominate the mechanical behavior of LLDPE and HDPE under uniaxial stretching.

The crystals in PE form hierarchical structures, as shown in Fig. 1 [1]. The structures include crystalline lattice structures, where molecular chains are systematically folded and packed; lamellar structures, where crystalline and amorphous parts are alternately stacked; branch structures consisting of the lower crystalline region (LCR) and higher crystalline region (HCR); and spherulitic structures filled with the branch structure. The changes in the hierarchical structures under deformation induce a yield point in stress–strain (S–S) curves during the uniaxial stretching of PE at room temperature (cold drawing) as shown in Fig. 2. The yield point is a measure of the tenacity of PE and the control of the yield point is important in PE material design. One yield point is observed in the S–S curve of HDPE during cold drawing. However, some LLDPEs exhibit two yield points in the S–S curve [2], and the presence of these two yield points gives them characteristic mechanical behaviors.

In previous studies, the yielding behaviors of LLDPE and HDPE have been discussed in terms of the changes in crystalline lattice and lamellar structures, which are investigated by small-angle X-ray scattering (SAXS) and wide-angle X-ray scattering (WAXS), during cold drawing. However, researchers have not investigated the effects of the changes in the submicron structures on the yielding behaviors, though it is expected that the structures on the submicron scale themselves would also affect the yielding behaviors [2]. The USAXS technique that uses synchrotron radiation enables us to perform *in situ* observations on the submicron scale [3]. We thus investigated the changes in the LCR and HCR of the submicron branch structures in LLDPE and HDPE during uniaxial stretching by time-resolved USAXS, as well as the changes in the lamellar and lattice structures by time-resolved SAXS and WAXS. We, then, clarified how the changes in the submicron structures affect the yielding behaviors.

The USAXS, SAXS, and WAXS measurements during drawing were performed with an incident wavelength of 0.2 nm in the second hutch of beamline at SPring-8 **BL03XU** [4]. The drawing speed was 1 mm/min. The details of the experiments are shown elsewhere[1].

Figure 2 shows S–S curves for LLDPE and HDPE. Here, λ is an extension ratio defined as $\lambda = L/L_0$, where L_0 and L are the sample lengths before and after applying strain, respectively. Two yield points, one at λ = 1.07 or the 1st yield point (1YP) and the other at 1.17 or the 2nd yield point (2YP), were observed for LLDPE, while one yield point (YP) at λ = 1.05 was observed for HDPE.

As shown in Fig. 3, the USAXS patterns of LLDPE show the characteristic changes at each yield point. After 1YP, the so-called butterfly pattern associated

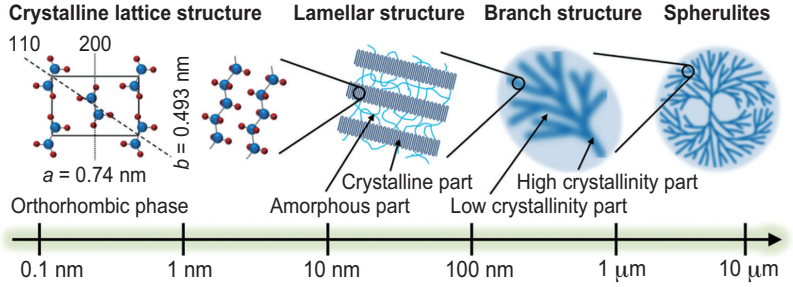

Fig. 1. Schematic illustration of the hierarchical structure of polyethylene spherulites.

with the enhancement of the density fluctuations on the sub-microscopic scale appears. The decrease in stress is caused by the reduction in the density of LCR. In HCR, the fragmentation of lamellar structures occurs, leading to the development of the chevron-type morphology, consequently. The mechanical melting of lamellar structures also occurs in HCR. After 2YP, the streak-like scattering perpendicular to the drawing direction appears in the USAXS patterns, reflecting the formation of string-like voids or necking. The formation of voids originates from further reduction in the density of LCR and enhances the reduction rate of the stress. In the HCR region, recrystallization occurs from the stretched polymer chains, and fibrillar structures are developed. The recrystallization causes the stress to rise gradually.

Figure 3 also shows the USAXS patterns of HDPE. After the YP, a strong inhomogeneity characterized by butterfly patterns is observed, and a strong streak develops, reflecting the immediate state of the generation and elongation of voids. The formation of chevron-type morphology and the mechanical melting occur in the same way as in LLDPE, but on the sub-microscopic scale, a strong enhancement of density fluctuations and void formation occur almost simultaneously, resulting in a single yield point.

The void formation does not occur at the 1YP but at the 2YP for LLDPE, while voids are formed at the YP in HDPE. This difference is caused by the fact that the lamellar structures in LLDPE are less stable than those in HDPE. The modulus of the lamellar structure in LLDPE is lower than that in HDPE, so the enhancement of density fluctuation with strain in HDPE is greater than that in LLDPE. The stability of the crystals in LLDPE depends on the comonomer species and their quantity in LLDPE so the yield behaviors may be strongly affected by these factors.

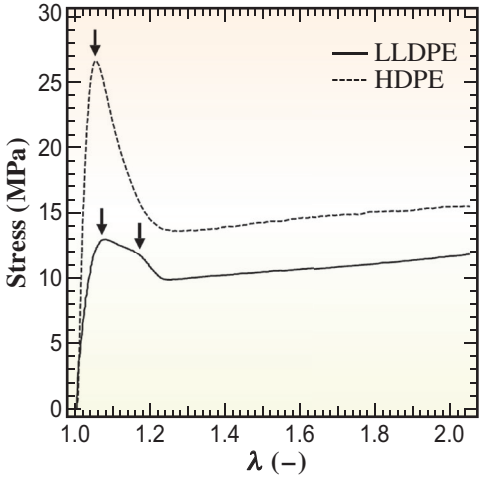

Fig. 2. S–S curves of LLDPE and HDPE. The arrows indicate the yield points.

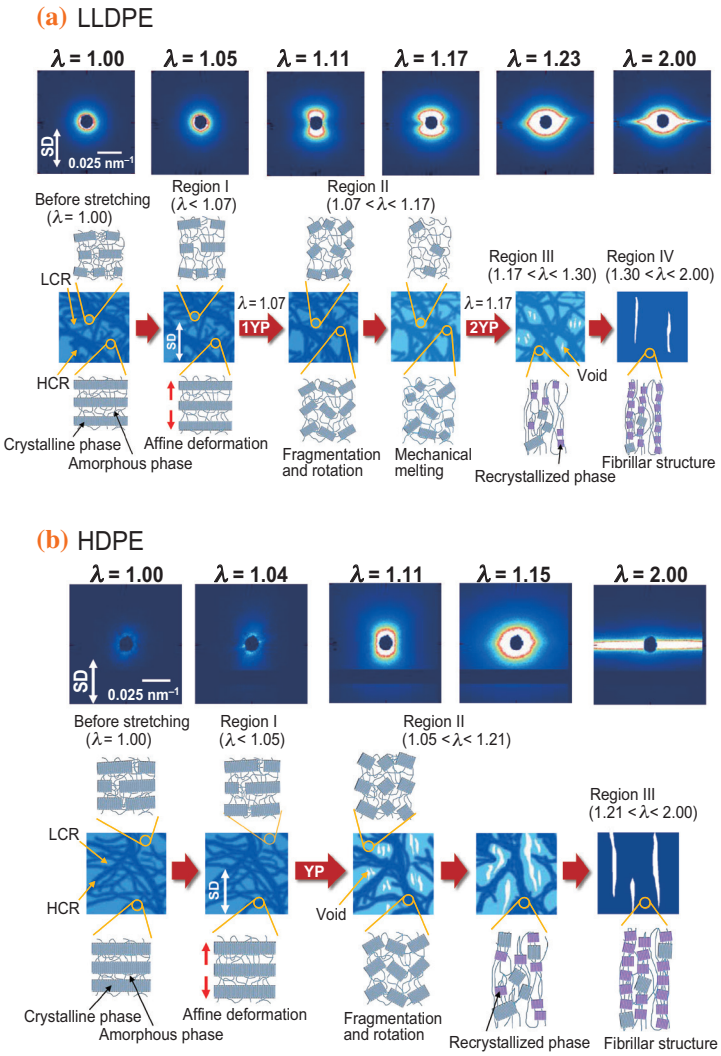

Fig. 3. Schematic illustrations of the changes in the hierarchical structures in **(a)** LLDPE and **(b)** HDPE.

Mikihito Takenaka

Institute for Chemical Research, Kyoto University

Email: takenaka@scl.kyoto-u.ac.jp

References

[1] *M. Kishimoto, K. Mita, H. Ogawa and M. Takenaka: Macromolecules* ***53*** *(2020) 9097.*
[2] R. Seguela and F. Rietsch: J. Mater. Sci. Lett. **9** (1990) 46.
[3] M. Takenaka *et al.*: Phys. Rev. E **75** (2007) 061802.
[4] H. Masunaga *et al.*: Polym. J. **43** (2011) 471.

High-sensitivity analysis of fluorescence XANES at Eu L_{III}-edge for the determination of oxidation state for trace amount of Eu in natural samples using Bragg-type crystal analyzer system

In natural samples, relative concentrations of rare-earth elements (REEs) normalized by the concentration of appropriate materials such as chondrite are frequently employed to discuss the migration of REEs in various natural systems. Europium (Eu), one of the REEs, has been an important REE in geochemistry, since Eu can be present both as Eu(II) and Eu(III) under physicochemical conditions of the Earth [1]. The results of many studies have suggested that an anomalous abundance of Eu compared with neighboring REEs such as Sm and Gd (= Eu anomaly) is observed presumably because of the presence of Eu(II), which behaves similarly to divalent cations such as Ca(II) but distinctively different from other REES present exclusively as the trivalent form, except for Ce that can be present as Ce(IV) and which can be directly detected in natural samples such as by XANES [2]. However, it is difficult to detect Eu(II) in natural samples directly by such spectroscopic methods, except for several instances of minerals with high concentrations of Eu (20–700 ppm), such as apatite [1]. The Eu(II)/Eu(III) ratio has been utilized to estimate the redox condition in the aqueous environment in which these minerals were formed. However, Eu contents in normal crustal materials are typically lower than 1 ppm, which cannot be measured by the normal fluorescence XAFS technique. In particular, the detection limit is not determined by the Eu concentration itself, but by the interference of Mn Kα emissions (Kα_1 and Kα_2: 5.900 and 5.889 keV, respectively) on Eu Lα emissions (Lα_1: 5.849.5 keV) for the fluorescence XAFS measurement at the L_{III}-edge [3]. Thus, the separation of Mn Kα and Eu Lα is essential for the high-sensitivity measurement of Eu L_{III}-edge fluorescence XANES.

In high-sensitivity XANES analysis, high-energy-resolution fluorescence detection (HERFD)-XANES [4] is important not only for reducing interference fluorescence X-rays from coexisting elements, but also for sharpening the XANES peak, which enables us to separate peaks otherwise overlapped in normal XANES spectra, owing to the suppression of inner-shell lifetime broadening related to the core-hole lifetime effect, as shown in this study. Consequently, it is possible to identify peaks corresponding to minor species such as Eu(II) in natural samples.

In this study, we employed HERFD-XANES to investigate trace amounts of Eu in feldspar by developing a technique of fluorescence XANES measurement using a crystal analyzer in the Bragg geometry [3]. We previously conducted sensitive fluorescence XANES measurement using a bent crystal Laue-type analyzer (BCLA) for osmium-187 produced by the decay of rhenium-187 in molybdenite mineral [5]. However, this method in the Laue geometry is not effective for measuring Eu Lα emissions around 5.8 keV, since the thickness of the Si crystal employed for BCLA is typically 0.2 mm, which absorbs more than 99.9% of fluorescence X-rays at 5.8 keV. Thus, we applied the Bragg-type crystal analyzer for the sensitive measurement of Eu L_{III}-edge fluorescence XANES in natural samples [3]. Wavelength-dispersive fluorescence XANES at the Eu L_{III}-edge was measured at SPring-8 **BL39XU**. For this analysis, Eu Lα_1 emission was measured during the scan of the incident photon energy from 6.95 to 7.05 keV using 13 Ge 333 spherically bent crystals (diameter of 40 mm) and the PILATUS 100 K detector mounted on a Rowland circle of a diameter of 820 mm [6].

Natural samples JF-1, a standard rock issued by Geological Society of Japan (GSJ) prepared from natural feldspar (Ohira Feldspar) from Nagiso, Nagano, Japan, were employed. In addition, raw feldspar was also collected in the study area in Nagiso (JF-1-raw). REE patterns of JF-1 and JF-1-raw normalized by that of CI chondrite in Fig. 1 showed a distinct Eu positive anomaly, which suggests the presence of Eu(II) in the sample. Concentrations of Eu and Mn measured for JF-1 were 0.64 and 3.4 mg/kg, while those for JF-1-raw were 0.42 and 5.2 mg/kg, respectively. In addition to the very low concentration of Eu, a Mn/Eu ratio larger than 5 can make it difficult to measure Eu L_{III}-edge XANES. In this study, however, the effective separation

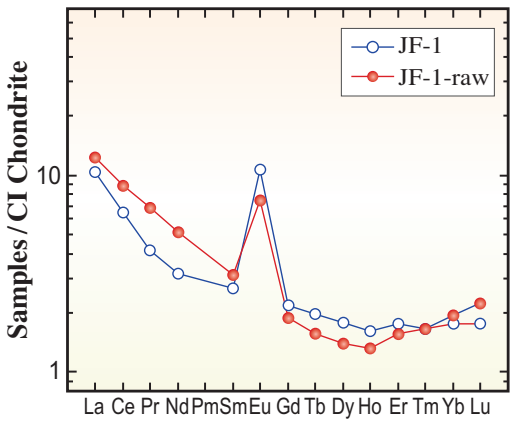

Fig. 1. Chondrite-normalized REE patterns for JF-1 (recommended and measured values).

of Eu $L\alpha_1$ from Mn Kα was attained by high-energy-resolution detection using the crystal analyzer system (Fig. 2). Consequently, the measurement of Eu L_{III}-edge XANES was possible for Eu at a concentration lower than 1 mg/kg in natural feldspar samples (Fig. 3).

The spectra of natural samples exhibit an intense peak at 6.983 keV assigned to Eu(III) with a small peak at 6.974 keV that can be assigned to Eu(II) [1]. The ratio of Eu(II) to Eu(III) was determined by fitting the Eu(II) and Eu(III) peaks in the spectra with a combination of Lorentzian and arctangent functions. As a result, the Eu(II)/Eu(III) ratios determined from the peak area ratio of the Lorentzian function were 0.010 and 0.015 for JF-1 and JF-1-raw, respectively. If we assume that (i) Eu_N^* (subscript N means the normalized value in Fig. 1) defined as $Eu_N^* = Sm_N^{0.5} \times Gd_N^{0.5}$ corresponds to Eu(II) and (ii) (Eu_N - Eu_N^*) to Eu(III), it is possible to estimate Eu(II)/Eu(III) from the REE pattern. The values were 4.0 and 2.1 for JF-1 and JF-1-raw, respectively, which are much higher than the 0.010 and 0.015 values determined by XANES. We suggest that the high Eu content in the feldspar relative to other REEs is caused by the (i) melting/dissolution of primary plagioclase with a positive Eu anomaly under the oxic condition and (ii) incorporation of Eu as Eu(III) into the feldspar samples during its crystallization/precipitation processes. Further study is needed to clarify the geochemical processes, but the high-sensitivity XANES analysis technique developed here is highly important for understanding the behavior of Eu in such natural systems.

HEFRD is effective for high-sensitivity XANES analysis based on (i) the decrease of the background level to measure the targeted fluorescence X-ray, such as a decrease of the interference of Mn in this study and (ii) the separation of independent peaks in XANES corresponding to different species owing to the sharpening of the XANES peak. HERFD-XANES spectra measured for Eu_2O_3 clearly reflected the sharpening effect, which makes it possible to observe clearly the Eu(II) peak in the XANES spectrum in Fig. 3, although the Eu(II) peak intensity is ca. 2% relative to that of Eu(III). The low detection limit of XANES analysis for trace amounts of Eu established in this study will contribute to a better understanding of the geochemical behavior of Eu, an important element among REEs.

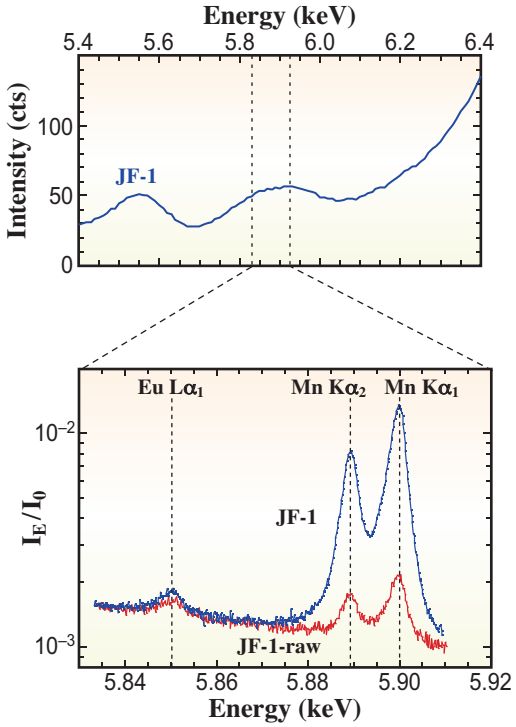

Fig. 2. X-ray fluorescence spectra (energy range from 5.83 to 5.91 keV) shown as I_E/I_0 (I_E: X-ray intensity determined by the PILATUS detector; I_0: intensity of incident X-ray) when irradiated at 7.05 keV.

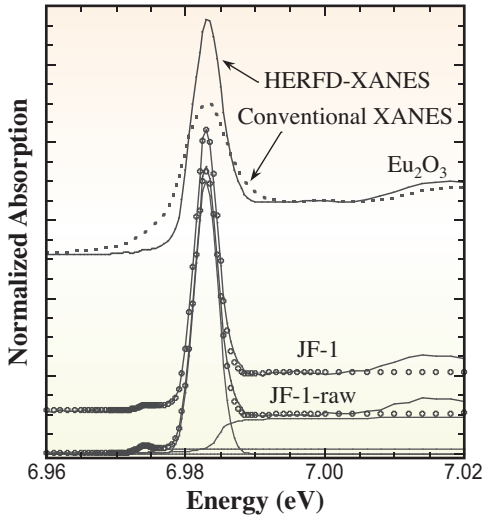

Fig. 3. Europium L_{III}-edge HERFD-XANES for Eu in Eu_2O_3, Eu in JF-1, and Eu in FJ-1-raw, and conventional XANES for Eu_2O_3 (dotted curve). Peak fitting results are shown as small circles for JF-1.

Yoshio Takahashi* and Rimi Konagaya

Department of Earth and Planetary Science,
The University of Tokyo

*Email: ytakaha@eps.s.u-tokyo.ac.jp

References

[1] Y. Takahashi *et al.*: Mineral. Mag. **69** (2005) 179.
[2] Y. Takahashi *et al.*: Geochim. Cosmochim. Acta **71** (2007) 984.
[3] *R. Konagaya, N. Kawamura, A. Yamaguchi and Y. Takahashi: Chem. Lett.* ***50*** *(2021) 1570.*
[4] Y. Takahashi *et al.*: Geochim. Cosmochim. Acta **71** (2007) 5180.
[5] R. Shimokasa *et al.*: Radiat. Phys. Chem. **175** (2020) 2018.
[6] O. Proux *et al.*: J. Environ. Qual. **46** (2017) 1146.

Widespread distribution of radiocesium-bearing microparticles from the Fukushima nuclear accident

The Fukushima Daiichi Nuclear Power Plant (FDNPP) accident in March 2011 emitted a considerable amount of radioactive materials. As a form of radioactive materials emitted from the FDNPP at the early stage of the accident, radiocesium-bearing microparticles (CsMPs) have been investigated by numerous researchers in recent years [1,2]. They are solid particles consisting primarily of silicate glass and contain trace amounts of various heavy elements associated with nuclear fuel and fission products (FPs). Because they do not easily dissolve in water, there is concern that they may have a long-term impact on the environment and human body.

A careful investigation of suspended particulate matter (SPM) collected hourly on filter tape at automated air pollution monitoring stations across Eastern Japan revealed that radioactive materials emitted from the FDNPP were transported over Eastern Japan via several major plumes during 12–23 March 2011 [3]. Among them, the second plume (P2) spread into the Kanto Plain, including the Tokyo metropolitan area, on 15 March. Hypothesizing that CsMPs were the major carrier of radioactive Cs in P2, we aim to verify the widespread distribution of CsMP in P2 over the greater Kanto Region (in and around the Kanto Region), focusing on how far CsMPs were transported southwest from the FDNPP. We examined radioactive aerosol particles from the SPM filter tape samples collected hourly on 15 March at several stations in the greater Kanto Region to compare their physical/chemical characteristics with those of previously reported CsMPs isolated from various environmental samples.

To nondestructively investigate the chemical characteristics of CsMPs isolated from the SPM filter tape samples in detail, multiple X-ray analyses using a synchrotron radiation microbeam (SR-μ) X-ray were conducted at SPring-8 **BL37XU** [4]. X-ray fluorescence (XRF) analysis using a high-energy SR-μ-X-ray was applied to carry out the nondestructive identification and qualitative detection of trace amounts of heavy elements within individual microparticles. The chemical state analysis of some metal elements in the particles was carried out by X-ray absorption near-edge structure (XANES) analysis. X-ray powder diffraction (XRD) analysis was also conducted to reveal the crystal structures of the particles. Brilliant X-rays from an advanced SR light source at SPring-8 enabled the use of a combination of these X-ray analytical techniques in a nondestructive manner.

Eight CsMPs were successfully isolated from SPM filter tape samples collected at seven monitoring stations (A–G) in the greater Kanto Region, including the Tokyo metropolitan area, on 15 March 2011 (see Fig. 1). The particles had a spherical shape with diameters of ~1 μm. Gamma-ray spectra of the eight particles indicated both ^{134}Cs and ^{137}Cs in each particle with activity ratios of ~1.0 (decay corrected as of March 2011), suggesting that these particles were emitted from either reactor No. 2 or 3 of FDNPP. As a result of the SR-μ-XRF analyses of individual particles, they were found to have qualitatively similar chemical compositions. The SR-μ-XRF spectra of four representative particles (A1, B1, C1, and E1) are shown in Fig. 2. The XRF analysis using a monochromatic SR-μ-X-ray with high energy (37.5 keV) for excitation can detect trace amounts of heavy elements within individual microparticles, although lighter elements (such as Si) that are major components of the particle could not be detected in the spectrum. In addition to sharp K-line peaks of Cs that had been identified by gamma-ray spectroscopy, the following eight heavy elements were detected in all particles: Fe, Zn, Rb, Mo, Sn, Sb, Te, and Ba. Several trace heavy elements (e.g., Zr, Ag, Cd, and U) specific to certain particles were also found. All elements identified in the CsMPs by SR-μ-XRF analyses can be associated with materials in the FDNPP: the nuclear fuel, FPs, and components of the reactors. The SR-μ-XANES analysis of the chemical states of four metal elements (Fe, Zn, Mo, and Sn) indicated that these elements exist as cations in silicate glass with high oxidation numbers, as

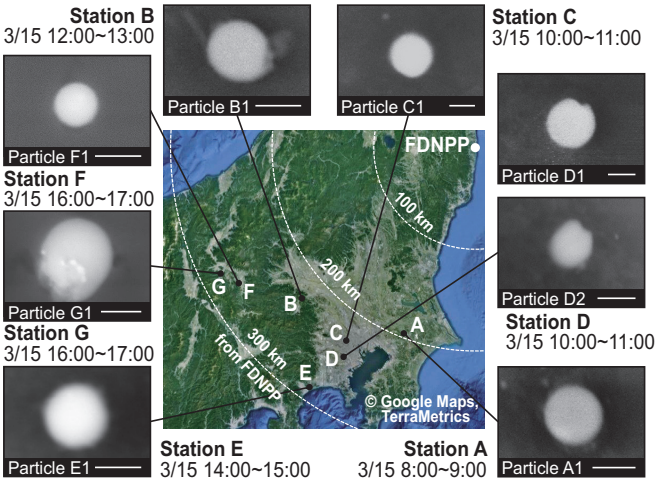

Fig. 1. Locations of monitoring stations A–G in the greater Kanto Region and eight radioactive particles isolated in this study. Collection times of the filters are shown for each station. The scale bars under the SEM images show a length of 1 μm.

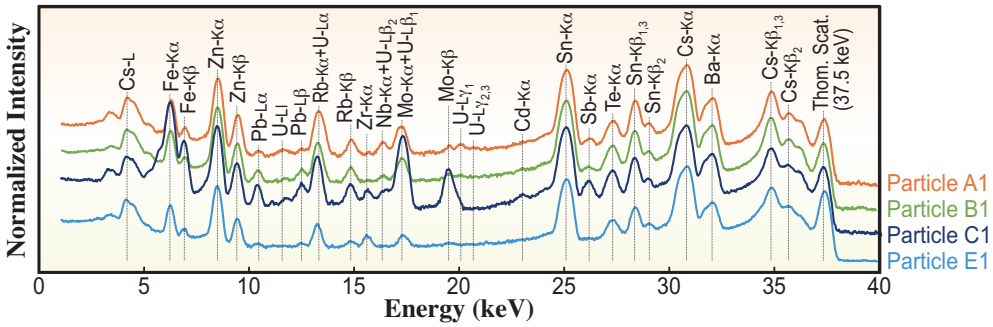

Fig. 2. SR-μ-XRF spectra of four representative CsMPs (A1, B1, C1, and E1). The intensities of each spectrum were normalized by the Thomson scattering peak and displayed on a logarithmic scale.

shown in Fig. 3. The SR-μ-XRD analysis of individual particles showed no diffraction peaks of a crystal structure for any of the particles, confirming that these particles have amorphous bodies.

Previously reported CsMPs can be categorized into two major types, type A and type B, based on the differences in physical/chemical characteristics [2]. All the analytical results on the eight CsMPs investigated in this study show that these particles are essentially the same as type A CsMPs. Type A CsMPs were first discovered from aerosols collected from the evening of 14 March to the morning of 15 March 2011 in Tsukuba, 170 km south-southwest of the FDNPP [1]. Since the discovery, a number of type A CsMPs have been identified from various environmental samples, mainly soils collected in Fukushima Prefecture. This is the first direct evidence demonstrating that type A CsMPs emitted from the FDNPP were widespread over the greater Kanto Region, farther than 250 km from the FDNPP, during the daytime of 15 March with a temporal resolution of one hour.

To estimate the emission time of type A CsMPs and identify their transport pathway(s) from the FDNPP to the greater Kanto Region, the trajectory analysis of air parcels that passed over the seven monitoring stations A–G was conducted. As a result, it was concluded that polluted air parcels containing type A CsMPs that passed over the greater Kanto Region on 15 March were emitted from the FDNPP between the evening of 14 March and the early morning of 15 March. Consistent with these estimated emission times, the pressure inside the reactor pressure vessel (RPV) in reactor No.2 decreased after the usage of a safety relief valve at around 19:03 JST on 14 March, followed by three sharp RPV pressure peaks at around 21:00 and 23:00 JST 14 March and 01:00 JST 15 March. At around 03:00 JST on 15 March, the pressure inside the primary containment vessel of reactor No.2 exceeded its designed value. In contrast, no incident was reported for reactor No.3 during the same period, except for a hydrogen explosion at 11:01 JST 14 March. It is therefore hypothesized that the incidents in reactor No. 2 were the most likely source of the type A CsMPs, rather than the hydrogen explosion in reactor No. 3.

Further investigation is necessary to estimate the environmental and health impacts of the CsMPs that travelled into the metropolitan area. Information regarding the widespread distribution of CsMPs can be useful toward calculating the inhalation dose of radionuclides during the early stage of the accident.

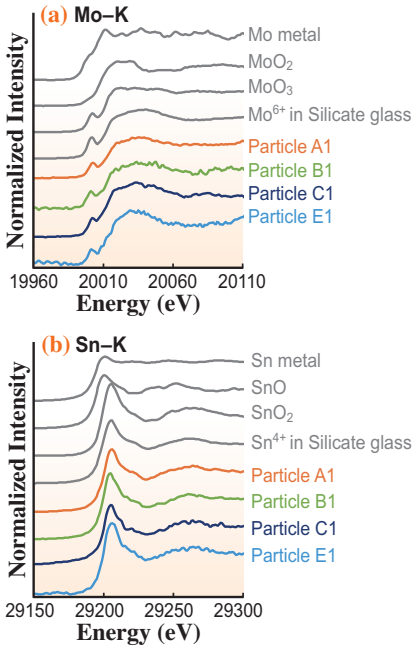

Fig. 3. SR-μ-XANES spectra of four representative CsMPs (A1, B1, C1, and E1) isolated from the SPM filter and reference materials. **(a)** Mo-*K* edge and **(b)** Sn-*K* edge.

Yoshinari Abe

Division of Material Science and Engineering,
Tokyo Denki University

Email: y.abe@mail.dendai.ac.jp

References

[1] K. Adachi *et al.*: Sci. Rep. **3** (2013) 2554.
[2] Y. Igarashi *et al.*: J. Environ. Radioact. **205-206** (2019) 101.
[3] H. Tsuruta *et al.*: Sci. Rep. **4** (2014) 6717.
[4] *Y. Abe, S. Onozaki, I. Nakai, K. Adachi, Y. Igarashi, Y. Oura, M. Ebihara, T. Miyasaka, H. Nakamura, K. Sueki, H. Tsuruta, Y. Moriguchi: Prog. Earth Planet. Sci. **8** (2021) 13.*

Identification of chemical species of iodine and mercury on iodine-impregnated activated carbon using X-ray absorption near-edge structure analysis

Mercury (Hg) is a global pollutant, and the significant adverse impacts caused by Hg and its compounds are of great concern. The Minamata Convention came into effect in August 2017 with the aim of protecting human health and the environment from the anthropogenic emission and release of Hg. Activated carbon (AC) is often used to remove Hg from various emission and release sources, but the capacity of virgin AC (AC-virgin) is limited. Because of the high cost of AC, it is often modified to enhance its capacity and for regeneration. AC impregnated with halogens exhibits excellent Hg^0 removal performance, and iodine-impregnated AC (I-AC) has high Hg^0 removal efficiency, low activation energy, and low volatility of the adsorption product, HgI_2, which increases the stability of the spent sorbent, compared with AC impregnated with other halogens such as Br and Cl.

The mechanism of the adsorption of Hg^0 by I-ACs, such as potassium iodide (KI)-impregnated AC, is via I_2, the formation of which is the key step in the chemisorption of Hg^0, as it reacts with Hg^0 to produce HgI_2. I_2 formation has been proposed to occur via the following reaction: $2\,KI + 1/2\,O_2 = K_2O + I_2$. However, starch–iodine tests showed that negligible I_2 is formed at temperatures lower than 300°C, and the Gibbs free energy of the proposed reaction has a positive value even at 1,000°C. Thus, whether I_2 can actually be formed in I-ACs remains unclear.

To elucidate the mechanism of Hg^0 adsorption by I-ACs, especially with regard to the occurrence and formation of I_2, we prepared a series of I-ACs with different iodine precursors including KI, NH_4I, and KIO_3 via one-step impregnation, denoted as AC-KI, AC-NH_4I, and AC-KIO_3, respectively [1]. Comparing AC-KI with AC-NH_4I and AC-KIO_3, we analyzed the effects of the cation element and valence state of iodine on Hg^0 removal. In an attempt to impregnate the AC with I_2 by the reaction $2\,CuSO_4(aq) + 4\,KI(aq) = 2\,CuI(s) + I_2(s) + 2\,K_2SO_4(aq)$, we conducted the co-impregnation of KI followed by $CuSO_4$. The product is denoted as AC-KI + $CuSO_4$. AC-virgin without any precursors was used as the reference material for evaluating the Hg^0 removal performance. We conducted X-ray absorption near-edge structure analysis (XANES) for iodine and Hg at SPring-8 **BL01B1**.

The iodine XANES spectra (Fig. 1) of AC-KI, AC-NH_4I, and AC-KI + $CuSO_4$ before and after the adsorption test were very similar. No similarity was detected between the sorbents and their precursors, KI, NH_4I, and CuI. As the spectrum of I_2 contained no distinct features (Fig. 1), we could not determine whether I_2 was present in the I-AC samples from only the iodine *K*-edge spectra. Thus, we conducted the linear combination fitting (LCF) of the XANES data for I-ACs prior to the adsorption test, applying principal component analysis (PCA) to exclude irrelevant reference materials from the spectra. I_2 accounted for approximately 9–16% of total iodine in these sorbents. Notably, the ranking of I_2 fractions among the I-ACs was consistent with the order of Hg^0 removal efficiency, which was as follows: AC-KI + $CuSO_4$ ≈ AC-NH_4I > AC-KIO_3 > AC-KI. Therefore, I_2 was confirmed to play an important role in Hg^0 removal by I-ACs. The formation of I_2 may occur during impregnation, drying (before the adsorption test), and adsorption. However, our results indicated no I_2

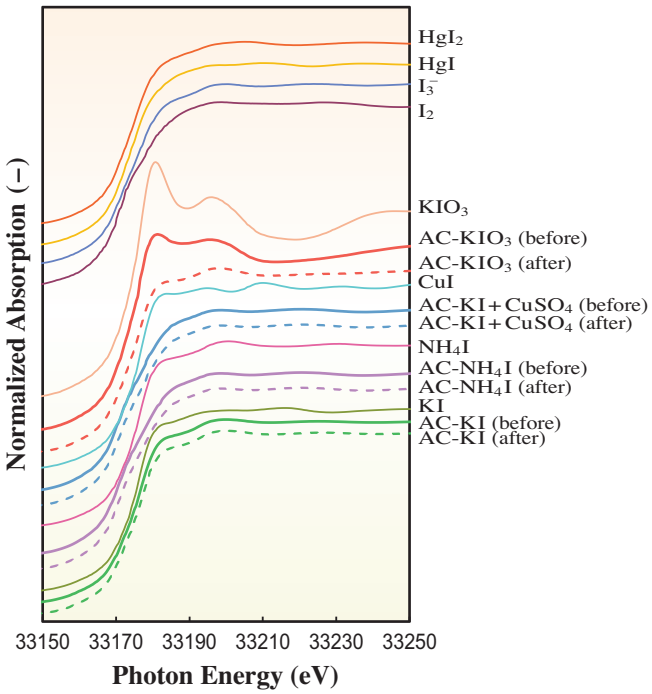

Fig. 1. Iodine *K*-edge X-ray absorption near-edge structure (XANES) spectra for reference materials (solid KI, solid NH_4I, solid CuI, solid KIO_3, solid I_2, I_3^- ion, solid HgI, and solid HgI_2) and impregnated ACs (AC-KI, AC-NH_4I, AC-KI+$CuSO_4$, and AC-KIO_3) before and after adsorption test (E_0 = 33,172 – 33,174 eV).

in AC-KI; instead, I_3^- and KI were detected. The LCF results revealed larger proportions of I_3^- in all I-ACs. Notably, sorbents with greater Hg^0 removal efficiency, namely, AC-KI + $CuSO_4$ and AC-NH_4I, contained larger fractions of I_3^- than did the other sorbents. Thus, in addition to I_2, I_3^- may serve as an I_2 donor and play an essential role in Hg^0 removal by I-ACs. Moreover, as the reaction of I_3^- with starch produces a black-blue color, I_3^- formation may have improved the Hg^0 removal performance in previous studies, in which KI was used as the impregnation precursor and the starch test was employed for I_2 detection.

We investigated the Hg species present after I-AC adsorption, which was assumed to be HgI_2 in previous research. The Hg L_{III}-edge XANES analysis of sorbents was conducted after the Hg^0 adsorption test to determine the chemical species of Hg (Fig. 2). Two references, $HgCl_2$ and $HgSO_4$, produced a marked shoulder peak at 12,282 eV; this shoulder peak was also produced by AC-virgin, which contains Cl and S, but not by the I-ACs. Therefore, $HgCl_2$ and $HgSO_4$ may have been present in AC-virgin, not adsorption products of I-ACs. LCF was conducted after PCA and target transformation to confirm the species of Hg in the spent sorbents and their ratios. The main species of Hg in I-ACs in this study were HgI_2 and HgI, with a higher proportion of HgI_2 than of HgI. The mechanism of HgI_2 generation in I-ACs, according to the adsorption test results, can be explained as follows. In I-ACs, HgI is more readily formed than HgCl because of its lower activation energy. This HgI can be further oxidized into HgI_2 by I_2, which is released from I_3^-. HgI_2 can also be formed via the direct oxidation of Hg^0 by I_2. Furthermore, HgI_2 is more stable than $HgCl_2$, which is in accord with our finding that HgI_2, rather than $HgCl_2$, dominates the I-AC samples.

In this study, the main Hg removal mechanism was clear from both the I-*K* and Hg-L_{III}-edge XANES spectra. The results were supported by those of other analyses such as X-ray diffraction and X-ray photoelectron spectroscopy. Future research should focus on the stability and regeneration of the spent sorbents.

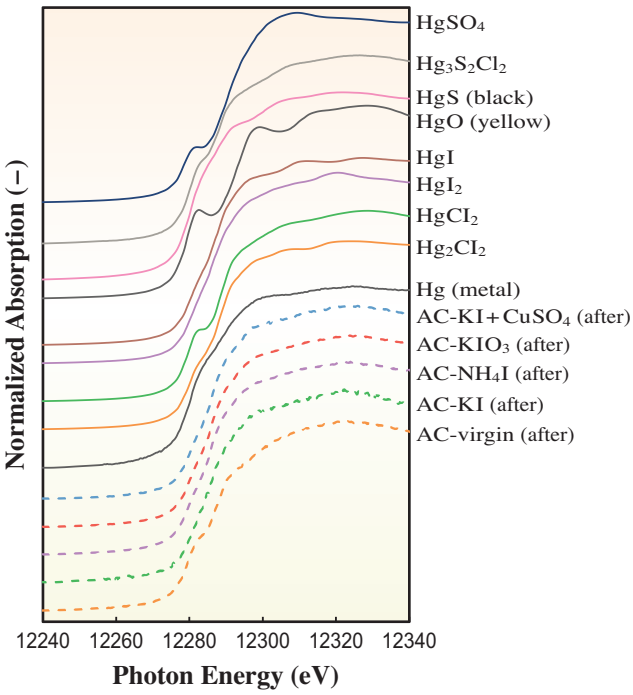

Fig. 2. Mercury L_{III}-edge XANES spectra for reference materials (metallic mercury, solid Hg_2Cl_2, solid $HgCl_2$, solid HgI_2, solid HgI, solid HgO [yellow], solid HgS [black], solid $Hg_3S_2Cl_2$, and solid $HgSO_4$), AC-virgin, and impregnated ACs (AC-KI, AC-NH_4I, AC-KIO_3, and AC-KI + $CuSO_4$) after adsorption test (E_0 = 12,284 eV).

Yingchao Cheng[a,b], Kenji Shiota[b] and Masaki Takaoka[b,*]

[a] National Institute for Environmental Studies
[b] Department of Environmental Engineering, Kyoto University

*Email: takaoka.masaki.4w@kyoto-u.ac.jp

References

[1] *Y. Cheng, K. Shiota, T. Kusakabe, K. Oshita, M. Takaoka: Chem. Eng. J.* ***402*** *(2020)126225.*

Broad-band high-energy-resolution hard X-ray spectroscopy using transition edge sensors (TESs) and its application to environmental samples

Speciation, the identification of chemical species of any elements in environmental samples, is basic information necessary to understand and predict the environmental behaviors of elements [1]. For example, the redox state and chemical bonding to neighboring atoms of an element of interest are essential for characterizing the element, such as its water solubility, toxicity to biota, and effect on climate change. X-ray absorption fine structure (XAFS) spectroscopy including X-ray absorption near-edge structure (XANES) and extended X-ray absorption fine structure (EXAFS) have been used as one of most powerful techniques for clarifying such information. In particular, XAFS measurement in the fluorescence mode by detecting X-ray fluorescence (XRF) has been widely used for trace elements in environmental and geochemical samples. However, there have been many cases where we cannot measure XAFS because of interference from the XRF of other elements and scattered X-rays even when using an energy-dispersive detector such as a silicon drift detector (SDD) with an energy resolution of around 130 eV.

Here, we have succeeded in operating a transition-edge sensor (TES) spectrometer to overcome the difficulties of interference at SPring-8 **BL37XU** [2]. The TES spectrometer consists of a 240-pixel NIST TES system with an energy resolution of 5 eV at 6 keV [3], which is an energy resolution that is more than 20 times higher than that of SDD. On the other hand, the count rate of X-ray allowed for the TES is generally around 1 count/s/pixel. The performance of the TES is studied over the energy range of 4–13 keV using a Mn target with different count rates and a Pb target with various beam energies. The energy resolution, which could depend on the template and its calibration lines, is approximately 6 eV at 6 keV at the total count rate of <2000 c/s, while it becomes a few 10 eV above 10 keV.

To demonstrate the capabilities of TES at BL37XU, a NIST standard silicate glass (NIST610) spiked with 61 trace elements was used as a target. The XRF spectra of NIST610 measured with the TES (sum of 220 pixels) and SDD are shown in Fig. 1. The spectrum obtained with the SDD is composed of some sharp peaks corresponding to K lines, for example, Fe (6.4 keV), Co (6.9 keV), and Ni (7.5 keV), but the spectrum obtained with the TES revealed that each peak actually consists of L lines of various lanthanides, which shows that the use of the TES enables us to detect L lines of heavier elements, which are usually hidden by K lines of transition elements when measured with the SDD.

Fluorescence XANES analysis using the TES spectrometer was conducted for a synthetic sample (NIST610) and natural materials that contained various elements. Among the elements of interest in environmental sciences, arsenic (As) and lead (Pb) are the most important in terms of their health risk and wide occurrence in the earth's crust. The two elements frequently coexist in specific environments such as sulfide mine tailing and coal [4], which warrants the study of the environmental chemistry of the two elements in the same system. However, the determination and speciation of the two elements in the same sample can sometimes be troublesome when using XRF and XAFS because of the difficulty in separating the As Kα and Pb Lα emissions, since the energy resolution of the SDD is insufficient for adequately resolving the lines. Thus, the Pb L_{III} edge

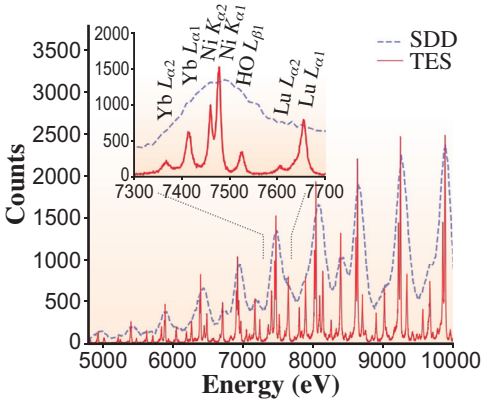

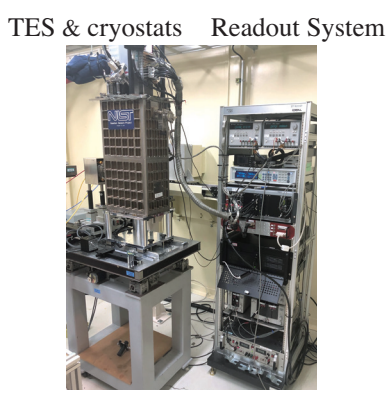

Fig.1. **(a)** Spectra of SRM610 taken with TES (red) and SDD (blue). **(b)** Experimental setup of TES system in BL37XU.

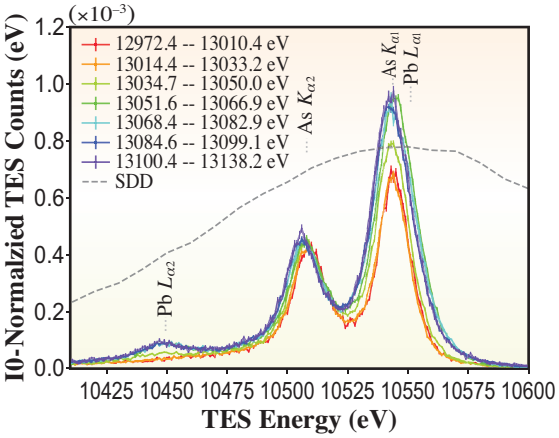

Fig. 2. X-ray emission spectra of TES spectrometer with seven different X-ray energies illuminating a sample of SRM 610 across the Pb L_3-edge (13035 eV). The SDD spectrum is overlaid as the dashed line.

XANES was measured using the TES to evaluate its potential for the chemical diagnosis of the heavy elements in complicated materials. As shown in Fig. 2, Pb Lα and As Kα severely interfere with each other and they cannot be resolved even by using the TES. In this case, it is effective to focus on Pb Lα$_2$, which is free from the interference of As K lines, to measure the Pb L_{III}-edge (Fig. 3). Note that the speciation of As using its *K*-edge XAFS does not interfere with Pb, since the absorption edges of Pb are higher than the As *K*-edge. However, there is a huge demand for the speciation of Pb in the presence of As. Thus, fluorescence XAFS using the TES is worth considering as an option for samples containing both As and Pb.

Another application of the TES is to measure a small quantity of material. Its high resolution can help to resolve the elements from the background and mitigate the risk of misinterpreting the spectra. Here, we chose iron (Fe) in aerosols sampled above the sea, since Fe at the sea surface supplied from marine aerosols affects marine bioproductivity, which is linked to the absorption of carbon dioxide by seawater and, in turn, to climate change. Moreover, the dissolution rate of Fe in marine aerosols in seawater is important in the quantification of the amount of Fe available to biota, which can be assessed by the speciation of Fe [5]. However, the amount of Fe in aerosols collected on aerosol filters is very small, as interfered from the scattered X-rays. The fluorescence XANES spectrum of Fe in marine aerosols collected on the filter was obtained using the SDD and TES. The TES XRF spectra showed a better signal-to-background ratio (the ratio of I0-normalized counts at the peak and pre-edge energies; ~5.2) than the SDD spectra (~1.1) because of the low interference of scattered X-rays and contamination. As a result, a fluorescence XANES at the Fe *K*-edge was successfully obtained, which will enable us to discuss the water solubility of Fe in the aerosol samples.

This study is the first important step toward the application of high-resolution spectroscopy for XRF and XAFS analyses in hard X-ray synchrotron facilities. The development of the TES is rapidly progressing; thus, its performance will improve in terms of the number of pixels, the effective area, and the energy range. In particular, further improvement of the energy resolution of TES technology approaching 1 eV as well as increasing the total count rate will make it a practical instrument for a high-energy-resolution fluorescence-detected XANES, which is a distinctive spectroscopy tool that can provide more information on electronic states than a normal XANES, in the future.

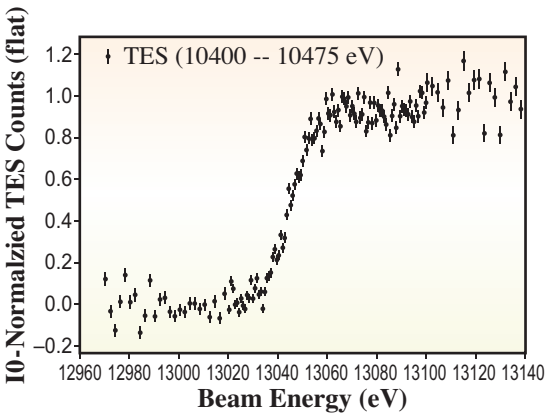

Fig. 3. XANES of Pb Lα$_2$ obtained by using TES with 10400 eV – 10475 eV.

Shinya Yamada[a,*] and Yoshio Takahashi[b]

[a] Department of Physics, Rikkyo University
[b] Department of Earth and Planetary Science, The University of Tokyo

*Email: syamada@rikkyo.ac.jp

References

[1] G.E. Brown and N.C. Sturchio: Review in Mineralogy & Geochemistry **49** (2002) 1.
[2] *S. Yamada, Y. Ichinohe, H. Tatsuno, R. Hayakawa, H. Suda, T. Ohashi, Y. Ishisaki, T. Uruga, O. Sekizawa, K. Nitta, Y. Takahashi, T. Itai, H. Suga, M. Nagasawa, M. Tanaka, M. Kurisu, T. Hashimoto, D. Bennett, E. Denison, W.B. Doriese, M. Durkin, J. Fowler, G. O'Neil, K. Morgan, D. Schmidt, D. Swetz, J. Ullom, L.R. Vale, S. Okada, T. Okumura, T. Azuma, T. Tamagawa, T. Isobe, S. Kohjiro, H. Noda, K. Tanaka, A. Taguchi, Y. Imai, K. Sato, T. Hayashi, T. Kashiwabara, K. Sakata: Rev. Sci. Instrum.* ***92*** *(2021) 013103.*
[3] F. Aharonian *et al.*: Nature **535** (2016) 117.
[4] J.R. Davenport and F.J. Peryea: Water Air Soil Pollut. **7** (1991) 1.
[5] M. Kurisu *et al.*: J. Geophys. Res. **121** (2016) 11119.

Ultrafast structure transformation of olivine to ringwoodite during laser-driven shock compression

Rocky terrestrial planets, as represented by Earth, were considered to form as consequences of numerous impact events of small planetary bodies 4.6 billion years ago. These events had continued until the completion of planet formation within a dusty disk surrounding the young sun. Although we cannot find any materialistic evidence of these early impact events in the rocks and minerals composing the current Earth, a number of topographical records remaining on surfaces of other smaller bodies in space consistently show that ancient impact events played essential roles in the growth of all solar system bodies. Indeed, many asteroids, for example, have numerous craters left over from ancient impact events, and there is a possibility that the materials in these craters had preserved another type of evidence induced by impact compression. In other words, it is reasonable to expect that the impact events were recorded as not only macroscopic geological evidence such as craters, but also as nanoscopic crystallographic evidence such as rearrangements of mineral structures. The most typical type of evidence of the latter type is the presence of high-density silicate structures within primitive meteorites that were formed in the early solar system and then remained in space until very recently [1].

Olivine [α-$(Mg,Fe)_2SiO_4$] is one of the most popular silicate minerals found on terrestrial planets and other rocky bodies in the solar system. It was previously reported that a fraction of this mineral in some primitive meteorites was transformed into denser structures named wadsleyite [β-$(Mg,Fe)_2SiO_4$] and ringwoodite [γ-$(Mg,Fe)_2SiO_4$] [1]. We have recently discovered that a portion of such natural ringwoodite was once again transformed into another dense structure, ε-$(Mg,Fe)_2SiO_4$, a new mineral that was not observed in the previous research and was named poirierite [2,3]. The macroscopic form of these meteorites containing the dense silicates is often extensively deformed, implying that they had been subjected to shock compression events induced by mutual collisions between their parent asteroids. During these natural shock events, minerals experienced dynamic high-pressure environments where the pressure rapidly increased and decreased with time. We aim to determine these pressure values and their durations induced by such events that triggered the crystallization of the denser minerals. Such work will provide invaluable information for understanding the early evolution history of the solar system. For this purpose, it is necessary to determine the relevant structure transformation mechanism and kinetics that occurred in transient high-pressure environments. Therefore, an ultrafast time-resolving X-ray probe was introduced to analyze the evolution of the crystal structure in laboratory-based shock experiments designed to reproduce the impact events.

The experiments were conducted at SACLA **BL3** EH5, where the formation of a ringwoodite structure within a shock-compressed olivine crystal was observed [4]. Schematic diagrams in Fig. 1 show the experimental setup and the observed structure transformation process. Using a high-power laser system installed onsite at SACLA, a single-crystal sample of synthetic forsterite olivine [α-Mg_2SiO_4] was compressed to reach pressures of 60 to 100 GPa. An optical laser pulse of 532 nm wavelength with a full width at half-maximum of 3.3 ± 0.2 ns was focused into a beam of about 250 μm diameter on the target. A hydrocarbon ablator absorbed this pulse to generate a shock wave that propagated into the olivine crystal to compress its lattice, comprising Mg, Si, and O atoms, along the propagation direction of the wave; this direction was set parallel to the *a*-axis of olivine, as shown in Fig. 1. A femtosecond 10-keV XFEL pulse was focused to be spatially and temporally overlapped with the shock-compressed sample volume. An X-ray diffraction image was immediately obtained to record the crystal structure under shock compression. The experiments were repeated with the variable delay time of the XFEL pulse from the optical laser pulse to analyze the time evolution of the sample structure. Taking into account the crystal axis orientations and the compression direction, as well as the incident angle of the XFEL pulse ω, the time evolution of the specific reflection (such as $g = 200$ or 300) of olivine was set to be selectively observed as a function of time.

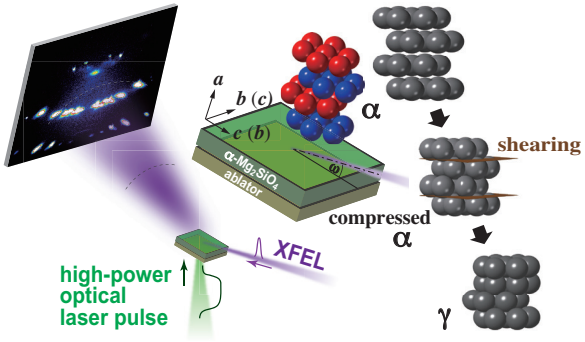

Fig. 1. Experimental setup at SACLA BL3 for analyzing time evolution of forsterite structure under compression, and the observed transformation process.

Figure 2(a) shows the evolution of $g = 200$ as a function of delay time t after the laser pulse arrived on the ablator. Figure 2(b) shows the corresponding one-dimensional diffraction patterns as a function of $d = \lambda/2\sin\theta$. In the olivine structure, oxygen atoms were hexagonally close-packed. The 2θ of the spotty reflections observed in Fig. 2(a) indicates the interlayer distance d_{200}. When the shock wave arrived at olivine at $t = 4$ ns, the position of d_{200} was suddenly shifted to indicate its reduction by shock compression, where it was split into two spots marked with E and P. These were from the regions compressed by the elastic (E) and plastic (P) waves both propagating through the olivine crystal. Both waves decayed with time as they propagated, and the oxygen interlayer distances in these regions were consistently increased. On the other hand, at $t \geq 7$ ns, another reflection marked with D suddenly emerged. It originated from a region of denser structure produced by a third wave that induced the transformation as it propagated. It appeared on the compressed side of P, indicating that the transformed structure had a distinctively higher density than that of the compressed olivine (including both E and P). Its intensity rapidly increased between $t = 6$ ns and 8 ns, indicating that the denser structure crystallized within a duration of a few nanoseconds, where the two cation species, in addition to the oxygen anions, were all appropriately rearranged. Such a complex process has never been observed at this time scale. While olivine has a hexagonal close-packed lattice of oxygen, any of the possible denser structures has a cubic close-packed lattice [2,3]. For this reason, the transformation mechanism must involve the shear deformation of oxygen layers while maintaining their orientation (Fig. 1). Indeed, this is what we observed in Fig. 2(a); it is therefore reasonable to conclude that the ultrafast shear deformation was actually induced. By further analysis of the atomic-scale transformation mechanism from the time evolution of another reflection, $g = 300$ [4,5], it was proved that the product structure was ringwoodite rather than wadsleyite or poirierite.

In summary, an ultrafast transformation mechanism of olivine to ringwoodite through shear deformation is driven efficiently by impact events without any limitation on the minimum body size, as long as the relative velocity between asteroids exceeds the threshold; the transformation proceeds through collisions of meter-sized bodies where the minerals are compressed within microseconds, which is still sufficient to drive the shearing. We suggest that the occurrences of nanoscale platelike dense minerals observed in natural olivine crystals may indicate their having experienced such a collision [4]. Pressure values of 60 to 100 GPa correspond to relative velocities of 5 to 7 km/s, which are the most common in the asteroid belt observed today. If we can extract such a record of the collision history and collision velocity by observing a wide variety of planetary materials, our understanding of the history of material evolution in the solar system will be markedly modified.

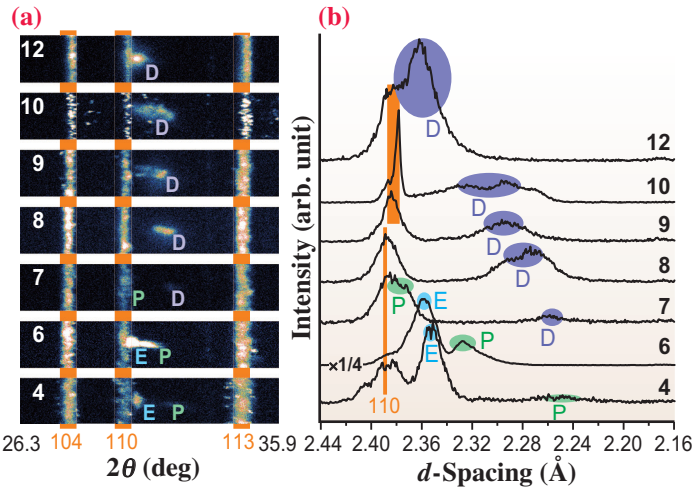

Fig. 2. **(a)** Time evolution of the X-ray diffraction image around the $g = 200$ reflection. The numbers indicate the delay t of the XFEL pulse in nanoseconds where the laser pulse started at $t = 0$. E, P, and D denote reflections originating from the regions compressed by elastic, plastic, and phase transition waves, respectively. In all three regions, the interlayer distance of oxygen stacking layers (see Fig. 1) was compressed parallel to the a-axis direction of forsterite. In these experiments, a thin sheet of polycrystalline Al_2O_3 was attached to the back of the target to indicate the arrival time of the shock wave after it passed through the forsterite. The three orange-indexed lines came from this Al_2O_3 layer. **(b)** X-ray diffraction patterns integrated from (a) as a function of $d = \lambda/2\sin\theta$, where λ is the wavelength (1.24 Å) and θ is the diffraction angle. Note that d decreases to the right.

Takuo Okuchi

Institute for Integrated Radiation and Nuclear Science, Kyoto University

Email: okuchi@rri.kyoto-u.ac.jp

References

[1] P. Gillet and A.E. Goresy: Ann. Rev. Earth Planet. Sci. **41** (2013) 257.
[2] N. Tomioka and T. Okuchi: Sci. Rep. **7** (2017) 17351.
[3] N. Tomioka *et al.*: Commun. Earth Environ. **2** (2021) 16.
[4] *T. Okuchi, Y. Seto, N. Tomioka, T. Matsuoka, B. Albertazzi, N.J. Hartley, Y. Inubushi, K. Katagiri, R. Kodama, T.A. Pikuz, N. Purevjav, K. Miyanishi, T. Sato, T. Sekine, K. Sueda, K.A. Tanaka, Y. Tange, T. Togashi, Y. Umeda, T. Yabuuchi, M. Yabashi and N. Ozaki: Nat. Commun.* ***12*** *(2021) 4305.*
[5] Y. Seto and M. Ohtsuka: J. Appl. Cryst. **55** (2022) 397.

Akimotoite-bridgmanite phase transition explains depressed 660-km seismic discontinuity in subduction zones

The seismic wave velocities abruptly increase at depths around 660 km in the Earth's interiors, referred to as the 660-km seismic discontinuity, separating the Earth's upper and lower mantles. One of the prominent features of the 660-km discontinuity suggested by seismology is significant depression down to 750 km structure beneath cold subduction zones [1]. This discontinuity is interpreted as the dissociation of $(Mg,Fe)_2SiO_4$ ringwoodite to $(Mg,Fe)SiO_3$ bridgmanite plus (MgFe)O ferropericlase. An earlier study reported that this reaction boundary has a negative slope, and the depression of the 660-km discontinuity in cold regions was orthodoxly interpreted by this slope [2]. However, a later study demonstrated that the slope of the ringwoodite dissociation is very gentle and cannot explain the significant depression in cold regions [3]. Thus, another phase transition with a steep negative slope is required to interpret the discontinuity depression. We hypothesized that the akimotoite-bridgmanite in $(Mg,Fe)SiO_3$ transition can cause the 660-km discontinuity depression in cold regions because akimotoite is a dominant mineral in cold regions of the bottom of the upper mantle.

In the current study [4], we determined the boundaries of the ringwoodite dissociation to bridgmanite plus periclase and akimotoite–bridgmanite phase transition in the MgO-SiO_2 system over a temperature range of 1250–2085 K using advanced multi-anvil techniques with *in situ* X-ray diffraction at SPring-8 **BL04B1** and P61B at DESY. In these experiments, we first synthesized higher-pressure assemblages (bridgmanite and bridgmanite plus periclase) at the lowest possible temperature in separate runs, and these assemblages were partially converted at the beginning of synchrotron experiments to lower-pressure assemblages also at the lowest possible temperature (Fig. 1). This method provided coexisting higher- and lower-pressure assemblages synthesized at the lowest temperature, which is essential because silicates become very inert once high-temperature conditions are experienced. Then, we observed the higher- and lower-pressure assemblages using *in situ* X-ray diffraction at spontaneously and gradually decreasing pressure and a constant temperature in a multi-anvil press. Stable assemblies were determined based on the relative increases/decreases in the ratio of their diffraction intensities (Fig. 1). Examples of the change in intensity ratio are shown in Fig. 2. We repeated this procedure with 50-K steps to determine the transition boundaries

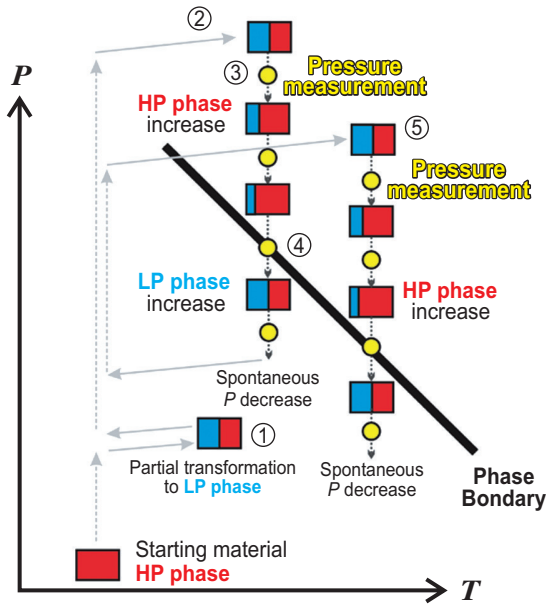

Fig. 1. Experimental strategy. The pressure spontaneously and gradually decreases while keeping the temperature and press load constant. In the high-pressure (HP) and low-pressure (LP) phase stability fields, the HP and LP phases increase with time to bracket the phase boundary. The numbers in the circles indicate the step numbers in the new strategy explained above.

tightly. Since this strategy strictly follows the principle of phase equilibrium, problems in determining phase stability caused by sluggish kinetics and surface energy are excluded.

The experimental results showed that the ringwoodite-dissociation boundary has a slightly concave curve, whereas the akimotoite-bridgmanite boundary has a steep convex curve (Fig. 3). The ringwoodite-dissociation boundary is located at pressures of 23.2–23.7 GPa in the temperature range of 1250–2040 K. Its slope varies from –0.1 MPa/K at temperatures less than 1700 K to –0.9 MPa/K at 2000 K with an averaged value of –0.5 MPa/K. The ringwoodite-dissociation boundary was thus found in agreement with previous experiments [3]. The slope of the akimotoite-bridgmanite boundary gradually changes from –8.1 MPa/K at low temperatures up to 1300 K to –3.2 MPa/K above 1600 K. The akimotoite-bridgmanite boundary intersects with the ringwoodite-dissociation boundary at 1260 K and around 24 GPa, which corresponds to 660 km depth (Fig. 3). Based

on these findings, we predict that, beneath cold subduction zones, ringwoodite should first dissociate into akimotoite plus periclase at around 660 km depth, and then akimotoite transforms to bridgmanite at greater depth. Furthermore, seismological studies also reported that the 660-km discontinuity is doubled in cold regions such as Tonga subduction zone, which is interpreted by the succession of dissociation of ringwoodite to akimotoite plus periclase and the akimotoite-bridgmanite transition (Fig. 3). Beneath warm subduction zones such as Peru, ringwoodite dissociates into bridgmanite plus periclase (Fig. 3).

The current results also have significant geodynamic implications since steep phase transition boundaries produce large buoyancy in slab dynamics [5]. When the upward buoyancy produced by the negative phase boundary exceeds the downward force due to the thermal expansion, mantle flows are hampered, and slabs stagnate above the 660-km discontinuity. Therefore, the steep negative boundary of the akimotoite-bridgmanite transition should result in cold-slab stagnation, which is supported by the seismological observations beneath cold (e.g., Tonga, Izu-Bonin) subduction zones.

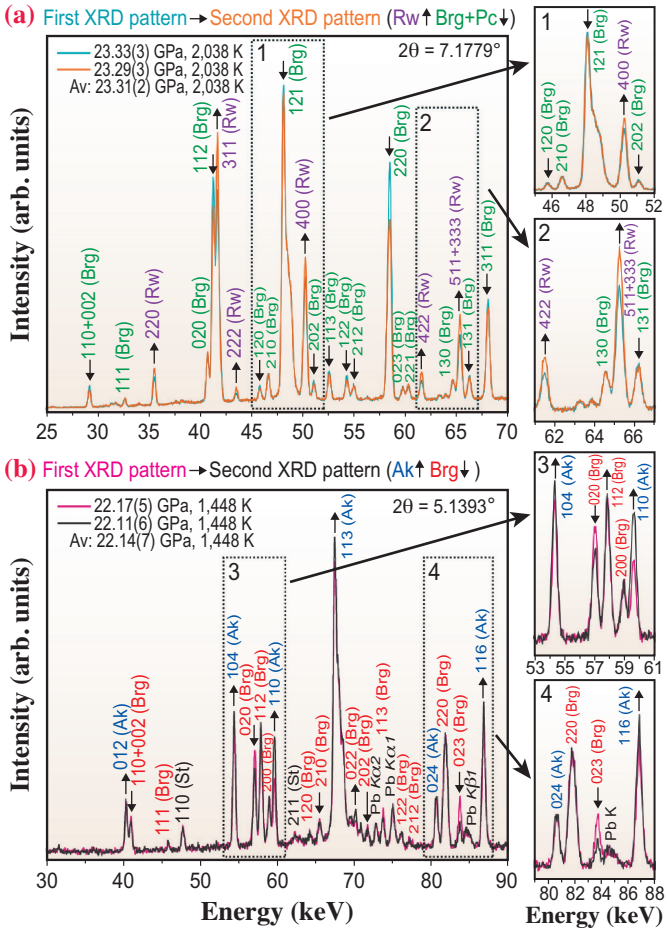

Fig. 2. **(a)** An example of the change of intensity ratio between ringwoodite and bridgmanite plus periclase at 2038 K and 23.31(2) GPa. **(b)** An example of the change of intensity ratio between akimotoite and bridgmanite at 1448 K and 22.14(7) GPa. The first diffraction patterns are shown in (a) blue and (b) pink, and the second patterns are displayed in (a) orange and (b) dark gray. The upward and downward arrows, respectively, indicate the peaks with increased and decreased intensities in the second diffraction patterns.

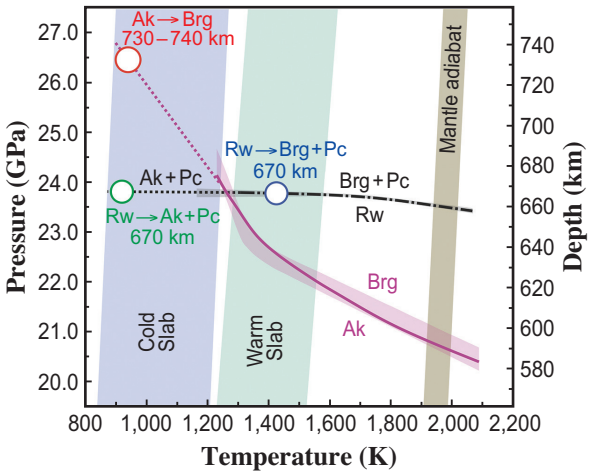

Fig. 3. Comparison of the ringwoodite dissociation and akimotoite–bridgmanite phase transition boundaries. Ak–$MgSiO_3$ akimotoite, Brg–$MgSiO_3$ bridgmanite, Pc–MgO periclase, Rw–Mg_2SiO_4 ringwoodite. Green, blue and red circles indicate Rw→Ak+Pc dissociation at 670 km depth, Rw→Brg+Pc dissociation at 670 km depth and Ak→Brg transition at 730–740 km depth, respectively.

Artem Chanyshev*, Takayuki Ishii and Tomoo Katsura

Bayerisches Geoinstitut, University of Bayreuth, Germany

*Email: artem.chanyshev@uni-bayreuth.de

References

[1] A. Deuss *et al.*: Science **311** (2006) 198.
[2] E. Ito and E. Takahashi: J. Geophys. Res. **94** (1989) 10637.
[3] T. Katsura *et al.*: Phys. Earth Planet. Inter. **136** (2003) 11.
[4] *A. Chanyshev, T. Ishii, D. Bondar, S. Bhat, E.J. Kim, R. Farla, K. Nishida, Z. Liu, L. Wang, A. Nakajima, B. Yan, H. Tang, Z. Chen, Y. Higo, Y. Tange and T. Katsura: Nature* ***601*** *(2022) 69.*
[5] G. Schubert *et al.*: Geophys. J. Int. **42** (1975) 705.

Crystal chemistry of bridgmanite in a subducting mid-ocean ridge basalt: incorporation mechanism of Fe and Al

Bridgmanite (simplified formula $MgSiO_3$) is the most abundant constituent in the Earth's lower mantle and crystallizes in an orthorhombic perovskite-type structure with space group *Pbnm* (Fig. 1). Pressure, temperature, and chemical dependences of its physical and crystal-structure properties provide essential information for a detailed understanding of the lower mantle. In particular, the effects of the incorporation of Fe and Al, the next major mantle elements after Mg and Si, into bridgmanite can have a large effect on the physical properties and rheology of the lower mantle.

Bridgmanite formed from a mid-ocean ridge basalt (MORB) component of subducting slabs contains larger amounts of Fe and Al than that formed from a pyrolytic composition [1]. This difference in bridgmanite composition can cause a difference in the incorporation mechanism of Fe and Al into the crystal structure between subducting slabs and their surrounding lower mantle. This should cause heterogeneity in the physical properties and rheology of the lower mantle. Elucidating the crystal chemistry of bridgmanite formed from the MORB composition is a key to resolving this issue. The precise crystal chemistry examined employing a single crystal is, therefore, significant for gaining a detailed understanding of lower-mantle dynamics. In particular, the use of ^{57}Fe-Mössbauer spectroscopy is indispensable for distinguishing the valence and spin states of Fe, which cannot be directly observed by X-ray diffraction. For this purpose, we characterized a bridgmanite single-crystal with the Fe and Al contents expected in MORB, by a combination of single-crystal X-ray diffraction, synchrotron ^{57}Fe-Mössbauer spectroscopy, and electron probe microanalysis (EPMA) [2].

Single crystals of bridgmanite were synthesized at 28 GPa and 1873 K using a Kawai-type multianvil apparatus. The experiment was conducted in a bulk composition of $0.650MgO \cdot 0.175Fe_2O_3 \cdot 0.650SiO_2 \cdot 0.175Al_2O_3$, which is close to that reported for bridgmanite formed from the MORB composition. The zero-pressure/room-temperature crystal structure was determined and refined using single-crystal X-ray diffraction intensities collected with a four-circle diffractometer having a laboratory Mo-$K\alpha$ radiation source. Energy-domain synchrotron ^{57}Fe-Mössbauer spectroscopy measurements at room temperature using a nuclear Bragg monochromator were conducted at SPring-8 **BL10XU**.

The EPMA of synthesized crystals gave a chemical composition of $Mg_{0.642(7)}Fe_{0.341(6)}Si_{0.656(10)}Al_{0.356(4)}O_3$, which is in excellent agreement with $Mg_{0.662(3)}Fe_{0.338(3)}Si_{0.662(3)}Al_{0.338(3)}O_3$ obtained from the structure refinement. The measured Mössbauer spectrum seems to consist of two absorption peaks with different intensities (Fig. 2(a)). These peaks were interpreted to be one asymmetric doublet on the basis of the following constraints: the coordination environments around the possible occupied sites of Fe are largely distorted, which should yield quadrupole splitting; the doublets measured using a single crystal can be asymmetric. The best fit based on this interpretation showed no significant residuals (Fig. 2(b)), resulting in an isomer shift of 0.40(3) mm/s and a quadrupole splitting of 0.86(4) mm/s, indicating that Fe ions exclusively occupy the eightfold (nominally 12-fold) coordinated A-site in the trivalent high-spin (HS) state. From the cation ratio indicated by EPMA, this leads to the conclusion that Al^{3+} ions exclusively occupy the sixfold-coordinated B-site and there are no vacancies. These cation distributions were also confirmed from the results of structure refinement ($R = 0.0189$, $wR = 0.0146$). In the present case where relatively large and equal amounts of Fe and Al are present, the following charge-coupled substitution is concluded to be predominant in the incorporation of both cations into bridgmanite:

$$^{A}Mg^{2+} + {}^{B}Si^{4+} \leftrightarrow {}^{A}Fe^{3+}(HS) + {}^{B}Al^{3+} \quad (1),$$

where the superscripts "A" and "B" represent the occupied sites. The incorporation of Fe^{3+} and Al via this substitution decreases the mean cation size on the A site ($<r_A>$) and increases that on the B site ($<r_B>$). We found that this incorporation of Fe^{3+} and Al enhances the structural distortion due to the tilting of BO_6 octahedra (Fig. 3(a)), yielding the unusual expansion of the mean <A–O> bond length owing to the flexibility of A–O bonds to the structural distortion (Fig. 3(b)), in contrast to the mean <B–O> bond length, which depends on the cation-size effect (Fig. 3(c)).

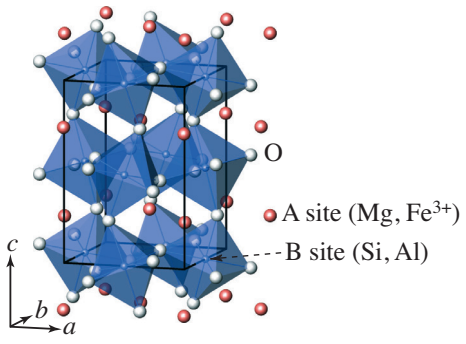

Fig. 1. Crystal structure of our (Fe^{3+}, Al)-bearing bridgmanite. Some of the Mg^{2+} on the eightfold (nominally 12-fold) coordinated A-site and Si^{4+} on the sixfold coordinated B-site are replaced with high-spin Fe^{3+} and Al^{3+}, respectively.

At the lowermost mantle, bridgmanite is believed to transform to the post-perovskite phase, associated with the D″ seismic discontinuity. However, a perovskite phase with a different symmetry can intervene between the *Pbnm* perovskite phase and the post-perovskite phase, as suggested for (Mg, Fe)SiO_3 bridgmanite at 64 GPa and 1850 K [3] and for $MgSiO_3$ bridgmanite above 83 GPa and 1700 K [4]. To examine the possibility of such phase transitions in perovskites at high pressures and high temperatures, it is effective to discuss the compressibility ratios (β_B/β_A) of the two coordination polyhedra [5], given by the rigidity ratio M_A/M_B defined from bond valence, where the subscripts "A" and "B" represent the AO_{12} and BO_6 polyhedra, respectively. In perovskites exhibiting zone-boundary phase transitions, such as bridgmanite, Clapeyron slopes (dP/dT_c) for the phase boundary are positive when $M_A/M_B < 1$ because the phase transition temperature T_c increases with pressure owing to the increased tilting of BO_6 octahedra, and they are negative when $M_A/M_B > 1$ because T_c decreases with increasing pressure owing to the decreased octahedral tilting [5]. The calculated M_A/M_B ratios under ambient conditions are 0.67 for the reported $MgSiO_3$ bridgmanite and 0.72 for our (Fe^{3+}, Al)-bearing bridgmanite. If a bridgmanite transforms to another perovskite phase under mantle conditions, its phase boundary has a positive Clapeyron slope. In addition, as described above, the incorporation of Fe^{3+} and Al increases the octahedral tilting (Fig. 3(a)). These show that the higher pressure and the higher Fe^{3+} and Al contents would raise T_c, implying that bridgmanites in subducting slabs have a much higher T_c than previously suggested ones [3,4] if the suggested phase transitions exist. The phase transition to another perovskite phase might be observed in slabs that have fallen/subducted into the lowermost mantle.

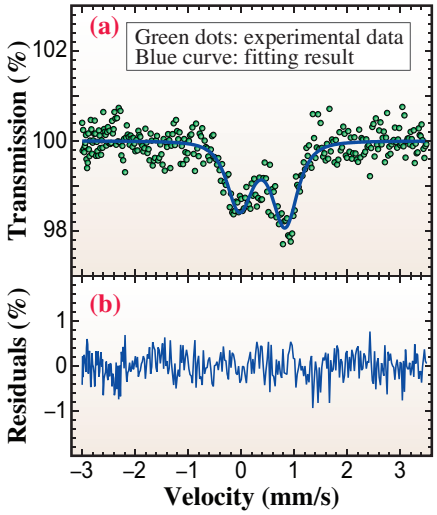

Fig. 2. **(a)** Mössbauer spectrum of our (Fe^{3+}, Al)-bearing bridgmanite single-crystal and **(b)** the fitted residuals.

We also revealed that the incorporation of Fe^{3+} and Al via substitution (1) does not change M_A, decreases M_B, and consequently increases β_B/β_A. The increase in β_B/β_A depends only on M_B and may correspond to the decrease in the bulk modulus K. The bulk sound velocity $V_B = \sqrt{K/\rho}$ would thus decrease with increasing Fe^{3+} and Al contents, which agrees with the reported results of theoretical calculation for (Fe^{3+}, Al)-bearing bridgmanite. This crystallographic approach can be effective for gaining important insights into the seismic properties within the lower mantle.

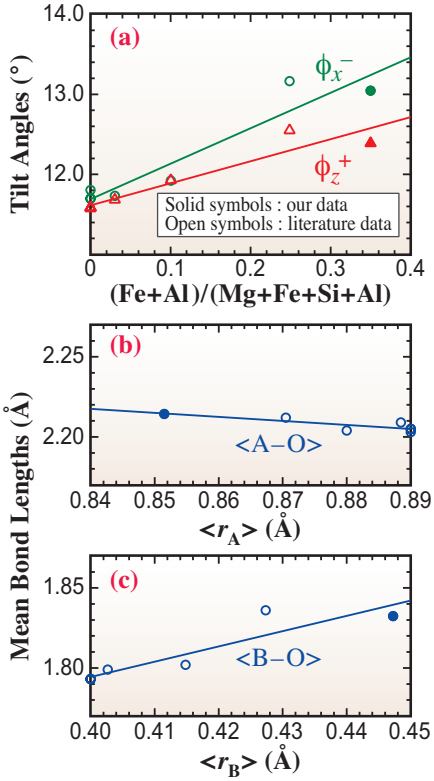

Fig. 3. **(a)** Tilt angles ϕ_x^- and ϕ_z^+ of BO_6 octahedra as functions of the ratio (Fe+Al)/(Mg+Fe+Si+Al), **(b)** mean <A–O> bond length as a function of the mean cation size on A site ($<r_A>$), and **(c)** mean <B–O> bond length as a function of the mean cation size on B site ($<r_B>$). Refer to [2] for details of tilt angles.

Akihiko Nakatsuka

Graduate School of Sciences and Technology for Innovation, Yamaguchi University

Email: tuka@yamaguchi-u.ac.jp

References

[1] K. Hirose and Y. Fei: Geochim. Cosmochim. Acta **66** (2002) 2099.
[2] *A. Nakatsuka, H. Fukui, S. Kamada, N. Hirao, M. Ohkawa, K. Sugiyama, T. Yoshino: Sci. Rep. **11** (2021) 22839.*
[3] C. Meade *et al.*: Science **268** (1995) 1743.
[4] S.-H. Shim *et al.*: Science **293** (2001) 2437.
[5] R.J. Angel *et al.*: Phys. Rev. Lett. **95** (2005) 025503.

CO_2-bearing fluid discovered in a meteorite: evidence of dynamic evolution of the solar system

Water is abundant in our solar system. Even outside of our own planet, water of different states and quantities has been detected, for example, ice on the moon, in Saturn's rings and in comets, liquid water on Mars and under the surface of Saturn's moon Enceladus, and traces of water vapor in the atmosphere of Venus. Water played an important role in the early evolution and formation of the solar system.

Many researchers have searched for evidence of liquid water in extraterrestrial materials such as meteorites. Most meteorites originate from asteroids that formed in the early solar system (e.g., [1]). It is widely accepted that minerals and ice were accreted together to form asteroids outside the snowline where it was cold enough for volatile components such as H_2O to condense into ice grains. Aqueous alteration by reactions of melted ice with anhydrous minerals occurred. This was recorded in some primitive meteorites called carbonaceous chondrites in which water is mostly present as hydroxyls and molecules in hydrous minerals, which are basically crystalline with some ionic or molecular water incorporated within them. Liquid water is expected to remain as fluid inclusions in minerals that precipitated in aqueous fluid. However, thus far, the only fluid inclusions from the early solar system have been those in salt (NaCl) crystals in less primitive ordinary chondrites [2], although their origin is not clear.

In searching for water inside meteorites, we focused on mineral grains of calcite ($CaCO_3$) in the Sutter's Mill meteorite, which is categorized as an aqueously altered Mighei-type (CM) carbonaceous chondrite. We reported the presence of CO_2-bearing fluid inclusions in a calcite grain for the first time and used the results to infer the origin of the meteorite parent body [3].

We conducted a specific analysis protocol to search for fluid inclusions, systematically combining scanning electron microscopy (SEM), focused-ion beam (FIB) microsampling, synchrotron radiation-based X-ray computed nanotomography (SR-XnCT) and transmission electron microscopy with a cryostage (cryo-TEM). We examined polished sections of the Sutter's Mill meteorite and searched for calcite grains appropriate for the present analysis (Fig. 1(a)). Grains ~30 μm in size were selected and extracted using FIB. The samples were imaged using SR-XnCT to obtain their three-dimensional (3D) images with absorption and phase-shift contrasts at SPring-8 **BL47XU** (e.g., [4]) with the spatial resolution of ~100 nm. Then, we found many inclusions larger than a few micrometers (micron-sized inclusions) inside the calcite grains (Fig. 1(b)). Most of them have facets suggesting the presence of water inside the inclusions. However, unfortunately, the inclusions were empty. The water that used to be there must have escaped sometime over the last 4.6 billion years.

When we took a much closer look, we found innumerable nanosized inclusions in the calcite (smaller than 1 μm) (Fig. 1(b)), where water might remain. We extracted areas containing these nanosized inclusions using FIB and TEM sections were made (Fig. 2(a)). If water is to be found there, it must have been frozen in there at low temperatures; then, TEM would be able to detect the crystalline ice using electron diffraction at low temperatures. In the TEM observation, in addition to finding diffraction spots that indicated calcite crystals at room temperature (20°C), new spots appeared at –100°C (Figs. 1(b,c)).

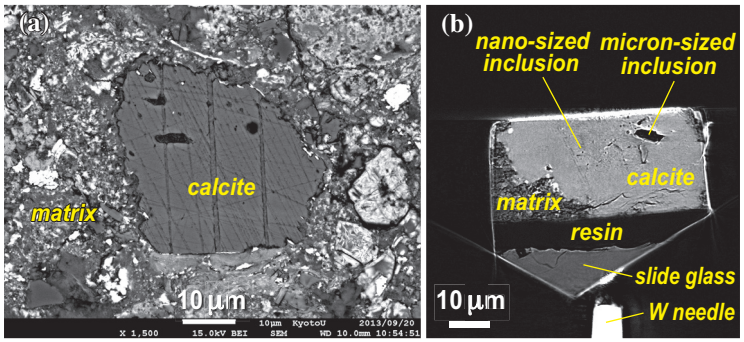

Fig. 1. SEM and XCT slice images of calcite grains. **(a)** Backscattered electron SEM image showing a typical calcite grain in matrix (a). **(b)** Absorption XCT image at 7 keV showing micron-sized inclusions and a large number of nanosized inclusions.

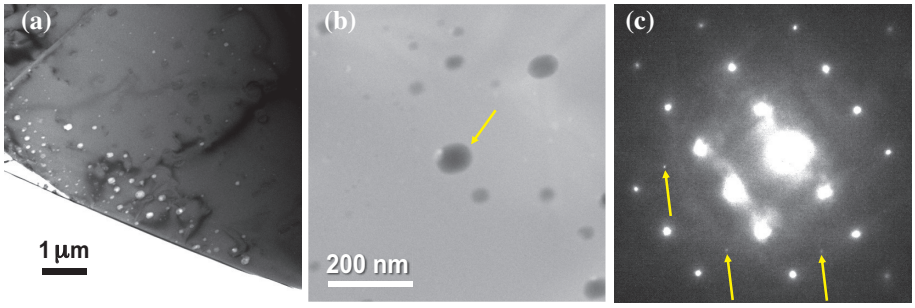

Fig. 2. TEM images of nanosized inclusions in calcite and SAED pattern of a nanosized inclusion in cryo-TEM. **(a)** Bright-field image of nanosized inclusions in calcite. They are distributed as bands. **(b)** STEM image. One inclusion (arrowed) has extra diffraction spots in cryo-TEM observation. **(c)** Selected-area electron diffraction (SAED) pattern of an area including the nanosized inclusion in (b) (arrow) cooled at 173 K. Yellow arrows show spots appearing only at 173 K.

These spots were identified not as ice formed by freezing water (H_2O) but as ice that is called CO_2 ice or CO_2 hydrate (CO_2·5.75H_2O). That is, the liquid in the inclusion was not simple liquid water (H_2O) but a fluid that contained CO_2. The ratio of CO_2 was found to be above 15% on the basis of the phase diagram of the system CO_2–H_2O. In addition, such CO_2-bearing fluid should exist at pressures of possibly >~200 bars that corresponds to the depth of an asteroid deeper than ~100 km.

From the existence of the CO_2-bearing fluid, it is possible to narrow down the area in which the asteroid or a meteorite's parent body was formed. In the early solar system, the low-temperature regions far from the sun had snow lines where ice of H_2O, CO_2, and CO would appear in that order. The present finding indicates that the parent body of the Sutter's Mill meteorite was formed outside the CO_2 snow line but inside the CO snow line (Fig. 3).

In recent solar system formation theories, it is considered that planets and small celestial bodies did not remain in the same location as their formation, but rather, their orbits changed (or moved) after their formation [5]. Following this model, Jupiter would have been formed inside the current orbit and later moved to its current location. If we were to infer the formation regions of the celestial bodies from the snow line, the parent body of the Sutter's Mill meteorite would have been formed in the low-temperature region outside the region where Jupiter was formed. Then, along with Jupiter's orbital change, it moved inward towards the main asteroid belt between Mars and Jupiter. The discovery of water containing CO_2 also raised the credibility of the new dynamic solar system formation model.

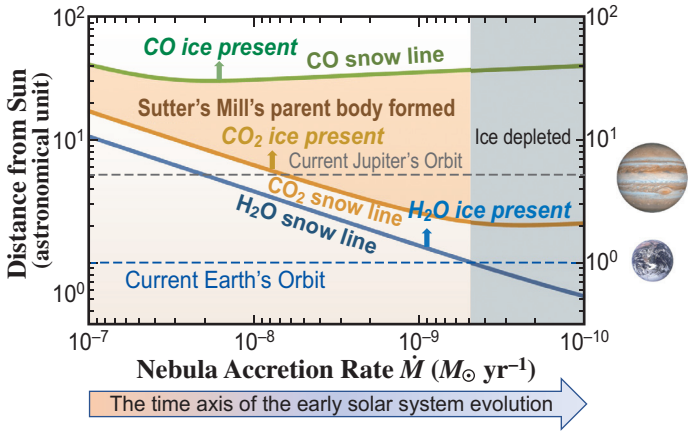

Fig. 3. H_2O, CO_2, and CO snow lines and formation of parent body of Sutter's Mill meteorite. During the evolution of the early solar system, the nebular accretion rate $\dot{M}$ decreased with time and the distances of the snow lines from the Sun decreased. A possible region of formation of parent body of Sutter's Mill meteorite is bounded by CO_2 and CO snow lines and the ice-depleted region. Current orbits of Jupiter and Earth are also shown.

Akira Tsuchiyama[a,b,c]

[a] Research Organization of Science and Technology, Ritsumeikan University
[b] CAS Key Laboratory of Mineralogy and Metallogeny, Guangzhou Institute of Geochemistry, China
[c] CAS Center for Excellence in Deep Earth Science, China

Email: Atsuchi@fc.ritsumei.ac.jp

References

[1] M. Yoshikawa *et al.*: Asteroids IV (University of Arizona, Tucson, 2015) p. 397.
[2] M.E. Zolensky *et al.*: Science **285** (1999) 1377.
[3] *A. Tsuchiyama, A. Miyake, S. Okuzumi, A. Kitayama, J. Kawano, K. Uesugi, A. Takeuchi, T. Nakano, M. Zolensky: Sci. Adv. 7 (2021) eabg9707.*
[4] M. Matsumoto *et al.*: Sci. Adv. **5** (2019) eaax5078.
[5] K.J. Walsh *et al.*: Meteorit. Planet. Sci. **47** (2012) 1941.

Investigation of reaction mechanism of crystalline aromatic dicarboxylate in Li^+ intercalation by hard X-ray photoelectron spectroscopy

While the demand for lithium-ion batteries (LIBs) is rapidly increasing with widespread electrification of energy systems, LIBs used in practice most often involve electrodes based on inorganic materials, causing ongoing discourse concerning the depletion of raw materials. Such a circumstance motivates researchers to develop sustainable battery technologies effectively using organic electrode materials. However, previous studies on organic electrode materials have focused only on their synthesis or properties. The lack of a systematic understanding of their charge storage mechanism prevents their practical application.

In this study, we systematically analyzed a series of crystalline aromatic dicarboxylate lithium salts, which is a promising group of organic electrode materials also known as intercalated metal-organic frameworks (iMOFs), by shedding light on their electrochemical reaction mechanism [1]. iMOFs, consisting of alternately layered π-stacked aromatic units and tetrahedral LiO_4 units, show reversible intercalation of two electrons with two Li^+ ions for charge compensation at the potential of 0.5–1.0 V *vs* Li/Li^+, as shown in Fig. 1 [2]. We discovered, through various electrochemical analyses, that the phase transition mechanism of iMOFs during Li^+ intercalation/deintercalation depends on the aromatic unit. As summarized in Fig. 2, iMOF with a naphthalene framework [2,6-Naph(COOLi)$_2$] strongly interacts with the intercalated Li^+ ions, resulting in the low Li^+ diffusivity and the two-phase coexistence at the initial stage of Li^+ intercalation and deintercalation. In contrast, iMOF with a biphenyl framework [4,4'-Bph(COOLi)$_2$], with a weak Li^+ interaction, provides high Li^+ diffusivity and the solid-solution phase over the entire region. These differences in the phase transition mechanism and Li^+ diffusivity can give rise to the difference in high-rate capability of charge/discharge performance [3].

To investigate the reaction mechanism and interactions between the host matrix of iMOFs and intercalated Li^+ ions in greater detail, hard X-ray photoelectron spectroscopy (HAXPES) experiments were performed at SPring-8 **BL16XU**. Compared with laboratory-scale X-ray photoelectron spectroscopy, HAXPES can provide more information about bonding states or energy states of electrode materials because hard X-rays can access deeper areas within electrodes. Figure 3 shows the obtained C1*s* HAXPES spectra of iMOFs with various amounts of intercalated Li^+ ions, *x*. In the spectra of both iMOFs, a new peak was observed at 283 eV after Li^+ intercalation, originating from the bond between aromatic carbon atoms and intercalated Li^+ ions (C–Li bond). This suggests that intercalated Li^+ ions are stabilized through their interaction with aromatic carbon atoms (i.e., Li^+–π interaction). Interestingly, the C–Li bond peaks of both samples were also observed in the spectra of post-Li^+-intercalated samples with $x = 0$, indicating that intercalated Li^+ ions are not fully deintercalated. The intensity of the C–Li bond peak relative to the C–C bond peak at 285 eV is higher for the 2,6-Naph(COOLi)$_2$ sample than for the 4,4'-Bph(COOLi)$_2$ sample, which suggests that more Li^+ ions remain in 2,6-Naph(COOLi)$_2$, probably because of the stronger interaction of the naphthalene framework with Li^+ ions. This is consistent with the results of electrochemical analyses (Fig. 2). Here, we consider factors governing the Li^+–π interaction in iMOFs. It is known that the Li^+–π interaction becomes stronger with decreasing distance between Li^+ ions and π-electron systems or increasing charge density of π-electrons [4]. Among these factors, the charge density of π-electrons is probably higher for 2,6-Naph(COOLi)$_2$ than for 4,4'-Bph(COOLi)$_2$ because the naphthalene framework exhibits high planarity compared with the biphenyl framework, whose planarity is lowered owing to the rotation

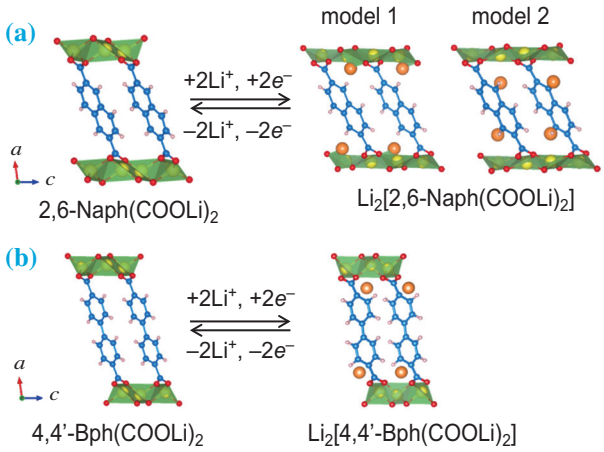

Fig. 1. Li^+ intercalation and deintercalation in iMOFs with **(a)** naphthalene framework [2,6-Naph(COOLi)$_2$] and **(b)** biphenyl framework [4,4'-Bph(COOLi)$_2$]. Blue, pink, red, yellow, and orange spheres represent C, H, O, pristine Li^+, and intercalated Li^+, respectively. 2,6-Naph(COOLi)$_2$ has two models of the Li^+-intercalated phases, that is, thermodynamically and kinetically stable phases (respectively, model 1 and model 2), whereas the Li^+ intercalation into 4,4'-Bph(COOLi)$_2$ results in the formation of only the "middle" phase [3,5].

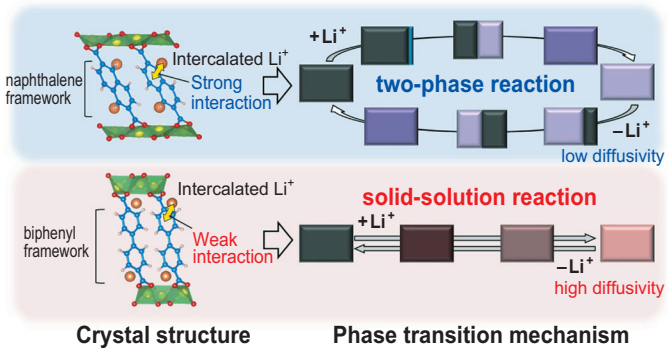

Fig. 2. Phase transition mechanism during Li^+ intercalation/deintercalation in iMOFs, and its relationship with the crystal structure.

of its single C–C bond. Consequently, the Li^+–π interaction can be stronger in 2,6-Naph(COOLi)$_2$ than in 4,4'-Bph(COOLi)$_2$.

Furthermore, we discuss the reaction mechanism of iMOFs in terms of the shift of the C–Li bond peak at 283 eV relative to the C–C bond peak at 285 eV in the C1*s* HAXPES spectra. The peak shift of the C–Li bond, depending on *x*, can be attributed to differential charging, the effects of the formation of a solid electrolyte interphase (SEI), and/or changes in the chemical states of samples. In our data, differential charging can be ignored because of their symmetric peak shapes. The effects of SEI formation can also be ignored because the peak shift occurs after SEI formation. Therefore, the peak shift probably originates from the change in the chemical states of samples. In the spectra of 4,4'-Bph(COOLi)$_2$ samples (Fig. 3(b)), the C–Li peak shifts to a higher binding energy with Li^+ intercalation. The observed peak shift can be simply attributed to the increase in the Fermi level as a result of the filling of the conduction band by Li^+ doping. In contrast, the peak shift towards a lower binding energy with Li^+ intercalation in the 2,6-Naph(COOLi)$_2$ samples (Fig. 3(a)) implies that reactions that lower the Fermi level can simultaneously proceed with Li^+ intercalation. From the band structure of 2,6-Naph(COOLi)$_2$ samples [5], we can propose the relaxation from the kinetically stable Li^+-intercalated phase (model 2 in Fig. 1(a)) to the thermodynamically stable phase (model 1 in Fig. 1(a)) as a possible reaction. These differences between 2,6-Naph(COOLi)$_2$ and 4,4'-Bph(COOLi)$_2$ are partly attributed to the fact that 4,4'-Bph(COOLi)$_2$ has only one Li^+-intercalated phase, which can ultimately be related to the strength of the Li^+–π interaction: the Li^+–π interaction in biphenyl frameworks is not very strong so the intercalated Li^+ ions are not tightly trapped between π-stacked layers, unlike in 2,6-Naph(COOLi)$_2$, resulting in the formation of only the "middle" phase in which intercalated Li^+ ions can be stabilized by both oxygen atoms of LiO_4 tetrahedra and carbon atoms of biphenyl frameworks.

To conclude, we demonstrated by HAXPES experiments and electrochemical analyses that the electrochemical reaction mechanism and the associated properties in iMOFs are predominantly affected by interactions between the aromatic units and the intercalated Li^+ ions. The Li^+–π interaction can be modified by the organic framework, particularly the curvature of the aromatic unit. We thus believe that these findings will be helpful in designing organic electrode materials with the aim of achieving fast-charging performance for their application.

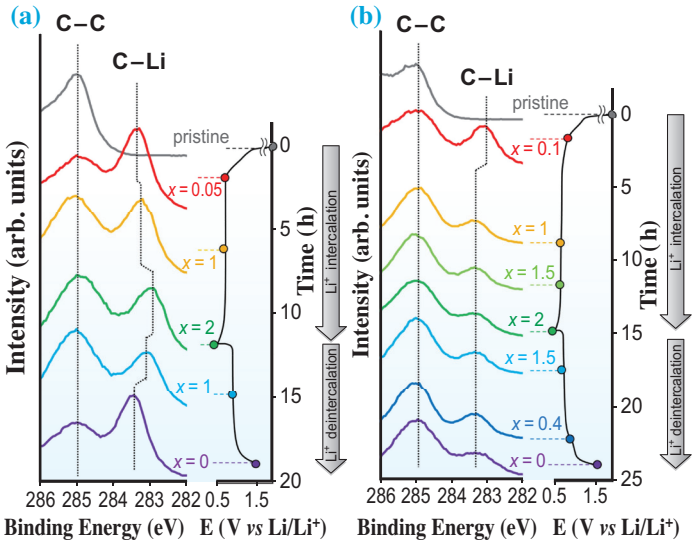

Fig. 3. *Ex situ* C1*s* HAXPES spectra of **(a)** 2,6-Naph(COOLi)$_2$ and **(b)** 4,4'-Bph(COOLi)$_2$ samples with various amounts of intercalated Li^+ ions, *x*. The samples were prepared using coin-type cells composed of iMOF as the working electrode and Li metal as the counter electrode. The cells were charged and discharged at a constant current of C/10, during which charging/discharging was stopped when predetermined amounts of Li^+ ions were intercalated in the 1st cycle. The resulting cells were disassembled in argon atmosphere, and the iMOF electrodes after washing with dimethyl carbonate were used for HAXPES experiments.

Riho Mikita and Nobuhiro Ogihara*

Toyota Central R&D Labs., Inc.

*Email: ogihara@mosk.tytlabs.co.jp

References

[1] *R. Mikita, N. Ogihara, N. Takahashi, S. Kosaka and N. Isomura: Chem. Mater.* ***32*** *(2020) 3396.*
[2] N. Ogihara *et al.*: Angew. Chem. Int. Ed. **53** (2014) 11467.
[3] Y. Ozawa *et al.*: Commun. Chem. **1** (2018) 65.
[4] A.S. Mahadevi *et al.*: Chem. Rev. **113** (2013) 2100.
[5] N. Ogihara *et al.*: Sci. Adv. **3** (2017) e1603103.

Moisturizing mechanism of glycerol and diglycerol on human stratum corneum

With regard to the moisturizing mechanism of glycerol and diglycerol, we found that there are two essential structural elements in the stratum corneum (SC). One is soft keratin in corneocytes, and the other is a domain formed by the orthorhombic hydrocarbon-chain packing (ORTHO) and the short lamellar structure (SLS). The former functions in storing water in the corneocytes, and the latter functions in regulating the water content of the corneocytes [1]. It is, however, difficult to detect the structural changes caused by these moisturizers without using synchrotron X-ray diffraction. In this study, we found that glycerol enhances both functions and that diglycerol negligibly affects soft keratin but greatly enhances water regulation [2]. Until now, the widely accepted result of a study on a lipid model system containing phospholipids, that is, glycerol has a significant effect on the appearance of a large amount of the liquid state, has led to the assumption that it provides the moisturizing effect [3]. In the present study using human SC we found that this is not the case in the moisturizing mechanism of glycerol. The X-ray diffraction experiments were performed at SPring-8 **BL40B2** and **BL19B2**. We measured the dynamic structural changes during the drying process under dry N_2 gas flow in SC samples treated with water or with aqueous solutions of polyol, including glycerol, diglycerol, or glycerol/ diglycerol.

In Fig. 1, the results for soft keratin in the corneocytes are summarized. Soft keratin is constructed of a rigid core and a terminal flexible segment. We can determine the inter-α-helix distance (approximately 1 nm) in a coiled-coil α-helix in the rigid core by X-ray diffraction measurement [1]. The relationship between the structures of the rigid core and the flexible terminal segment, which is directly affected by the polyols, is discussed later. The left side of Fig. 1 shows the change in the inter-α-helix distance in soft keratin during the process of drying a SC sample treated with water. The inter-α-helix distance decreased when the SC sample was dried. This is consistent with the result obtained as a function of the water content in static X-ray diffraction experiments [1]. The right side of Fig. 1 shows the decreasing rates of the inter-α-helix distance in the SC treated with water and the polyol aqueous solutions. The decreasing rates are characterized by two categories. The decreasing slope is steep in the SC treated with water and diglycerol but relatively gentle

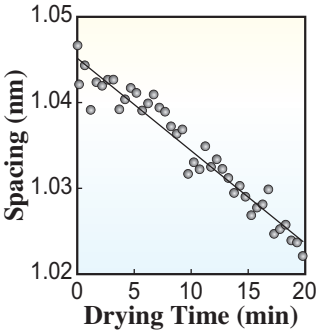

Solution	Decreasing slope (nm/min)
water	0.0011
10wt% Diglycerol	0.0009
10wt% Glycerol	0.0004
7wt% Glycerol / 3wt% Diglycerol	0.0002

Fig. 1. Temporal change of the inter-α-helix distance in the rigid core of soft keratin during process of drying the stratum corneum sample treated with water. The table on the right side shows the decreasing slope obtained in the stratum corneum samples treated with water and polyol aqueous solutions.

in the SC treated with glycerol and glycerol/diglycerol. Our results indicate that in the former, diglycerol hardly penetrates into the corneocytes since the SC treated with diglycerol aqueous solution shows a similar effect to that treated with water, but in the latter, the glycerol component penetrates into the corneocytes; therefore, the effect of glycerol lasts longer.

We consider the role of glycerol in soft keratin. As shown by a nuclear magnetic resonance study on the SC [4], natural moisturizing factor (NMF) combine with the flexible segment of soft keratin and, as a result, attract water. Importantly, the study showed the change in the mobility of the flexible terminal segment strongly affects the mobility in the rigid core. In our study, we observed that the inter-α-helix distance in the rigid core decreases relatively gently in the process of drying the SC sample treated with glycerol. This suggests that glycerol can be retained in the flexible segment more strongly than NMF and bound water around glycerol is stored for a long time (Fig. 2). The role of diglycerol will be described later.

The intercellular lipids present around the corneocytes form the lamellar structures. The SLS has water layers and regulates water in the SC [1]. We observed the changes in the spacing of the ORTHO (approximately 0.42 and 0.37 nm). These spacing changes of 0.42 and 0.37 nm were not significantly different. Therefore, we show the changes in the spacing at 0.42 nm as a representative. The ORTHO and the SLS are in the common domain. Since the

X-ray diffraction peak for the spacing at 0.42 nm was narrow and strong, we were able to detect the slight change of the peak in the synchrotron X-ray diffraction experiment, notwithstanding that the change due to hydration and dehydration was only about 0.1%. The left side of Fig. 3 shows the change of the 0.42 nm spacing during the process of drying the SC sample treated with water. The spacing increased during wetting, whereas during drying it exhibited a complex behavior. During the drying process, first the spacing decreased rapidly, became nearly flat at the minimum, turned to increase, and finally remained almost unchanged. In the interval where the spacing was minimum, the peak became sharp, that is, the full width at half-maximum became narrow. This finding indicates that the domain of the ORTHO/SLS is in a stable state, where the water content may be about 25 wt%. A similar complex behavior was seen in the polyol aqueous solutions, but the rapid changes at transients became slightly broad. The right side of Fig. 3 shows the time for which the stable state was maintained, including transient intervals. The time is longer when samples are treated with polyol aqueous solutions than with water. These results suggest that the polyols stabilize the soft keratin structure that is related to the function of regulating water in the SC. It can be presumed that these retention times prolonged by the polyols are due to the interaction between the hydroxyl group of the polyols and the hydrophilic head group of intercellular lipids. It might be interpreted that diglycerol interacts with many intercellular lipid head groups, since diglycerol has a larger molecular length than glycerol. As a result, it is speculated that the polyols act on the intercellular lipid structure and the hydrocarbon chains become packed. This contradicts the results of the study by Froebe *et al.* on a lipid model, in which glycerol was said to transform the intercellular lipid structure to the liquid state, that is, glycerol produces the disordered structure [3]. The contradiction seems to lie in the fact that they used the lipid model containing phospholipids, which showed a rather different behavior from that of the intercellular lipids in the SC.

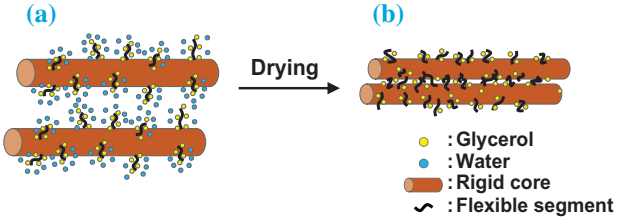

Fig. 2. Structure of soft keratin under two conditions. **(a)** Glycerol was applied to the stratum corneum. **(b)** The glycerol-applied stratum corneum was dried.

In conclusion, the polyols enhance the moisturizing function of the SC; specifically, in addition to the role of the NMF, glycerol acts on soft keratin in the corneocytes to reinforce water storage, and diglycerol acts on intercellular lipids to reinforce the ability of SC to regulate the water content. Therefore, it is highly possible that the combination of glycerol and diglycerol improved the moisturizing effect synergistically, and the water content of the SC could be retained for a long time under a dry condition. This is supported by the result of our previous study that the increase in the water content of the SC treated with the glycerol and diglycerol solution could be measured by electrical capacitance [5]. Cosmetics formulated with both glycerol and diglycerol would provide an enhanced moisturizing effect, that can be presumed to maintain healthy skin, of which 25 wt% of its water content is at the surface. The combined effect of glycerol and diglycerol revealed by the present scientific evidence has attracted attention in the cosmetic industry and has become popular. Nowadays, cosmetics formulated with glycerol and diglycerol are distributed worldwide.

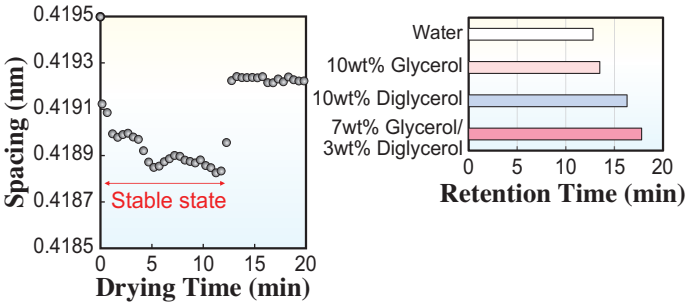

Fig. 3. Temporal change of the spacing of the orthorhombic hydrocarbon-chain packing structure during process of drying the stratum corneum sample treated with water. The right side shows the retention time of the stable state.

Akari Habuka[a], Takeshi Yamada[a,*] and Ichiro Hatta[b]

[a] Research & Development Laboratory, Sakamoto Yakuhin Kogyo Co., Ltd.
[b] Nagoya Industrial Science Research Institute (NISRI)

*Email: yamada@sy-kogyo.co.jp

References

[1] H. Nakazawa *et al.*: Chem. Phys. Lipids **165** (2012) 238.
[2] *T. Yamada, A. Habuka and I. Hatta: Inter. J. Cosmet. Sci. **43** (2021) 38.*
[3] C.L. Froebe *et al.*: J. Soc. Cosmet. Chem. **41** (1990) 51.
[4] Y. Jokura *et al.*: J. Invest. Dermatol. **104** (1995) 806.
[5] A. Tomiie *et al.*: J. Oleo Sci. **65** (2016) 681.

Accelerators & Beamlines Frontiers

SPring-8 Beam Performance

Recent update of accelerators

We have fully replaced the 1 GeV linear accelerator (linac) and the 8 GeV booster synchrotron with the 8 GeV linac of SACLA for injection to the SPring-8 storage ring [1]. Since SACLA is constantly operated for the X-ray Free Electron Laser (XFEL), we now operate only one injector, i.e., the 8 GeV linac, for both the storage ring and XFEL. As a result, we can significantly suppress power consumption in the accelerator complex by not operating the 1 GeV linac and the 8 GeV booster.

SPring-8 and SACLA issued a green facility statement in August 2021. The facilities are used for research activities related to the Sustainable Development Goals (SDGs) and carbon neutrality. At the same time, we promote energy saving in the facility including the accelerator complex. Thus, the full-energy direct injection setup from the SACLA linac to the storage ring has been built for a more energy efficient facility.

We needed to build the new injection setup in such a way that SACLA experiments would not be affected after adding the new function of full-energy direct beam injection to the storage ring. Yet, the injection system must deliver electron beams to the storage ring whenever it is demanded from the storage ring. For that, we developed a new timing system in which on-demand beam injections could be executed without interfering with XFEL experiments.

In addition, some experiments at SPring-8 require a bunch purity of 10^{-8} or better. The bunch purity is the ratio of the number of electrons in the satellite bunches to that expected to fill specific RF buckets in the filling patterns for each operation mode. Before the new injection setup from SACLA was introduced, undesired electrons in the satellite buckets were removed using the RF knock-out in the 8 GeV booster synchrotron. With the new injection setup, it was no longer possible to remove such undesired electrons in the booster, so we developed a new bunch cleaner in the storage ring. The new bunch cleaner is composed of a signal-generating digital processor, amplifiers, and a stripline kicker. The stripline kicker is installed in cell 30 of the storage ring, and the beam scraper is placed in cell 48. As a result, sufficiently high bunch purities of the order of 10^{-9} or better are constantly delivered in current user operations. We note that our high-definition bunch purity monitor developed in SPring-8 also plays a key role in securing such a high bunch purity.

Almost two years have passed since the new injection setup was started. Now, highly reliable beam injection at the same level as that using the 1 GeV linac and the 8 GeV booster and sufficiently high bunch purities are consistently achieved while saving energy.

Not only the accelerator reliability but also stability are achieved. Until recent years, orbit fluctuations excited by pulsed kicker magnets at ID 23 and 25 had long been observed, which distorted some user experiments. Therefore, we have developed and optimized an adaptive feedforward orbit correction system [2]. Presently, almost no orbit fluctuation due to ID 23 or 25 kickers is observed in the user time.

Shiro Takano and Takahiro Watanabe*

Japan Synchrotron Radiation Research Institute (JASRI)

*Email: twatanabe@spring8.or.jp

References

[1] T. Hara *et al.*: Phys. Rev. Accel. Beams **24** (2021) 110702.
[2] M. Masaki *et al.*: J. Synchrotron Rad. **28** (2021) 1758.

Hard X-ray nanobeam scanning using advanced Kirkpatrick-Baez mirrors and prisms

Scanning X-ray microscopy (SXM) is one of the major X-ray microscopy techniques. In SXM, a focused X-ray beam is irradiated onto a sample and images are acquired by scanning the relative positions of the beam and the sample. The spatial resolution of SXM is basically determined by the focused spot size. However, the resolution is practically limited by the scanning accuracy. Recent advances in synchrotron radiation sources and X-ray nanofocusing optics have markedly reduced the focused beam size to the single-nanometer scale [1]. The SXM performance has eventually become no longer limited by the size of the X-ray beam, but by the scanning system. In scanning electron microscopies that have achieved an outstanding resolution, the beam is precisely controlled by an electromagnetic deflector. In contrast, X-ray beams are rarely steered in SXM in the same way as in electron microscopy owing to the lack of appropriate X-ray optical components, and hence, a mechanical scanning device for the sample, not for the X-ray beam, has been explored for over half a century. In recent years, scanning systems with an accuracy of ~20 nm have been constructed, but complex equipment such as positioning stages with closed-loop feedback using additional measurement devices, heat-insulated mechanics, and massive granite bases have led to difficulties in achieving further precision without constraining the sample environment. Although fourth-generation high-brightness SR sources can significantly enhance the SXM performance, sample scanning restrictions have been a barrier to the widespread use of ultrahigh resolution SXM for diverse samples.

In this work, we propose an optical scheme of the hard X-ray nanobeam scanner for ultrahigh resolution SXM [2]. The optics consists of an X-ray prism to deflect the incident X-ray beam and an advanced Kirkpatrick-Baez (AKB) mirror to generate nanobeams (see Fig. 1). The AKB mirror approximately satisfies Abbe's sine condition and thus has an excellent imaging property with a wide angle of view. Reciprocally, when AKB mirrors are used in a focusing configuration, one can keep a wide range in which the focus size will not change regardless of the incident angle. Taking advantage of this characteristic, the focused beam with AKB mirrors can be scanned with a nanometer-level accuracy by changing the incident angle by adjusting the X-ray prism. The deflection angle of the incident beam induced by prism rotation is very small and can be precisely controlled with a nanoradian accuracy by degree-order rotation of the prism. We note that the total reflection focusing mirror can generate high-intensity X-ray nanobeams owing to its larger spatial acceptance and higher reflectivity than the focusing zone plate.

Using a prism with an apex angle of 90°, the deflection angle of the X-ray prism $\Delta\theta$ is approximately given by [3]

$$\Delta\theta \approx \frac{2\delta}{\sin 2\theta} . \qquad (1)$$

where δ denotes the phase-shifting part of the refractive index and θ denotes the glancing incident angle, as illustrated in Fig. 2(a). In Fig. 2(b), $\Delta\theta$-*versus*-θ relationships are shown as solid lines, which were calculated for the rotation of the prism made of glassy carbon (density ρ = 1.51 g/cm^3) and photon energies of 10 and 12 keV. Note here that $\Delta\theta$ is in units of μrad, whereas θ is in degrees, which leads to high-accuracy scanning by prism rotational scanning. The transmittance of the prism is acceptable for SXM when one chooses a higher photon energy above ~10 keV and low-atomic-weight materials for the prism.

A nanobeam scan experiment was performed at SPring-8 **BL29XU** with a photon energy of 10 keV. X-ray prisms with apex angles of 90° made of glassy carbon were utilized. The incident and exit surfaces of the prism were polished. First, the deflection property was tested. An X-ray beam from a slit with a 15-μm-square aperture irradiated the prism arranged in the horizontal direction. The deflected beam was monitored using a high-resolution X-ray camera (Fig. 2(c)) placed 0.988 m downstream from the prism. The incident angle was varied by rotating the prism,

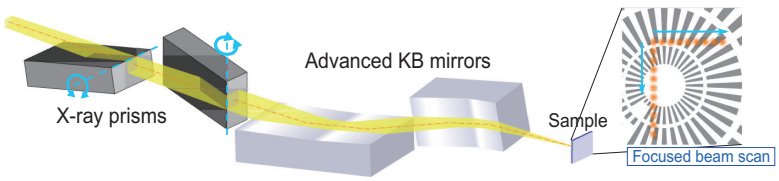

Fig. 1. Conceptual schematic of the hard X-ray nanobeam scanner.

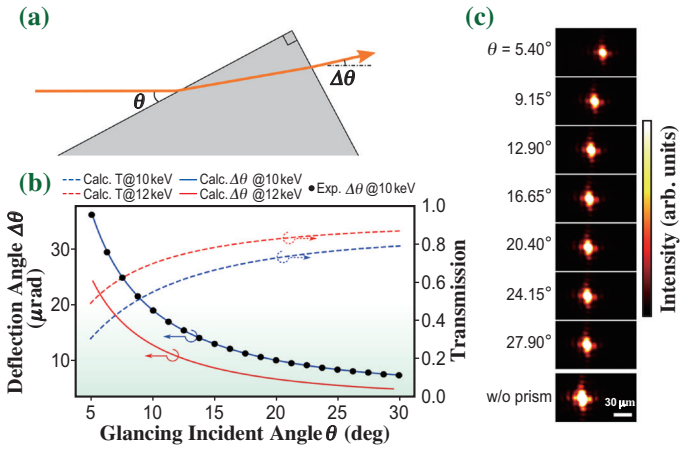

Fig. 2. **(a)** Schematic of an X-ray prism and trajectory of the deflected X-ray beam. **(b)** Incident angle dependence of the deflection angle and transmission of the prism. The solid blue (red) line indicates the calculated deflection angle at a photon energy of 10 keV (12 keV). The dashed blue (red) line indicates the calculated transmission at 10 keV (12 keV) when the incident beam width is 0.6 mm (see Suppl.). Black dots indicate the deflection angles examined by experiment. **(c)** Images of the deflected X-ray beams while the incident angle to the prism was varied from 5.4 to 27.9 degrees. The bottom image is that without the prism.

whose rotation center was at the apex. The obtained relationship between the deflection angle and the glancing incident angle was in good agreement with the calculation, as shown by the black dots in Fig. 2(b).

The estimated deflection accuracy was 17 nrad root mean square (rms), including the uncertainty of the deflection angle measurement, which guaranteed a scanning accuracy of at least 2.9 nm rms on the focal plane.

Subsequently, a vertical prism and AKB focusing mirrors were added and aligned. The mirrors were developed in a previous study [4] and achieved nearly diffraction-limited performance. From the results of knife-edge scanning measurements with 50 μmϕ gold wires, the focus size was measured to be 52.5 (vertical)×53.2 (horizontal) nm² full width at half-maximum (FWHM) (see Fig. 3(a)). An SXM image was obtained using the nanobeam scanner. X-ray transmission through a radial test pattern was acquired using two intensity monitors placed immediately upstream of the mirrors and downstream of the pattern. The result is shown in Fig. 3(b). A clear image, in which the innermost structures were 50 nm lines and spaces, could be obtained. The high-resolution image without notable distortion represents the accuracy and validity of the proposed scheme.

The hard X-ray nanobeam scanner demonstrated here is based on a simple principle and can readily achieve single-nanometer accuracy that is nearly free from scanning error and the thermal instability of mechanical stages. It will pave the way toward the use of ultimate-resolution SXM for various scientific investigations, especially in 4th-generation SR sources.

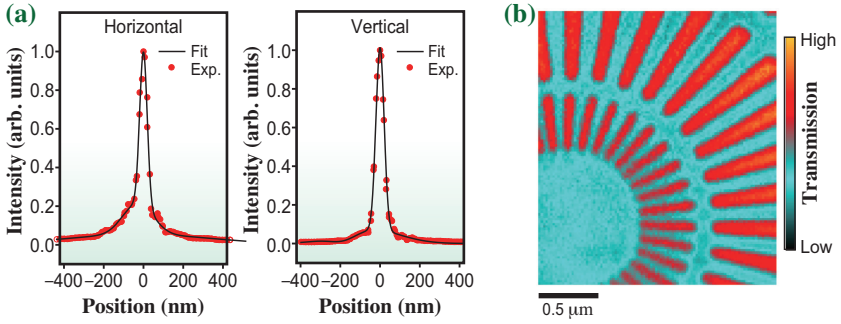

Fig. 3. **(a)** Focusing profiles in the horizontal (left) and vertical (right) directions. Red dots indicate the experimental data. Black solid lines represent the fitting results with the sum of three Gaussian functions. The focus size was 53.2 nm (horizontal) × 52.5 nm (vertical) FWHM. **(b)** SXM image obtained using the nanobeam scanner. Transmission image of the radial test pattern made of 500-nm-thick tantalum.

Jumpei Yamada[a,b,*] and Makina Yabashi[a,c]

[a] RIKEN SPring-8 Center
[b] Division of Precision Engineering and Applied Physics, Osaka University
[c] Japan Synchrotron Radiation Research Institute (JASRI)

*Email: yamada@spring8.or.jp

References

[1] K. Yamauchi *et al.*: J. Phys. Condens. Matter **23** (2011) 394206.
[2] *J. Yamada, I. Inoue, T. Osaka, T. Inoue, S. Matsuyama, K. Yamauchi and M. Yabashi: IUCrJ 8 (2021) 713.*
[3] I. Inoue *et al.*: J. Synchrotron Rad. **25** (2018) 346.
[4] S. Matsuyama *et al.*: Sci. Rep. **7** (2017) 46358.

Guidelines for high-efficiency/accuracy data collection with multiple small-wedge data collection using the automatic data collection ZOO system

In protein crystallography, the data collection method is modified in accordance with the combination of crystal and X-ray beam sizes, such as in rotation data collection, helical data collection, small-wedge synchrotron crystallography (SWSX), and serial synchrotron rotation crystallography (SSROX) experiments [1]. In SWSX, a cryoloop with multiple crystals is raster-scanned with X-rays, 5–20° small-wedge data are collected from each crystal, and a large number of small-wedge datasets are merged to produce a highly complete dataset after individual data reduction [2]. SPring-8 **BL45XU** was designed to enable fully automatic measurements. All beamline components are controlled by the beamline control software BSS [3]. The ZOO system [4] has achieved automated data collection for all goniometer-based data collections in protein crystallography by communicating with BSS. Small crystals such as LCP crystals of membrane proteins (membrane protein crystals) are measured by SWSX combined with microbeams using the ZOO system at SPring-8. However, there has been no systematic study of the effect of the absorbed dose on the final merged dataset in SWSX.

We performed experiments to evaluate the optimal dose for SWSX using microcrystals of the same size and microbeams in order to efficiently collect highly accurate data. The optimal dose for obtaining highly accurate data was investigated by sulfur-SAD (S-SAD) phasing. The evaluation samples used were lysozyme crystals with a controlled size of approximately 20 μm. All SWSX datasets were automatically collected using the ZOO system at BL45XU. The beam size for data measurement was 18(H)×20(V) μm^2. 10° small-wedge data were collected from each crystal with 18 combinations of a wavelength set of 1.0, 1.4, and 1.7 Å, and doses of 1, 2, 5, 10, 20, and 40 MGy (Fig. 1). More than 400 small-wedge datasets were collected under each condition. The dose per crystal of the data measured using the ZOO system was estimated by RADDOSE 3D [5]. Data processing and merging for each small-wedge dataset were performed by XDS using KAMO [6]. The clustering process for data merging was BLEND [7]. For each merged dataset, S-SAD phasing was performed using SHELXC, SHELXD, and SHELXE in SHELX [8]. Among the six doses at a wavelength of 1.0 Å, only the dose of 5 MGy resulted in successful phasing by S-SAD (Table 1). At a wavelength of 1.4 Å, the doses of 1, 2, 5, 10, and 20 MGy resulted in successful phasing by S-SAD, but not the dose of 40 MGy. Experimental phases were successfully determined for all doses at a wavelength of 1.7 Å.

Furthermore, to determine the contribution of the number of merged datasets at wavelengths of 1.4 and 1.7 Å in phase determination, CCmap for each dose was plotted (Fig. 2). The number of merged datasets was set to eight patterns (25, 50, 75, 100, 125, 150, 175, and 200 sets), and 10 repetitions of random dataset extraction and merging were independently conducted for each number of merged datasets for two different wavelengths, 1.4 and 1.7 Å. For both wavelengths, CCmap increased with the number of merged datasets, except at a dose of 40 MGy at a wavelength of 1.4 Å. It was clearly shown that the higher the number of merged datasets, the easier the phase determination becomes at any dose.

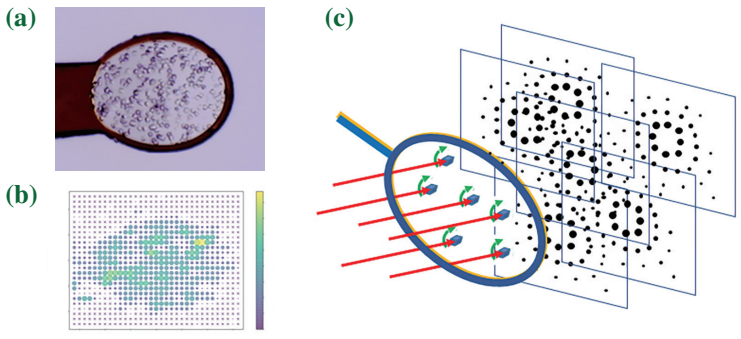

Fig. 1. Details of SWSX data collection. **(a)** Multiple crystals in cryoloop. **(b)** Results of an X-ray raster scan of multiple crystals in a cryoloop. **(c)** 5–20° small-wedge data are collected from each crystal.

For both wavelengths of 1.4 and 1.7 Å, the dose of 5 MGy produced the least number of datasets and increased CCmap, and the second-best doses were 2 and 10 MGy. The number of merged datasets that increased CCmap was higher at a wavelength of 1.7 Å than at a wavelength of 1.4 Å. This is because the Bijvoet ratio of lysozyme in S-SAD is 1.76% (f"= 0.67) at a wavelength of 1.7 Å, which is larger than 1.23% (f"= 0.47) at a wavelength of 1.4 Å. These results indicate that a dose of approximately 5 MGy at any wavelength enables the phase determination of S-SAD at the lowest number of datasets, which can be measured in a shorter time. The higher the number of merged datasets, the easier the phase determination becomes. This shows that data accuracy improves with the number of merged datasets in SWSX. For high doses of 20 MGy at a wavelength of 1.4 Å and 20 and 40 MGy at a wavelength of 1.7 Å radiation damage was severe and the data accuracy decreased. S-SAD phasing was made possible by increasing the number of datasets to be merged and improving the accuracy. However, at a higher dose of 40 MGy at a wavelength of 1.4 Å, the degraded data accuracy due to radiation damage could not be recovered by the merging process.

On the other hand, at the lower doses of 1 and 2 MGy at both wavelengths of 1.7 and 1.4 Å, the signal was insufficient, but it was recovered by increasing the number of datasets to be merged. The general dose slicing strategy is to add the sliced data in a merging process to ensure accurate measurements. However, this is not efficient because it requires a long measurement time for a number of repetitions.

Table 1. Numbers of merged crystals and S-SAD phasing statistics of lysozyme crystals at different doses at a wavelengths of 1.0, 1.4, and 1.7 Å.

Dose (MGy)	1	2	5	10	20	40
Wavelength	1.0 Å					
Number of crystals	366	357	384	243	428	399
S-SAD Phasing	Failure	Failure	Success	Failure	Failure	Failure
Wavelength	1.4 Å					
Number of crystals	335	400	404	219	316	348
S-SAD Phasing	Success	Success	Success	Success	Success	Failure
Wavelength	1.7 Å					
Number of crystals	353	453	358	395	218	298
S-SAD Phasing	Success	Success	Success	Success	Success	Success

In SWSX, increasing the number of crystals in the merging process makes the phase determination easier. The dose of 5 MGy at both wavelengths of 1.7 and 1.4 Å was the most efficient in degrading the accuracy through radiation damage and in recovering the accuracy in accordance with the number of merges. In this study, we suggested that the optimal condition for high-efficiency/accuracy data collection condition with SWSX is to acquire one data set at a dose of 5 MGy per crystal.

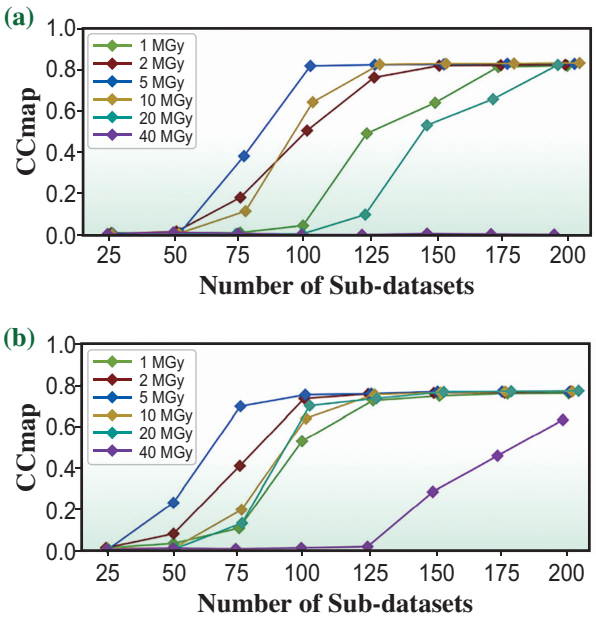

Fig. 2. Correlation between the number of datasets merged for each dose and CCmap for wavelength of **(a)** 1.4 Å and **(b)** 1.7 Å. The mean CCmap values derived from the phase determination for 10 randomly selected datasets are plotted against the number of datasets merged.

Seiki Baba

Japan Synchrotron Radiation Research Institute (JASRI)

Email: baba@spring8.or.jp

References

[1] K. Hasegawa *et al.*: J. Synchrotron Rad. **24** (2017) 29.
[2] V. Cherezov *et al.*: J. R. Soc. Interface. **6** (2009) S587.
[3] G. Ueno *et al.*: J. Synchrotron Rad. **12** (2005) 380.
[4] K. Hirata *et al.*: Acta Cryst. **D75** (2019) 138.
[5] O. B. Zeldin *et al.*: J. Appl. Crystallogr. **46** (2013) 1225.
[6] K. Yamashita *et al.*: Acta Cryst. **D74** (2018) 441.
[7] J. Foadi *et al.*: Acta Cryst. **D69** (2013) 1617.
[8] G. M. Sheldrick: Acta Cryst. **D66** (2010) 479.

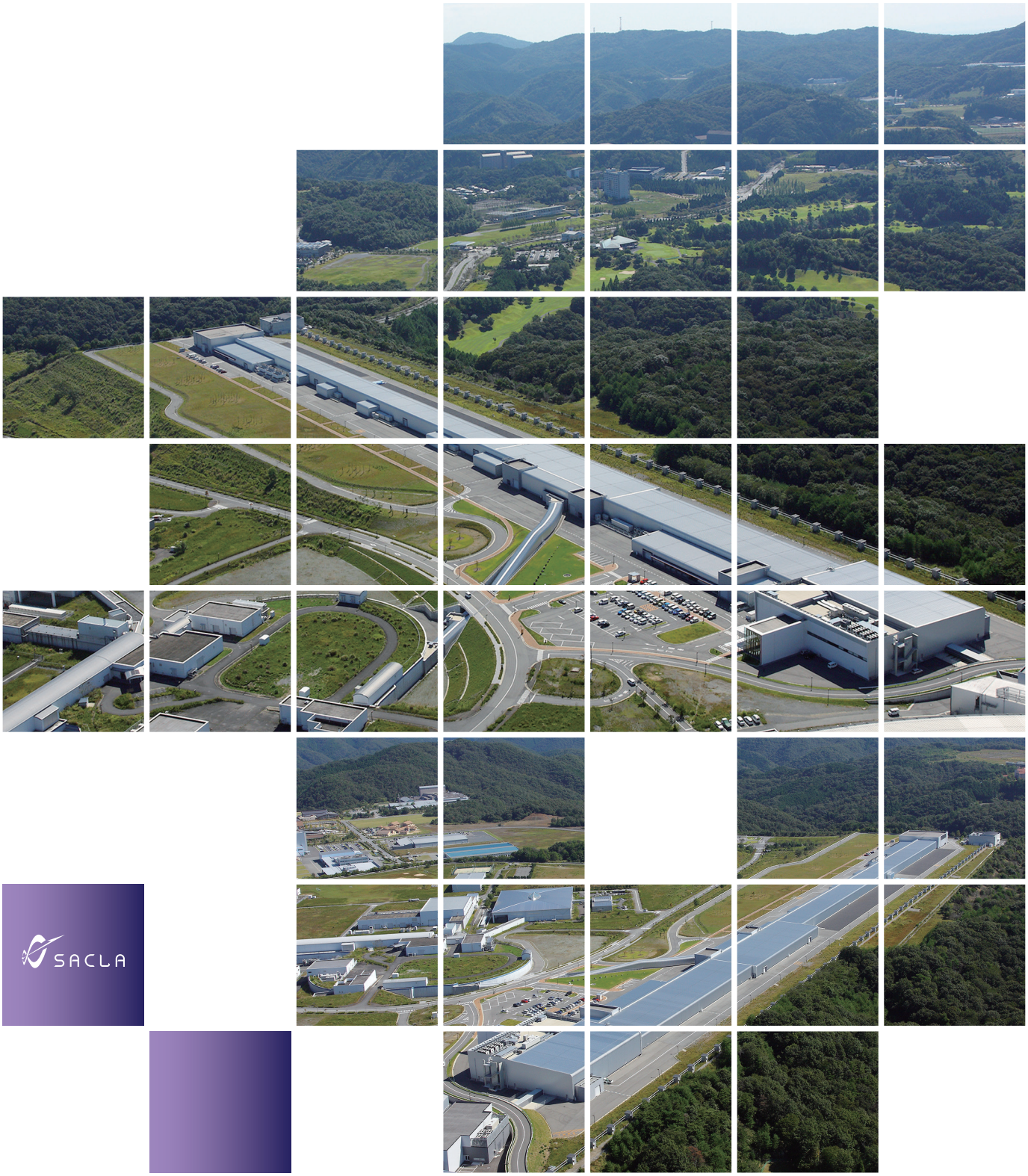

SACLA Beam Performance

During 2021, timesharing of the SACLA linac as a ring injector was established as a standard operation. By means of this new standard operation, the SACLA accelerator system can provide throughout the year not only stable and high performance XFELs, but also reliable and stable top-up injections for SPring-8 experimental users.

Aiming at establishing highly efficient accelerator tuning to reproduce the XFEL performance, we previously developed a model-free tuning tool using a Gaussian process regression (GPR) optimizer. This tool is routinely used to prepare machine parameter sets that provide the XFEL performance required for user experiments. It has been utilized effectively to increase the energy of laser pulses to sufficient levels under specified wavelengths and pulse widths. On the other hand, owing to the low spectral resolution of in-line single-shot spectrometers, it is currently not possible to adequately control narrow spectral widths. The SACLA Beamline Group has developed a new in-line single-shot spectrometer with sufficiently high resolution and installed the prototype in the BL3 experimental hutch. Using precise spectral data, BL3 is now able to provide brilliant XFELs with narrow spectral widths for user experiments. Figure 1 shows an example of a narrow-spectrum XFEL obtained with this new in-line spectrometer. To fully utilize the developed spectrometer for tuning, it will be moved from the experimental hutch to the optics hutch during the summer shutdown period in 2022. The developed spectrometer will be installed in the BL2 optical hutch after winter 2022 to deliver narrow spectral XFELs at BL2.

In parallel with the improvement of tuning procedures, the upgrade of the accelerator system to achieve higher pulse energy in multi-beamline operations has been investigated. To control the electron beam envelope on a pulse-by-pulse basis, the DC quadrupole magnet system downstream of the linac after the third bunch compressor will be successively replaced by a system in which focusing force is adjustable pulse-by-pulse.

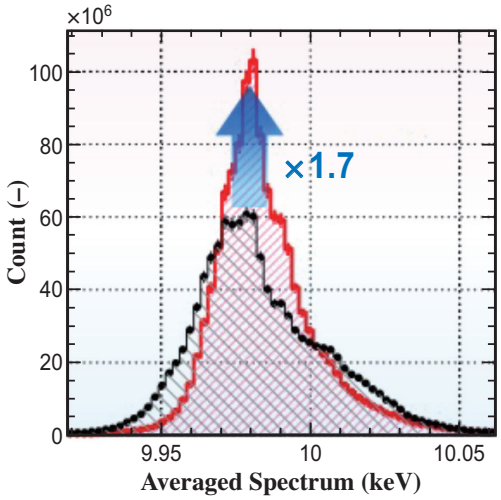

Fig. 1. XFEL spectra. Red and black lines show the spectrum obtained with and without the use of the inline spectrometer, respectively

Hitoshi Tanaka

RIKEN SPring-8 Center

Email: tanaka@spring8.or.jp

FACILITY STATUS

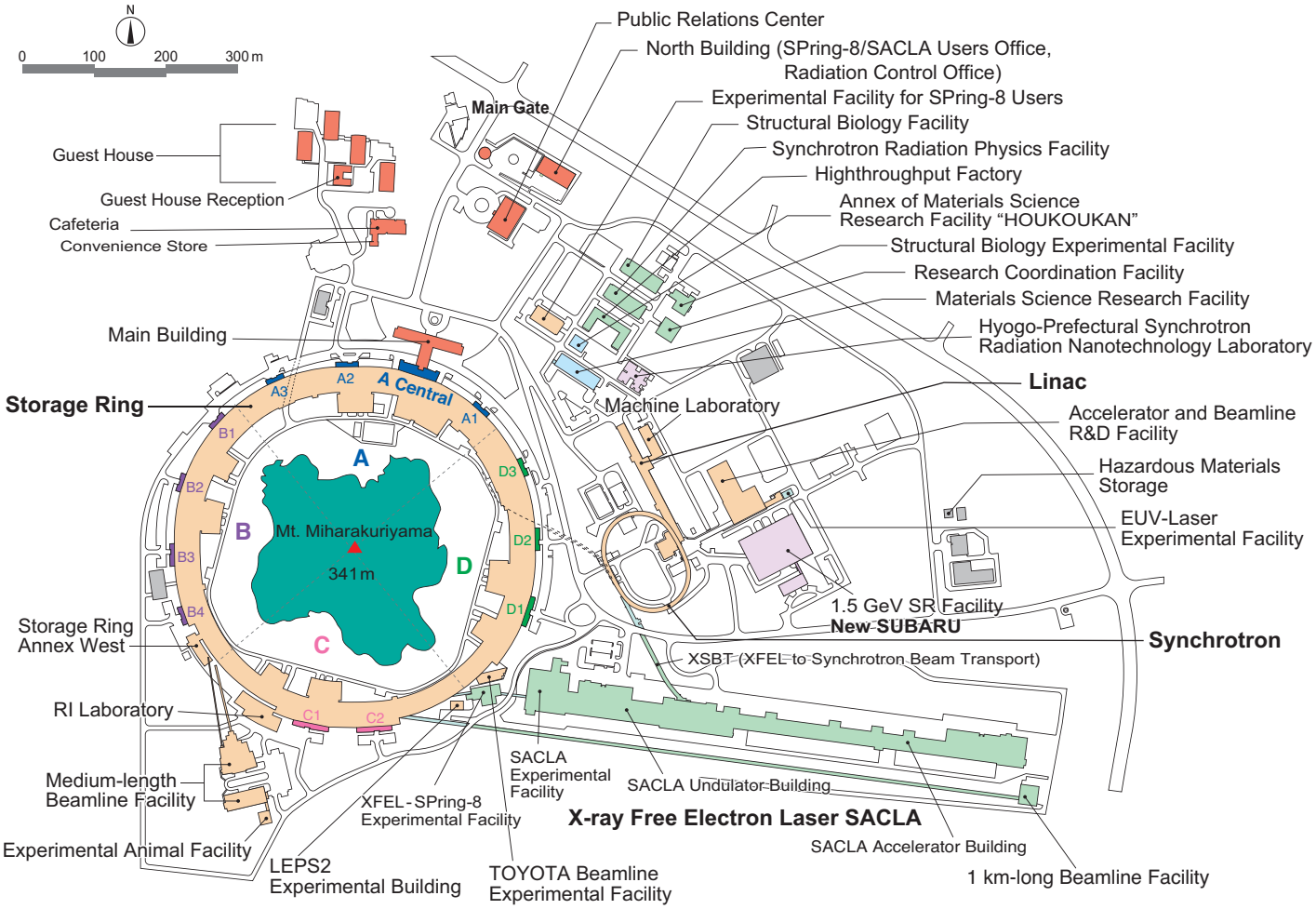

SPring-8

I. Introduction

SPring-8 was stably operated throughout FY2021 with the total operation time of the accelerator complex and the total user beam time of 5300.2 h and 4426.9 h, respectively, and a total downtime of 10.0 h. SPring-8 had to complete all its operations by the middle of February 2022.

Three interim reviews were conducted for contract beamlines SUNBEAM ID (BL16XU, SUNBEAM Consortium), SUNBEAM BM (BL16B2, SUNBEAM Consortium), Macromolecular Assemblies (BL44XU, Institute for Protein Research, Osaka University) and TOYOTA (BL33XU, TOYOTA Central R&D Labs., Inc.), and the projects were authorized to continue. Because of contract cancellation, the postevaluation of WEBRAM (BL15XU, National Institute for Materials Sciences) was conducted. At present, the number of SPring-8 users is as high as 12,000, all of whom are members of the SPring-8 User Community (SPRUC).

It is important for SPring-8 to jointly organize scientific events with SPRUC, such as the SPring-8 Symposium, to facilitate dialogue between users and the facility staff. In 2021, the SPring-8 Symposium was held online on September 17 and 18 owing to COVID-19, with 480 participants. SPring-8 also facilitates communication between users and industry. The Joint Conference on Industrial Applications of SPring-8 was held in Hyogo Prefecture on September 1 and 2, 2021, with 295 participants (126 were online participants). As part of its continuous effort towards fostering human resources in synchrotron sciences, SPring-8 organized the 21st SPring-8 Summer School with 74 students of graduate schools nationwide, in cooperation with University of Hyogo, Kwansei Gakuin University, The University of Tokyo, Okayama University, Osaka University, Ibaraki University, Japan Atomic Energy Agency, National Institutes for Quantum and Science and Technology, and RIKEN. Furthermore, SPring-8 and SPRUC organized the 5th SPring-8 Autumn School with 59 participants, which included university students and corporate researchers.

II. Machine Operation

The operation statistics for the last five fiscal years are shown in Fig. 1. The linear accelerator of the X-ray Free-Electron Laser (XFEL) facility, SACLA, has been used as a full-time injector for the SPring-8 storage ring since 2020. In FY2021, all the user time was taken up by beam accumulation and topping-up by beam injecting from the SACLA linac. The operation time of the storage ring was 5300.2 h, 83.5% of which (4426.9 h) was devoted to the SR experiments. This excellent figure for the user time represents a storage ring availability of 99.7%. The total downtime caused by failures amounted to 10.0 h, accounting for 0.22% of the total user time. For 99.6% of the user time in FY2021, the stored beam current stayed at 100 mA by the top-up operation wherein the stored beam was filled up on demand at any time. Extreme stability of the light source intensity of better than 0.1% was achieved by the top-up operation.

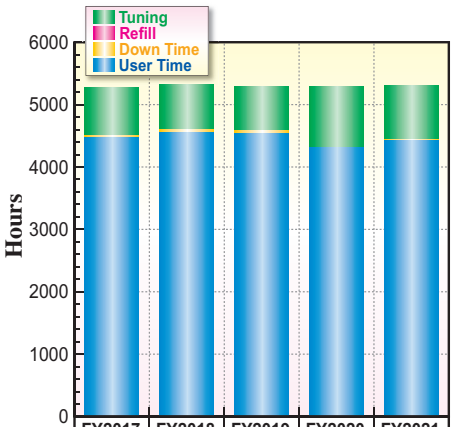

	FY2017	FY2018	FY2019	FY2020	FY2021
Accelerator Operation Time	5281.6	5329.8	5285.7	5284.6	5300.2
Storage Ring Operation Time	5270.4	5316.7	5271.2	5274.8	5300.2
Tuning & Study (Acc. & BL)	769.6	721.8	701.7	964.6	860.2
Refill	4.6	5.3	5.6	3.6	3.1
Down Time	28.7	43.1	40.5	7.4	10.0
Mean Time Between Failures	194.7	168.9	206.3	718.2	553.4
Achieved User Time	4478.7	4559.6	4537.9	4309.0	4426.9
Planned User Time	4512.0	4608.0	4584.0	4464.0	4440.0
Availability (%)	99.3	98.9	99.0	99.7	99.7

Fig. 1. Operation statistics for five most recent fiscal years.

Table 1. Operation modes in FY2021

	Single bunch current (mA)	Share of operation time (%)
203 bunches		41.1
4 bunch-train × 84		3.2
11 bunch-train × 29		30.8
1/7-filling + 5 single bunches	3	8.1
2/29-filling + 26 single bunches	1.4	0
1/14-filling + 12 single bunches	1.6	3.2
4/58-filling + 53 single bunches	1.0	0
406 × 11/29-filling + 1 single bunch	5	13.5

The variety of operation modes for the SR experiments is one of the characteristics of SPring-8. The operation modes are classified into two types, the several-bunch and hybrid-filling modes. The several-bunch mode consists of equally spaced bunches or trains of bunches such as 203 bunches or 29 trains of 11 bunches. The hybrid-filling mode is composed of a long train of bunches and isolated single bunches. The operation modes of SPring-8 are listed in Table 1 with the share of each operation mode in FY2021. In the operation with beam injection from the SACLA linac, the spurious bunch sweeping system in the SACLA linac and the bunch cleaning system in the storage ring are activated to maintain a sufficient isolated bunch purity. Table 2 summarizes the beam parameters of the storage ring.

Table 2. Beam parameters of SPring-8 storage ring

Energy [GeV]	8
Number of buckets	2436
Tunes (ν_x / ν_y)	41.14 / 19.325
Current [mA]:	
single bunch	12
multi bunch	100
Bunch length (σ) [psec]	13
Horizontal emittance [nm·rad]	2.4 *
Vertical emittance [pm·rad]	4.8 *
Coupling [%]	0.2
RF Voltage [MV]	14.4 ** ~ 16
Momentum acceptance [%]	3.2 (~256 MeV)
Beam size (σ_x / σ_y)* [μm]	
Long ID section	333 / 7
ID section	316 / 5
BM1 section	94 / 12
BM2 section	100 / 12
Beam divergence ($\sigma_{x'}$ / $\sigma_{y'}$)* [μrad]	
Long ID section	8 / 0.7
ID section	9 / 1.0
BM1 section	58 / 0.5
BM2 section	68 / 0.5
Operational chromaticities (ξ_x / ξ_y)	+2 / +2 ***
Lifetime [hr]:	
100 mA (multi bunch)	~250
1 mA (single bunch)	~30
Horizontal dispersion [m]:	
Long ID section	0.153
ID section	0.146
BM1 section	0.039
BM2 section	0.059
Fast orbit stability (0.1 – 200 Hz) [μm]:	
horizontal (rms)	~4
vertical (rms)	~1

* Assuming 0.2% coupling
** Power saving mode
*** With bunch-by-bunch feedback

III. Beamlines

The SPring-8 storage ring can accommodate up to 62 beamlines: 34 insertion devices, 4 long undulators, and 24 bending magnets. At present, 57 beamlines are in operation, covering a wide variety of research fields involving synchrotron radiation science and technology. The beamlines are classified into the following three types.

(1) Public Beamlines (26 beamlines operating),
(2) Contract Beamlines (17 beamlines operating), and
(3) RIKEN Beamlines (14 beamlines operating).

There are now 26 public beamlines in full operation. The beamlines that have been proposed and constructed by external organizations, such as universities, research institutes, private companies and consortiums, are called contract beamlines, which are used exclusively by the contractors for their own research purposes. At present, 17 contract beamlines are in operation. The beamlines constructed by RIKEN or transferred to RIKEN, except for public beamlines, are called RIKEN beamlines, which are mainly used for RIKEN's own research activities, with partial availability for public use. RIKEN is now operating 14 beamlines. To illustrate the beamline portfolio of SPring-8, a beamline map is shown in Fig. 2 together with the beamline classification. The research fields of each beamline are presented in Table 3.

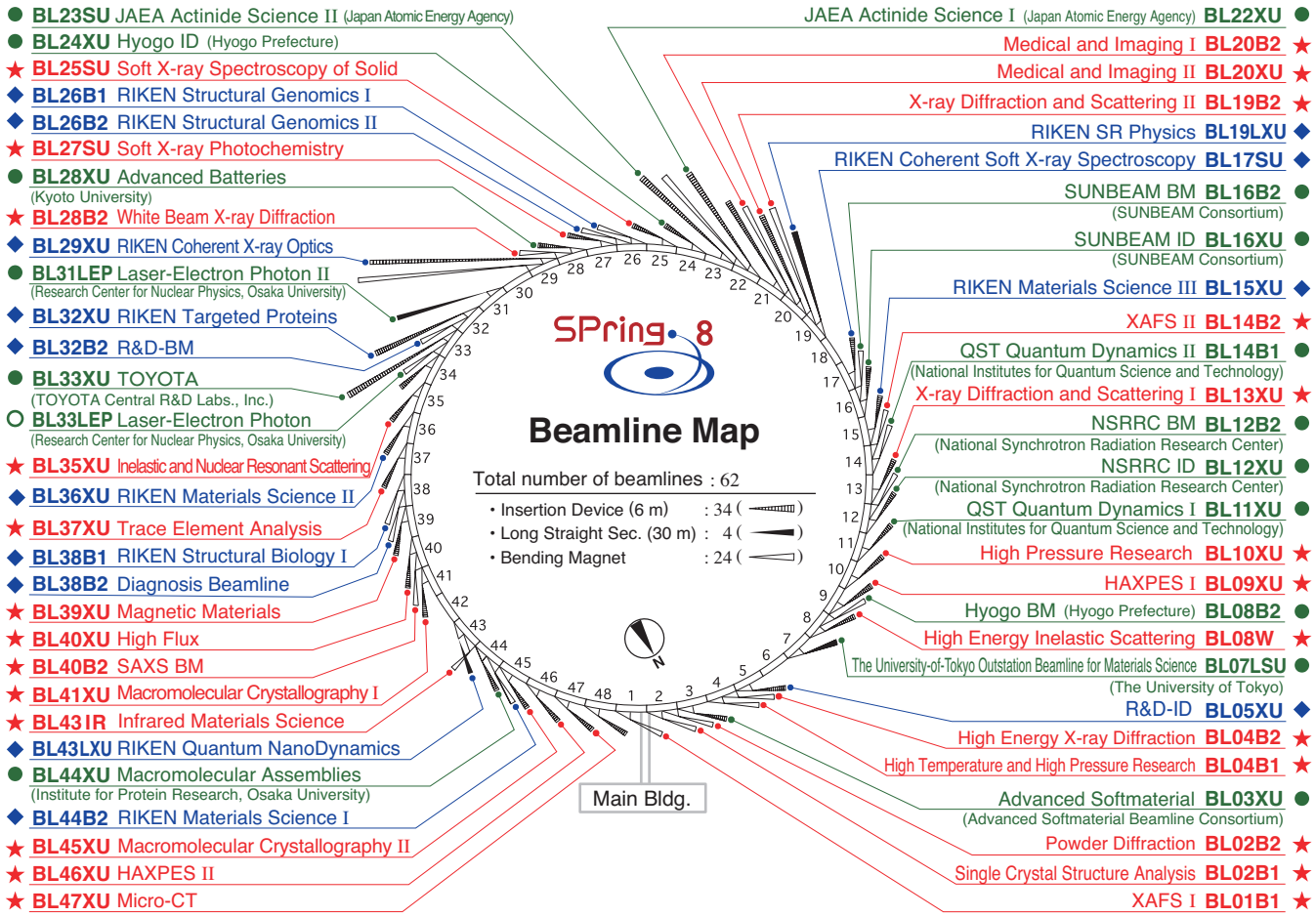

BL: Beamline
B1, B2: Bending Magnets
XU: X-ray Undulator
SU: Soft X-ray Undulator
W: Wiggler

IR: Infrared Radiation
LEP: Laser-Electron Photon
LXU: Long-length X-ray Undulator
LSU: Long-length Soft X-ray Undulator

NSRRC: National Synchrotron Radiation Research Center, Taiwan

★ : Public Beamlines
● : Contract Beamlines
◆ : RIKEN Beamlines

○ : Under removal work

Fig. 2. Beamline map.

Table 3. List of beamlines

BL #	Beamline Name	(Public Use) or (First Beam)	Areas of Research and Available Techniques
★ Public Beamlines as of April 2022			
BL01B1	XAFS	(Oct. 1997)	Wide energy range (3.8–113 keV), XAFS of dilute systems and thin films, time-resolved XAFS by quick scan (time-resolved QXAFS), depth-resolved XAFS. XAFS at low and high temperatures. Simultaneous XAFS and XRD measurements. Simultaneous XAFS and IR measurements.
BL02B1	Single Crystal Structure Analysis	(Oct. 1997)	Charge density study using high energy X-ray. *In situ* single crystal experiments. Microcrystal structure analysis.
BL02B2	Powder Diffraction	(Sept. 1999)	Charge density study from powder diffraction. Structural phase transition. *Ab initio* structure determination from powder diffraction. Crystal structure refinement by Rietveld method. *In situ* powder diffraction experiment under gas and vapor adsorption/desorption.
BL04B1	High Temperature and High Pressure Research	(Oct. 1997)	X-ray diffraction measurements and radiography under extreme conditions using large-volume press.
BL04B2	High Energy X-ray Diffraction	(Sept. 1999)	Structural analysis of glass, liquid, and amorphous materials.
BL08W	High Energy Inelastic Scattering	(Oct. 1997)	Magnetic Compton scattering. High-resolution Compton scattering. Compton scattering imaging. High-energy X-ray scattering. High-energy X-ray fluorescence analysis (XRF). Time-resolved pair distribution function analysis (PDF).
BL09XU	HAXPES	(Oct. 1997)	Resonant hard X-ray photoelectron spectroscopy (HAXPES). Polarization-dependent HAXPES using diamond phase retarder. Depth analysis of electron state. Materials science and applied materials science.
BL10XU	High Pressure Research	(Oct. 1997)	Crystal structure analysis under high pressure using diamond-anvil cells, *in situ* /*operando* observation of phase transition and compression behavior under extreme conditions. Material sciences under extreme conditions. High pressure Earth and Planetary science.
BL13XU	Surface and Interface Structures	(Sept. 2001)	X-ray diffraction and reflectivity measurements. Atomic-scale structural analysis of crystal surfaces and interfaces, ultrathin films, and nanostructures. Residual stress measurement. Time-resolved X-ray diffraction. *In situ* process observation using X-ray diffraction. *Operando* X-ray diffraction. High-resolution powder X-ray diffraction and X-ray total scattering. Structural refinement using Rietveld analysis. *In situ* /*operando* powder X-ray diffraction. Time-resolved powder X-ray diffraction. Analysis of local structures using micro/nano beam.
BL14B2	Engineering Science Research II	(Sept. 2007)	X-ray imaging. XAFS in a wide energy range (5–72 keV). XAFS of dilute systems and thin films. Time-resolved XAFS by quick scan (Time-resolved QXAFS).
BL19B2	Engineering Science Research I	(Nov. 2001)	Residual stress measurement. Structural analysis of thin film, surface and interface. Powder X-ray diffraction. X-ray topography. Ultrasmall-angle X-ray scattering.
BL20XU	Medical and Imaging II	(Sept. 2001)	X-ray micro-/nano-imaging: micro-CT, nano-CT (15–37.7 keV), refraction/phase contrast imaging. X-ray diffraction tomography (XRD-CT), microbeam/scanning X-ray microscope. Research and development of X-ray optics and optical elements, coherent X-ray optics. Ultra small-angle X-ray scattering (USAXS, 23 keV).
BL20B2	Medical and Imaging I	(Sept. 1999)	Micro-radiography, micro-angiography, micro-tomography, and refraction-contrast imaging are the mainly used techniques. BL20B2 is also applicable to small-animal experiments for medical research. Research and development of basic techniques for evaluation of optical devices and X-ray imaging.
BL25SU	Soft X-ray Spectroscopy of Solid	(Apr. 1998)	Research on electron states by photoemission spectroscopy (PES). Research on electronic band structures by angle-resolved photoemission spectroscopy (ARPES). Study of magnetic states by magnetic circular dichroism (MCD) of soft X-ray absorption. Analysis of surface atomic arrangement by photoelectron diffraction (PED). Nano-spectroscopic analysis using low-energy/photoemission electron microscope (SPELEEM).
BL27SU	Soft X-ray Photochemistry	(May 1998)	Soft X-ray photoabsorption spectroscopy of dilute samples in partial fluorescence yield mode. Surface and interface analysis using depth-resolved soft X-ray photoabsorption spectroscopy. Soft X-ray photoabsorption spectroscopy under ambient atmospheric pressure. Spectroscopy using soft X-ray microbeam. Observation of electron state in solids by soft X-ray emission spectroscopy.
BL28B2	White Beam X-ray Diffraction	(Sept. 1999)	White X-ray diffraction: X-ray topography. Energy-dispersive strain measurement. Time-resolved energy-dispersive XAFS (DXAFS) for studies of chemical and/or physical reaction process. Radiation therapy. High energy (~200 keV) X-ray microtomography.
BL35XU	Inelastic and Nuclear Resonant Scattering	(Sept. 2001)	Phonons in solids and atomic dynamics in disordered materials by inelastic X-ray scattering. Atomic and molecular dynamics by nuclear resonant inelastic scattering and quasi-elastic scattering. Synchrotron-radiation-based Mössbauer spectroscopy. Nuclear excitation.
BL37XU	Trace Element Analysis	(Nov. 2002)	X-ray microbeam/nano-beam spectrochemical analysis. X-ray spectroscopic imaging. Ultratrace-element analysis. High-energy X-ray fluorescence analysis. Projection/scanning/imaging XAFS microscopy. High brightness XAFS. Coherent diffraction imaging XAFS microscopy.
BL39XU	Magnetic Materials	(Oct. 1997)	X-ray magnetic circular dichroism (XMCD) spectroscopy and element-specific magnetometry (ESM). X-ray emission spectroscopy (XES) and its magnetic circular dichroism. XMCD magnetic imaging and local ESM using micro/nanobeam, XAFS microscopy and local ESM, XAFS and XMCD at high pressure. X-ray spectroscopy using variable X-ray polarization (horizontally/perpendicularly linear or circular).
BL40XU	High Flux	(Apr. 2000)	Fast time-resolved X-ray diffraction and scattering experiments. X-ray photon correlation spectroscopy, X-ray fluorescence analysis. Microbeam X-ray diffraction and scattering experiments. Micro-crystallography.
BL40B2	Structural Biology II	(Sept. 1999)	Small-angle X-ray scattering (SAXS).
BL41XU	Structural Biology I	(Oct. 1997)	Macromolecular crystallography. Micro-crystallography. Ultra-high resolution structural analysis.
BL43IR	Infrared Materials Science	(Apr. 2000)	Infrared microspectroscopy.
BL45XU	Structural Biology III	(Apr. 2019)	Macromolecular crystallography. Micro-crystallography. Automation and high throughput data collection for protein crystallography.
BL46XU	Engineering Science Research III	(Nov. 2000)	Hard X-ray photoemission spectroscopy.
BL47XU	HAXPES·μCT	(Oct. 1997)	X-ray optics. Planetary science. Materials science. Applied materials science.

BL #	Beamline Name	(Public Use) or (First Beam)	Areas of Research and Available Techniques
	● Contract Beamlines as of April 2022		
BL03XU	**Advanced Softmaterial** (Advanced Softmaterial Beamline Consortium)	(Nov. 2009)	Structural characterization of softmaterials using small- and wide-angle X-ray scattering. Grazing-incidence small- and wide-angle X-ray scattering for thin films.
BL07LSU	**The University-of-Tokyo Outstation Beamline for Materials Science** (The University of Tokyo)	(Oct. 2009)	Ambient pressure photoemission spectroscopy, nano-beam photoemission spectroscopy, high-resolution soft X-ray emission spectroscopy, and any methods requiring the highly brilliant soft X-ray beam.
BL08B2	**Hyogo BM** (Hyogo Prefecture)	(Jun. 2005)	XAFS in a wide energy region. Small angle X-ray scattering. X-ray topography. Imaging. X-ray diffraction for multipurpose.
BL11XU	**QST Quantum Dynamics I** (National Institutes for Quantum Science and Technology)	(Oct. 1998)	Nuclear resonant scattering. Surface and interface structure with MBE. Resonant inelastic X-ray scattering. X-ray emission spectroscopy.
BL12B2	**NSRRC BM** (National Synchrotron Rad. Res. Center)	(Oct. 2000)	X-ray absorption spectroscopy. Powder X-ray diffraction. High resolution X-ray scattering. Protein crystallography.
BL12XU	**NSRRC ID** (National Synchrotron Rad. Res. Center)	(Dec. 2001)	Non-resonant or resonant inelastic X-ray scattering. Hard X-ray photoemission spectroscopy.
BL14B1	**QST Quantum Dynamics II** (National Institutes for Quantum Science and Technology)	(Dec. 1997)	Materials science at high pressure. XAFS. Time-resolved energy-dispersive XAFS (DXAFS).
BL16B2	**SUNBEAM BM** (SUNBEAM Consortium)	(Oct. 1998)	Characterization of secondary battery related materials, semiconductors, fuel cells, catalysts, and several industrial materials with using X-ray absorption fine structure measurements, X-ray diffraction (including X-ray reflectivity technique), X-ray topography and computed tomography/laminography.
BL16XU	**SUNBEAM ID** (SUNBEAM Consortium)	(Oct. 1998)	Characterization of secondary battery related materials, semiconductors, fuel cells, catalysts, and structural materials using X-ray diffraction, X-ray microbeam based evaluation techniques (including X-ray magnetic circular dichroism), hard X-ray photoelectron spectroscopy and fluorescence X-ray analysis.
BL22XU	**JAEA Actinide Science I** (Japan Atomic Energy Agency)	(May 2002)	HAXPES. XAFS. Residual stress/strain distribution analysis. High-pressure science. Coherent X-ray diffraction. Surface X-ray diffraction. High-energy X-ray diffraction. Time-resolved X-ray diffraction.
BL23SU	**JAEA Actinide Science II** (Japan Atomic Energy Agency)	(Feb. 1998)	Surface chemistry with supersonic molecular beam. Photoelectron spectroscopy. Magnetic circular dichroism. STXM.
BL24XU	**Hyogo ID** (Hyogo Prefecture)	(May. 1998)	Microbeam small- and wide-angle X-ray scattering for local structure analysis. Scanning and imaging microscope, micro-tomography, coherent diffraction. Microbeam X-ray diffraction and bright field X-ray topography for electronic device materials. Near-ambient pressure hard X-ray photoelectron spectroscopy.
BL28XU	**Advanced Batteries** (Kyoto University)	(Apr. 2012)	Characterization of rechargeable battery reactions and battery related materials by resonant X-ray diffraction, X-ray absorption spectroscopy (XAS), X-ray diffraction spectroscopy (XDS), and hard X-ray photoemission spectroscopy (HAXPES).
BL31LEP	**Laser-Electron Photon II** (RCNP, Osaka University)	(Oct. 2013)	Production of high intensity GeV photon beam by laser-backward Compton scattering. Hadron physics via photonucleon and photonuclear reactions. Test and calibration of detectors with GeV gamma-ray and converted electrons/positrons.
BL33LEP	**Laser-Electron Photon** (RCNP, Osaka University)	(Jun. 1999)	Under removal work.
BL33XU	**TOYOTA** (TOYOTA Central R&D Labs., Inc.)	(Apr. 2009)	Time-resolved XAFS. 3DXRD. Characterization of industrial materials and devices (e.g. catalysts, lightweight bodies, secondary batteries, fuel cells, and power modules).
BL44XU	**Macromolecular Assemblies** (IPR, Osaka University)	(May 1999)	Crystal structure analysis of biological macromolecular assemblies (e.g., membrane protein complexes, protein complexes, protein-nucleic acid complexes, and viruses).
	◆ RIKEN Beamlines as of April 2022		
BL05XU	**R&D-ID**	(Mar. 2004)	R&D of high-energy X-ray optics, instruments, and applications; structural and dynamical research using small and wide angle scattering.
BL15XU	**RIKEN Materials Science III**	(Oct. 2021)	Advanced diffraction and scattering with high-energy X-rays.
BL17SU	**RIKEN Coherent Soft X-ray Spectroscopy**	(Sept. 2003)	High resolution photoemission spectroscopy; soft X-ray emission spectroscopy; soft X-ray diffraction spectroscopy; soft X-ray microspectroscopy.
BL19LXU	**RIKEN SR Physics**	(Oct. 2000)	SR science with highly brilliant X-ray beam.
BL26B1	**RIKEN Structural Genomics I**	(Apr. 2002)	Structural biology research based on single crystal X-ray diffraction.
BL26B2	**RIKEN Structural Genomics II**	(Apr. 2002)	Structural biology research based on single crystal X-ray diffraction.
BL29XU	**RIKEN Coherent X-ray Optics**	(Dec. 1998)	X-ray optics, especially coherent X-ray optics.
BL32XU	**RIKEN Targeted Proteins**	(Oct. 2009)	Protein microcrystallography.
BL32B2	**R&D-BM**	(May 2002)	X-ray computed tomography; X-ray diffraction; X-ray absorption fine structure; R&D of SR instruments.
BL36XU	**RIKEN Materials Science II**	(Apr. 2020)	Time resolved XAFS and X-ray diffraction; 2D/3D scanning XAFS imaging; 3D computed tomography/laminography XAFS imaging; X-ray emission spectroscopy; ambient pressure hard X-ray photoelectron spectroscopy; pink beam experiments.
BL38B1	**RIKEN Structural Biology I**	(Oct. 2000)	Structure study of non-crystalline biological materials using small-angle scattering and diffraction techniques.
BL38B2	**Diagnosis Beamline**	(Sept. 1999)	Accelerator beam diagnostics.
BL43LXU	**RIKEN Quantum NanoDynamics**	(Oct. 2011)	High resolution inelastic X-ray scattering for investigating atomic and electronic dynamics.
BL44B2	**RIKEN Materials Science I**	(Feb. 1998)	Structural materials science research using powder X-ray diffraction.

IV. User Program and Statistics

SPring-8 calls for public use proposals twice a year, in principle. The submitted proposals are reviewed by the SPring-8 Proposal Review Committee (SPring-8 PRC). Since 1997, SPring-8 has accepted a variety of proposals. For the promotion of research on industrial applications at SPring-8, currently, Industrial Application Proposals account for approximately 16%–19% of the total number of proposals conducted at various public beamlines. There will always be companies and research institutes that find it difficult to retain specialized staff and to accommodate the need for quick access to SPring-8. To appropriately respond to such circumstances, the SPring-8 Measurement Service is provided.

In this branch of service, JASRI staff members perform measurements on behalf of users. Users may choose either to come to SPring-8 and be present during the measurements or to simply send their samples to SPring-8. Currently, JASRI has been expanding the purview of the SPring-8 Measurement Service to five measurement methods (XAFS, Powder X-ray Diffraction, HAXPES, GIXD/XRR, and SAXS). In addition, JASRI provides Protein Crystallography Automatic Data Collection at Macromolecular Crystallography beamlines. Therefore, users can choose either to come to SPring-8 and be present during the measurements or to simply send their samples to SPring-8. Since the 2022A period, JASRI has been calling for long-term graduate student proposals. The purpose of the Long-Term Graduate Student Proposals is to contribute to the development of human resources who will support and further develop synchrotron radiation sciences. SPring-8 has been affected by COVID-19 to a small extent in FY2021; as a result, the SPring-8 Measurement Service and the Protein Crystallography Automatic Data Collection have become more widely used. Furthermore, SPring-8 is developing a remote-operation system that allows users to control experimental instruments remotely to promote remote access. The number of experiments conducted at and the number of user visits to the public and contract beamlines are summarized in Fig. 3. Some of the proposals are for proprietary use, for which refereed reports are not required. Figures 4 to 13 show information on user programs.

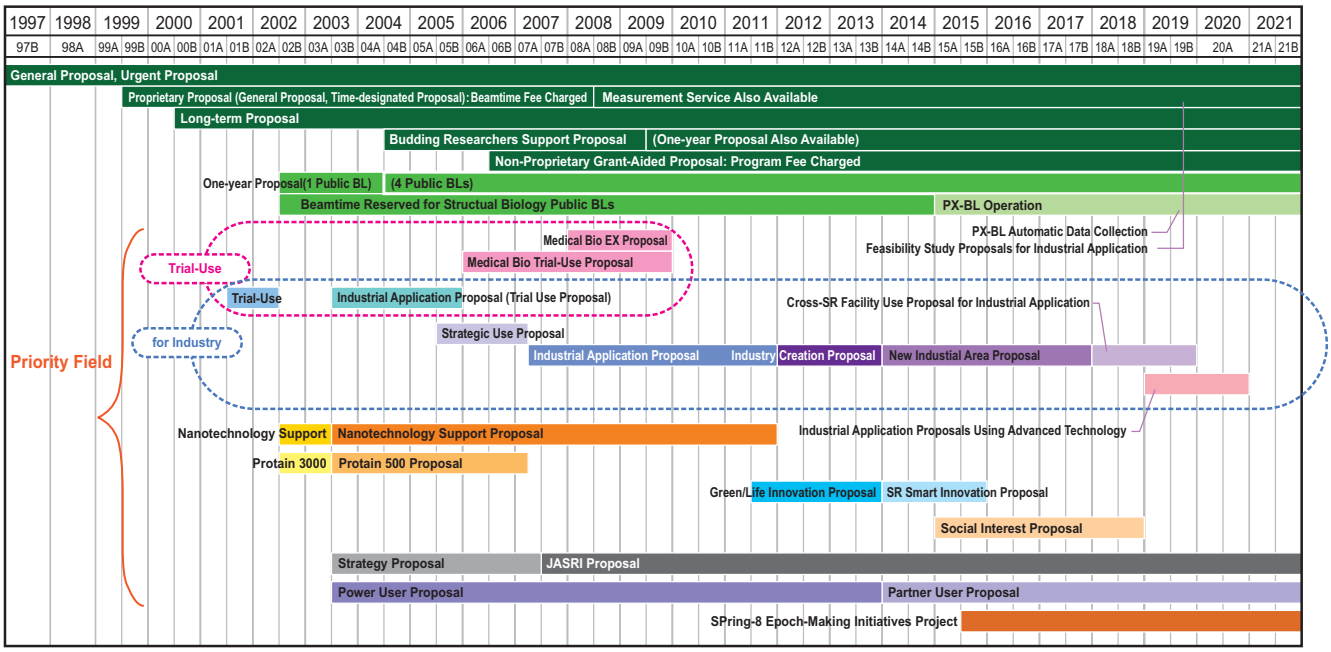

Fig. 3. Categories of proposals for the public beamlines.

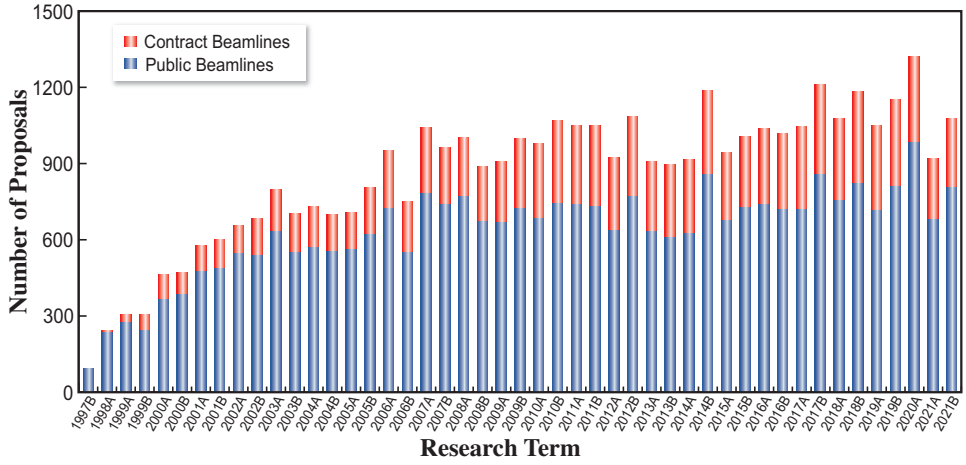

Fig. 4. Numbers of conducted experiments.

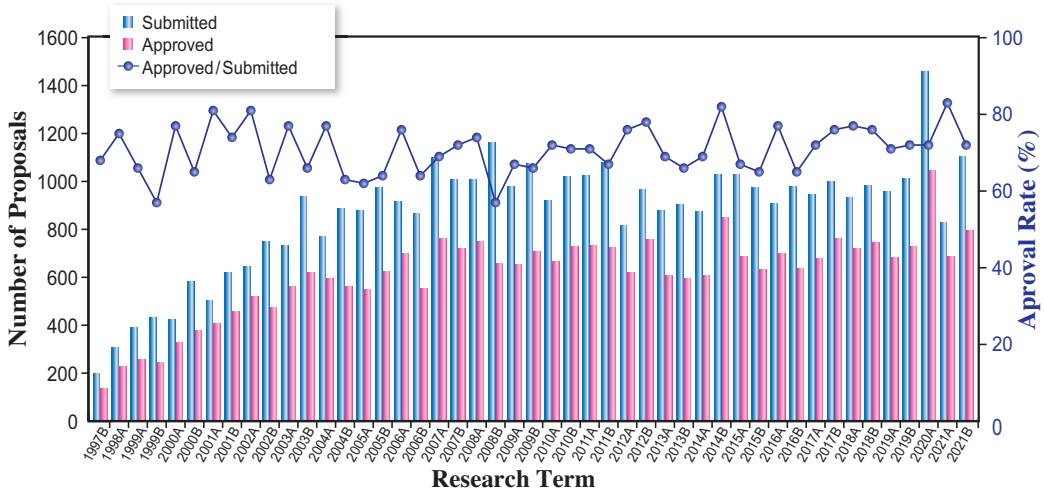

Fig. 5. Numbers of submitted proposals and approved proposals by research term (public beamlines).

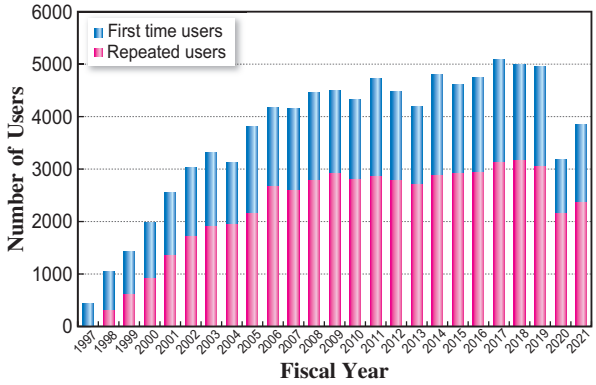

Fig. 6. Numbers of users by fiscal year.

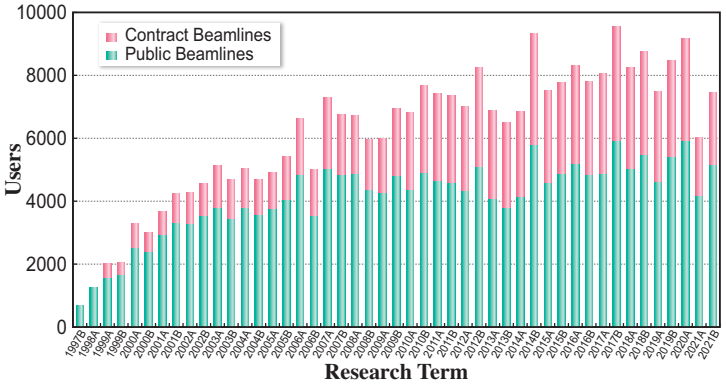

Fig. 7. Numbers of users visits by research term.

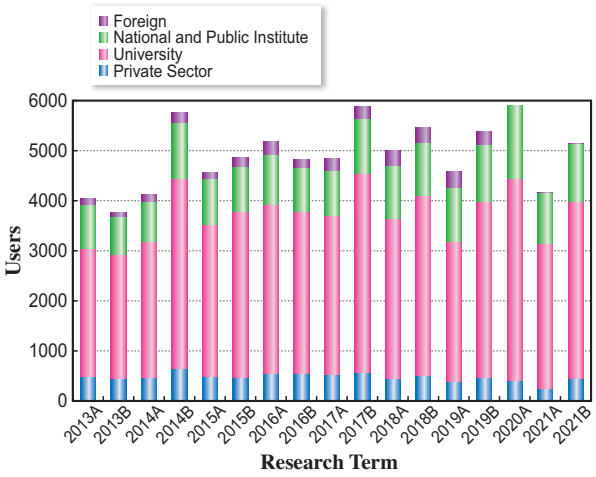

Fig. 8. Numbers of users by affiliation categories (public beamlines).

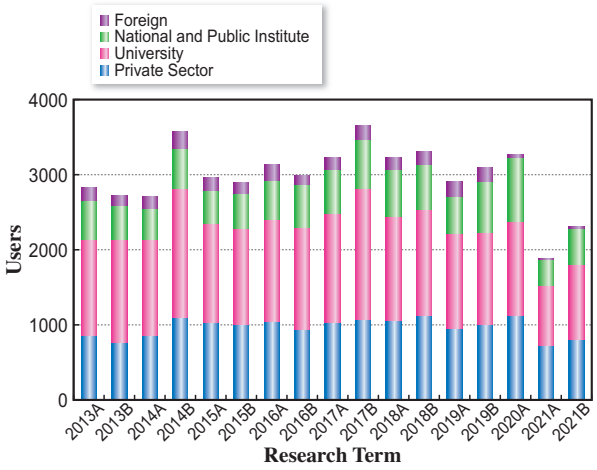

Fig. 9. Numbers of users by affiliation categories (contract beamlines).

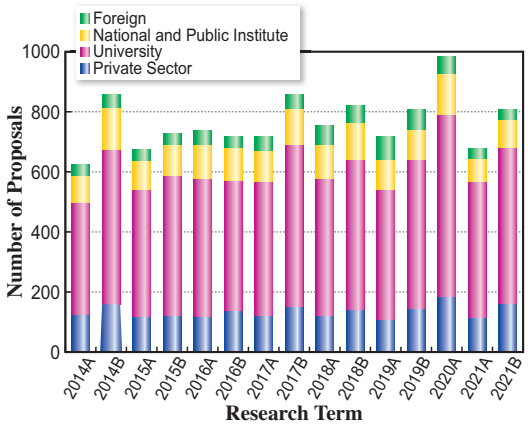

Fig. 10. Numbers of conducted proposals by affiliation (public beamlines).

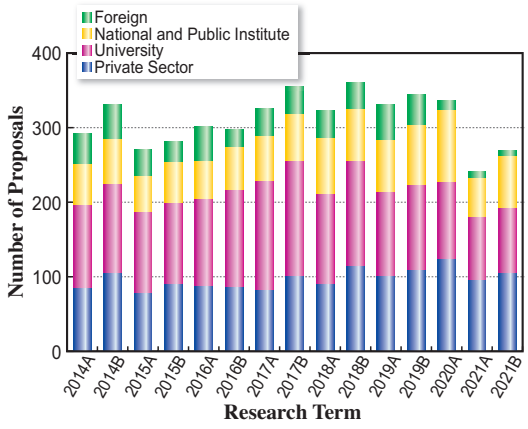

Fig. 11. Numbers of conducted proposals by affiliation categories (contract beamlines).

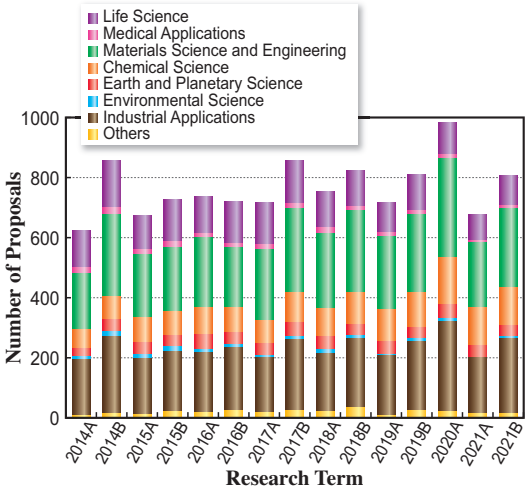

Fig. 12. Numbers of conducted proposals by research area (public beamlines).

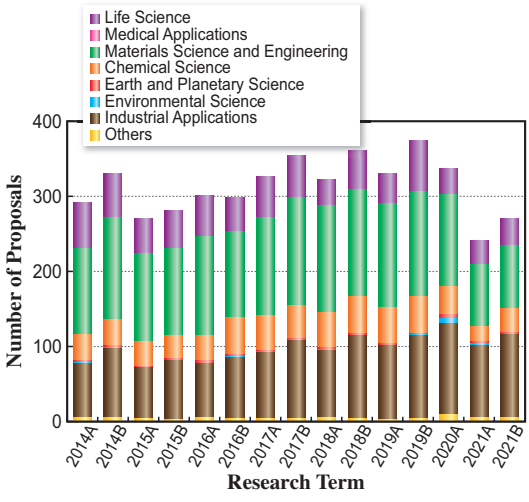

Fig. 13. Numbers of conducted proposals by research area (contract beamlines).

V. Research Outcome

As of March 2022, the total number of registered refereed papers from SPring-8 was 19,735. Figure 14 shows the annual statistics of refereed papers.

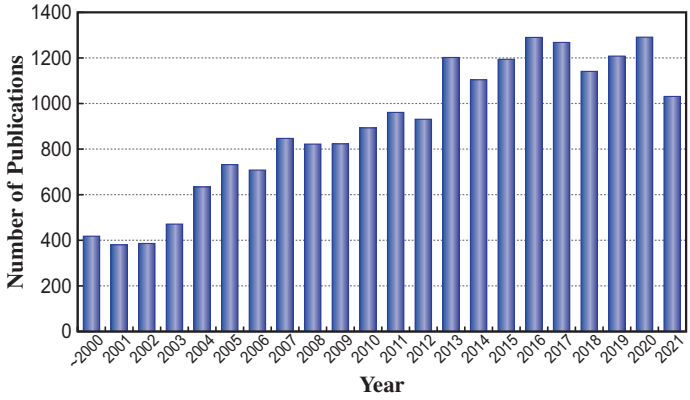

Fig. 14. Number of refereed publications.

VI. Budget and Personnel

When SPring-8 started operation in 1997, it was jointly managed by RIKEN, JAERI (now JAEA), and JASRI. However, JAERI withdrew from the management of SPring-8 on September 30, 2005. SPring-8 is currently administered by RIKEN and JASRI collaboratively.

The total budget for the operation of SPring-8 in FY2021 was about 9.1 billion yen. As of October 2021, RIKEN and JASRI have a total of 462 staff members. Figure 15 shows the annual budget allocated to operations, maintenance, and promotion of SPring-8. Figure 16 shows the manpower at RIKEN and JASRI.

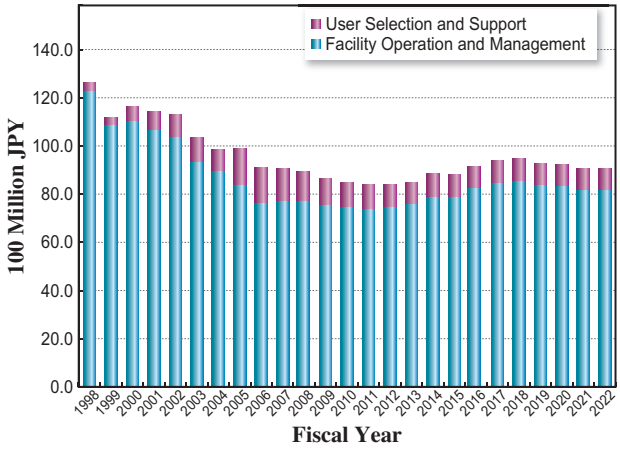

Fig. 15. SPring-8 budget.

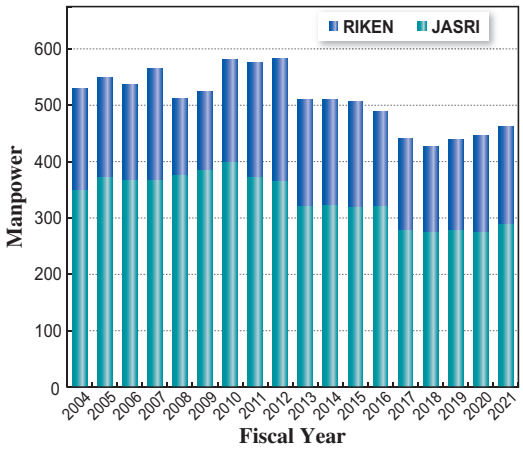

Fig. 16. Personnel at SPring-8: JASRI and RIKEN.

VII. Research Complex

The facilities of SPring-8, SACLA, and NewSUBARU form the Center of Excellence (COE) at the SPring-8 campus where JASRI, public beamline users, the contractors of contract beamlines, RIKEN, and University of Hyogo work in close cooperation, forming a research complex where all members play their own role in delivering high-quality results to the field of synchrotron radiation science and technology. The organizational charts of RIKEN and JASRI, which are at the center of this research complex, are shown in Figs. 17 and 18, respectively.

Fig. 17. RIKEN Harima Campus chart as of April 2022.

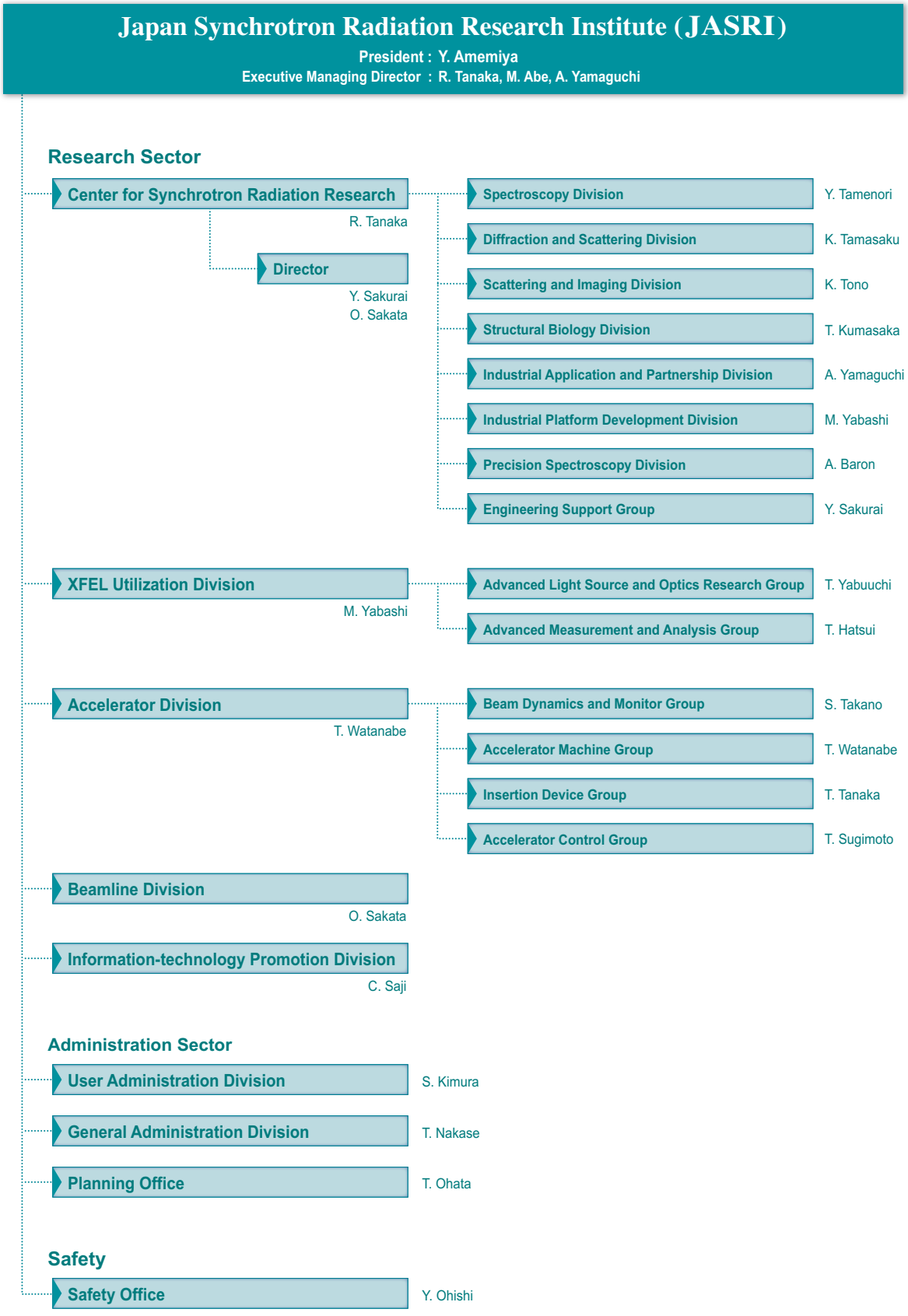

Fig. 18. JASRI chart as of April 2022.

VIII. SPring-8 Users Community (SPRUC)

Prof. A. Kimura
Hiroshima University
SPRUC Chairman FY2020

SPRUC is a user society that consists of all users of SPring-8/SACLA. In addition to individuals, representative organizations of 26 institutes (principal universities, national/international research institutes, industries, and beamline consortiums) participate in SPRUC to discuss further promotion of the utilization of SPring-8 from strategic and perspective viewpoints. Prof. Akio Kimura, Hiroshima University, has been serving as the president of SPRUC for a two-year term since FY2020.

As one of the key activities of SPRUC, the SPring-8 Symposium is held annually at the site of one of the representing organizations jointly with RIKEN and JASRI. SPring-8 Symposium 2021 "Backcasting from SPring-8 Future Vision " was held on September 17 and 18 with a hybrid style of on-site and online presentations. As indicated by the theme, the major issue of the symposium was not how to respond to the rapidly changing modern society on the spot, but rather to draw a future vision of SPring-8 and discuss the current and future use of the facility, including the importance of human resource development, by backcasting it as a goal we should achieve. The ceremony to present the SPRUC 2021 Young Scientist Award, which was conferred on Dr. Yuki Takayama, Graduate School of Science, University of Hyogo, and Dr. Natsuki Tomida, Research Center for Nuclear Physics, Osaka University, was also held. The holding of SPring-8 Symposium 2022 will be considered on the basis of the future status of the COVID-19 pandemic.

SPRUC supported the “SPring-8 Summer School” for the enhancement of users’ research competency and also hosted the “SPring-8 Autumn School” with JASRI to acquire new users and develop human resources. For the Autumn School, the SPRUC research groups contributed to planning the lectures. Although the Autumn School had been scheduled to be held in September, the plan was forced to be postponed to December owing to the recurring COVID-19 pandemic. Despite the difficult situation, both schools were successfully held. We would like to take this opportunity to thank all the people involved.

SPRUC2021 Young Scientist Award
Prof. A. Kimura, Dr. N. Tomida, and Dr. Y. Takayama

SPRUC continues to cohost the beamline upgrade workshop, the fourth of which was held on March 14 with RIKEN and JASRI. The workshop was planned to vitalize information exchange between members of SPRUC and the facility. The workshop focused mainly on mutual consensus regarding the reorganization and upgrade of diffraction and scattering beamlines such as BL13XU, spectroscopy beamlines such as BL39XU, and imaging and small angle X-ray scattering beamlines. The facility presented the latest situation of their reorganization, future prospects and related problems, and the members discussed demands and suggestions for beamline upgrades.

The fifth-term SPRUC research groups were voluntarily organized in each research field, and the research groups actively conducted research meetings. Each SPRUC research group has been collecting ideas and needs for beamline reorganization and innovative experimental techniques toward SPring-8 II, and has presented opinions and demands obtained through discussion in each field. As in the past, the sixth-term SPRUC research groups were recruited in the four research fields, namely, Life Science, Fundamental Characterization, Applied Materials, and Measurements, and will be launched next fiscal year.

IX. Outreach Activities

To reach out to new users in unexplored fields of application, SPring-8 holds various serialized seminars named “Workshop on Advanced Techniques and Applications at SPring-8”. From last year, most of the workshops are being held as video conferences because of COVID-19. Here are some representatives.

- 63rd: Advances in Measurement Informatics and Data Processing Using External Computational Resources
  August 31, 2021 • Video conference
- 65th: X-ray Emission Spectroscopy Analysis Technology and Beamline Reconstruction Plan in SPring-8-II
  October 22, 2021 • Video conference
- 64th: Frontiers of Development in Energy Catalysts and Fuel Cells
  December 3, 2021 • AP Shinagawa and Video conference

Also taking advantage of video conferencing, we held a weekly “Seminar on Advanced Techniques and Applications at SPring-8”. It has been held every Tuesday evening since January 2021. Over 2,500 participants in total took part in the eight seminars in the period from 11 May to 29 June.

SACLA

I. Machine Operation & Beamlines

Our tenth year of operations proceeded without any significant issues. Operation statistics are summarized in Table 1. The ratio of downtime to user time was kept below 4%, a reasonably low rate for linac-based light sources.

Table 1. Operation Statistics for FY2021

		Time (h)
Total operation time		5813.7
User time		
	BL1	1512
	BL2	2004
	BL3	2628
Facility tuning time		754
Downtime		199.3

In 2012, two beamlines, BL3 for XFEL and BL1 for broadband spontaneous light, were opened for users, while all experiments were conducted at BL3. As the newest beamline, construction of BL2 was completed during the summer shutdown of 2014, and first laser amplification was achieved on October 21. An upgraded beamline for soft X-ray FEL, BL1, which combines the prototype accelerator of SACLA (SCSS), started operation in 2016. Parallel user operation of BL2 and BL3 started in 2018.

II. User Program and Statistics

SACLA normally calls for public user proposals twice per year. Moreover, SACLA Feasibility Study Program has started since 2021A to provide an opportunity to experience the use on a trial basis for the purpose of dissemination and enlightenment.

In FY2016, JASRI introduced the proprietary research of General Proposals and the Proprietary Time-Designated Proposals. The project leaders of these proprietary proposals are not required to publish their research results, but required to pay each beamtime fee. In addition, to apply for the proprietary research the project leaders should be affiliated with a corporate enterprise located and registered in Japan.

Figures 1 and 2, and Table 2 provide statistics on proposals, users, and beamtime.

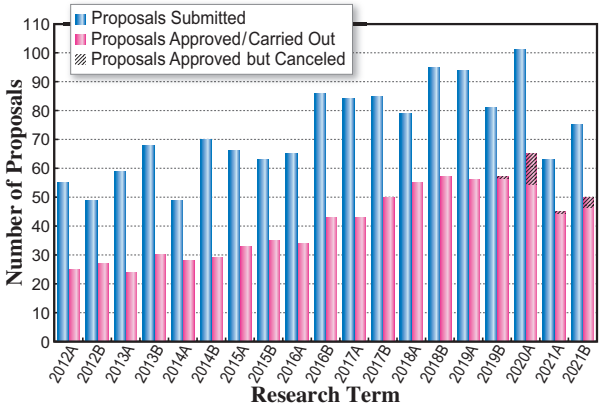

Fig. 1

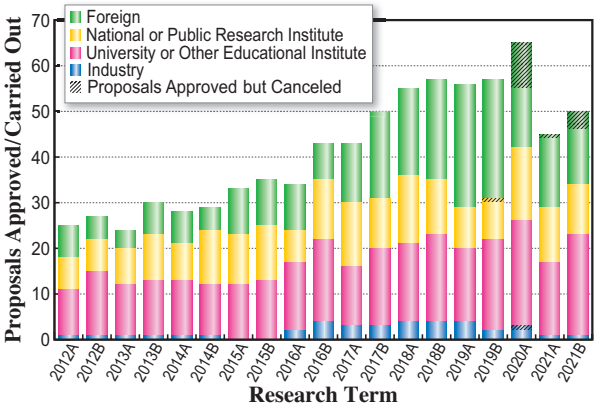

Fig. 2

Table 2. Number of proposals submitted, proposals approved/carried out, cumulative users, and beamtime available by research term

Half-year Research Term	Proposals Submitted	Proposals Approved / Carried Out					Cumulative Users	Beamtime Carried Out (Shifts)
			Priority Strategy Proposals	Non-proprietary	Proprietary			
				General Proposals	General Proposals	Time-Designated Proposals		
2012A	55	25	(12)	(13)	–	–	297	126
2012B	49	27	(19)	(8)	–	–	461	154
2013A	59	24	(15)	(9)	–	–	268	117
2013B	68	30	(19)	(11)	–	–	410	139
2014A	49	28	(20)	(8)	–	–	400	147
2014B	70	29	(17)	(12)	–	–	430	140
2015A	66	33	(23)	(10)	–	–	527	144
2015B	63	35	(23)	(12)	–	–	552	152
2016A	65	34	(21)	(12)	(1)	–	538	158
2016B	86	43	(21)	(20)	(1)	(1)	650	197
2017A	84	43	–	(43)	(0)	(0)	577	210
2017B	85	50	–	(50)	(0)	(0)	642	244
2018A	79	55	–	(55)	(0)	(0)	643	257
2018B	95	57	–	(56)	(0)	(1)	653	264
2019A	94	56	–	(55)	(0)	(1)	564	259
2019B	81	57	–	(56)	(0)	(0)	650	266
2020A	101	65	–	(54)	(0)	(0)	461	276
2021A	63	45	–	(44)	(0)	(0)	465	248
2021B	75	50	–	(46)	(0)	(0)	468	254

One shift = 12 hours at SACLA beamlines

Editor
Naoto Yagi
Japan Synchrotron Radiation Research Institute (JASRI)

Editing, Design & Layout
Marcia M. Obuti-Daté
Japan Synchrotron Radiation Research Institute (JASRI)

Printing
Hokuoh Printing Co.

JASRI
Information & Outreach Section
Users Administration Division

1-1-1 Kouto, Sayo-cho, Sayo-gun
Hyogo 679-5198 • JAPAN
Tel: +81-(0)791-58-2785 Fax: +81-(0)791-58-2786

Email: frontiers@spring8.or.jp
http://www.spring8.or.jp/

August 2022

SPring-8 SACLA

http://www.spring8.or.jp

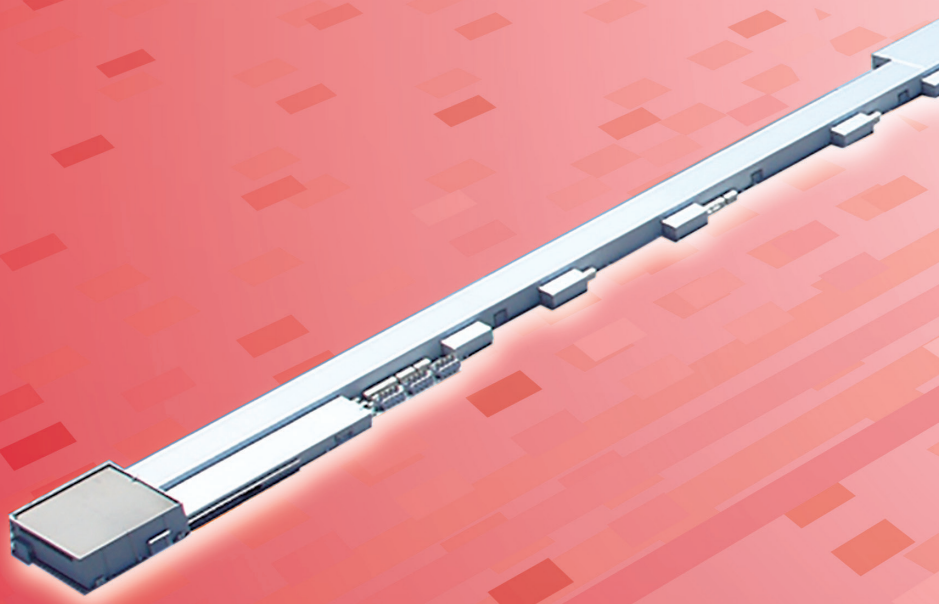

Japan Synchrotron Radiation Research Institute (JASRI)
1-1-1 Kouto, Sayo-cho, Sayo-gun, Hyogo 679-5198, Japan